Damage initiation and propagation in composite materials. Boundary element analysis using weak interface and cohesive zone models

The present thesis deals with:

- The development and implementation of different fracture mechanics models in Boundary Element Method codes, used as a numerical tool to solve elastic problems. In particular, in this thesis a linear elastic-brittle (weak) interface model and a cohesive zone model are implemented.

- The study of some mechanical properties of composite materials and different damage and/or failure mechanisms on macro, meso and micro scale that can be developed in these materials and their adhesively bonded joints.

The long-term and general objective of this thesis is to contribute to the development of physically based failure criteria for composite materials and their joints.

Ph.D. Thesis by Luis Távara Universidad de Sevilla - 2010

Damage initiation and propagation in composite materials. Boundary element analysis using weak interface and cohesive zone models

Ph.D. Thesis by
Luis Arístides Távara Mendoza

June 2010

GERM
GRUPO DE ELASTICIDAD Y RESISTENCIA DE MATERIALES

Thesis

DAMAGE INITIATION AND PROPAGATION IN COMPOSITE MATERIALS. BOUNDARY ELEMENT ANALYSIS USING WEAK INTERFACE AND COHESIVE ZONE MODELS

Presented to obtain the PhD. academic degree in Engineering
in fulfilment with the requirements for the European Doctorate
Mention at Universidad de Sevilla

Author: Luis Arístides Távara Mendoza

Advisors: Dr. Vladislav Mantič Leščišin

Dr. Enrique Graciani Díaz

Institution: Universidad de Sevilla,
Escuela Superior de Ingenieros,
Departamento de Mecánica de Medios Continuos
Teoría de Estructuras e Ingeniería del Terreno,
Grupo de Elasticidad y Resistencia de Materiales

Seville, June 2010

To my parents

Acknowledgements

In the following lines I would like to express my gratitude to all the people that took part, directly or indirectly, in the present PhD thesis during the last years.

First of all, I would like to express my sincere appreciation to my PhD advisors Dr. Vladislav Mantič and Dr. Enrique Graciani and also to the director of the group of Elasticity and Strength of Materials Dr. Federico París. Not only for the confidence they had in me, four years ago already, but for much more, for their attention and support, as well as all the opportunities they gave to me along this period, which have enabled my growth as a person and a researcher.

I also would like to express my gratitude to all the people that work in the group for their kindness and for bringing their attention and help when it was necessary. I can not forget either Ana Galindo, her patience and help with multitude bureaucratic issues.

During the fulfilment of this work, I had the opportunity to collaborate in two Research Groups. This would not have been possible without the kindness of Dr. Len Gray, from *The Oak Ridge National Laboratory* (USA) and of Dr. Alberto Salvadori, from *Dipartimento di Ingegneria Civile, Architettura, Territorio e Ambiente, Università degli Studi di Brescia* (Italy). The excellent treatment, their attention and experience and knowledge shared with me, allowed the maximum use of those research periods.

It would be unfair not to appreciate my colleagues and friends, Dr. Jhonny Ortiz, Dr. Ramón Rojas, Federico C. Buroni, Alejandro Estefani and José Reinoso, their support and their help in those things which do not appear directly in this thesis, but were completely necessary to the realization of this work. I can not forget my friends José Ramón, Diogenes, Chicho, Diego, Oscar and Carlos for their friendship and for sharing with me moments that make me feel like home.

And last, and probably the most important, to my family. To my parents, it is impossible to express in a few lines all the things they have always done for me, for their support and full confidence in me and all the decisions I have ever made. To Carolina, for supporting me always and for being herself.

"...When you want something, all the universe conspires in helping you to achieve it... It's the possibility of having a dream come true that makes life interesting..."

The Alchemist - Paulo Coelho.

Contents

List of Figures

List of Tables

Chapter 1

Introduction

The present thesis has been developed in the Grupo de Elasticidad y Resistencia de Materiales, Departamento de Mecánica de Medios Continuos, Teoría de Estructuras e Ingeniería del Terreno de la Universidad de Sevilla (Group of Elasticity and Strength of Materials, Department of Continuum Mechanics at the University of Seville).

The work is included in two fundamental research lines of the Grupo de Elasticidad y Resistencia de Materiales:

(i) The development and implementation of different fracture mechanics models in some Boundary Element Method (BEM) codes, used as a numerical tool to model the elastic problem. In particular, in this thesis a linear elastic-brittle (weak) interface model and a cohesive zone model are implemented.

(ii) The study of some mechanical properties of composite materials and different damage and/or failure mechanisms on macro, meso and micro scale that can be developed in these materials and their adhesively bonded joints.

The long-term and general objective of this thesis is to contribute to the development of physically based failure criteria for composite materials and their joints.

In the last years, many Finite Element Method (FEM) codes try to include some Cohesive Zone Models (CZM) to solve fracture problems. The CZM is characterized by a non-singular stress field in the crack tip neighborhood allowing for an efficient modeling of crack onset and growth using (quasi) uniform meshes. Thus, the initial motivation of the present study was to develop a numerical tool based on the BEM that included some non-singular fracture mechanics models, including CZM and possibly other models. Due to the fact that all the non-linearities that arise in the use of

cohesive zone models are located in the boundary, the BEM seemed to be a nice tool to solve the corresponding non-singular fracture problems.

1.1 Damage and Failure of Composite Materials. Motivation

The use of composite materials in the manufacturing of engineering components and structures has increased significantly during the last years. Composites versatility leads to their use in a wide variety of industries such as aeronautical, automobile, naval, wind energy and others where high technology is needed. In general, it can be said that technical composites are a combination of materials with final properties different, and superior in some sense, than those of the initial materials.

In composites reinforced by long fibres, the fibres are oriented in the direction where a greater stiffness and strength is needed. Composite materials are a preferable option for structural applications where a high values of the strength/weigth and stiffness/weigth ratios are required. In particular this is the reason why the use of fibre reinforced composites is becoming more extended in the manufacturing of aeronautical structures. Nowadays, composites are included in critical parts of aircrafts, giving a higher responsibility to this kind of materials.

A better and physically based knowledge of the damage and failure of these materials has become more important. Some of the most important damage and failure mechanism take place at different scales of the composite. At macro scale the onset and propagation of cracks in the adhesive layers that join the composite laminas is an important issue to be studied. Similarly, at meso scale the delamination problem between differently oriented plies in a composite laminate is another important damage mechanism. At micro scale, of the order of fibre radius size approximately, first the breakage of a single fibre when the load is applied in the direction of the fibre has been studied in the last years. Also as mentioned before, it is usual that fibre reinforced composites are designed to work specially in the fibre direction (longitudinal direction), thus a common failure mechanism occurs in the direction transversal to the fibres.

The present knowledge on damage and failure mechanisms in composite materials is not deep enough to allow for developing physically based failure criteria. Nevertheless, the use of composites is getting more and more extensive. These facts make specially interesting to carry out research in this area. The use of alternative models with different assumptions in com-

parison with the classical Linear Elastic Fracture Mechanics, seems to be a promising tool to, first, understand the different problems described and their failure mechanisms and, then, to carry out the design of composite structures.

1.2 Non-singular fracture mechanics models: Cohesive Zone Models and Linear Elastic-Brittle (Weak) Interface Model. Background

The majority of methods used to simulate crack propagation, based on the classical Linear Elastic Fracture Mechanics (LEFM), made difficult the study of crack initiation occurring in the first step of fracture process, since they assume the presence of a crack. Recently, other models have been intensively developed, e.g., cohesive crack models [12, 32, 33, 34, 35, 82, 106, 124, 128] and linear elastic interface models [58, 68, 69, 80, 92].

In particular, Cohesive Zone Models (CZM) assume different hypotheses to those adopted in LEFM avoiding the presence of stress singularity at the crack tip. During the sixties the cohesive zone like models were used to simulate two different behaviors: brittle fracture [12] and ductile fracture [55]. In CZM a tension softening in front of the traction-free crack tip is assumed, in the so-called fracture process zone. In the simplest, most usual formulation of the CZM, all the body volume remains elastic, and linear elasticity may be used to solve the response of the media surrounding the crack. The nonlinearity is included in the boundary conditions along the crack line [6, 15]. The CZM has been widely used to model the behavior of quasi brittle materials, especially concrete-like materials [34, 35, 36], by means of the Finite Element Method (FEM). Needleman used the CZM to study the decohesion along a fibre-matrix interface [124], introducing an exponential law that is extensively used nowadays. Ortiz and co-workers [32, 128] also presented works regarding CZM. More recently, Maier introduced the CZM into a Symmetric Galerkin Boundary Element Method (SGBEM) code, by means of the linear complementary problem concept. The CZM has also been used to study the delamination problem in composite materials [33]. Although, in its beginnings the CZM was used to study the behavior of concrete-like materials, its recent use in composites open a wide range of research topics at different scales. Thus, as mentioned before, at the micromechanical scale the behavior of fibre-matrix interfaces can be studied, at the meso scale the delamination among composite laminas can be modeled and, finally, at the macro scale the behavior of adhesively

bonded joints can be analyzed.

A different way to describe the behavior of (adhesively) bonded solids is to model an (adhesive) elastic layer, sometimes called interphase, as a continuous distribution of linear elastic springs with appropriate stiffness parameters. The introduction of this model is attributed to Goland and Reissner [69], and is called *Linear Elastic Interface*, *Weak Interface* or *Imperfect Interface* [58]. Klarbring [92] and Geymonat *et al.* [68], assuming small thickness and small stiffness of the elastic layer, developed asymptotic expansion methods to obtain a simplified model (linear elastic interface model) in which the elastic layer is treated as a material surface, disappearing from a geometrical point of view but being represented by its energy of adhesion. A comprehensive review of pioneering works in this kind of interface models is given in [68]. Benveniste and Miloh [16] and Hashin [80] developed novel approaches for the deduction of general constitutive laws for imperfect interfaces, not requiring small stiffness of the elastic layer in comparison with the adjacent solids.

An in-depth analysis of a crack within a linear elastic interface between two isotropic half planes subjected to remote uniform stresses was presented by Lenci [102]. Lenci obtained the integral equation that governs this problem and solved it numerically using classical solutions for elastic isotropic half-planes subjected to a point force as Green functions. Lenci also computed the ERR rate of a crack as the stored energy in the unbroken spring situated at the crack tip. This fact was also independently shown later by Carpinteri *et al.* [37].

With reference to this model, similar approaches by means of Finite Element Method (FEM) were developed. Particularly worthy of mention is the numerical implementation of imperfect interfaces developed and discussed by Nairn [122]. More recently, Lebon and Zaittouni [97] have modeled a soft thin elastic layer under unilateral contact and dry friction conditions, using asymptotic expansions.

1.3 Boundary Element Method. Background

Although the application of Boundary Integral Equations (BIEs) to the solution of problems governed by partial differential equations was developed long time ago, it is widely accepted that the Boundary Element Method (BEM), as an approach to the numerical solution of the BIEs, applied to the elastic problem in its direct formulation, starts with the fundamental contribution of Rizzo and Cruse [144]. The BEM acquired a bigger rele-

vance in the 1970s and 1980s, in engineering, as an alternative to the Finite Element Method (FEM).

The principal advantage of BEM against FEM is that the geometry discretization is substantially easier, as only the boundaries are meshed. This fact makes BEM specially interesting to study fracture mechanics problems. Less data preparation time is usually needed. Also, a high accuracy of stresses computed by BEM is advantageous for engineering applications. Nevertheless it has some drawbacks, in its traditional formulation, as it is limited to a less number of applications and that the non-symmetric matrices generated are fully populated for single domain problems.

There are two basic procedures that are generally used to reduce the continuous boundary integral equations to a finite system. The simpler procedure is collocation, wherein the fulfilment of the boundary integral equations is explicitly enforced at a finite set of points. In its simplest form, these collocation points are chosen to be the nodes used to discretize the boundary [5, 10, 39, 120, 131] and the final matrix obtained is non-symmetrical. The advantages of the traditional collocational approach include a simpler formulation and implementation, reliable results guaranteed by a large experience in the solution of engineering problems. Among its drawbacks, it is noticeable that it is insufficient to solve fracture mechanics problems efficiently. In order to solve this problem several modifications of the collocational approach have been proposed.

In contrast to collocation, the Galerkin approach does not require that the integral equations are satisfied at any point. Instead the equations are enforced in a weighted average sense. The symmetric-Galerkin formulation was introduced by Sirtori [159] and studied by Hartmann *et al.* [78], and then extensively developed by Maier and co-workers [95, 107, 109, 160]. Excellent reviews of SGBEM can be found in [27, 95, 161]. Recent applications of SGBEM to the solution of domain decomposition problems by enforcing coupling conditions in a weak form can be found in [172].

In general, Galerkin is more accurate than collocation, and also provides a more elegant treatment of boundary corners [161]. A symmetric linear system with positive and negative defined blocks in the diagonal allows an efficient solution in terms of time and memory computing. The problem of extra unknowns, that sometimes is presented in the collocational approach, disappears. An easy and efficient treatment of cracks is obtained. The associated unknown, in the BIEs used to discretize the crack, is the jump of displacements between the crack faces inside an homogeneous material. Its main drawback is the more complex theoretical formulation and implemen-

tation due to the double integration needed and the use of the hypersingular boundary integral equation (HBIE).

1.4 Objectives of the thesis

The Grupo de Elasticidad y Resistencia de Materiales started to study fracture problems in composite materials and to develop suitable BEM tools at the beginning of 1990s. Thus, at the beginning of this thesis a well based knowledge of different composite material problems was already established in the research group. The aim of the present thesis is the study and development of non-singular fracture mechanics models and their implementation in BEM codes, applied to some particular problems of damage and failure in composites. The long term objective of this research is to contribute to the generation of physically based failure criteria at a macro, meso and micro scale for composite materials.

The tasks carried out to contribute to fulfill these general objectives are described in the following.

Development of theoretical formulation and codes implementation:

- Cohesive Zone Model, to study the crack onset and growth inside homogeneous materials and at interfaces, including:
  - Suitable implementation of a cohesive zone model into a 2D Symmetric Galerkin BEM code for the analysis of plane problems.
  - The development and use of arc-length algorithms, to solve nonlinear problems in presence of Cohesive Zone Models, with several variants.
- Linear Elastic-Brittle Interface Model, to study the crack onset and growth at interfaces, requiring:
  - Suitable implementation of linear elastic-brittle model into the collocational BEM code for the analysis of plane and axisymmetric problems, that allows the use of non-conforming meshes and contact zones.
  - The development and use of a sequentially linear solving algorithm.
  - A computing time improvement by the use of an efficient linear solver in the collocational BEM code.

- Application of BEM to the solution of 3D problems of composite materials, involving:
  - The development of general and efficient expressions of the fundamental solutions and its derivatives for transversely isotropic materials.
  - Implementation of the fundamental solutions and its derivatives in a collocational 3D BEM code.

Study of relevant particular cases of damage mechanisms, in form of cracks onset and growth, in composite materials at macro, meso and micro scale by means of the Linear Elastic-Brittle Interface Model introduced.

- Analysis of a crack in a thin adhesive layer in a DCB specimen (macro scale).
- Delamination cracks in [0/90] symmetric laminates (meso scale).
- The single fibre fragmentation test (micro scale).
- Micro-mechanical behavior of cracks between matrix and fibre under transversal loads (micro scale).

1.5 Organization of the thesis

The present thesis is organized in 14 Chapters. Leaving aside the present introduction and the last chapter of conclusions and future developments, it can be divided in three parts:

Part 1: Revision of different damage and failure mechanisms: A brief introduction and bibliographic review of some damage and failure mechanisms of composite materials and their joints are presented in Chapter 2.

Part 2: Development of models and numerical tools: Chapter 3 to Chapter 9 and the Appendix A are included in this part. Chapters 3 and 4 introduce the non-singular fracture mechanics models that will be used to study the particular problems detailed in Chapter 2. Thus, some of the principal cohesive models are described in Chapter 3, including some slight modification of one of them. The new linear elastic-brittle interface formulation is introduced and explained in Chapter 4. The BEM has proved

to be an efficient tool to study fracture problems, thus the Boundary Integral Equations as well as the BEM and its two main approaches are described in Chapter 5. In Chapter 6 the implementation of an efficient linear solver in BEM codes are discussed. Also non-linear solving algorithms, in particular a sequentially linear analysis and an arc-length algorithm are described in this chapter. This algorithms are necessary due to nonlinearities introduced by the non-singular fracture mechanics models employed. The formulation and implementation of a cohesive zone model in the 2D SGBEM code is presented in Chapter 7, along with some numerical results for the validation of the present SGBEM implementation. In Chapter 8, the implementation of the linear elastic-brittle interface formulation in the collocational BEM code is described and verified, using an analytic and numerical study of cracks in an adhesive layer between orthotropic materials modeled by means of the linear elastic-brittle interface formulation. Finally, in Chapter 9 the formulation and implementation of transversely isotropic materials in 3D BEM is shown, presenting some numerical examples in order to validate the fundamental solutions developed and their implementation.

Part 3: Study cases of damage and failure in composite materials at micro, meso and macro scale: In this part, particular problems related to damage and failure of composite materials are studied by means of the linear elastic-brittle interface formulation implemented in the 2D and axisymmetric collocational BEM code. The interlaminar fracture toughness test of composite materials is modeled in Chapter 10, where a comparison of experimental data with some numerical results is also presented. An initial study of delamination cracks in [0/90] symmetric laminates is presented in Chapter 11. Some numerical results for the single fibre fragmentation test are presented in Chapter 12. Finally, the micro-mechanical behavior of cracks between matrix and fibre under transversal loads is studied in detail in Chapter 13. First, an isolated fibre embedded in a matrix under transversal uni-axial tension loads or biaxial transverse loads model (either tension-tension or tension-compression) is studied. Thus, an initial study of a fibre cluster embedded in a large matrix (multi-fibres problem) is also presented.

Chapter 2

Some damage and failure mechanisms of composite materials and their joints

In this thesis some of the relevant failure modes in composite materials are going to be studied. In the present chapter a revision of some damage and failure mechanisms of composite materials reinforced by long fibres and their joints (at macro, meso and micro scale) is presented as well as most important previous contributions are commented.

2.1 Interlaminar Fracture Toughness Test (Macro scale)

A good understanding and characterization of the adhesive layer behavior is very important in the quality evaluation of adhesively bonded joints, and particularly in determining the parameters that characterize their resistance to fracture and failure. These parameters can then be used in the design and quality control of the production processes. The quality of an adhesive joint between composite laminates is usually evaluated by the Interlaminar Fracture Toughness Test, where an estimation of the critical interlaminar fracture energy (G_{Ic}) is obtained. The tests used to evaluate the interlaminar fracture toughness in composite-composite joints are performed by well-known standard procedures [2, 87]. The specimen usually used is the Double Cantilever Beam (DCB), formed by two laminates joined by an adhesive layer. This test method can serve to establish quantitatively

the effect of fibre surface treatment, local variations in fibre volume fraction, and processing and environmental variables on G_{Ic} in an adhesively bonded joint of a particular composite material. A set up of this test in the laboratory can be seen in Fig. 2.1.

Figure 2.1: Interlaminar fracture toughness test set-up.

The interlaminar fracture toughness test is also used as a prediction method for delamination growth and to compare the performance of different composite laminates [67]. The test method for mode I delamination was suggested by Wilkins *et. al.* [176] using again a double cantilever beam (DCB) similar to that used for the adhesive joint. A comprehensive review of several works considering the delamination process and the DCB test can be found in [67, 164].

Tools of the classical Fracture Mechanics Principles have often been employed in the analysis of delamination in composites, by means of the Virtual Crack Closure Technique. However, there are alternatives to Fracture Mechanics, such as damage mechanics and different interfacial models. The analysis of delaminations depends heavily on computational methods, particularly finite elements [164]. Recent efficient formulations that more accurately capture the stress and strain state near the delamination front

are now available. These numerical tools, coupled with well-designed experiments, should greatly enhance our understanding of the delamination behavior in composites.

An analysis of this problem by means of the Linear Elastic-Brittle Interface Model will be studied in Chapter 10.

2.2 Delamination cracks in [0/90] symmetric laminates (Meso scale)

The characterization of the mechanism of failure of cross ply laminates is still an open topic. A comprehensive review of state of the art of the present problem was done by Garg [67]. In particular, several aspects related with causes of delamination, i.e. free edge effect, impact and transversal cracking, are discussed in [67].

Particularly, for the damage in a [0/90] laminate, it is generally accepted that it appears in accordance with the following steps: the application of tension load generates almost immediately the appearance of transverse microcracks in the 90° ply; the coalescence of these microcracks leads to the appearance of a transverse macrocrack that can propagate in the 90° ply towards the interface with the 0° ply; once reaching the interface, it may initiate single or double deflection at the ply interface, then propagating along the interface as a delamination crack. Many relevant contributions to the understanding of this damage mechanism have recently been reviewed in an excellent paper by Berthelot [17]. A picture of a cracked [0/90] laminate, is represented in Fig. 2.2.

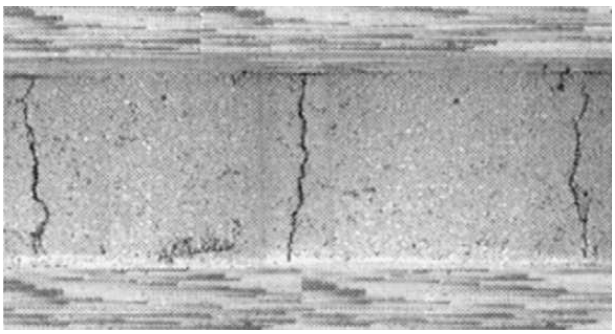

Figure 2.2: [0/90] laminate with damage produced by a longitudinal load. Taken from [24].

Since this review, several papers have appeared shedding more light on the understanding of this basic problem. A significant number of papers is devoted to the numerical modeling of this kind of damage and its connection with different scales of modeling. The study of the effect of the spatial distribution of the transverse cracks has also been addressed, as well as some particular questions regarding the effect of fatigue, the influence of mixed mode fracture and the effect of residual stresses [130].

Transversal cracking analysis is an important issue because these cracks reduce the effective stiffness and strength of the laminates. Transversal cracks induce local stress concentrations at the crack tip and could originate an important delamination along the interface of the 90° ply with 0° ply. Longitudinal cracks of the matrix and rupture of the fibre in the 0° ply are only activated at very high values of load in the case of static loading or for a high number of cycles in the case of fatigue loading [23].

The presence of transversal cracks in the matrix in the 90° ply leads to a redistribution of the load in the adjacent plies (0°). That is why, laminates with 90° and 0° plies usually have the 0° plies in the outer parts of the laminates. Under static loading most transversal cracks go through the whole 90° ply thickness. For this reason, the reduction of the whole problem to the stress and strain distribution analysis using a 2D model of an elemental cell between two consecutive cracks seems to be a reasonable approximation. This elemental cell is characterized by the distance between the transversal cracks and the thicknesses of the plies. One of the first 2D models was developed by Berthelot [17].

In Chapter 11, an initial study regarding this topic is done by means of the Linear Elastic-Brittle Interface Model introduced herein.

2.3 Single fibre Fragmentation Test (Micro scale)

Single fibre fragmentation test is an experimental technique widely used to characterize fibre–matrix interface in composite materials. In this test a small sample containing one sufficiently long fibre embedded in a resin matrix is loaded in the direction of the fibre. The aim of the test is to obtain, as a result of the applied load, a series of fibre cracks which split the fibre into an increasing number of fragments and debonding cracks that appear at the ends of the fibre cracks and grow along the fibre-matrix interface (see, e.g., Kelly and Tyson [91] for fundamentals of this test method and Graciani et al. [72] for an analysis of the different mechanisms of failure that can be observed in the sample). In the present thesis we will focus on

the study of the SFFT in a glass-epoxy composite material.

As the fibre presents brittle fracture behavior, and the maximum allowable strain is much lower in the fibre than in the matrix, after reaching a certain value of the applied load the fibre breaks at its weakest location. After breaking, the axial stress in the fibre decays to zero at the plane of failure, as depicted in Fig. 2.3(a). After this first failure occurs, a slight increase on the applied load results in the successive fragmentation of the fibre, as shown in Fig. 2.3(b). In addition, due to the high amount of energy released, after the fibre breakage takes place, small debond cracks appear in the fibre-matrix interface. In the final stage, depicted in Fig. 2.3(c), the debond cracks grow rapidly and, consequently, axial stress in the fibre is not high enough to cause the appearance of new fragments and an increase on the applied load causes only a further debond growth. On the other hand, if the matrix and the interface are tough enough, the second and third stages of the test may not take place. In this case, as the fragmentation process progresses, the amount of fibre which is subjected to high axial stresses diminishes, and consequently, saturation is reached when the fragment sizes are too small to allow that the axial stress in the fibre reaches a value high enough to cause new fragments in the fibre, as shown in Fig. 2.3(d).

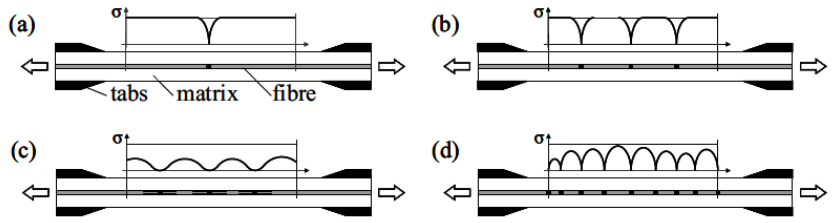

Figure 2.3: SFFT stages: (a) First fibre failure. (b) Fragmentation process. (c) Debond growth. (d) Saturation without debond growth. Taken from [71].

There are distinct approaches for characterizing interface failure properties from the results of the single fibre fragmentation test. Differences arise in the use of analytical, experimental or numerical techniques for estimating the stress state in the sample, and also in the use of failure criteria based on the interface strength or failure criteria based on fracture mechanics [71].

The exact solution of stresses at the interface contains shear singular stresses in the vicinity of the crack tips when modeled by means of the Lin-

ear Elastic Interfacial Fracture Mechanics, considering a perfectly bonding between fibre and matrix ahead of the crack tip. For this reason, the energy approach is considered more appropriate for the characterization of the interface failure in presence of singular stress states [170]. This approach considers that crack propagation would take place when the total energy released per unit length during the propagation, i.e. the Energy Release Rate (ERR), equals the work needed to create the new unit crack surfaces. As the propagation takes place under pure mode II, failure of the interface is characterized by the interface fracture toughness, which is the critical value of the mode II ERR (usually denoted as G_{IIc}) [72].

As the problem is axially symmetric, assuming that fragments are long enough and evenly distributed, the elastic solution in the vicinity of each fibre break is repetitive and can be obtained from the axi-symmetric analysis of the piece of sample corresponding to one half of a fragment.

This problem is solved by means of the axisymmetric BEM code and the Linear Elastic-Brittle Interface Model as will be detailed in Chapter 12.

2.4 Fibre matrix debonding under transversal loads (Micro scale)

Composite unidirectional laminates usually exhibit a failure mechanism called matrix failure or interfibre failure when they are subjected to loads transverse to the fibres. This failure mechanism is characterized by the debonding of some fibres when the tension loads are driving the failure process. The connection between the initial debonds and the final macro crack has several steps: the onset and growth of the debonds (as fibre-matrix interface cracks), the kinking of some of these cracks into the matrix and the final coalescence of the cracks kinked from different fibre-matrix interfaces, see París *et al.* [132], Correa *et al.* [47, 46] and Mantič *et al.* [113]. Fig. 2.4 represents a micrograph of the damage observed in a part of the composite.

The problem of an elastic circular (in 2D) or cylindrical (in 3D) inclusion embedded in an elastic matrix with a partial debond at their interface (modeled as an interface crack) subjected to a remote uniaxial load at infinity has been intensively studied in the past. A theoretical basis for any analysis of this problem was established by the seminal work of Toya [169], where the perfect fibre-matrix interface model and the open model of interface cracks were assumed. Toya deduced analytical expressions for stresses, displacements and the total Energy Release Rate (ERR) as a function of the debond angle and applied the latter in a fracture criterion to assess the

Figure 2.4: Damage in a composite material under tension transverse to the fibres. Taken from [46].

debond growth along the fibre-matrix interface.

Zhang *et al.* [184] presented experimental results for transverse single-fibre specimens, and Varna *et al.* [170] studied the debond growth along the fibre-matrix interface modifying Toya's [169] ERR based fracture criterion in order to take into account an increasing participation of the shear fracture mode when the debond grows. París *et al.* [134] and Varna *et al.* [171] compared different aspects of Toya's [169] solution and the elastic solution obtained by the collocational Boundary Element Method (BEM) [5, 10, 39, 120, 131] using a contact algorithm [25]. Recently, Mantič [112] applied Toya's solutions for stresses and ERR to characterize the debond onset by means of a coupled stress and energy criterion. A study of matrix crack growth across clusters of circular inclusions was presented by Williams *et al.* [177] and Roberts *et al.* [146] using a Symmetric Galerkin BEM code [161].

With reference to fibres embedded in a matrix, many works considered that the condition of perfect bonding at the undamaged fibre-matrix interface is often inadequate in describing the physical nature and mechanical behavior of this interface. See Gao [66] and Hashin [80] for a review of related works modeling the fibre-matrix interface as an elastic layer with vanishing thickness. Hashin [79] and Gao [66] obtained closed-form solu-

tions of a circular inclusion problem, assuming an undamaged linear-elastic interface, under remote uniform shear and tension, respectively. Recently, Wang *et al.* [174] obtained a solution for an elliptical inclusion under remote tension, generalizing the solution obtained in [66]. Another generalization of the solution for a circular inclusion introduced in [66] was presented by Bigoni *et al.* [18] considering a general remote load. According to [18, 66], the stresses are homogeneous inside the circular inclusion, with an undamaged linear-elastic interface under remote loads when the stiffnesses of the continuous spring distribution in radial and tangential directions are equal. A study of the interaction of a matrix crack and a circular inclusion with an undamaged linear-elastic interface was also introduced in [18]. An efficient numerical approach to solve the problem of an infinite isotropic elastic plane containing a large number of randomly distributed circular elastic inclusions with imperfect interfaces was introduced by Mogilevskaya and Crouch [119]. They used a Galerkin method to solve a complex hypersingular integral equation with the unknown tractions and displacement discontinuities at each circular boundary approximated by truncated complex Fourier series.

Some other works made use of the well known cohesive models to represent the behavior of the inclusion-matrix interface. Needleman [124] developed a cohesive model to study the debonding of a spherical inclusion using FEM. Han *et al.* [76] used a softening decohesion model to describe the evolution of interfacial failure in fibre-reinforced materials. Xie and Levy [182] studied a circular inclusion embedded in an unbounded matrix subjected to different remote load configurations, using the cohesive law introduced by Needleman. The role of the fibre size on the instability phenomena (e.g. snap-back) in fibrous metal matrix composites was studied by Carpinteri *et al.* [38], by means of a cohesive model, describing both decohesion and contact at bi-material interfaces. The influence of different parameters of the PPR (Park-Paulino-Roesler) potential-based cohesive model on the macroscopic behaviour of a composite with cylindrical inclusions, accounting for inclusion-matrix debonding, was recently studied by Ngo *et al.* [125], where also an approach for the determination of the cohesive model parameters from a real macroscopic behaviour of a composite was introduced.

An analysis of crack onset and propagation in this problem by means of the Linear Elastic-Brittle Interface Model will be presented en Chapter 13.

Chapter 3

Cohesive Zone Models

The majority of methods used to simulate crack propagation, based on the classical Linear Elastic Fracture Mechanics (LEFM), made difficult the study of crack initiation occurring in the first step of fracture process, since they assume the presence of a crack. Recently, other models have been intensively developed, like energetically based delamination model [93, 147] or cohesive crack models [32, 33, 34, 35, 82, 106, 124]. In particular, cohesive crack models assume hypotheses different to those adopted in LEFM avoiding the presence of stress singularity at the crack tip. These models are suitable to study both the crack initiation and crack propagation.

3.1 Review of some holonomic cohesive models

In a number of engineering situations, especially when the main external actions vary with a monotonically increasing load factor, irreversible behaviors such as local unloading in damaged zones can a priori be assumed to play a minor role in the overall structural response. In such cases non-linear material behaviors which actually are irreversible (i.e. history-dependent, nonholonomic) may be interpreted as reversible i.e. holonomic [152].

Cohesive Zone Models (CZM) combine the Fracture Mechanics formulation with Strength of Materials for both crack initiation and propagation. In a cohesive zone formulation, displacement discontinuities across the crack, δ_i $(i = 1, 2, 3)$, are related to the traction vector, t_i, in a zone located ahead of the actual crack tip [32, 40, 128], see Fig. 3.1. A physically justified constitutive law is required for modeling the behavior of the material in the process zone.

The constitutive law of a holonomic CZM may be formally written

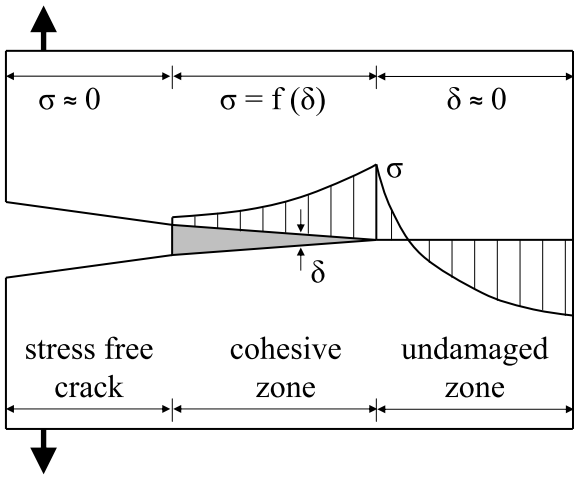

Figure 3.1: Cohesive crack model in mode I with the boundary conditions along the central line: zero stress along the broken part, softening law along the cohesive zone and zero relative displacements along the uncracked ligament.

as $\mathbf{t} = \mathbf{t}(\boldsymbol{\delta})$. This relation is in its essence a non-linear and non-invertible relation. This law is called holonomic, as it may work only when external loads are monotonically increasing and no secondary effects (friction, among others) may cause local unloadings. A fundamental aspect in the formulation of the constitutive model is the requirement that the energy dissipated during crack propagation must be equal to the fracture energy, i.e., the following relation must be satisfied:

$$G_c = \sum_{i=1}^{3} \int_0^{\delta_i^f} t_i d\delta_i \tag{3.1}$$

where δ_i^f is the "final" value (not necessarily finite) of the relative displacement leading to the vanishing of cohesive forces.

Some of the most important cohesive zone models, in their holonomic form, are briefly described in the following. Nevertheless, it is important to notice that all these models can be generalized to a non-holonomic form considering a suitable unloading-reloading path.

Hillerborg´s model

It appears that Hillerborg and coworkers [82] were the first proposing explicit relations between cohesive tractions and relative displacements with a softening branch. These relations are very simple, including relations with an initial plateau, see Fig. 3.2(a) and Fig. 3.2(b). A linear softening monotonic curve is assumed for pure fracture mode I.

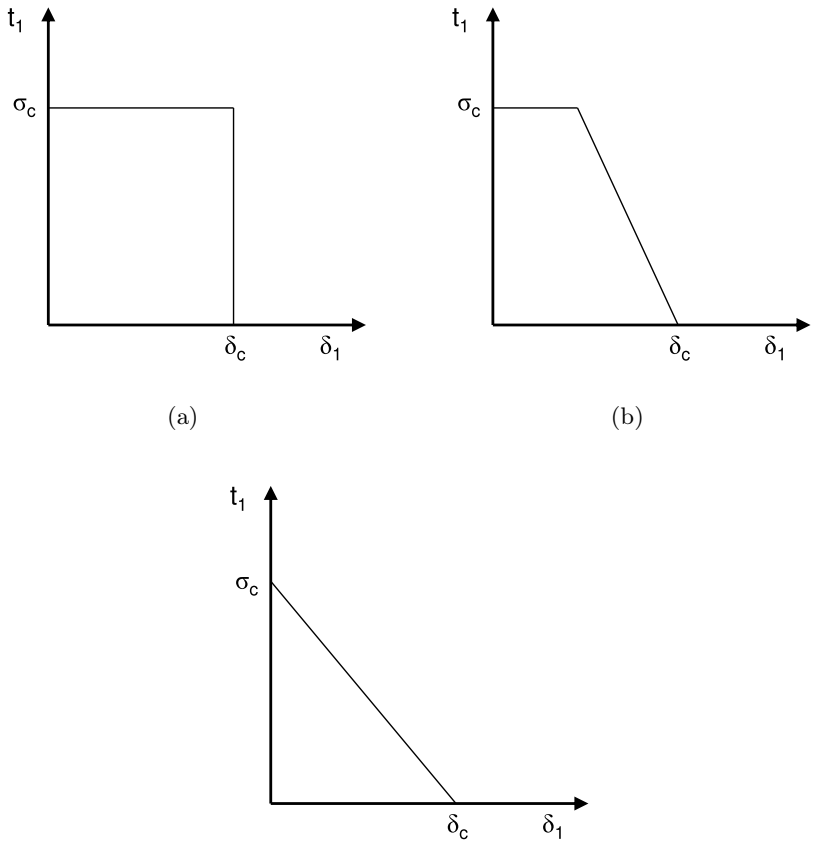

Figure 3.2: Examples of possible assumptions of variation of normal stress t_1 with crack opening δ_1 as assumed by Hillerborg *et. al.* [82].

At $\delta_1 = 0$ the maximum normal traction t_1 equals the tensile strength, σ_c. The cohesive traction vanishes at $\delta_1 = \delta_c$, the critical opening dis-

placement in mode I. As discussed in [82], it seems that for many materials the best choice, among the laws presented therein, is the law depicted in Fig. 3.2(c). The linear softening curve of this law is described by the relations:

$$t_1 = \sigma_c \left(1 - \frac{\delta_1}{\delta_{1c}}\right) \tag{3.2}$$

$$\delta_{1c} = 2\frac{G_{Ic}}{\sigma_c} \tag{3.3}$$

This cohesive law requires two material parameters, σ_c and G_{Ic} for instance. Neither damage nor unloading-reloading are considered. It is noticeable that the value of the fracture toughness in mode I, G_{Ic}, is usually the most used parameter to characterize a cohesive zone model. Modifications of this linear model which includes mixed mode propagation have been developed in the last years [33, 50, 56].

Bilinear softening model

This model is a generalization of the linear model described previously, see Fig. 3.2(c). The bilinear softening branch with break point has been found to approximate accurately mode I experimental results concerning concrete-like materials and seems to be advocated by several researchers in the field, see [56, 138] and references therein.

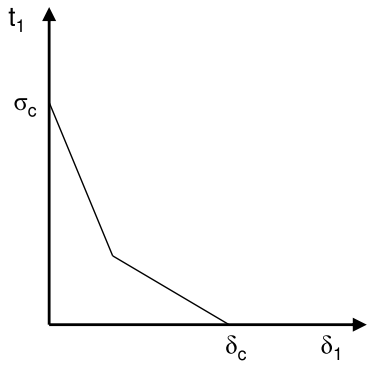

Figure 3.3: General bilinear softening cohesive function.

The dependence of t_1 on δ_1 is defined by four material parameters. These are, e.g. the tensile strength σ_c, the coordinates of the "break point" and the critical opening displacement δ_c, see Fig. 3.3, above which full

traction-free separation of the crack faces appears. Instead of this last parameter, the fracture energy G_{Ic} can be taken. An alternative choice of material parameters, in order to express the bilinear law in terms of a linear complementarity problems, is presented in [152].

This law has also been used to study problems involving composite materials and mixed mode propagation [50].

Xu-Needleman model

The relation between tractions and relative displacements in this model arises from an expression of free energy density per unit deformed area [183]. This idea was initially based on a study of void nucleation appearing at atomic level.

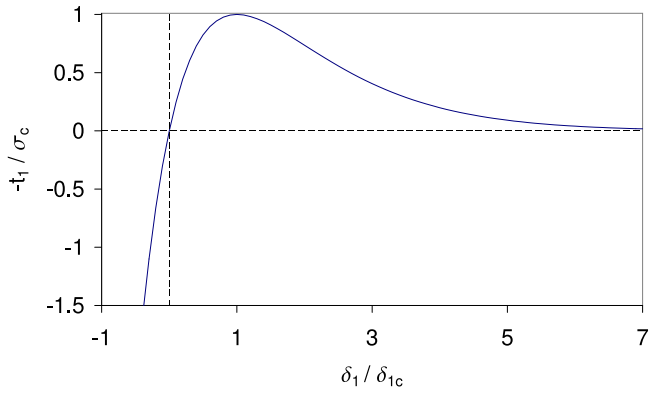

Figure 3.4: Normal tractions across the cohesive surface as a function of δ_1 with $\delta_2 = 0$ in Xu-Needleman CZM [183].

The final expressions of this cohesive law, see Fig. 3.4 and Fig. 3.5, take the form for normal tractions:

$$t_1 = e\sigma_c e^{-\frac{\delta_1}{\delta_{1c}}} \left\{ \frac{\delta_1}{\delta_{1c}} e^{-\frac{\delta_2^2}{\delta_{2c}^2}} + \frac{1-q}{r-1} \left[1 - e^{-\frac{\delta_2^2}{\delta_{2c}^2}} \right] \left[r - \frac{\delta_1}{\delta_{1c}} \right] \right\} \tag{3.4}$$

and for tangential tractions:

$$t_2 = e\sigma_c \left(\frac{2\delta_2\delta_{1c}}{\delta_{2c}^2} \right) \left\{ q + \left(\frac{r-q}{r-1} \right) \frac{\delta_1}{\delta_{1c}} \right\} e^{-\frac{\delta_1}{\delta_{1c}}} e^{-\frac{\delta_2^2}{\delta_{2c}^2}} \tag{3.5}$$

where, $e \simeq 2.718$ is the base of the natural logarithm, σ_c is the maximum

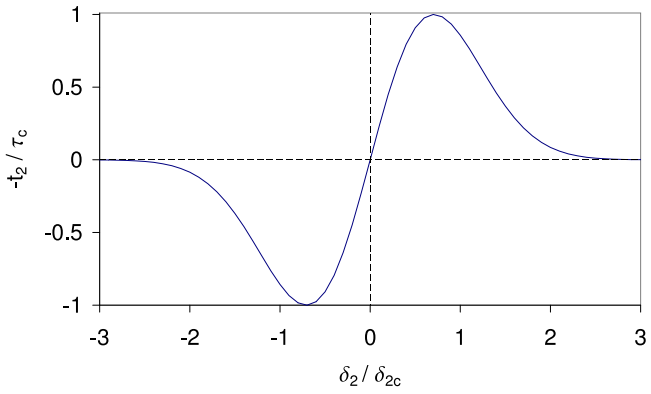

Figure 3.5: Shear tractions across the cohesive surface as a function of δ_2 with $\delta_1 = 0$ in Xu-Needleman CZM [183].

cohesive normal traction in mode I, τ_c is the maximum cohesive tangential traction in mode II, δ_{1c} is a characteristic normal opening displacement in correspondence with the value σ_c, δ_{2c} is a characteristic tangential displacement in correspondence with the value τ_c, τ_c is reached when $|\delta_2| = \sqrt{2}\delta_{2c}/2$. The parameters q and r are defined as:

$$q = \sqrt{\frac{1}{2e}}\frac{\tau_c \delta_{2c}}{\sigma_c \delta 1c} \qquad \text{and} \qquad r = \frac{\delta_1^*}{\delta_{1c}}$$

where δ_1^* is the normal opening displacement in correspondences with the complete shear sliding with $t_1 = 0$ (a sort of "measure of dilatancy").

It appears that this model served as a motivation to Ortiz and coworkers [32, 128] to develop another somewhat simpler CZM. In fact, the solution for mode I, described by (3.4), coincides with the corresponding expression obtained in the model due to Ortiz and Pandolfi [128] in the positive normal traction part. The Ortiz and Pandolfi model will be described in the following in more details because it is the one that has been implemented in the present thesis.

3.2 Ortiz-Pandolfi model

The Ortiz-Pandolfi model [128] has been implemented and used in the present thesis. The reason for this choice was the simplicity of this model, with only a few parameters. In fact only two parameters associated to mode I and one parameter characterizing sensitivity to a fracture mode mixity are required to be defined. This fact makes easy to adjust the values

of the model parameters. It should be mentioned that, a small modification of the Ortiz-Pandolfi model has been introduced for mode I in the present thesis to cover in a reasonable way the compressive behavior ahead of the crack tip.

The relation between tractions and relative displacements in the cohesive zone proposed in [32, 128] requires the definition of the *effective opening displacement* δ:

$$\delta = \sqrt{\delta_1^2 + \beta\delta_2^2}. \tag{3.6}$$

Different weights are assigned to the normal opening displacement (δ_1) and sliding (tangential) displacement (δ_2) through the parameter β. Following [32, 128], the existence of a free energy density per unit undeformed area, ϕ, is postulated. In isothermal conditions, under the assumption of an isotropic material, it has the form:

$$\phi = \phi(\delta, \boldsymbol{q}), \tag{3.7}$$

where $\boldsymbol{q}$ is a suitable collection of internal variables which describe the elastic processes participating in the decohesion process. From the first and second laws of thermodynamics, it is possible to show that the cohesive law takes the form:

$$\boldsymbol{t} = \mathrm{grad}_\delta[\phi]. \tag{3.8}$$

Finally, the evolution of internal variables is governed by a set of kinetics relations of the general form:

$$\dot{\boldsymbol{q}} = f(\delta, \boldsymbol{q}), \tag{3.9}$$

if it is assumed that the free energy ϕ depends on δ only through the effective opening displacement. This implies that:

$$\boldsymbol{t} = \mathrm{grad}_\delta[\phi] = \frac{\partial\phi}{\partial\delta}\frac{\partial\delta}{\partial\delta_1}\boldsymbol{n}_1 + \frac{\partial\phi}{\partial\delta}\frac{\partial\delta}{\partial\delta_2}\boldsymbol{n}_2 = \frac{\partial\phi}{\partial\delta}\left(\frac{\delta_1}{\delta}\boldsymbol{n}_1 + \beta^2\frac{\delta_2}{\delta}\boldsymbol{n}_2\right), \tag{3.10}$$

where $\mathbf{n}_i$ is the unit vector in the i-direction ($i = 1$ normal and $i = 2$ tangential). If no unloading is considered, $(\partial\phi/\partial\delta)$ may be taken to be independent of $\boldsymbol{q}$. In such a case a simple expression for the potential ϕ is furnished by the Smith and Ferrante universal binding law [128]:

$$\phi(\delta) = e\sigma_c\delta_c\left[1 - \left(1 + \frac{\delta}{\delta_c}\right)e^{-\frac{\delta}{\delta_c}}\right], \tag{3.11}$$

where e $\approx$ 2.718 is the base of the natural logarithm, σ_c is the maximum cohesive normal traction and δ_c is a characteristic opening displacement. From (3.11) it is easy to get:

$$\frac{\partial \phi}{\partial \delta}(\delta) = t = e\sigma_c \frac{\delta}{\delta_c} e^{-\frac{\delta}{\delta_c}}, \tag{3.12}$$

where $t = |\boldsymbol{t}|$ is the modulus of the traction vector. It is interesting to specify the final expression of the cohesive law, obtained combining (3.12) and (3.10):

$$t_1 = e\sigma_c \frac{\delta_1}{\delta_c} e^{-\frac{\delta}{\delta_c}}, \qquad t_2 = \beta^2 e\sigma_c \frac{\delta_2}{\delta_c} e^{-\frac{\delta}{\delta_c}}. \tag{3.13}$$

The normal traction, t_1, as funtion of δ_1 is shown in Figure 3.6, while the shear traction, t_2, as funtion of δ_2 is shown in Fig. 3.7.

For computer implementation purposes it is also important to calculate the values of tangential stiffnesses k_{ij} that appear in the following relation, obtained from (3.13):

$$\dot{t}_i = k_{ij}\dot{\delta}_j \tag{3.14}$$

where $\dot{t}_i$ and $\dot{\delta}_j$ are rates of the tractions and displacements.By differentiating expressions in (3.13) the following expressions for k_{ij} can be obtained:

$$k_{11} = \frac{\sigma_c(\delta\delta_c - \delta_1^2)e^{\left(1-\frac{\delta}{\delta_c}\right)}}{\delta\delta_c^2}, \tag{3.15}$$

$$k_{12} = k_{21} = \frac{\beta^2\sigma_c\delta_1\delta_2 e^{\left(1-\frac{\delta}{\delta_c}\right)}}{\delta\delta_c^2}, \tag{3.16}$$

$$k_{22} = \frac{\beta^2\sigma_c(\delta\delta_c - \beta^2\delta_2^2)e^{\left(1-\frac{\delta}{\delta_c}\right)}}{\delta\delta_c^2}. \tag{3.17}$$

Notice that the matrix k_{ij} is symmetric, thus the cohesive law has some symmetry implications when it is written in its rate form.

Nevertheless, the compressive behavior in mode I obtained by using (3.13), see Fig. 3.6, is not satisfactory from a physical point of view. An expected and physically more reasonable behavior was obtained for example in Xu-Needleman's approach presented previously, see Fig. 3.4. Thus, a modification of the Ortiz-Pandolfi CZM for fracture mode I problems is proposed in what follows. The final expression of the normal cohesive law

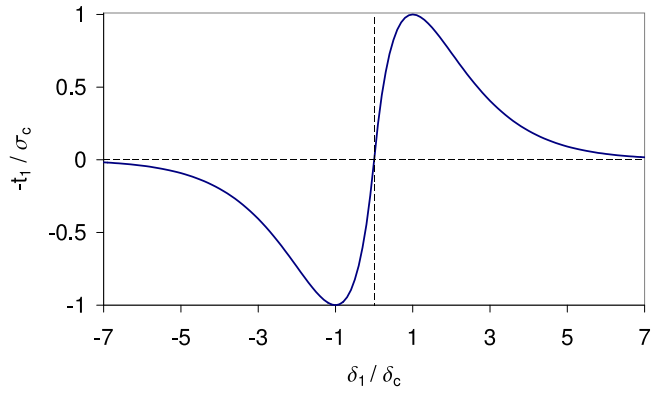

Figure 3.6: Normal traction across the cohesive surface as a function of δ_1 with $\delta_2 = 0$ according to (3.13) in the Ortiz-Pandolfi CZM.

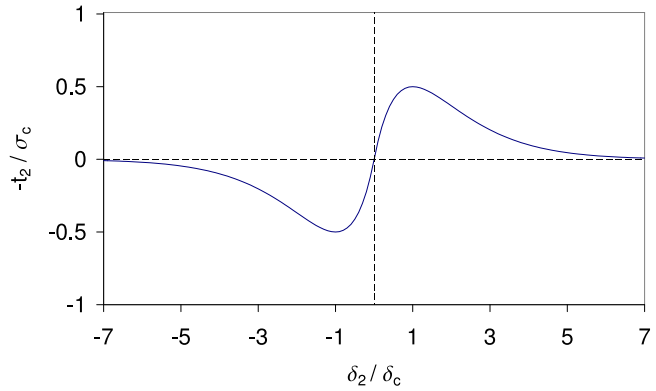

Figure 3.7: Shear traction across the cohesive surface as a function of δ_2 with $\delta_1 = 0$ and $\beta = 0.707$ according to (3.13) in the Ortiz-Pandolfi CZM.

is:

$$t_1 = e\sigma_c \frac{\delta_1}{\delta_c} e^{-\frac{\delta}{\delta_c}\text{Sign}[\delta_1]}, \tag{3.18}$$

where Sign[ ] is the signum function. By using (3.18) an expected mode I behavior can be obtained.

In Fig. 3.8 the mode I behavior obtained with the original Ortiz-Pandolfi law and the behavior obtained with the modified law proposed herein is presented.

The k_{11} term for the modified Ortiz-Pandolfi cohesive model takes the form:

$$k_{11} = \frac{\sigma_c(\delta\delta_c - \text{Sign}[\delta_1]\delta_1^2)e^{\left(1-\text{Sign}[\delta_1]\frac{\delta}{\delta_c}\right)}}{\delta\delta_c^2}. \tag{3.19}$$

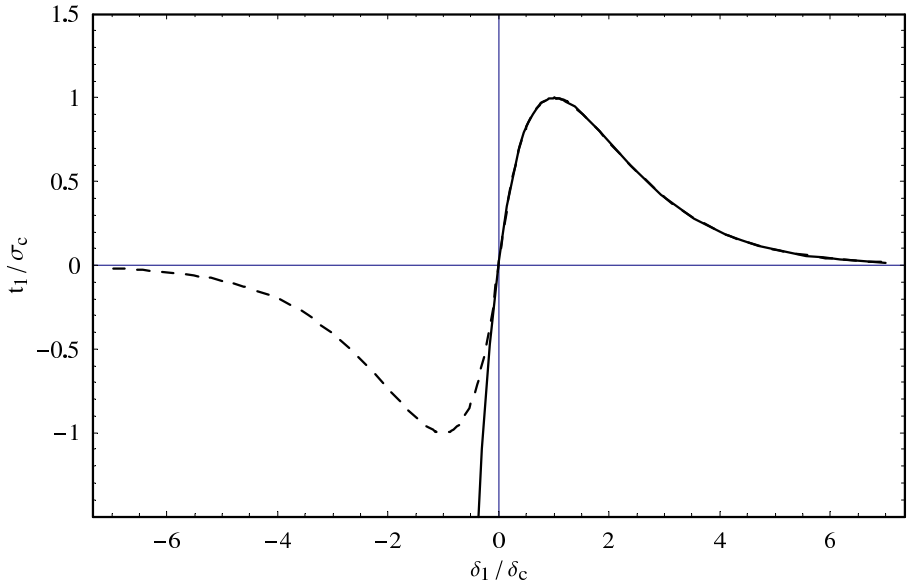

Figure 3.8: Normal traction across the cohesive surface as a function of δ_1 with $\delta_2 = 0$ using the equation (3.13), dashed line (original Ortiz-Pandolfi CZM), and using (3.18), continuous line (modified Ortiz-Pandolfi CZM).

Chapter 4

Weak interface. A Linear Elastic-Brittle Interface Model

In many practical situations, the behavior of adhesive joints can be described by modeling the thin adhesive layer as a continuous distribution of linear elastic springs [58] with appropriate stiffness parameters. This model of adhesive layer is usually called weak interface, imperfect interface or elastic interface [16, 68, 80, 102]. In the present thesis a linear elastic-brittle constitutive law is adopted for the springs representing the weak interface in order to allow an easy modeling of crack propagation along the interface.

In this chapter, firstly, some details of the linear elastic-brittle model are shown and, secondly, a new interface failure criterion is introduced.

4.1 Constitutive law of the spring distribution

A linear elastic interface is considered as a simple and useful model of a thin linear elastic (adhesive) layer between two surfaces. The undamaged layer (considered as a linear elastic solid of Young's modulus E_ℓ, Poisson ratio ν_ℓ, shear modulus μ_ℓ, Lame's parameter λ_ℓ, length L, width w and a small thickness h) can be modeled by a continuous spring distribution.

It is useful to clarify relations between the isotropic elastic layer parameters $(E_\ell, \nu_\ell, \mu_\ell, \lambda_\ell)$, its thickness (h) and the stiffness parameters of the spring constitutive law written in terms of a normal stress-displacement law, $\sigma - \delta_n$, and a tangential stress-displacement law, $\tau - \delta_t$.

Consider an isolated portion of the adhesive layer, given by a prismatic block of section $L \times w$ and height h, subjected to either uniform normal or shear stresses, $\sigma = \sigma_{11}$ and $\tau = \sigma_{12}$ respectively, see Figure 4.1. σ and τ

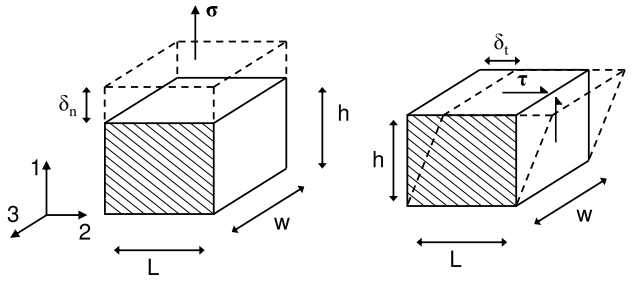

(a) (b)

Figure 4.1: Portion of a linear elastic layer under (a) normal stress, (b) tangential stress.

can be related to normal and tangential strains as:

$$\sigma_{11} = E_\ell \varepsilon_{11} \qquad \text{where} \quad \varepsilon_{11} = \frac{\delta_n}{h}, \tag{4.1}$$

$$\sigma_{12} = \mu_\ell 2\varepsilon_{12} \qquad \text{where} \quad 2\varepsilon_{12} = \frac{\delta_t}{h}, \tag{4.2}$$

where δ_n and δ_t represent relative normal and tangential displacements between the top and bottom surfaces of the elastic layer.

Then, using (4.1), the following form of the normal stress-displacement constitutive law is easily obtained:

$$\sigma = k_n \delta_n, \qquad \text{where} \quad k_n = \frac{E_\ell}{h}, \tag{4.3}$$

and, in a similar manner, the use of (4.2) yields the tangential stress-displacement law:

$$\tau = k_t \delta_t, \qquad \text{where} \quad k_t = \frac{\mu_\ell}{h}. \tag{4.4}$$

It has been assumed in the above considerations for normal compression or tension in direction 1, that the adhesive layer is free to expand or contract due to Poisson effect in directions 2 and 3. Nevertheless, if an adhesive layer is placed between two elastic solids, and assuming relatively small thickness and stiffness of the elastic layer with respect to the adjacent two elastic solids, the mechanical behavior of the layer changes. Thus, the boundary conditions that appear at the extremes of the arbitrary length, L, can be

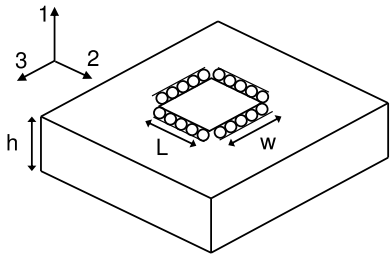

(a)

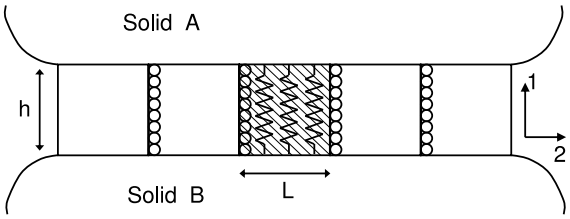

(b)

Figure 4.2: (a) Portion of an adhesive layer, (b) 2D layer modeled as a continuous spring distribution. Constraints indicated are considered for normal stresses only.

extended to any position (as indicated in Figure 4.2) due to a null expansion in directions 2 and 3 being assumed in a thin layer between finite solids, i.e., $u_2 = u_3 = 0$, yielding $\varepsilon_{22} = \varepsilon_{33} = 0$. Then, using constitutive equations of linear elasticity and applying conditions $\varepsilon_{22} = \varepsilon_{33} = 0$, the following relation for stress and strain normal to the interface is obtained:

$$\sigma_{11} = (2\mu_\ell + \lambda_\ell)\varepsilon_{11} = \frac{E'_\ell}{(1-\nu'^2_\ell)}\varepsilon_{11}, \tag{4.5}$$

where $E'_\ell = E_\ell/(1-\nu_\ell^2)$ and $\nu'_\ell = \nu_\ell/(1-\nu_\ell)$. Taking into account that $\sigma = k_n\delta_n$ and $\varepsilon_{11} = \delta_n/h$, the value of k_n can be expressed as:

$$k_n = \frac{2\mu_\ell + \lambda_\ell}{h} = \frac{E'_\ell}{h(1-\nu'^2_\ell)} = \frac{E_\ell(1-\nu_\ell)}{(1+\nu_\ell)(1-2\nu_\ell)}, \tag{4.6}$$

while the value of k_t is the same as in (4.4), as no Poisson effect is associated to shear stresses.

Then from (4.4) and (4.6) the relation k_n/k_t becomes:

$$\frac{k_n}{k_t} = \frac{2\mu_\ell + \lambda_\ell}{\mu_\ell} = \frac{2}{1-\nu'_\ell} = \frac{2(1-\nu_\ell)}{1-2\nu_\ell} \tag{4.7}$$

which implies $2 \leq k_n/k_t < \infty$. Sometimes it is useful to consider the inverse ratio:

$$\frac{k_t}{k_n} = \frac{1-2\nu_\ell}{2(1-\nu_\ell)} \tag{4.8}$$

where $0 \leq k_t/k_n < 0.5$, see Fig. 4.3.

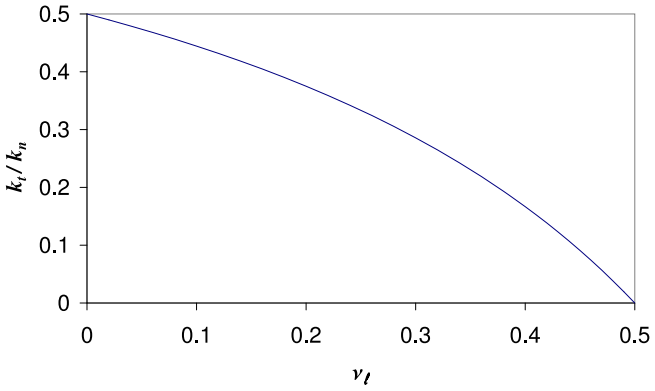

Figure 4.3: Relation between k_t/k_n and ν_ℓ.

It is noteworthy that considering very thin adhesive layers with vanishing thickness, $h \to 0$, a constant value of k_n implies, see (4.6) and (4.4), vanishing values of the adhesive Young's modulus, $E_\ell \to 0$, whereas constant values of E_ℓ imply increasing values of k_n, $k_n \to \infty$.

A similar analysis for k_n and k_t was presented in [79] for fibre coated composites and in [53] for adhesive lap joints. The above described behavior was also proved mathematically by asymptotic analyses in [16, 80].

If an orthotropic adhesive layer is considered, the ratio k_t/k_n would not have the above mentioned restrictions.

4.2 Interface failure criterion

The linear elastic interface model implies the absence of stress singularities at the crack tip. In the present work, damage and/or rupture of a portion

of this layer is modeled as an abrupt decrease (jump) of stresses in this portion of the layer, subsequently leading to a free separation/sliding of both surfaces when a point on the fracture locus (in (σ, τ) plane, as will be shown later) is achieved in the portion of the layer. The threshold normal and shear stresses (σ_c and τ_c) depend on the fracture mode mixity, which can be characterized by different fracture mode mixity angles: ψ_G energy based angle, ψ_σ stress angle and ψ_u relative displacement angle, which will be defined in this section.

The continuous spring distribution that models the adhesive layer is governed by the following simple linear elastic-brittle law written at an interface point x, shown also in Figure 4.4:

$$\begin{array}{ll} \text{L-E} & \left\{ \begin{array}{ll} \sigma(x) = k_n \delta_n(x) & \delta_n(x) \leq \delta_{nc}(\psi_G(x)) \text{ and} \\ \tau(x) = k_t \delta_t(x) & |\delta_t(x)| \leq \delta_{tc}(\psi_G(x)) \end{array} \right. \\ \text{Broken} & \left\{ \begin{array}{l} \sigma(x) = \left\langle \begin{array}{ll} 0 & \delta_n(x) > 0 \\ k_n \delta_n(x) & \delta_n(x) \leq 0 \end{array} \right. \\ \tau(x) = 0 \end{array} \right. \end{array} \tag{4.9}$$

where $\sigma(x)$ and $\tau(x)$ are, respectively, the normal and tangential stresses in the elastic layer, $\delta_n(x)$ and $\delta_t(x)$ are, respectively, the normal and tangential relative displacements between opposite interface points. $\delta_n(x)$ and $\delta_t(x)$ are sometimes referred to as the value of the opening and sliding between the interface sides. k_n and k_t denote the normal and tangential stiffnesses of the spring distribution.

Notice that all the critical variables $\sigma_c(\psi_G)$, $\delta_{nc}(\psi_G)$, $\tau_c(\psi_G)$ and $\delta_{tc}(\psi_G)$ are functions of the fracture mode mixity angle ψ_G (which will be defined in the following) at an interface point. Thus, different values of these critical variables may be obtained at different interface points. We can thus define that the "spring" at a point breaks when either δ_n or δ_t reaches its critical value, $\delta_{nc}(\psi_G)$ or $\delta_{tc}(\psi_G)$. At this moment the tangential stiffness are set to zero at this point and subsequently $\tau(\psi_G(x))$ is set to zero as well.

Regarding the normal linear elastic-brittle law once a portion of interface is broken, a negative normal displacement, $\delta_n < 0$, can be allowed leading to an interface overlapping, or it can be restricted by using an elastic friction-less contact condition, see (4.4) and Fig. 4.4(c). The use of an elastic friction-less contact is based on the idea that once the assumed interface layer is broken some portions of this layer remains on the interface surfaces. Thus, when these surfaces enter in contact, it seems reasonable that the portions of the layer could compress with the same stiffness in

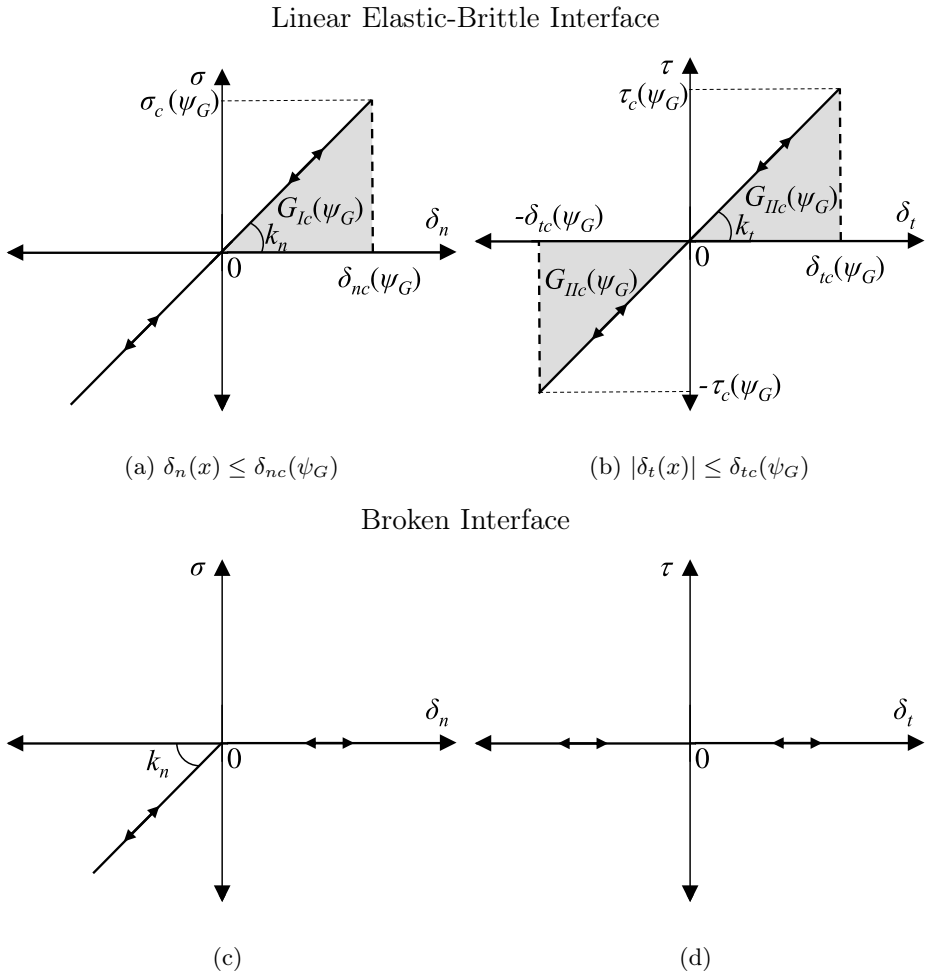

Figure 4.4: (a) Normal and (b) tangential linear elastic-brittle law in the undamaged interface, and (c) normal and (b) tangential linear elastic-brittle law in the broken interface.

normal direction as it had before breaking.

The present linear elastic-brittle model of an interphase layer represents a simple approximation of a real behavior of the layer. Some materials, for example, present a softening branch which may affect the energy dissipation. Nevertheless, as the experience shows with other non-singular fracture mechanics models as cohesive zone models, the (critical) fracture energy is the most important parameter in this kind of model. In fact, using different cohesive zone models but keeping constant the value of fracture energy

frequently leads to similar results. Thus, even if a layer material behavior presents a small softening branch, an acceptable result for the global behavior of a structure can be expected using the linear elastic-brittle model, provided that the actual fracture energy is employed and the zone in which a non-linear behavior is obtained is relatively small.

The interface failure criterion, proposed here, is based on the Energy Release Rate (ERR) concept. The ERR in a linear interface model is defined as the stored elastic strain energy per unit length in the unbroken "crack-tip interface spring" (infinitesimal interface segment situated at the crack tip) as shown in [102] and recently independently also in [37]. Thus, the ERR of a mixed mode crack in a linear elastic interface is defined as:

$$G = G_I + G_{II} = \frac{\sigma\delta_n}{2} + \frac{\tau\delta_t}{2}, \tag{4.10}$$

It can also be defined in terms of crack tip stresses σ and τ or relative displacements δ_n and δ_t

$$G = \frac{\sigma^2}{2k_n} + \frac{\tau^2}{2k_t} = \frac{\delta_n^2 k_n}{2} + \frac{\delta_t^2 k_t}{2}, \tag{4.11}$$

The definition $G_I = \sigma\delta_n/2$ is only valid for $\sigma \geq 0$ (and $\delta_n \geq 0$), whereas for $\sigma < 0$ (and $\delta_n < 0$) G_I is considered to be zero.

As will be shown, the fracture mode mixity angle can be defined in three ways. First, let us rewrite equation (4.10) as follows:

$$G = G_I + G_{II} = G_I(1 + \tan^2\psi_G), \tag{4.12}$$

where

$$\tan^2\psi_G = \frac{G_{II}}{G_I}. \tag{4.13}$$

According to the definition of G_I, for $\sigma \leq 0$ (and $\delta_n \leq 0$) this yields $G = G_{II}$ and $\psi_G = 90°$. This definition of ψ_G in (4.13) coincides with the definition of the energy based fracture mode mixity angle ψ_G in classical interfacial fracture mechanics [117].

Expression (4.12) can also be written as:

$$G = G_I + G_{II} = G_I(1 + \frac{k_n}{k_t}\tan^2\psi_\sigma) = G_I(1 + \frac{k_t}{k_n}\tan^2\psi_u), \tag{4.14}$$

where

$$\tan\psi_\sigma = \frac{\tau}{\sigma} \quad \text{and} \quad \tan\psi_u = \frac{\delta_t}{\delta_n}. \tag{4.15}$$

It can be shown that for $\sigma \geq 0$,

$$\tan\psi_\sigma = \sqrt{\frac{k_t}{k_n}}\tan\psi_G, \quad \text{and} \quad \tan\psi_u = \sqrt{\frac{k_n}{k_t}}\tan\psi_G. \tag{4.16}$$

The angle ψ_G defines the ERR based fracture mode mixity, and the angles ψ_σ and ψ_u the stress and relative displacement based fracture mode mixities respectively. Thus $\psi_G = 0^\circ \Rightarrow \psi_\sigma = \psi_u = 0^\circ$ defines a pure fracture mode I (opening mode) and $\psi_G = 90^\circ \Rightarrow \psi_\sigma = \psi_u = 90^\circ$ defines a pure fracture mode II (shear mode).

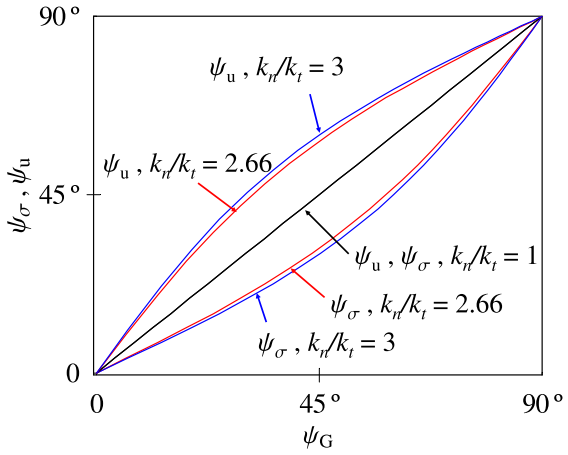

Figure 4.5: Relation between fracture mode mixity angles ψ_σ, ψ_u and ψ_G in the linear elastic constitutive law for different ratios of k_n/k_t.

The relation between ψ_G, ψ_σ and ψ_u for different values of the ratio k_n/k_t can be observed in Figure 4.5.

It is assumed that a crack propagates when the ERR, G, reaches the fracture energy G_c, that is:

$$G = G_c, \tag{4.17}$$

A strong dependence on the mode mixity of G_c has been observed in extensive experiments by Evans *et. al.* [59] and Banks-Sills and Askhenazi [11] among others. Thus, ψ_G (ψ_σ and ψ_u) are important parameters governing the interface crack growth. From several phenomenological laws for G_c suggested in the past [85], the following family of expressions of the fracture energy (representing the fracture toughness) is considered to be representative of a large number of bimaterial systems:

$$G_c = G_{Ic}[1 + \tan^2((1-\lambda)\psi_G)], \tag{4.18}$$

where

$$G_{Ic} = \frac{\bar{\sigma}_c \bar{\delta}_{nc}}{2} = \frac{\bar{\sigma}_c^2}{2k_n} = \frac{k_n \bar{\delta}_{nc}^2}{2} \tag{4.19}$$

corresponds to fracture energy in pure opening mode I. λ is a fracture mode-sensitivity parameter, e.g., the typical range $0.2 \leq \lambda \leq 0.3$ characterizes interfaces with moderately strong fracture mode dependence. $\bar{\sigma}_c$ and $\bar{\delta}_{nc}$ are the critical normal stress and opening displacement reached when the spring breaks in mode I. Thus, $\bar{\sigma}_c = \sigma_c(0°)$ and $\bar{\delta}_{nc} = \delta_{nc}(0°)$.

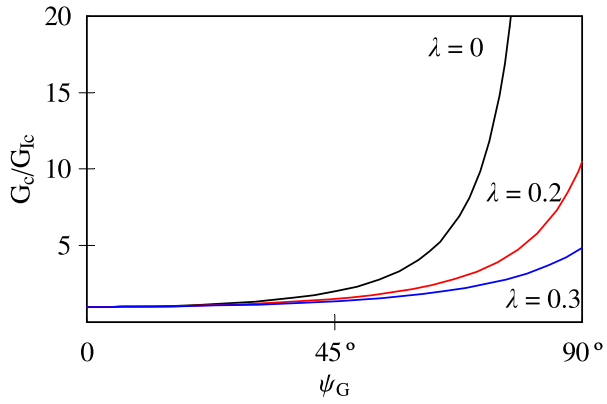

Figure 4.6: Fracture energy G_c as a function of ψ_G for different values of λ.

As can be seen in Figure 4.6, if $\lambda = 0$ the interface will never break in pure mode II, due to the asymptotic behavior of the function G_c defined in (4.18). As mentioned before, the use of $0 < \lambda < 1$ in (4.18) yields a more realistic behavior, allowing for the interface to fail in pure mode II. As shown in Figure 4.6 for higher values of λ, the failure in pure fracture mode II becomes easier (G_c value becomes lower).

Writing the crack propagation criteria along a linear elastic-brittle interface, making use of (4.12 - 4.19), the following general expression of the critical normal stress as a function of the angle ψ_G is obtained:

$$\sigma_c(\psi_G) = \bar{\sigma}_c \sqrt{1 + \tan^2[(1-\lambda)\psi_G]}.\cos\psi_G \quad \text{and} \quad \delta_{nc}(\psi_G) = \frac{\sigma_c(\psi_G)}{k_n}. \tag{4.20}$$

In a similar way the critical tangential stress for mixed mode, shown in Figure 4.4, can be expressed, in terms of $\sigma_c(\psi_G)$ and ψ_G, as:

$$\tau_c(\psi_G) = \sqrt{\frac{k_t}{k_n}}\bar{\sigma}_c\sqrt{1+\tan^2[(1-\lambda)\psi_G]}.\sin\psi_G \quad \text{and} \quad \delta_{tc}(\psi_G) = \frac{\tau_c(\psi_G)}{k_t}. \tag{4.21}$$

The plot of interface failure loci parameterized by equations (4.20) and (4.21) is shown in Figure 4.7, where a ratio $k_n/k_t = 3$ has been considered. The normal and tangential critical stress in mixed mode were normalized with the normal critical stress in mode I, $\bar{\sigma}_c$.

It should be mentioned that for $\lambda = 0$, the expression of G_c in (4.18) becomes similar to that obtained in [11], although it was used in a different interface model. Also $\sigma_c(\psi_G)$ in (4.20) equals $\bar{\sigma}_c$ (the critical normal stress in Mode I, see Figure 4.7) for all values of ψ_G when $\lambda = 0$.

The use of the angle ψ_σ instead of ψ_G in families of expressions of the fracture energy similar to (4.18) might at first sight appear more adequate, as e.g. in classical Interface Fracture Mechanics due to its direct relation with Stress Intensity Factors [117]. Nevertheless, it has been checked that the use of ψ_σ in the present formulation leads to a non-convex safe-region defined by the failure loci $(\sigma_c(\psi_\sigma), \tau_c(\psi_\sigma))$ in the (σ, τ) plane.

From Fig. 4.7, it can be seen that if normal compressions appear at the crack tip (crack closed) the formulation is still able to predict a crack growth.

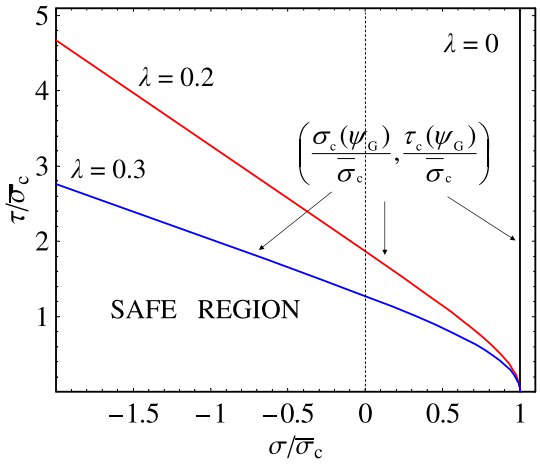

Figure 4.7: Interface failure loci in (σ, τ) plane for different values of λ with $k_n/k_t = 3$.

Chapter 5

Boundary Element Method

The Boundary Element Method (BEM) has proved to be an efficient tool to study elastic problems, especially those concerned mainly with boundary values of displacements and stresses, as in the case of Fracture Mechanics. In the present chapter, first the Boundary Integral Equations (BIE) governing the elastic problems are defined. Then, some of the characteristics of the BEM codes used to solve these BIEs are described.

5.1 Displacement and traction boundary integral equations in 2D and 3D

5.1.1 Boundary integral equations in 2D for elastic materials

Consider a linear elastic domain $\Omega \subset \mathbb{R}^2$, with a bounded Lipschitz and piecewise smooth boundary $\Gamma = \partial\Omega$. Let $\Gamma_s \subset \Gamma$ denote the smooth part of Γ (excluding corners). The primary boundary integral equation for elasticity, u-BIE, is an expression for the boundary displacements [49, 144],

$$\begin{aligned} \mathcal{U}(\boldsymbol{x}') &= C_{ik}(\boldsymbol{x}')u_i(\boldsymbol{x}') + \oint_\Gamma T_{ik}(\boldsymbol{x},\boldsymbol{x}')u_i(\boldsymbol{x})\mathrm{d}S(\boldsymbol{x}) \\ &\quad - \int_\Gamma U_{ik}(\boldsymbol{x}-\boldsymbol{x}')t_i(\boldsymbol{x})\mathrm{d}S(\boldsymbol{x}) = 0 \ , \end{aligned} \tag{5.1}$$

where $\boldsymbol{x}' \in \Omega \cup \Gamma$, $u_i(\boldsymbol{x})$ and $t_i(\boldsymbol{x})$, respectively, are boundary displacements and tractions. The displacement kernel $\boldsymbol{U}(\boldsymbol{x}-\boldsymbol{x}')$ is generally taken as the Kelvin fundamental solution of the Lamé system (Navier equation), giving the displacement at $\boldsymbol{x}$ originated by a unit point load at $\boldsymbol{x}'$ in an infinite

medium. The first (strongly singular) integral in (5.1) is evaluated in the Cauchy principal value sense, whereas the second (weakly singular) integral in (5.1) is evaluated as an improper integral. For two dimensional isotropic elasticity the Kelvin fundamental solution is [5, 27, 29, 131]

$$U_{ik}(\boldsymbol{x}-\boldsymbol{x}') = \frac{1}{8\pi\mu(1-\nu)}\left[-(3-4\nu)\delta_{ki}\log(r) + r_{,i}r_{,k}\right] . \qquad (5.2)$$

The notation introduced in this equation is that ν is Poisson's ratio, μ is shear modulus, δ_{ki} is the Kronecker delta, $r = \|\boldsymbol{x}-\boldsymbol{x}'\|$, $r_{,i} = \partial r/\partial x_i$, and x_i is the i-th coordinate of the field point $\boldsymbol{x}$. The corresponding traction kernel $\boldsymbol{T}(\boldsymbol{x},\boldsymbol{x}')$ is obtained by differentiating $\boldsymbol{U}$ and using the linear elastic constitutive law to form the traction, resulting in

$$\begin{aligned} T_{ik}(\boldsymbol{x},\boldsymbol{x}') &= -\frac{1}{4\pi(1-\nu)r}\left[\left\{(1-2\nu)\delta_{ki} + 2r_{,i}r_{,k}\right\} r_n \right. \\ &\quad \left. -(1-2\nu)\left\{n_k(\boldsymbol{x})r_{,i} - n_i(\boldsymbol{x})r_{,k}\right\}\right] , \end{aligned} \qquad (5.3)$$

where $\boldsymbol{n}$ is the unit outward normal to Γ at $\boldsymbol{x}$, and $r_n = r_{,1}n_1(\boldsymbol{x}) + r_{,2}n_2(\boldsymbol{x})$ is the normal derivative or r. $C_{ik}(\boldsymbol{x}')$ is the coefficient tensor of the free term [111], where $C_{ik}(\boldsymbol{x}') = \delta_{ik}$ for $\boldsymbol{x}' \in \Omega$, and $C_{ik}(\boldsymbol{x}') = \frac{1}{2}\delta_{ik}$ for $\boldsymbol{x}' \in \Gamma_s$.

For boundary integral fracture analysis, and for Symmetric-Galerkin BIE formulation in general, the integral equation for the boundary tractions is essential. Formally differentiating (5.1) with respect to $\boldsymbol{x}' \in \Gamma_s$ yields an equation for boundary tractions, t-BIE, of the form:

$$\mathcal{T}(\boldsymbol{x}') = \frac{1}{2}t_i(\boldsymbol{x}') + \neq\!\!\!\!\int_\Gamma S_{ik}(\boldsymbol{x},\boldsymbol{x}')u_i(\boldsymbol{x})\mathrm{d}S(\boldsymbol{x}) - \int_\Gamma T^*_{ik}(\boldsymbol{x},\boldsymbol{x}')t_i(\boldsymbol{x})\mathrm{d}S(\boldsymbol{x}) = 0 . \qquad (5.4)$$

The singular and hypersingular kernels for the traction integral equation can be expressed as [49, 115, 116]

$$\begin{aligned} T^*_{ik}(\boldsymbol{x},\boldsymbol{x}') &= \frac{1}{4\pi(1-\nu)r}\left[\left\{(1-2\nu)\delta_{ki} + 2r_{,i}r_{,k}\right\} r_n \right. \\ &\quad \left. -(1-2\nu)\left\{n_k(\boldsymbol{x}')r_{,i} - n_i(\boldsymbol{x}')r_{,k}\right\}\right] , \\ S_{ik}(\boldsymbol{x},\boldsymbol{x}') &= \frac{\mu}{2\pi(1-\nu)r^2}\left[\delta_{ik}n_j(\boldsymbol{x}')n_j(\boldsymbol{x}) + \left\{r_{,i}n_k(\boldsymbol{x}') + r_{,k}n_i(\boldsymbol{x}')\right\} r_{,j}n_j(\boldsymbol{x}) \right. \\ &\quad + \left\{r_{,i}n_k(\boldsymbol{x}) + r_{,k}n_i(\boldsymbol{x})\right\} r_{,j}n_j(\boldsymbol{x}') \\ &\quad \left. -8r_{,i}r_{,k}r_{,j}n_j(\boldsymbol{x}')r_{,l}n_l(\boldsymbol{x})\right] . \end{aligned} \qquad (5.5)$$

It should be noticed that according to [116] there is no material parameters

in the expression of S_{ik}, except for the prefactor $\mu/(1-\nu)$. It is worth re-emphasizing at this point that the derivation of (5.4) is purely formal. Due to the singularity in the kernel functions at $r = 0$, moving the derivative with respect to $\boldsymbol{x}'$ under the integral is, in general, not justified. It is therefore necessary to develop viable definitions for the singular integrals, most especially for the hypersingular kernel $\boldsymbol{S}$. In this regard, the Galerkin formulation is highly useful.

For the elastic orthotropic case the kernels used for the displacement and stress boundary integral equation are the ones developed in [9], where simple explicit formulae in complex variable of all the integral kernels and the free term tensor is presented. The correctness of these expressions has been proved in several works [23, 114].

5.1.2 Boundary integral equation in 3D for transversely isotropic elastic materials

Consider a linearly elastic transversely isotropic solid $\Omega \subset \mathbb{R}^3$ with a bounded piecewise smooth Lipschitz boundary $\Gamma = \partial\Omega$. The Somigliana displacement identity, called also displacement Boundary Integral Equation (u-BIE) for internal source point ($\boldsymbol{x}'$) is similar to (5.1), with $C_{ik} = 1$. The, the stress field σ_{ij} is can be expressed as

$$\sigma_{ij}(\boldsymbol{x}') + \int\!\!\!\!\!\!-_{\Gamma} S_{ijk}(\boldsymbol{x}, \boldsymbol{x}') t_k(\boldsymbol{x}) \mathrm{d}S(\boldsymbol{x}) = \int_{\Gamma} D_{ijk}(\boldsymbol{x} - \boldsymbol{x}') u_k(\boldsymbol{x}) \mathrm{d}S(\boldsymbol{x}), \quad (5.6)$$

and represent the Somigliana stress identity at an internal source point ($\boldsymbol{x}'$). In this equation, S_{ijk} and D_{ijk} contain the derivatives of $T_{ik}(\boldsymbol{x}, \boldsymbol{x}')$ and $U_{ik}(\boldsymbol{x} - \boldsymbol{x}')$, respectively. S_{ijk} and D_{ijk} kernels are directly related, by multiplying with the normal n_j, with the kernels S_{ik} and T^*_{ik} appearing in (5.5).

Expressions of the integral kernels for the displacement and stress boundary integral equation for 3D transversely isotropic materials will be introduced in a cartesian coordinate system associated to the material (x_3-axis being the symmetry axis) in Chapter 8.

An application of these expressions in a different coordinate system, cartesian or curvilinear, may be required sometimes. Rizzo and Shippy [145] analyzed the corresponding transformations considering these fundamental solutions as two-point tensor functions. In the simpler case of a different cartesian coordinate system, it will be sufficient, first to evaluate these fundamental solutions in the material coordinate system, obtaining values U^*_{mn}

and T^*_{mn}, and second to apply the standard transformation rule for second rank tensors:

$$U_{ik} = Q_{im}Q_{kn}U^*_{mn}, \qquad T_{ik} = Q_{im}Q_{kn}T^*_{mn}, \tag{5.7}$$

$\boldsymbol{Q}$ being an orthogonal transformation matrix. It should be stressed that the coordinates of the radius vector $\boldsymbol{x} - \boldsymbol{x}'$ between the field and source points and the normal vector appearing in the expressions of U^*_{mn} and T^*_{mn} should be given in the material coordinate system.

The free-term coefficient tensor $C_{ik}(\boldsymbol{x}')$ for a boundary point $\boldsymbol{x}' \in \Gamma$ can be evaluated as:

$$C_{ik}(\boldsymbol{x}') = -\lim_{\varepsilon\to 0_+} \int_{S_\varepsilon(\boldsymbol{x}')\cap\Omega} T_{ik}(\boldsymbol{x},\boldsymbol{x}')\mathrm{d}S(\boldsymbol{x}) = -\fint_\Gamma T_{ik}(\boldsymbol{x},\boldsymbol{x}')\mathrm{d}S(\boldsymbol{x}), \tag{5.8}$$

where $S_\varepsilon(\boldsymbol{x}')$ is a spherical surface of radius ε centred at $\boldsymbol{x}'$. Equation (5.8) implies that $C_{ij}(\boldsymbol{x}') = \frac{1}{2}\delta_{ij}$ for $\boldsymbol{x}'$ placed at a smooth part of Γ, whereas for $\boldsymbol{x}'$ at an edge or a corner its value depends on the local form and spatial orientation of Γ at $\boldsymbol{x}'$ and on the elastic material properties. An application of the Stokes theorem to obtain a more explicit formula for $C_{ik}(\boldsymbol{x}')$ at edge and corner points, advantageous for numerical (and possibly for analytic) computations, in a similar way as was previously done for isotropic materials [111], would also require an analogous decomposition of T_{ik}. In fact, such a decomposition is related to the Burgers formula [30] giving displacement field originated by a unit dislocation loop. A generalization of the Burgers formula to general anisotropic materials was developed by Indenbom and Orlov [86], see also Lothe [105], and introduced in the framework of the Symmetric Galerkin BEM by Rungamornrat [148] recently. According to these works, T_{ik} can be decomposed as

$$T_{ik}(\boldsymbol{x},\boldsymbol{x}') = -\frac{\delta_{ik}n_j r_{,j}}{4\pi r^2} + D_{ij}\left(P_{jk}(\boldsymbol{x}-\boldsymbol{x}')\right), \tag{5.9}$$

where $r = |\boldsymbol{x}-\boldsymbol{x}'|$ and $r_{,j} = (x_j - x'_j)/r$, D_{ij} is the antisymmetric (tangential) differential operator defined by $D_{ij} = n_i(\boldsymbol{x})\partial_{x_j} - n_j(\boldsymbol{x})\partial_{x_i}$ and the weakly singular integral kernel P_{jk} can be expressed using a line integral similar to that appearing in (9.5). Then, the Stokes theorem, after the limit $\varepsilon \to 0$ leads to

$$C_{ik}(\boldsymbol{x}') = \frac{\Phi(\boldsymbol{x}')}{4\pi}\delta_{ik} + \int\limits_{\partial S_1(\boldsymbol{x}',\Omega)} \varepsilon_{ijl}P_{jk}(\boldsymbol{x}-\boldsymbol{x}')\mathrm{d}x_l, \tag{5.10}$$

where $\partial S_1(\boldsymbol{x}', \Omega)$ is the closed contour representing the boundary of the so-called characteristic surface $S_1(\boldsymbol{x}', \Omega)$ of Γ at $\boldsymbol{x}'$ (a polygon cut on the unit sphere $S_1(\boldsymbol{x}')$ by the tangential planes to Γ at $\boldsymbol{x}'$). $\Phi(\boldsymbol{x}')$ is the solid angle of $S_1(\boldsymbol{x}', \Omega)$ viewed from $\boldsymbol{x}'$. Formula (5.10) represents a generalization to anisotropic materials of the analogous formula for $C_{ik}(\boldsymbol{x}')$, in terms of $\Phi(\boldsymbol{x}')$ and regular line integrals over $\partial S_1(\boldsymbol{x}', \Omega)$, obtained previously for isotropic materials [111]. Notice that the regular angular integrals over edges of $\partial S_1(\boldsymbol{x}', \Omega)$ can be evaluated numerically by standard quadratures. A study of the possibility of an analytic evaluation of these integrals would require a closed-form expression of P_{jk}, *e.g.* in a similar form to that shown for U_{ik} in Sections 9.1.2 and 9.2.2. To the knowledge of the present author such a formula is not available at present.

5.2 Collocational Boundary Element Method

The simpler procedure to reduce u-BIE to a linear algebraic system is the so-called *collocation* approach, wherein the u-BIE is explicitly enforced at a finite set of boundary points. In its simplest form, these collocation points are chosen to be the nodes used to discretize the boundary. Thus, a collocation approximation of the u-BIE can be simply stated as, *c.f.* (5.1),

$$\mathcal{U}(\boldsymbol{x}'_k) = 0 \ , \tag{5.11}$$

where $\boldsymbol{x}'_k$, $1 \leq k \leq M$ are the selected boundary points. If the boundary displacement and traction (in elasticity) are interpolated from their values at these M selected boundary points, then the boundary conditions usually provide $2M$ of these $4M$ values. The point-wise enforcement of (5.11) then provide the $2M$ equations needed to solve for the unknown values. Collocation necessarily leads to non-symmetric matrices [161].

Generally speaking, engineers prefer the collocation approach to the Galerkin approach [27, 131]. The essential reason is that we have simpler integrals to compute or to approximate and that the deduction is somewhat simpler in the sense that we are neither averaging on the boundary elements nor considering an intermediate variational formulation. There are however some aspects to be taken into account for solving problems with collocation approach:

- Not every choice of collocation nodes is going to work. For instance at a vertex and/or corner the normal vectors are not uniquely defined.

- There is not a satisfactory theory for collocation method working even for smooth surfaces. This should not worry too much a practitioner of the method: most people are convinced that the theory will arrive in due time. However, the Galerkin setting gives more confidence to mathematically oriented users of the boundary element method.

- In some instances, practitioners of the method use more collocation points than unknowns and solve the incompatible equations by least squares. This has the advantage that we have to solve a symmetric positive definite system.

5.3 Symmetric Galerkin Boundary Element Method

5.3.1 Symmetric Galerkin Scheme

In a Galerkin formulation, the displacement and traction integral equations, u-BIE and t-BIE, are enforced 'on average', in the form, see (5.1) and (5.4),

$$\begin{aligned} \int_\Gamma \psi_l(\boldsymbol{x}')\ \mathcal{U}(\boldsymbol{x}')\mathrm{d}S(\boldsymbol{x}') = 0\ , \\ \int_\Gamma \psi_l(\boldsymbol{x}')\ \mathcal{T}(\boldsymbol{x}')\mathrm{d}S(\boldsymbol{x}') = 0\ . \end{aligned} \tag{5.12}$$

The weight function $\psi_l(\boldsymbol{x}')$ is comprised of all shape functions that are equal to one at the node $\boldsymbol{x}'_l$, and thus there are sufficient equations to solve for the boundary unknowns. The shape functions themselves are determined by the choice of how the boundary displacements and tractions are interpolated.

The symmetric-Galerkin formulation was first considered by Sirtori [159] and Hartmann *et al.* [78], and then extensively developed by Maier and co-workers [109, 95, 160, 107]. Note that in Galerkin approach the source and field points $\boldsymbol{x}'$ and $\boldsymbol{x}$ are treated equally, and the kernels $\boldsymbol{U}$ and $\boldsymbol{S}$ are themselves symmetric, *i.e.*

$$U_{ik}(\boldsymbol{x}-\boldsymbol{x}') = U_{ki}(\boldsymbol{x}-\boldsymbol{x}'), \qquad S_{ik}(\boldsymbol{x},\boldsymbol{x}') = S_{ki}(\boldsymbol{x},\boldsymbol{x}'), \tag{5.13}$$

and also fulfill the reciprocity relation

$$U_{ik}(\boldsymbol{x}-\boldsymbol{x}') = U_{ki}(\boldsymbol{x}'-\boldsymbol{x}), \qquad S_{ik}(\boldsymbol{x},\boldsymbol{x}') = S_{ki}(\boldsymbol{x}',\boldsymbol{x}). \tag{5.14}$$

Thus, according to (5.14), if displacements are specified everywhere on the boundary, the displacement equation in Eq. (5.12) leads to a symmet-

ric system of equations for the unknown tractions. Similarly the traction equation yields a symmetric matrix if the boundary data are entirely known tractions. In general, if the displacement equation is employed on the part of the boundary where displacements are specified, while the traction equation is employed on the part of the boundary where tractions are known, then the resulting linear equations are symmetric. This follows from (5.14) and the fact that $\boldsymbol{T}$ and $\boldsymbol{T}^*$ are directly related, both being first order derivatives of $\boldsymbol{U}$, thus

$$T_{ik}(\boldsymbol{x}, \boldsymbol{x}') = -T^*_{ik}(\boldsymbol{x}', \boldsymbol{x}). \tag{5.15}$$

For standard fracture analysis problems, wherein the boundary condition on the crack is specified traction, the symmetry is remarkably simple: the above prescription (writing the traction equation on the crack surface) retains the symmetry, with the proviso that the unknowns on the fracture surface are now the jump in displacement, and the complementary variable is the sum of the known tractions. See for example [28, 160].

5.3.2 Singular Integration

The key task in the numerical implementation of Eq. (5.12) is the evaluation of the singular integrals, and an advantage of the Galerkin approach is that the extra boundary integration makes defining and computing the hypersingular $\boldsymbol{S}$ kernel integral significantly easier. The singular integration (for all kernels) may be efficiently accomplished by means of direct hybrid analytical/numerical algorithms that result from defining the integrals as a limit to the boundary [74, 161]. In this approach, one sees that the individual, *i.e.* coincident and adjacent element, hypersingular integrals are divergent. However, the divergent terms that show up in the limit process can be shown to cancel, and the complete limit of the integral is finite.

Nevertheless, is should be noted that there are a number of other singular integration techniques available [64, 83, 106]. For fracture in particular, schemes based upon integration by parts [41, 63] have been highly successful.

5.4 Weak formulation of contact and interface conditions

In order to allow the use of conforming or non-conforming discretizations at interfaces, the idea of imposing the boundary conditions at interfaces,

described in [25], is used. The use of non-conforming meshes could lead to a reduction of the final system of equations.

Thus, the equilibrium and compatibility conditions along the interface zone between the two solids A and B are imposed in a weak manner, derived from the principle of virtual work [25, 72]. In this way, stresses along the interface zone are defined as the tractions along $\Gamma_i^A \subset \Gamma^A$, the interface part of the boundary of solid A.

Equilibrium is imposed in a weak form at all points y along the interface part of the boundary of solid B, $\Gamma_i^B \subset \Gamma^B$, which means that

$$\triangle t_i^B(y) + \triangle t_i^A(y) = 0, \tag{5.16}$$

is guaranteed by the fulfilment of the following integral equation considered at Γ_i^B:

$$\int_{\Gamma_i^B} [\triangle t_i^B(y) + \triangle t_i^A(y)] \triangle u_i^{B\psi} d\Gamma_i^B = 0 \qquad i = n, t, \tag{5.17}$$

for all fields of compatible displacements $\triangle u_i^{B\psi}(y)$.

Accordingly, displacements along the interface are defined by the displacements at Γ_i^B. Compatibility is imposed in a weak form at all points y belonging to Γ_i^A, which means

$$\triangle \delta_i^A(y) = \triangle u_i^A(y) - u_i^B(y) \tag{5.18}$$

with $\triangle \delta^A(y)$ being the relative displacements between opposite points of the adjacent solids, by the fulfilment of the following integral equation considered at Γ_i^A:

$$\int_{\Gamma_i^A} \triangle t_i^{A\psi} [\triangle u_i^A(y) - \triangle t_i^B(y) - \triangle \delta_i^A(y)] d\Gamma_i^A = 0 \tag{5.19}$$

for all traction fields in equilibrium $\triangle t_i^{A\psi}(y)$.

The implementation of the interface conditions related to the Linear Elastic-Brittle Interface Model, introduced in Chapter 4, will be described in Section 8.1.

5.5 Boundary Element codes

In this thesis, three different BEM codes has been used and modified in order to include the new features developed: non-singular fracture mechanics

models and 3D transversely isotropic materials kernels. Some additional modifications needed to solve some of the application problems as: non-linear solving algorithms and methods to remove rigid body motions in the displacements field have been carried out.

5.5.1 2D Collocational Boundary Element code

A 2D BEM collocational code (written in Fortran 90) for the numerical solution of u-BIE (5.1) is used. This code was originally developed in [71]. The main features of this code were as follow: *i)* 2-node Lagrangian linear continuous boundary elements [131]; *ii)* isotropic axisymmetric and anisotropic plane problems can be modeled, including multiple perfectly bonded solids or contact zones between them; (iii) equilibrium and compatibility conditions, along contact zones, are imposed in a weak form, allowing an easy use of non-conforming discretizations [25, 72].

The new features included in this code are: *i)* possibility of defining linear elastic-brittle interfaces between the elastic solids; *ii)* equilibrium and compatibility conditions, along linear elastic-brittle interfaces, are imposed in a weak form. *iii)* a sequentially linear analysis to solve crack growth problems with the linear elastic-brittle interface model is implemented. In the specific case of linear elastic-brittle interfaces, a non-conforming discretization is possible since the normal stress-displacement law and the tangential stress-displacement law are not mesh dependent. From (4.4) and (4.6), it can be seen that the stiffness parameters k_n and k_t are independent of the distances L and w.

5.5.2 2D Symmetric Galerkin Boundary Element code

A 2D Symmetric Galerkin BEM code (written in Fortran 90) for the numerical solution of u-BIE (5.1) and t-BIE (5.4) was used. This code was originally developed in [135]. The main features of this code were as follow: *i)* 3-node Lagrangian quadrilateral continuous boundary elements [131]; *ii)* isotropic plane problems can be modeled, including multiple perfectly bonded solids; *iii)* cracks can be modeled by meshing just one crack side;

The new features included in this code are: *i)* cohesive cracks inside an homogeneous media can be modeled by meshing just one crack side; *ii)* possibility of defining cohesive interfaces between the elastic solids; *iii)* use of the *Method* S [172] to remove the rigid body motion in the displacement field when using traction boundary conditions. *iv)* several variants of the arc-length method are implemented. They are used as the non-linear solving

algorithm to solve the cohesive crack problems.

5.5.3 3D Collocational Boundary Element code

A 3D collocational BEM code (written in Fortran 90) for the numerical solution of u-BIE (5.1) was also used in the present thesis. The main features of this BEM code originally developed in [127] follow: *i)* 9-node Lagrangian quadrilateral boundary elements with quadratic shape functions; *ii)* a numerical evaluation of regular integrals by 8×8 Gaussian quadrature with adaptive subdivison of elements in the case of quasi-singular integrals [96]; *iii)* the polar coordinate transformation applied for a numerical evaluation of weakly singular integrals with the integral kernel U_{ik}; *iv)* the rigid-body-motion procedure applied for a numerical evaluation of the sum of the free-term coefficient tensor C_{ik} and the Cauchy principal value integral with the integral kernel T_{ik}. *v)* allow to model transversely isotropic materials and functionally graded materials (FGM).

The new feature included in this code is the implementation of new general, real-variable and efficient expressions of the integral kernels for the solution of transversely isotropic materials, valid for any combination of material properties (previous solution had some difficulties due to the use of complex variables and it is not valid for some combination of material properties).

Chapter 6

Implementation of linear and non-linear solvers in the BEM codes used

In the present chapter a review and brief description of linear system solvers is carried out first. The success of the numerical tools developed are highly related to an efficient linear solver that will be implemented in home made BEM codes. Then, as the problems to be studied in the present thesis need a non-linear solving algorithm a sequentially linear analysis is developed for the use with the Linear Elastic-Brittle Interface (LEBI) formulation and the 2D collocational BEM code. While, the arc-length method with several variants is implemented in the 2D SGBEM code to solve problems that include a Cohesive Zone Model (CZM).

6.1 Linear system solver improvement

Due to the use of home-made BEM codes, an initial part of the work was researching different Linear System Solvers. The principal aim was to improve the time used to solve the system of equations obtained by the BEM. Especially, the 2D Collocational-BEM code that had implemented a *Gauss-Jordan Elimination* solver, which used too much time [71].

After the review of the different methods and libraries available, direct solvers based on LU factorization were chosen to be implemented in the different codes used. This fact led to the use of IMSL libraries when the codes are running under Windows platform and Linpack [54] and Lapack [7] libraries when the codes are running under LINUX environment.

The problem of solving a linear system $\mathbf{Ax} = \mathbf{b}$ is central in scientific computation. In the following some main features of the methods used are detailed, when $\mathbf{A}$ is square, dense and unstructured.

6.1.1 Gauss-Jordan Elimination

For inverting a matrix, *Gauss-Jordan Elimination* is about as efficient as any other method. For solving sets of linear equations, *Gauss-Jordan Elimination* produces directly the solution of the equations for one or more right-hand side vectors b. However, its principal weaknesses are that (i) it requires all the right-hand sides to be stored and manipulated at the same time, and (ii) when the inverse matrix is not desired, *Gauss-Jordan Elimination* is three times slower than the LU procedure that will be described in the next subsection [70, 139].

Gaussian elimination procedure can be divided in two parts. The first part is called forward elimination and it reduces a given system to triangular form. This is accomplished through the use of elementary row operations. The second step is done to find the solution of the system above by means of back substitution. Computing *Gauss-Jordan Elimination* requires $2n^3$ floating point operations, ignoring lower order terms.

Gaussian elimination is numerically stable for diagonally dominant or positive-definite matrices. For general matrices, Gaussian elimination is usually considered to be stable in practice if the partial pivoting is used, even though there are examples for which it is unstable [139].

The subroutine originally used was "pivot.f" taken from [131], which implements the above mentioned *Gauss-Jordan Elimination* procedure. This subroutine was also implemented in the improved 2D collocational BEM code [71].

6.1.2 LU solvers

The LU decomposition can be considered as a "high level" algebraic description of Gaussian elimination [70]. The LU decomposition assumes we are able to write a matrix as the product of a lower triangular matrix (L - has elements only on the diagonal and below) and an upper triangular matrix (U - has elements only on the diagonal and above).

The advantage of breaking up one linear system into two successive ones, is that the solution of a triangular set of equations is quite trivial [70, 139]. Thus, one set of equations can be solved by forward substitution (L matrix

involved) while the other set of equations can be solved by back substitution (U matrix involved).

Computing LU decomposition requires $2n^3/3$ floating point operations, ignoring lower order terms. Notice that, once we have the LU decomposition of the matrix **A**, we can solve the corresponding system with as many right-hand sides as we need, one at a time. This is a distinct advantage over the Gauss-Jordan Elimination.

The subroutines implemented were "DL2ARG.f" from IMSL on Windows environment in the different BEM codes. In Linux platform, "dsytrf.f" and "dsytrs.f" from Linpack library [54] were used for the SGBEM code; while "dgesv.f" from Lapack was used for the 2D and 3D collocational BEM code.

6.1.3 Parallel LU solvers

Once we obtained a very nice improvement on computing time by using the LU solvers, the next step is to parallelize the different codes so larger problems can be solved over a distributed memory. Thus, the use of a MPI programming was started specially for the 3D code. A suitable solver used was taken from the library ScaLapack [19].

The ScaLAPACK (or Scalable LAPACK) library includes a subset of LAPACK routines redesigned for distributed memory MIMD parallel computers. It is currently written in a Single-Program-Multiple-Data style using explicit message passing for interprocessor communication. The subroutine chosen was "pdgesv.f'" (parallel version of the subroutine used previously).

6.2 Sequentially Linear Analysis

The present algorithm is developed for the use with the Linear Elastic-Brittle Interface (LEBI) formulation and the 2D collocational BEM code. The LEBI formulation allows to solve the non-linear problem as a set of different linear problems, see Section 4.2.

The numerical solution of the non-linear problem formulated is usually based on a gradual application of the loads and displacements imposed, by means of a load factor, $0 \leq F \leq 1$. The solution procedure is given by a series of lineal stages, "load steps". At the beginning of each load step the actual interface zone bonded by the adhesive layer is established, which defines the actual linear system of equations.

By solving this system of equations the corresponding elastic solution is obtained. Thus, the solution of the problem will be divided into a number

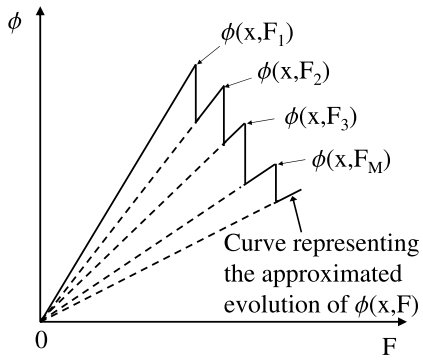

Figure 6.1: Example of evolution of a variable $\phi(x, F)$

M (a priori unknown) of load steps where all variables behave linearly:

$$\phi(x, F) = F \triangle_m \phi(x), \tag{6.1}$$

with $F_{m-1} \leq F \leq F_m$, $m = 1, ..., M$, and $F_0 = 0$, and where $\phi(x, F)$ is the value of any problem variable at a point x after an F-fraction of the load is applied. $\triangle_m \phi(x)$ is the value of the increment of the variable $\phi(x)$ corresponding to the unit increment of the load factor F (or equivalently the derivative of $\phi(x)$ with respect to F), and it is obtained in the solution of the linear system of equations corresponding to the m-th load step.

This solution fulfills all the conditions of the linear elastic interface formulation (and also of the frictionless contact formulation, if needed in the damaged zone) up to a certain maximum value F_m of the load factor F associated to this load step. A further increment of the load factor leads to rupture of some springs (or to a change in contact conditions). Consequently, values of variable ϕ at the end of each load step are defined as $\phi(x, F_m) = F_m \triangle_m \phi(x)$ for $F = 1, ..., M$. This procedure is illustrated in Figure 6.1.

This sequentially linear analysis was implemented in the 2D collocational BEM code. Among its main features it can be said that is a very simple and absolutely robust algorithm, nevertheless it is less efficient when a fine mesh is used.

6.3 Arc-length Algorithm for non-linear problems

The arc-length method is a powerful solution algorithm, allowing the evolution of the equilibrium states of a problem to be solved at various load levels [48, 61, 156]. All these equilibrium states trace the load-displacement

response of the structure in which all the applied loads vary proportionally as a function of a unique load parameter called herein λ. In such a case, for a non-linear system $\mathbf{Ax} = \mathbf{b}$ with n degrees-of-freedom (DOF), the $n + 1$ unknowns $\mathbf{t} = (\mathbf{x}, \lambda)$ completely define the problem, where $\mathbf{t}$ is the vector of total unknowns, $\mathbf{x}$ the vector of unknowns in displacement and tractions in the BEM case and λ is the unknown load factor. The BEM, based on continuum mechanics, provides n relationships describing the equilibrium state of a structure. This is expressed in a single equation

$$\mathbf{R}(\mathbf{x}, \lambda) = \lambda f_{ext} - f_{int}(\mathbf{x}) = 0 \tag{6.2}$$

The parameters of this equation are $\mathbf{R}(\mathbf{x}, \lambda)$ = the residual out-of-balance vector; λ = scalar load factor; f_{ext} = the external loads and constraints vector and $f_{int}(\mathbf{x})$ = the resultant of the internal loads and constraints vector.

In the following, one of the most efficient arc-length procedure [140], will be described in detail for its computer implementation. Also, two classical arc-length procedures are described.

6.3.1 Normal Flow Method

Several variants of the arc-length method have been proposed in literature [48] in its discrete formulation. The one used in the present work is the normal-flow algorithm [140, 156], where successive Newton-Raphson iterations converge to the equilibrium solution along a path which is normal (in an asymptotic sense) to the so-called Davidenko flow [140]. The Davidenko flow can be described by considering a small perturbation, δ, to the nonlinear system of equations:

$$\mathbf{R}(\mathbf{x}, \lambda) = \delta \tag{6.3}$$

As the perturbation parameter varies, small changes will occur in the solution curve for (6.3). The family of curves generated by varying δ is known as the Davidenko flow. The dashed lines in Fig. 6.2 are a representation of the Davidenko flow for a one-dimensional problem.

In Figure 6.3, the variables used in the arc-length method are shown, where the vector u_p (p = step number), in the case of BEM, is formed by the unknown displacements and tractions in a converged equilibrium point, while x_i (i = iteration number) is the vector of unknowns in the Newton-Raphson iterations between two converged equilibrium points, before equilibrium is reached. Thus, x_i becomes u_{p+1}, when x_i has converged

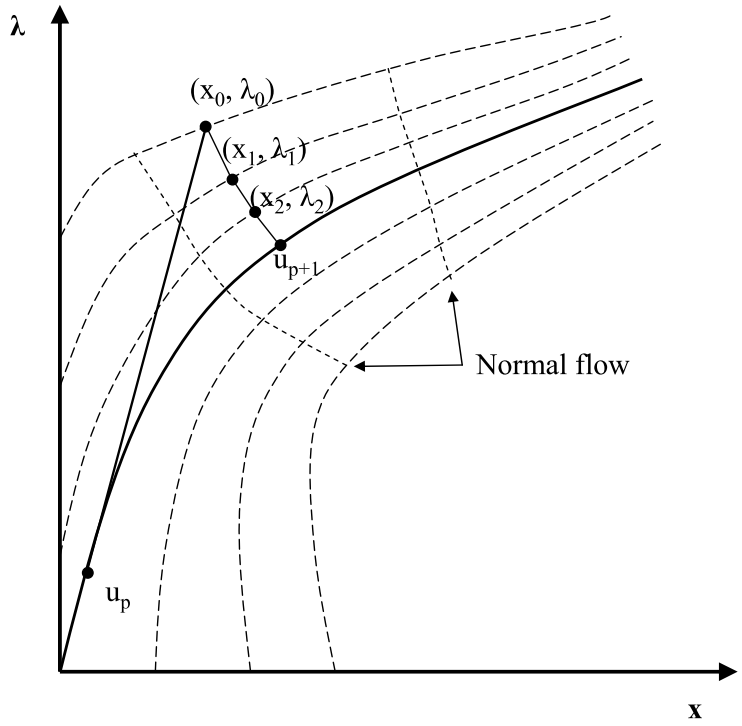

Figure 6.2: Normal flow arc-length procedure.

to an equilibrium point. (x_0, λ_0) corresponds to a predictor estimation.

A very important issue of the procedure is to define a suitable scaling of the known and unknown variables involved in the solution of a nonlinear system of equations. The variables in the final system should have similar orders of magnitude, so as to aid the performance of the non-linear numerical solver.

As mentioned the present solution algorithm was implemented using the full Newton-Raphson method and includes a predictor phase and a corrector phase.

Predictor phase.

The predictor phase includes the determination of the arc-length step size at each increment after equilibrium is reached. In Fig. 6.4, the predictor phase is depicted.

In the first step, an appropriate value for the increment of the arc length load factor, $d\lambda_{0|_{p=0}}$, defined by the user is needed. The increment of the

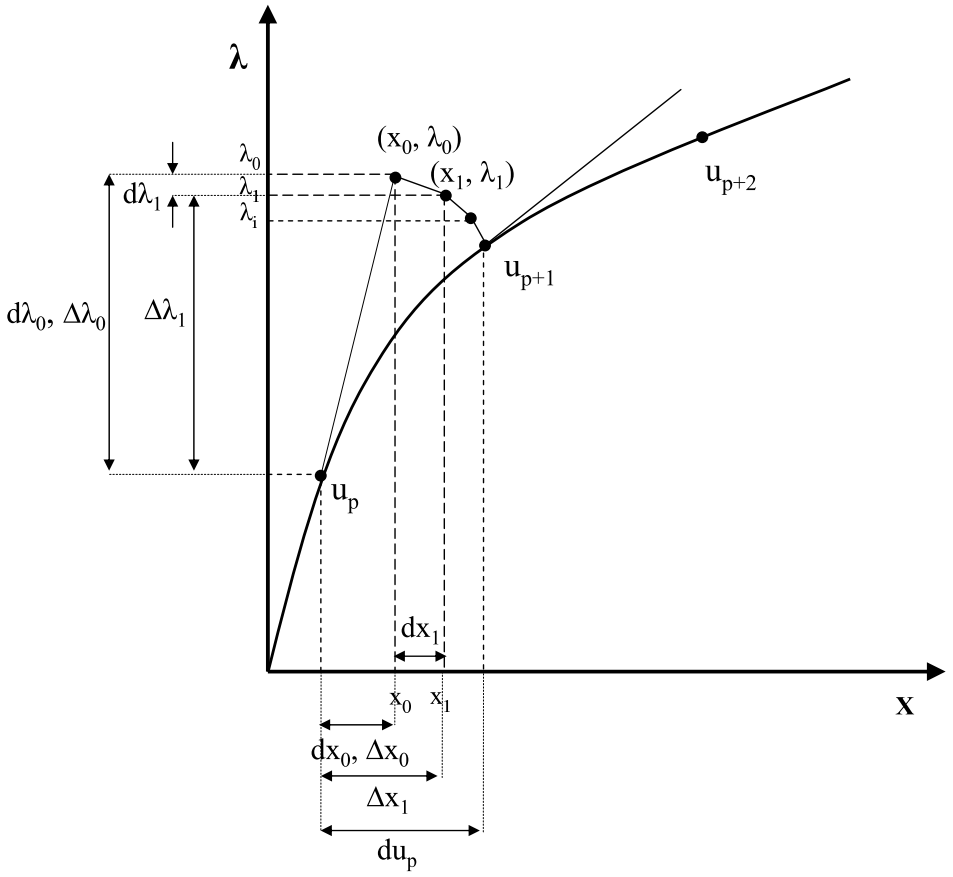

Figure 6.3: Graphic of the arc-length method with the Newton-Raphson method as iterative scheme.

arc-length load factor for the next steps are adjusted from one step to the next using the following simple formula:

$$\mathrm{d}\lambda^*_{0|_p} = \frac{n}{m}\,\mathrm{d}\lambda_{0|_{p-1}} \tag{6.4}$$

where m is the number of iterations that were required at the previous step and n is the (user specified) desired number of iterations at each step. This procedure allows larger steps to be taken when the solution is converging easily, and forces the solver to take smaller steps when the convergence is more difficult. For the present work, n was selected between 3 and 4 so as to achieve the most favorable results in terms of computational time.

After $d\lambda^*_{0|_p}$ for the load step p is calculated, the vector d_{II} is calculated

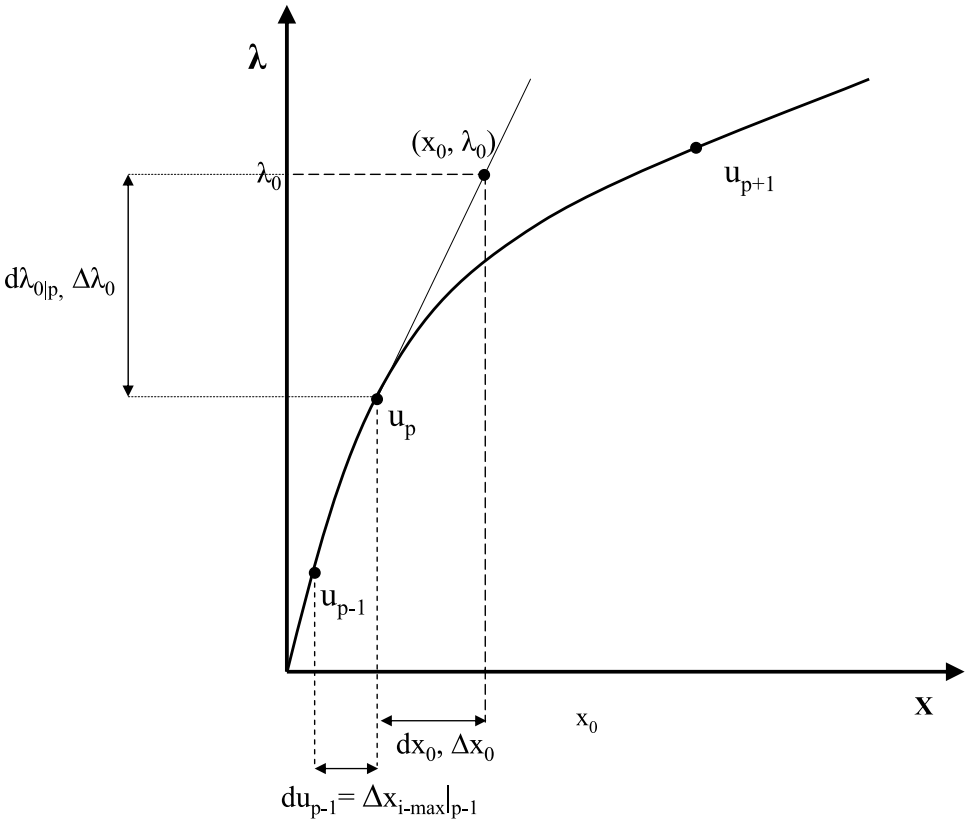

Figure 6.4: Predictor phase of the arc-length method.

by:

$$d_{II|_{x_0,p}} = [K_t^{-1}|_{0,p}]\{f_{ext}\}, \tag{6.5}$$

where $\{f_{ext}\}$ is the external load and constraints vector, see (6.2), and K_t is the tangential stiffness matrix of the considered structure in the FEM framework, in the present BEM case it can be defined as:

$$K_t = \frac{\mathrm{d}f_{int}(u_p)}{\mathrm{d}x}. \tag{6.6}$$

Then, the sign of the increment is calculated by means of the following relation:

$$sig = \mathrm{Sign}[du_{p-1}^T . d_{II|_{x_0,p}}] \tag{6.7}$$

with Sign[ ] being the Signum function, $\mathrm{d}u_{p-1} = u_p - u_{p-1}$ the vector that contains the difference between the last two converged solution points.

Then, the load factor $d\lambda_{0|_p}$ becomes:

$$d\lambda_{0|_p} = sig\, d\lambda^*_{0|_p} = \text{Sign}[du^T_{p-1}.\, d_{II|_{x_0,p}}]\, d\lambda^*_{0|_p}, \tag{6.8}$$

Finally, the predictor estimation is reached by:

$$dx_{0|_p} = d\lambda_{0|_p}\, .\, d_{II|_{x_0,p}} \tag{6.9}$$

$$x_0 = u_p + dx_{0|_p} \tag{6.10}$$

Corrector phase.

In the corrector phase, the full Newton-Raphson method is used in the present thesis. A scheme of this corrector phase is depicted in Fig. 6.5.

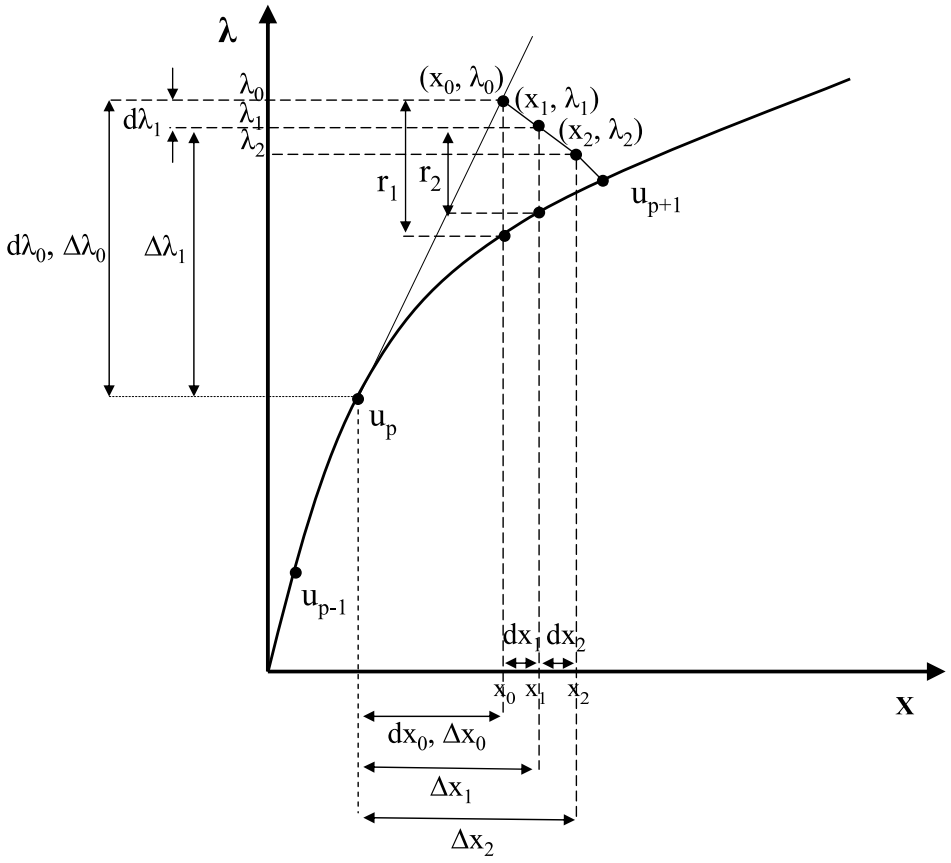

Figure 6.5: Corrector phase of the arc-length method.

In order to achieve a new iteration solution first the residual vector, $\{r_i\}$ is calculated for the i-iteration. In our BEM case, we made use of the following relation:

$$\{r_i\} = \mathbf{Hu} - \mathbf{Gt} \tag{6.11}$$

where $\mathbf{u}$ and $\mathbf{t}$ are the vectors of the actualized (taking into account the last iteration) displacement and traction solutions and/or boundary conditions. While, $\mathbf{G}$ and $\mathbf{H}$ are the matrixes obtained by the BEM, they are related to the fundamental solutions (Green's functions) in displacements and tractions respectively [131]. Notice that in order to calculate $\{r\}$ the variables are not taken in rate form.

Then, the vectors d_I and d_{II} for the i-iteration are calculated by:

$$d_{I|_{x_i,p}} = [K_t^{-1}|_{i,p}]\{r_i\}, \tag{6.12}$$

$$d_{II|_{x_i,p}} = [K_t^{-1}|_{i,p}]\{f_{ext}\}, \tag{6.13}$$

Then, the variation (increment or decrement) of the load factor in each iteration $d\lambda_i$ is determined by:

$$d\lambda_i = -\frac{[d_{II}|_{x_i}]^T.[d_I|_{x_i}]}{[d_{II}|_{x_i}]^T.[d_{II}|_{x_i}]} \tag{6.14}$$

Finally, the i-prediction of the corrector is reached by:

$$dx_i = d\lambda_i \,.\, d_{II|_{x_i,p}} + d_{I|_{x_i,p}} \tag{6.15}$$

$$x_i = x_{i-1} + dx_i \tag{6.16}$$

Once the value of the norm of the residual vector is smaller than a tolerance value (the residual vector usually tends to zero during the corrector iterations), the solution x_i is considered to be converged to an equilibrium state. Thus, the algorithm pass the to the next load step.

In order to stop the algorithm the user defines a load (usually a fraction of the maximum load reached during the solution).

It is also useful to clarify the difference between dx_i and $\triangle x_i$ as presented in Fig. 6.5. While $dx_i = x_i - x_{i-1}$ is the difference between Newton-Raphson iterations, $\triangle x_i = x_i - x_p$ is the difference between the i-th Newton-Raphson iteration and the last converged solution p. Thus, when $i = 0$ (predictor phase) $dx_0 = \triangle x_0$. In Fig. 6.6 a flow chart of the whole procedure is presented.

```
Loop on steps (p = 1, p_max)
   (Predictor phase)
   If p = 1 then
      assign dλ_0
   else
      dλ*_{0|p} = (n/m) dλ_{0|p-1}
   end If
   sig = Sign[du^T_{p-1} . d_{II|x_0,p}]
   dλ_{0|p} = sig . dλ*_{0|p}
   dx_{0|p} = dλ_{0|p} . d_{II|x_0,p}
   x_0 = u_p + dx_{0|p}
   Loop on iterations (i = 1, i_max)
      (Corrector phase)
      dλ_i = -([d_II|_{x_i}]^T . [d_I|_{x_i}]) / ([d_II|_{x_i}]^T . [d_II|_{x_i}])
      dx_i = dλ_i . d_{II|_{x_i},p} + d_{I|_{x_i},p}
      x_i = x_{i-1} + dx_i
      Convergence test
   End loop
End loop
```

Figure 6.6: Flow chart of the normal flow procedure.

6.3.2 Riks and Ramm Methods

As mentioned before, many authors have used different approaches for the arc-length method. Probably the most important variants are the ones developed by Riks[143], Ramm[141] and Crisfield [48, 61, 156].

Besides the normal flow procedure, described in detailed in the previous section, two other arc-length methods have been implemented in the 2D SGBEM code the Riks and Ramm arc-length procedures. It is noteworthy that the algorithm procedure described in the previous section and summarized in Fig. 6.6 was written in way that only changing equation (6.14) in the corrector phase allow the use of the different approaches.

Riks procedure.

The Riks' procedure is also called Normal plane Fig. 6.7(a). In this procedure the Newton-Raphson iterations are enforced to go along a line orthogonal to the tangent prediction increment. The original method was proposed in [143].

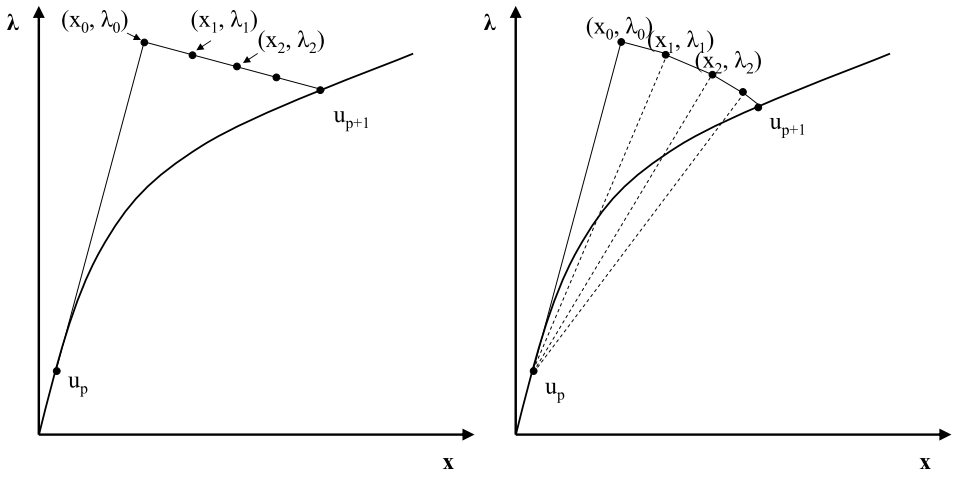

(a) (b)

Figure 6.7: Iterations path in the (a) Riks and (b) Ramm arc-length procedures.

As mentioned before, the Riks' arc length procedure can be obtained by using the procedure described in the previous subsection and just replacing (6.14) with:

$$d\lambda_i = -\frac{[d_{x0}]^T.[d_I|_{x_i}]}{[d_{x0}]^T.[d_{II}|_{x_i}]} \tag{6.17}$$

Ramm procedure.

This procedure is also called Updated Normal plane and it was proposed in [141]. In this procedure the Newton-Raphson iterations are orthogonal to the previos "secant increment", see Fig. 6.7(b). In a similar way, the Ramm's arc length procedure can be obtained by using the procedure described in the previous subsection and just replacing (6.14) with:

$$d\lambda_i = -\frac{[\triangle x_i]^T.[d_I|_{x_i}]}{[\triangle x_i]^T.[d_{II}|_{x_i}]} \tag{6.18}$$

It should be mentioned that preliminary test comparing the three arc-length procedures described previously have been carried out. The normal flow procedure being the fastest one, less iterations and/or steps were necessary.

Chapter 7

Formulation, implementation and validation of a Cohesive Zone Model in a 2D SGBEM code

In the present Chapter a Cohesive Zone Model will be included in a 2D Symmetric Galerkin BEM formulation. At first glance, it would appear that symmetry would be out of the question for a cohesive fracture model. However it is desirable and possible to obtain a symmetric formulation, as shown in [108] and elaborated on in this chapter for cracks inside an homogeneous domain, as well as for interface cracks [153].

After the formulations for cohesive cracks inside and homogeneous media and for cracks placed along an interface. Some numerical examples were solved in order to see the capability of the formulation introduced.

7.1 Pressurized cracks in homogeneous media in 2D SGBEM

Consider a linear elastic body of arbitrary shape Ω which contains a crack, see Fig. 7.1. The boundary Γ of the body Ω is composed of the non-crack boundary Γ_b and the crack surface Γ_c. The crack surface Γ_c consists of two coincident surfaces Γ_c^+ and Γ_c^- which represent the so-called upper and lower crack surfaces respectively. As explained in [4, 3, 5, 75, 108, 135] it suffices to discretize one crack surface (e.g. the upper one) as the crack

surfaces are usually symmetrically loaded, i.e. $\mathbf{t} = \mathbf{t}_c^+ = -\mathbf{t}_c^-$, where $\mathbf{t}$ represent the traction vector.

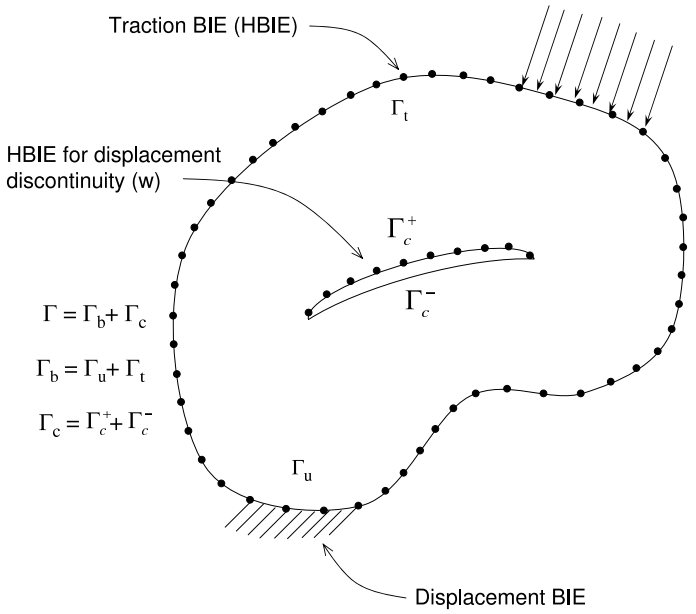

Figure 7.1: Configuration of the fracture scheme using SGBEM.

Thus the Somigliana displacement (u-BIE) and traction (t-BIE) identities, see (5.1) and (5.4) respectively, written for a point $\boldsymbol{x}'$ in a smooth part of the boundary take the following form:

$$\frac{1}{2}u_i(\boldsymbol{x}') = \fint_{\Gamma_b} \left[U_{ik}(\boldsymbol{x}-\boldsymbol{x}')t_i(\boldsymbol{x}) - T_{ik}(\boldsymbol{x},\boldsymbol{x}')u_i(\boldsymbol{x})\right] dS(\boldsymbol{x}) - \fint_{\Gamma_c^+} \left[T_{ik}(\boldsymbol{x},\boldsymbol{x}')w_i(\boldsymbol{x})\right] dS(\boldsymbol{x}) \qquad \boldsymbol{x}' \in \Gamma_u \quad (7.1)$$

$$\frac{1}{2}t_i(\boldsymbol{x}') = \fint_{\Gamma_b} \left[T^*_{ik}(\boldsymbol{x},\boldsymbol{x}')t_i(\boldsymbol{x}) - S_{ik}(\boldsymbol{x},\boldsymbol{x}')u_i(\boldsymbol{x})\right] dS(\boldsymbol{x}) - \fint_{\Gamma_c^+} \left[S_{ik}(\boldsymbol{x},\boldsymbol{x}')w_i(\boldsymbol{x})\right] dS(\boldsymbol{x}) \qquad \boldsymbol{x}' \in \Gamma_t \quad (7.2)$$

$$t_i(\boldsymbol{x}') = \neq\!\!\!\!\int_{\Gamma_b} \left[T^*_{ik}(\boldsymbol{x},\boldsymbol{x}')t_i(\boldsymbol{x}) - S_{ik}(\boldsymbol{x},\boldsymbol{x}')u_i(\boldsymbol{x})\right] dS(\boldsymbol{x}) \\ - \neq\!\!\!\!\int_{\Gamma_c^+} \left[S_{ik}(\boldsymbol{x},\boldsymbol{x}')w_i(\boldsymbol{x})\right] dS(\boldsymbol{x}) \qquad \boldsymbol{x}' \in \Gamma_c^+ \qquad (7.3)$$

where $\mathbf{w} = \mathbf{u}_c^+ - \mathbf{u}_c^-$ is the relative displaments between the crack faces. The non-crack boundary Γ_b is formed by Γ_u and Γ_t, where Γ_u is the portion of the boundary with prescribed displacements $\mathbf{u}_u$ and Γ_t is the portion of the boundary with prescribed tractions $\mathbf{t}_t$. As tractions are prescribed on the crack surface, only t-BIE is written for source points on Γ_c^+. Discretizing a weak form of Equations (7.1-7.3) by using a Galerkin scheme, see Section 5.3, the following system is obtained in block matrix form:

$$\begin{bmatrix} \frac{1}{2}\mathbf{M}_{uu} + \mathbf{T}_{uu} & \mathbf{T}_{ut} & \mathbf{T}_{uc} \\ \mathbf{S}_{tu} & \mathbf{S}_{tt} & \mathbf{S}_{tc} \\ \mathbf{S}_{cu} & \mathbf{S}_{ct} & \mathbf{S}_{cc} \end{bmatrix} \begin{Bmatrix} \mathbf{u}_u \\ \mathbf{u}_t \\ \mathbf{w}_c \end{Bmatrix} \\ = \begin{bmatrix} \mathbf{U}_{uu} & \mathbf{U}_{ut} & 0 \\ \mathbf{T}^*_{tu} & -\frac{1}{2}\mathbf{M}_{tt} + \mathbf{T}^*_{tt} & 0 \\ \mathbf{T}^*_{cu} & \mathbf{T}^*_{ct} & -\mathbf{M}_{cc} \end{bmatrix} \begin{Bmatrix} \mathbf{t}_u \\ \mathbf{t}_t \\ \mathbf{t}_c^+ \end{Bmatrix} \qquad (7.4)$$

where, the subscripts u, t, and c represent respectively the terms corresponding to the non-crack boundary with prescribed displacements Γ_u, to the non-crack boundary with prescribed tractions Γ_t, and to the crack surface Γ_c^+. The first subscript in each matrix operator (denoted by capitals) defines where the exterior integral test function, like in (5.12), is considered and the second subscript is on which part of the boundary the inner integral is considered, or which is the variable where the corresponding displacement or traction integral equation is considered.

The vector $\mathbf{t}_u$ represents unknown tractions and $\mathbf{u}_t$ represents unknown displacements on the boundary Γ_u and Γ_t respectively; $\mathbf{M}$ is a 'mass matrix' obtained from the free term of the integral equations. $\mathbf{T}$ and $\mathbf{U}$ represents the matrixes obtained from the traction (T_{ik}) and displacement (U_{ik}) fundamental solutions in the u-BIE respectively. While $\mathbf{T}^*$ and $\mathbf{S}$ represents respectively the matrixes obtained from the integral kernels (T^*_{ik}) and (S_{ik}) used in the t-BIE.

This formulation allows solving cracks with a symmetrical pressure on the crack faces. Note that if there are no tractions on the crack faces the present formulation would be the same as that presented for a traction free crack in [161, 135].

7.2 Cohesive cracks in homogeneous media in 2D SGBEM

In this section a crack inside an homogeneous media, as the one in Fig. 7.1, will be considered to behave according to a cohesive law. In order to introduce the Cohesive Zone Model behaviour into the crack, equation (7.4) is rearranged into a suitable rate form $[A]\{\dot{x}\} = \{\dot{b}\}$ by:

- Formulating the problem in an incremental form, the variables involved can be written in terms of rates, $\dot{x} = \triangle(x)$, where for this specific formula x represent any variable.
- Multiplying the t-BIEs by -1 (for symmetry).
- Making use of the relation $\dot{t}_i = k_{ij}\dot{\delta}_j$ in the crack cohesive zone, see (3.14), which relates the traction rate ($\dot{\mathbf{t}}(\mathbf{x}) = \dot{\mathbf{t}}_c^+(\mathbf{x})$) along the crack cohesive surface with the crack opening displacement rate ($\dot{\mathbf{w}}(\mathbf{x}) = -\dot{\boldsymbol{\delta}}(\mathbf{x})$), at a point $\mathbf{x} \in \Gamma_c$, associated to a certain increment of the load factor.

In this way we finally arrive at the system written in terms of rates of elastic variables:

$$\begin{bmatrix} -\mathbf{U}_{uu} & \mathbf{T}_{ut} & \mathbf{T}_{uc} \\ \mathbf{T}^*_{tu} & -\mathbf{S}_{tt} & -\mathbf{S}_{tc} \\ \mathbf{T}^*_{cu} & -\mathbf{S}_{ct} & -\mathbf{S}_{cc}+\mathbf{K}\mathbf{M}_{cc} \end{bmatrix} \begin{Bmatrix} \dot{\mathbf{t}}_u \\ \dot{\mathbf{u}}_t \\ \dot{\mathbf{w}}_c \end{Bmatrix} = \begin{Bmatrix} -(\frac{1}{2}\mathbf{M}_{uu}+\mathbf{T}_{uu})\dot{\mathbf{u}}_u + \mathbf{U}_{ut}\dot{\mathbf{t}}_t \\ \mathbf{S}_{tu}\dot{\mathbf{u}}_u + (\frac{1}{2}\mathbf{M}_{tt}-\mathbf{T}^*_{tt})\dot{\mathbf{t}}_t \\ \mathbf{S}_{cu}\dot{\mathbf{u}}_u - \mathbf{T}^*_{ct}\dot{\mathbf{t}}_t \end{Bmatrix} \quad (7.5)$$

It is noteworthy to mention that for sake of simplicity in the above matrix form the whole crack was considered as a cohesive zone, nevertheless a non-cohesive crack can also be involved in the formulation either as a part of the same crack or as a different crack in the homogeneous body (where the usual crack formulation is adopted as described in Section 7.1, this is to say that $\mathbf{t}_c^+$ will be a boundary condition and part of the right hand side of the linear system).

The final coefficient matrix of this system is symmetric due to the reciprocity relations of the integral kernel tensors as shown in [28, 75, 161], *i.e.* $\mathbf{T}_{ut} = (\mathbf{T}^*_{tu})^T$, $\mathbf{T}_{uc} = (\mathbf{T}^*_{cu})^T$ and $\mathbf{S}_{tc} = (\mathbf{S}_{ct})^T$, see also (5.14) and (5.15).

In [75] a similar matrix is obtained for the case of traction free cracks. The only difference here with the previous work and what is in fact new in the present procedure with respect to previous works is the diagonal term $-\mathbf{S}_{cc}+\mathbf{K}\mathbf{M}_{cc}$, where $\mathbf{K}$ is the tangent elastic stiffness matrix obtained from the cohesive law, see (3.14). It can be shown that the product $\mathbf{K}\mathbf{M}_{cc}$ keeps the desired symmetry, if $\mathbf{K}$ is symmetric. This is, for example, the case of the Ortiz-Pandolfi cohesive zone model (Section 3.2) where a symmetric matrix $\mathbf{K}$ is obtained.

7.3 Cohesive cracks at interfaces in 2D SGBEM

The formulation for the problem of several domains connected by cohesive interfaces was presented in [152, 153, 154]. A review of this formulation is given in this section using the present notation.

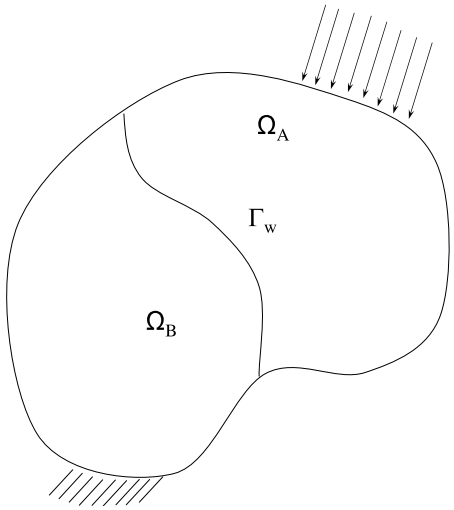

Figure 7.2: Configuration of an interface problem.

For the sake of simplicity, let us consider two domains Ω^A and Ω^B with a single common interface Γ_w, see Fig. 7.2. The geometrical description of the interface is similar to the geometrical description of the crack, shown in the previous section. Then we can define $\dot{\mathbf{w}}(\mathbf{x}) = \dot{\mathbf{u}}^{\mathbf{A}}_{\mathbf{w}}(\mathbf{x}) - \dot{\mathbf{u}}^{\mathbf{B}}_{\mathbf{w}}(\mathbf{x})$ and $\dot{\mathbf{t}}(\mathbf{x}) = \dot{\mathbf{t}}^{\mathbf{A}}_{\mathbf{w}}(\mathbf{x})$ at a point $\mathbf{x} \in \Gamma_w$. Cohesive tractions $\mathbf{t}$ and relative opening displacements $\mathbf{w}$ are related by a non-linear vector function $\mathbf{t}(\mathbf{w}(\mathbf{x}))$, $\forall \mathbf{x} \in$

Γ_w. Let us define vectors $\mathbf{v}$ and $\mathbf{z}$ as follows:

$$\dot{\mathbf{v}} = \tfrac{1}{2}(\dot{\mathbf{u}}^{\mathbf{A}}_{\mathbf{w}} + \dot{\mathbf{u}}^{\mathbf{B}}_{\mathbf{w}}) \quad , \quad \dot{\mathbf{z}} = \tfrac{1}{2}(\dot{\mathbf{u}}^{\mathbf{A}}_{\mathbf{w}} - \dot{\mathbf{u}}^{\mathbf{B}}_{\mathbf{w}}) = \tfrac{1}{2}\dot{\mathbf{w}} \tag{7.6}$$

Then, using (7.1) and (7.2) for each domain, including three linear combinations of them for the interface (u-BIE^A $-$ u-BIE^B, t-BIE^A $+$ t-BIE^B, t-BIE^A $-$ t-BIE^B), a suitable arrangement of the system of equations can be written in block matrix form

$$[\mathbf{A}']\{\dot{\mathbf{x}}'\} = \{\dot{\mathbf{b}}'\} \tag{7.7}$$

where:

$$\{\dot{\mathbf{x}}'\} = \{\dot{\mathbf{t}}^A_u, \dot{\mathbf{u}}^A_t, \dot{\mathbf{t}}^B_u, \dot{\mathbf{u}}^B_t, \dot{\mathbf{t}}_w, \dot{\mathbf{v}}_w, \dot{\mathbf{z}}_w\},$$

$$\{\dot{\mathbf{b}}'\} = \left\{ \begin{array}{c} (\frac{1}{2}\mathbf{M}_{uu} + \mathbf{T}_{uu})\dot{\mathbf{u}}^A_u - \mathbf{U}_{ut}\dot{\mathbf{t}}^A_t \\ -\mathbf{S}_{tu}\dot{\mathbf{u}}^A_u + (\frac{1}{2}\mathbf{M}_{tt} - \mathbf{T}^*_{tt})\dot{\mathbf{t}}^A_t \\ (\frac{1}{2}\mathbf{M}_{uu} + \mathbf{T}_{uu})\dot{\mathbf{u}}^B_u - \mathbf{U}_{ut}\dot{\mathbf{t}}^B_t \\ -\mathbf{S}_{tu}\dot{\mathbf{u}}^B_u + (\frac{1}{2}\mathbf{M}_{tt} - \mathbf{T}^*_{tt})\dot{\mathbf{t}}^B_t \\ \mathbf{T}_{wu}\dot{\mathbf{u}}^A_u - \mathbf{U}_{wt}\dot{\mathbf{t}}^A_t - \mathbf{T}_{wu}\dot{\mathbf{u}}^B_u + \mathbf{U}_{wt}\dot{\mathbf{t}}^B_t \\ -\mathbf{S}_{wu}\dot{\mathbf{u}}^A_u - \mathbf{T}^*_{wt}\dot{\mathbf{t}}^A_t - \mathbf{S}_{wu}\dot{\mathbf{u}}^B_u - \mathbf{T}^*_{wt}\dot{\mathbf{t}}^B_t \\ -\mathbf{S}_{wu}\dot{\mathbf{u}}^A_u - \mathbf{T}^*_{wt}\dot{\mathbf{t}}^A_t + \mathbf{S}_{wu}\dot{\mathbf{u}}^B_u + \mathbf{T}^*_{wt}\dot{\mathbf{t}}^B_t \end{array} \right\} \begin{array}{l} \text{on} \quad \Gamma^A_u \\ \text{on} \quad \Gamma^A_t \\ \text{on} \quad \Gamma^B_u \\ \text{on} \quad \Gamma^B_t \\ \text{on} \quad \Gamma_w \\ \text{on} \quad \Gamma_w \\ \text{on} \quad \Gamma_w \end{array}$$

$$
[\mathbf{A}'] = \begin{bmatrix}
-\mathbf{U}^A_{uu} & \mathbf{T}^A_{ut} & 0 & 0 & -\mathbf{U}^A_{uw} & \mathbf{T}^A_{uw} & \mathbf{T}^A_{uw} \\
\mathbf{T}^{A*}_{tu} & -\mathbf{S}^A_{tt} & 0 & 0 & \mathbf{T}^{A*}_{tw} & -\mathbf{S}^A_{tw} & -\mathbf{S}^A_{tw} \\
0 & 0 & -\mathbf{U}^B_{uu} & \mathbf{T}^B_{ut} & \mathbf{U}^B_{uw} & \mathbf{T}^B_{uw} & -\mathbf{T}^B_{uw} \\
0 & 0 & \mathbf{T}^{B*}_{tu} & -\mathbf{S}^B_{tt} & -\mathbf{T}^{B*}_{tw} & -\mathbf{S}^B_{tw} & \mathbf{S}^B_{tw} \\
-\mathbf{U}^A_{wu} & \mathbf{T}^A_{wt} & \mathbf{U}^B_{wu} & -\mathbf{T}^B_{wt} & -(\mathbf{U}^A_{ww} + \mathbf{U}^B_{ww}) & (\mathbf{T}^A_{ww} - \mathbf{T}^B_{ww}) & (\mathbf{T}^A_{ww} + \mathbf{T}^B_{ww} + \mathbf{M}_{ww}) \\
\mathbf{T}^{A*}_{wu} & -\mathbf{S}^A_{wt} & \mathbf{T}^{B*}_{wu} & -\mathbf{S}^B_{wt} & (\mathbf{T}^{A*}_{ww} - \mathbf{T}^{B*}_{ww}) & -(\mathbf{S}^A_{ww} + \mathbf{S}^B_{ww}) & -(\mathbf{S}^A_{ww} - \mathbf{S}^B_{ww}) \\
\mathbf{T}^{A*}_{wu} & -\mathbf{S}^A_{wt} & -\mathbf{T}^{B*}_{wu} & \mathbf{S}^B_{wt} & (\mathbf{T}^{A*}_{ww} + \mathbf{T}^{B*}_{ww} - \mathbf{M}_{ww}) & -(\mathbf{S}^A_{ww} - \mathbf{S}^B_{ww}) & -(\mathbf{S}^A_{ww} + \mathbf{S}^B_{ww})
\end{bmatrix}
$$

Multiplying by $\mathbf{K^T}$ the rows related with the variable $\dot{t}$ and setting $\dot{\mathbf{t}} = -\mathbf{K}\dot{\mathbf{z}}$, the system can be written in block matrix form $[\mathbf{A}]\{\dot{\mathbf{x}}\} = \{\dot{\mathbf{b}}\}$ where:

$$[\mathbf{A}] = \left[\begin{array}{c|c|c|c|c|c}
-\mathbf{U}^A_{uu} & \mathbf{T}^A_{ut} & 0 & 0 & \mathbf{U}^A_{uw}\mathbf{K} + \mathbf{T}^A_{uw} & \mathbf{T}^A_{uw} \\ \hline
\mathbf{T}^{A*}_{tu} & -\mathbf{S}^A_{tt} & 0 & 0 & -(\mathbf{T}^{A*}_{tw}\mathbf{K} + \mathbf{S}^A_{tw}) & -\mathbf{S}^A_{tw} \\ \hline
0 & 0 & -\mathbf{U}^B_{uu} & \mathbf{T}^B_{ut} & -(\mathbf{U}^B_{uw}\mathbf{K} + \mathbf{T}^B_{uw}) & \mathbf{T}^B_{uw} \\ \hline
0 & 0 & \mathbf{T}^{B*}_{tu} & -\mathbf{S}^B_{tt} & \mathbf{T}^{B*}_{tw}\mathbf{K} + \mathbf{S}^B_{tw} & -\mathbf{S}^B_{tw} \\ \hline
\begin{array}{c}\mathbf{K}^T\mathbf{U}^A_{wu} \\ +\mathbf{T}^{A*}_{wu}\end{array} & \begin{array}{c}-\mathbf{K}^T\mathbf{T}^A_{wt} \\ -\mathbf{S}^A_{wt}\end{array} & \begin{array}{c}-\mathbf{K}^T\mathbf{U}^B_{wu} \\ -\mathbf{T}^{B*}_{wu}\end{array} & \begin{array}{c}\mathbf{K}^T\mathbf{T}^B_{wt} \\ +\mathbf{S}^B_{wt}\end{array} & \begin{array}{c}-\mathbf{K}^T(\mathbf{U}^A_{ww} + \mathbf{U}^B_{ww})\mathbf{K} \\ -\mathbf{K}^T(\mathbf{T}^A_{ww} + \mathbf{T}^B_{ww}) \\ -(\mathbf{T}^{A*}_{ww} + \mathbf{T}^{B*}_{ww})\mathbf{K} \\ -(\mathbf{S}^A_{ww} + \mathbf{S}^B_{ww})\end{array} & \begin{array}{c}-\mathbf{K}^T(\mathbf{T}^A_{ww} - \mathbf{T}^B_{ww}) \\ -(\mathbf{S}^A_{ww} - \mathbf{S}^B_{ww})\end{array} \\ \hline
\mathbf{T}^{A*}_{wu} & -\mathbf{S}^A_{wt} & \mathbf{T}^{B*}_{wu} & -\mathbf{S}^B_{wt} & \begin{array}{c}-(\mathbf{T}^{A*}_{ww} - \mathbf{T}^{B*}_{ww})\mathbf{K} \\ -(\mathbf{S}^A_{ww} - \mathbf{S}^B_{ww})\end{array} & -(\mathbf{S}^A_{ww} + \mathbf{S}^B_{ww})
\end{array}\right]$$

$$\{\dot{\mathbf{x}}\} = \left\{\dot{\mathbf{t}}_u^A, \dot{\mathbf{u}}_t^A, \dot{\mathbf{t}}_u^B, \dot{\mathbf{u}}_t^B, \dot{\mathbf{v}}, \dot{\mathbf{z}}\right\}^T$$

$$\{\dot{\mathbf{b}}\} = \left\{ \begin{array}{c} (\frac{1}{2}\mathbf{M}_{uu} + \mathbf{T}_{uu})\dot{\mathbf{u}}_u^A - \mathbf{U}_{ut}\dot{\mathbf{t}}_t^A \\ -\mathbf{S}_{tu}\dot{\mathbf{u}}_u^A + (\frac{1}{2}\mathbf{M}_{tt} - \mathbf{T}_{tt}^*)\dot{\mathbf{t}}_t^A \\ (\frac{1}{2}\mathbf{M}_{uu} + \mathbf{T}_{uu})\dot{\mathbf{u}}_u^B - \mathbf{U}_{ut}\dot{\mathbf{t}}_t^B \\ -\mathbf{S}_{tu}\dot{\mathbf{u}}_u^B + (\frac{1}{2}\mathbf{M}_{tt} - \mathbf{T}_{tt}^*)\dot{\mathbf{t}}_t^B \\ \mathbf{K}^T(-\mathbf{T}_{wu}\dot{\mathbf{u}}_u^A + \mathbf{U}_{wt}\dot{\mathbf{t}}_t^A + \mathbf{T}_{wu}\dot{\mathbf{u}}_u^B - \mathbf{U}_{wt}\dot{\mathbf{t}}_t^B) - \mathbf{S}_{wu}\dot{\mathbf{u}}_u^A - \mathbf{T}_{wt}^*\dot{\mathbf{t}}_t^A + \mathbf{S}_{wu}\dot{\mathbf{u}}_u^B + \mathbf{T}_{wt}^*\dot{\mathbf{t}}_t^B \\ -(\mathbf{S}_{wu}\dot{\mathbf{u}}_u^A + \mathbf{T}_{wt}^*\dot{\mathbf{t}}_t^A + \mathbf{S}_{wu}\dot{\mathbf{u}}_u^B + \mathbf{T}_{wt}^*\dot{\mathbf{t}}_t^B) \end{array} \right\}$$

7.4 Validation of the SGBEM-CZM and arc-length implementation

In order to verify the capability of the Ortiz-Pandolfi cohesive zone model implemented into a 2D SGBEM code to model crack growth in a homogeneous media, two experimental tests were simulated. It should be mentioned that the formulation for pressurized cracks shown in Section 7.1 was previously verified. Crack problems with analytic solutions were solved and excellent accurate results were obtained.

7.4.1 Wedge split test

The wedge split test for a concrete mix, studied in [52], is modeled by the SGBEM code with the homogeneous cohesive crack approach (Section 7.2).

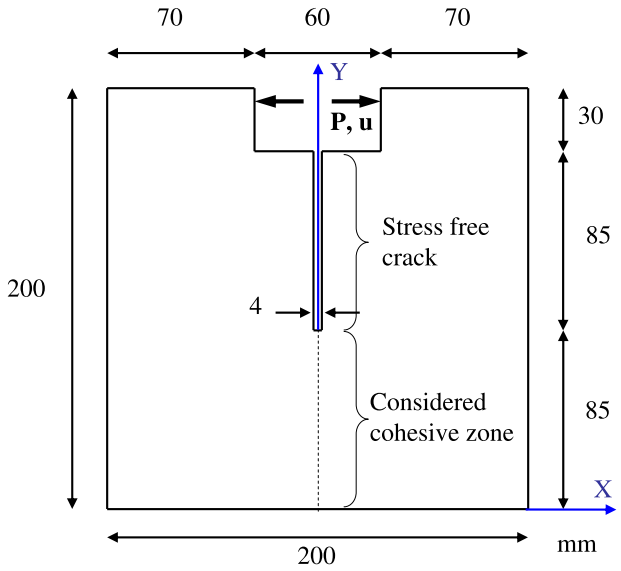

Figure 7.3: Specimen configuration of the wedge split test.

The material characteristics are considered homogeneous and linear isotropic, with Young´s modulus $E = 25.2$GPa, Poisson ratio $\nu = 0.22$, specific fracture energy $G_{Ic} = 101\text{J/m}^2$, and the parameter values for the Ortiz-Pandolfi model are maximum cohesive stress $\sigma_c = 2.5$MPa and critical opening displacement $\delta_c = 1.48623\text{x}10^{-5}$m. It is important to mention that in this case the parameter β, defined in (3.6), is not used, due to the

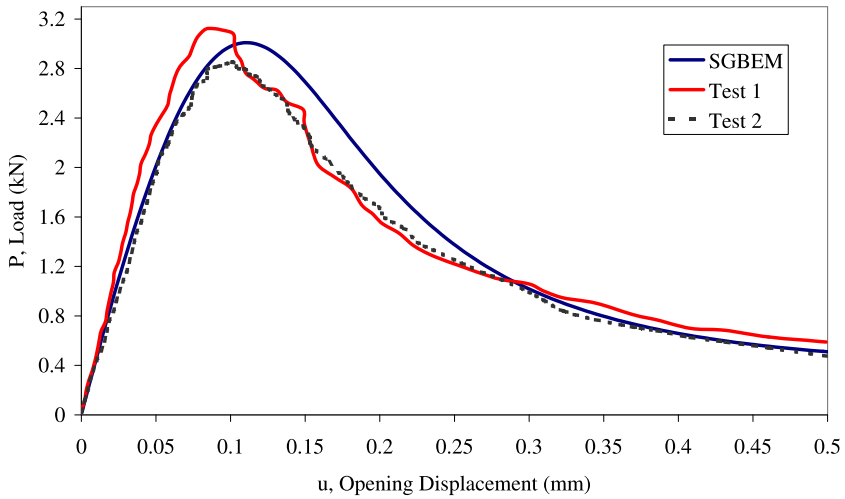

Figure 7.4: Wedge split test load-displacement curve prediction and experimental results [52].

Mode I character of the problem.

The specimen dimensions are shown in Fig. 7.3. Notice that although experimentally the pre-crack has 4 mm width (because of the machine tool) a stress free crack with no width is considered in the BEM model. A plain strain state is considered for this problem. 206 quadratic boundary elements were used to model the problem by means of a uniform mesh (element size is 5 mm). As the formulation allows it, only one side of the stress free crack, as well as in the cohesive zone, is meshed. Displacements are applied over one element ($u_y = 0, u_x = \pm\lambda u$), in the points where the load is applied experimentally.

In the present problem 1/10 fraction of the maximum load reached is defined as stop criteria of the nonlinear solution algorithm. The numerical results obtained with the SGBEM code are represented by the load - displacement global response curve shown in Fig. 7.4, the load and displacements are measured as shown in Fig. 7.3.

Fig. 7.5 and Fig. 7.6 show the boundary element mesh used, deformed at various load levels, while in Fig. 7.7 the normal stresses along the crack path for the same load levels are shown. Notice that, in Fig. 7.5 and Fig. 7.6 only one side of the crack is meshed (as mentioned before). As the relative displacements between the crack faces is directly obtained, the deformed configuration of the crack faces is obtained by symmetry (different color for each crack face). Also, in Fig. 7.7 it can be observed that compressions

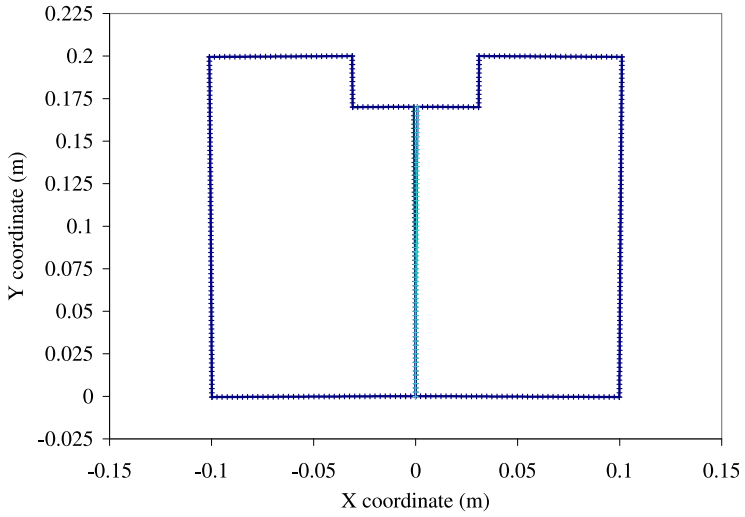

(a)

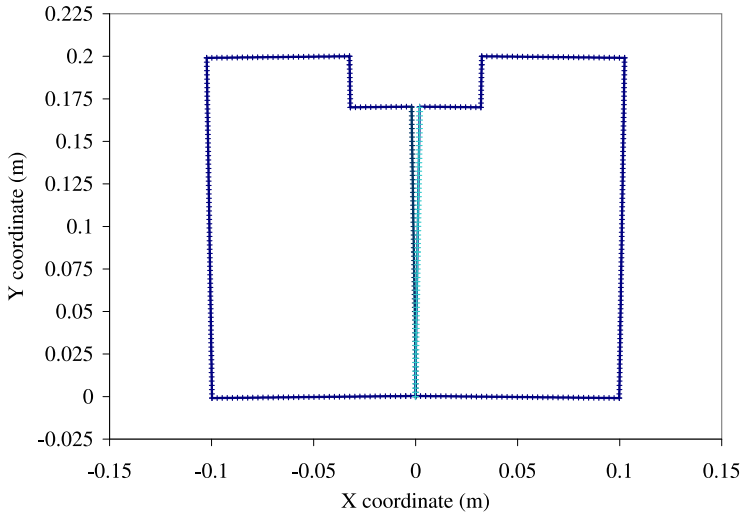

(b)

Figure 7.5: Deformed boundary element mesh of the wedge split test (with displacements multiplied by a factor of 20) for different load steps at the softening branch (a)$P = 3008N$ peak load and (b) $P = 1497N$.

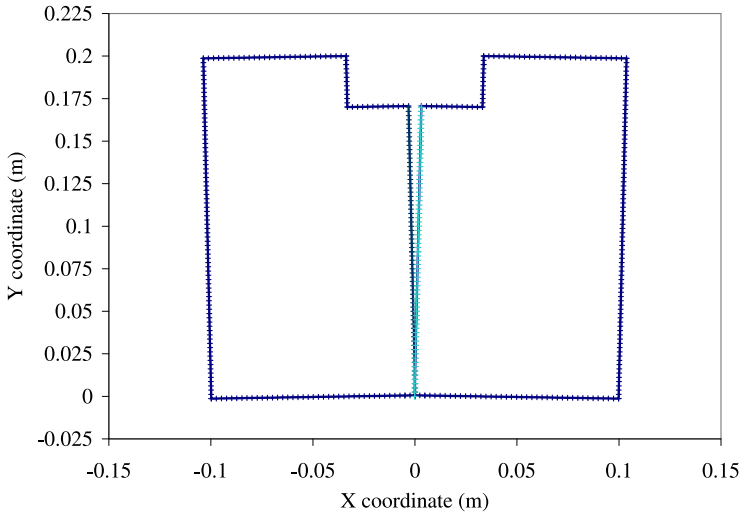

(a)

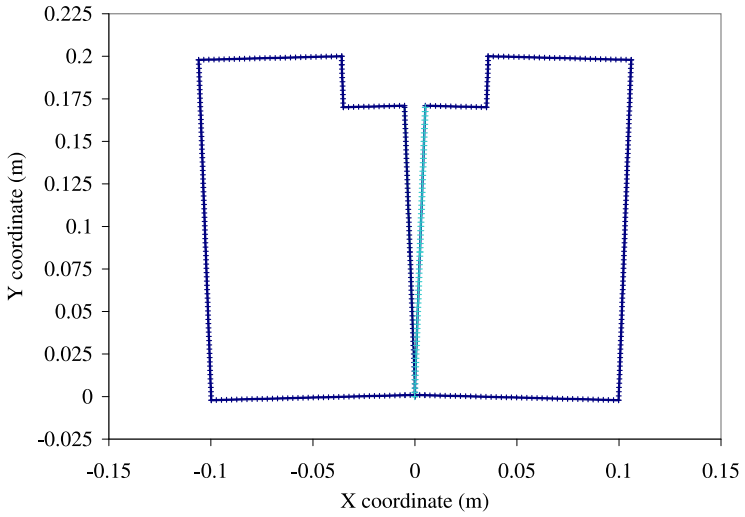

(b)

Figure 7.6: Deformed boundary element mesh of the wedge split test (with displacements multiplied by a factor of 20) for different load steps at the softening branch (a)$P = 749N$ and (b) $P = 451N$.

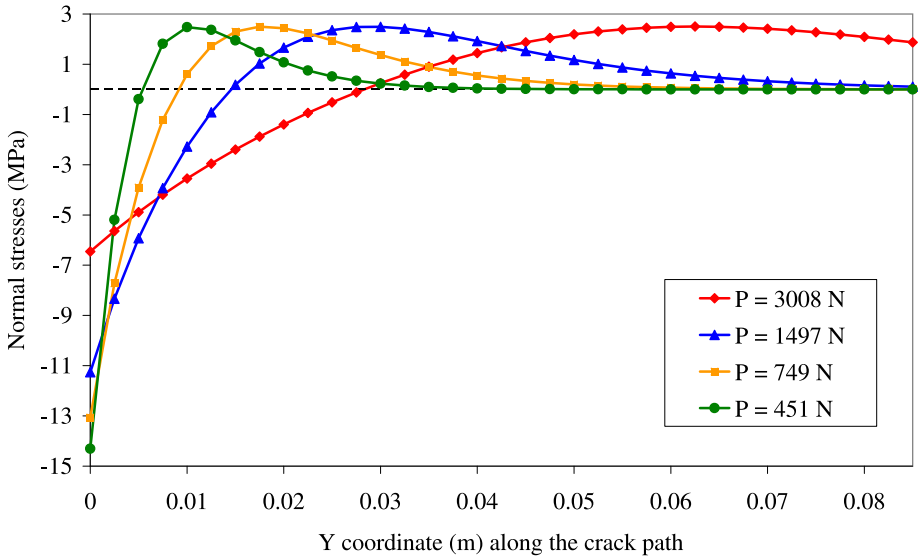

Figure 7.7: Normal stresses along the crack path for different load steps at the softening branch in the wedge split test.

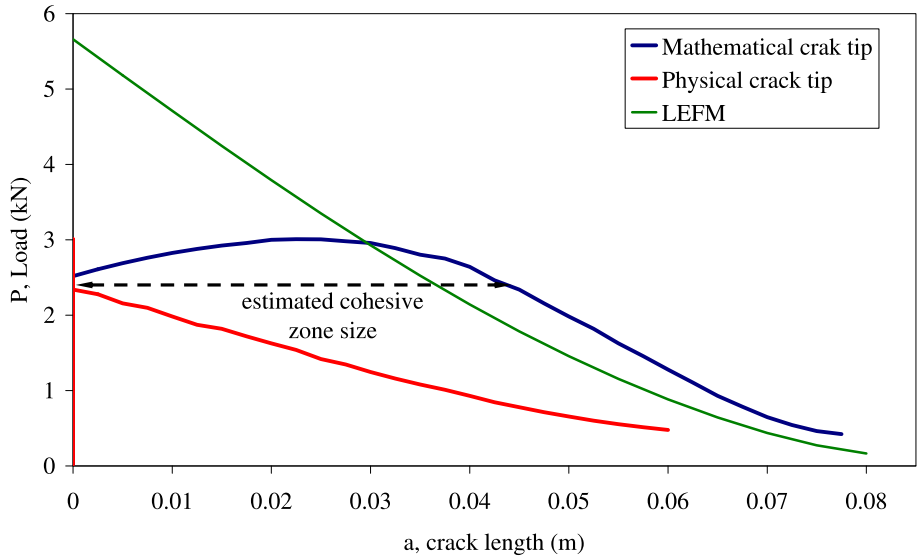

Figure 7.8: Crack length defined by the position of the mathematical and physical cohesive crack tips as well as the crack length obtained by means of LEFM in the wedge split test.

appear in the part ahead of the crack tip due to an equilibrium of momentums. The use of the modification of the Ortiz-Pandolfi CZM proposed in Section 3.2 allowed to catch this behavior. It is noteworthy that if the original Ortiz-Pandolfi CZM is used an artificial (non-physically based) large overlapping/interpenetration is produced, this overlapping could be even greater than the opening produced in the crack front.

A comparison of the crack length obtained considering the mathematical and physical cohesive crack tip as well as the crack length obtained by means of LEFM is shown in Fig. 7.8, where the mathematical crack tip is the location of the node in which the critical stress is reached, and the physical crack tip (for this case) is the location of the node in which one fifth of the critical stress in the softening branch is reached. The curve using LEFM is obtained by evaluating the fracture toughness (K_{Ic}) at various crack sizes, in these cases no cohesive zone is considered. Fig. 7.8 clearly indicates, that for a concrete structure with the described size the application of LEFM instead of CZM leads to a strong overestimation of the maximum load. Also the size of the cohesive zone, see Fig. 3.1, can be estimated from Fig. 7.8 as the difference between coordinates of the mathematical and estimated physical crack tip.

7.4.2 Three-point bending test

Three-point bending test, Fig. 7.9(a), for a concrete mix is modeled. The growth of a cohesive crack in such a specimen was studied extensively in [36] using the Finite Element Method (FEM) and the node release technique for a linear cohesive law. In the present work the influence of the initial crack depth and the value of fracture energy are studied.

The dimensions of the specimen considered are height $b = 0.15$m, thickness $t = b$ and span $l = 4b$. A uniform boundary element mesh (with element size 0.005m) with 672 nodes and 330 quadratic elements are employed in the numerical simulation of this specimen. The anticipated straight crack path is modeled by a mesh placed inside the single domain representing the specimen tested. The point-supports are imposed by means of the *Method S* [172]. This method allowed an adequate simulation of the three-point bending test, as the point-support boundary condition can be situated at a single node (similar to FEM), rather than fixing an entire element. The point supports at the two bottom corners are shown in Fig. 7.9(a), and as only one node is constrained at each support, rotation around these points is allowed. Constant distributions of pressures, which fulfill the condition of global equilibrium, were imposed over two elements at the centre top of

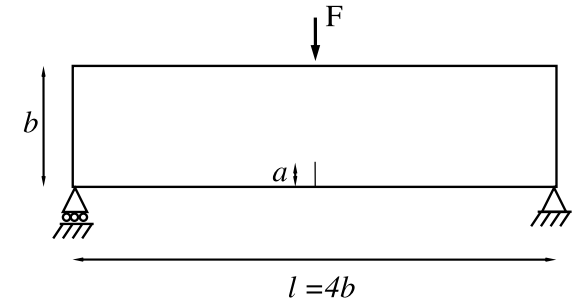

(a)

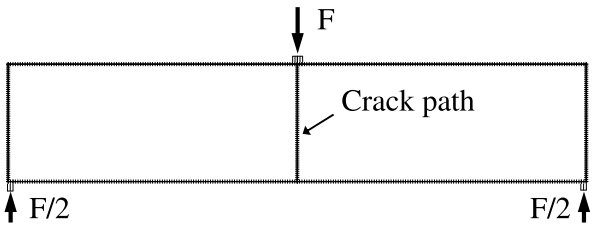

(b)

Figure 7.9: (a) A three-point bending specimen configuration and (b) BEM mesh used and the boundary conditions employed.

the specimen and on one element at each bottom corner, Fig. 7.9(b). The mechanical properties of the concrete-like material are Young's modulus $E = 36.5$GPa and Poisson ratio $\nu = 0.1$. Two different values of fracture toughness $G_{Ic} = 50$ and 10 J/m^2 are considered. The parameter values for the Ortiz-Pandolfi model are maximum cohesive stress, $\sigma_c = 3.19$MPa, and critical opening displacement, δ_c, which has two values: $\delta_c = 5.77\text{x}10^{-6}$m and $\delta_c = 1.15\text{x}10^{-6}$m, for each of the two different values of fracture energy respectively. It is important to mention that in the present study the parameter β is irrelevant, due to the Mode I character of the problem.

For each considered value of fracture toughness, different initial values of crack depth, a, are considered from $a = 0$ (initially uncracked specimen) to $a = 0.06m$, with increments of $0.01m$. For all these cases considered, the load deflection F-δ curves are obtained. These F-δ curves, shown in Fig. 7.10 for $G_{Ic} = 50$J/m^2 are related to different initial crack depths. In a similar way as in [36] initial stiffness and maximum loading capacity of the specimen decrease by increasing the initial crack depth a. Also the

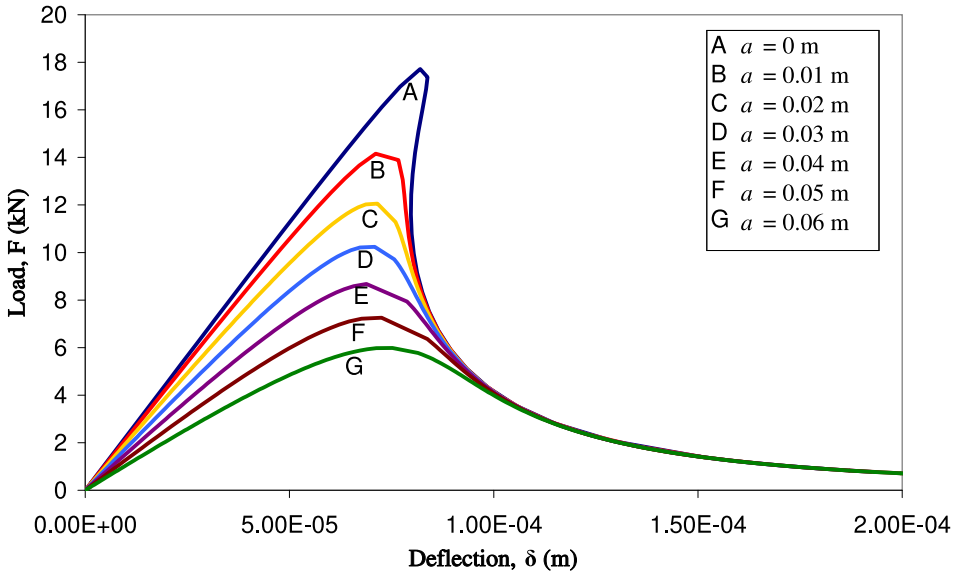

Figure 7.10: Three-point bending test load-deflection plots for different initial crack depths, a, for $G_{Ic} = 50\text{J/m}^2$.

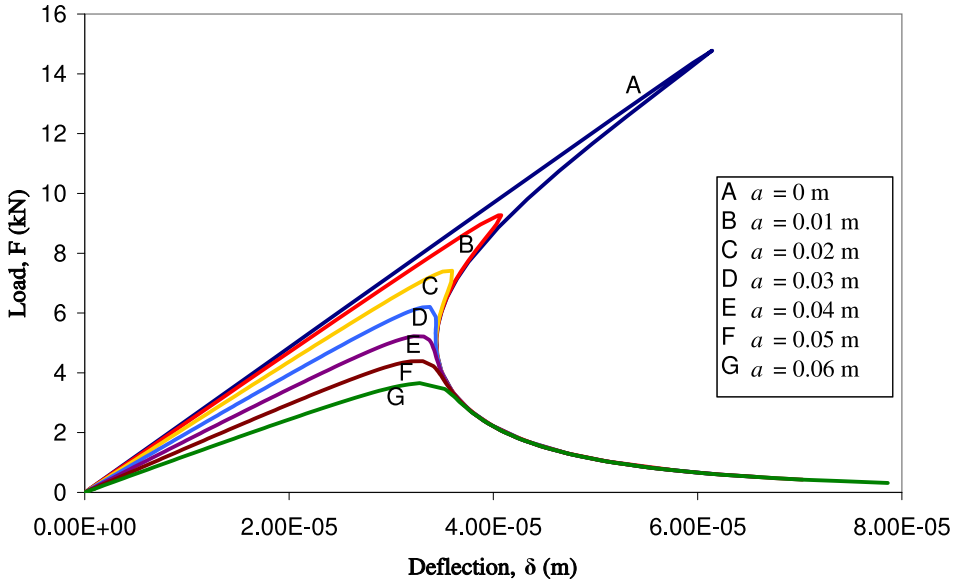

Figure 7.11: Three-point bending test load-deflection plots for several initial crack depths, a, for $G_{Ic} = 10\text{J/m}^2$.

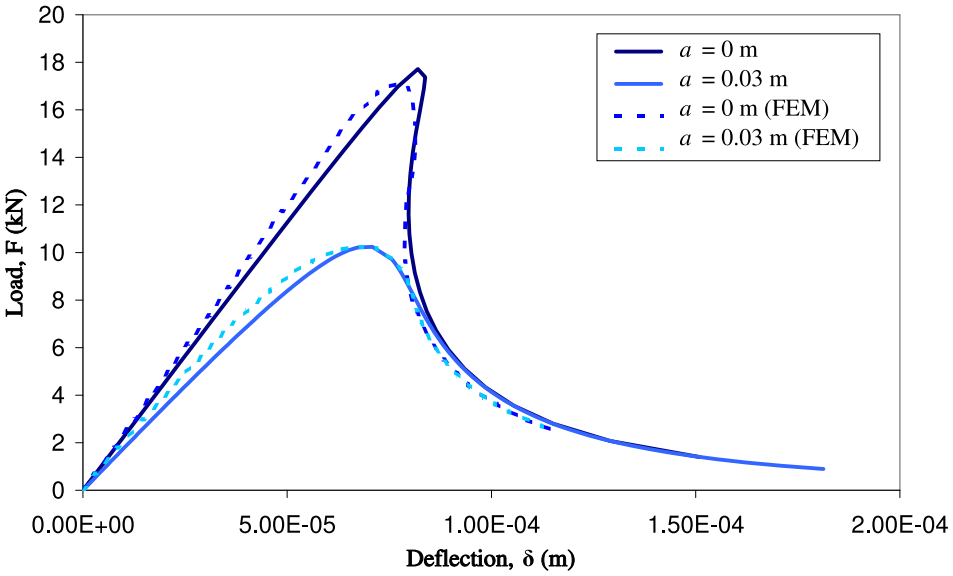

Figure 7.12: Three-point bending test BEM and FEM load-deflection plots for $G_{Ic} = 50\text{J/m}^2$.

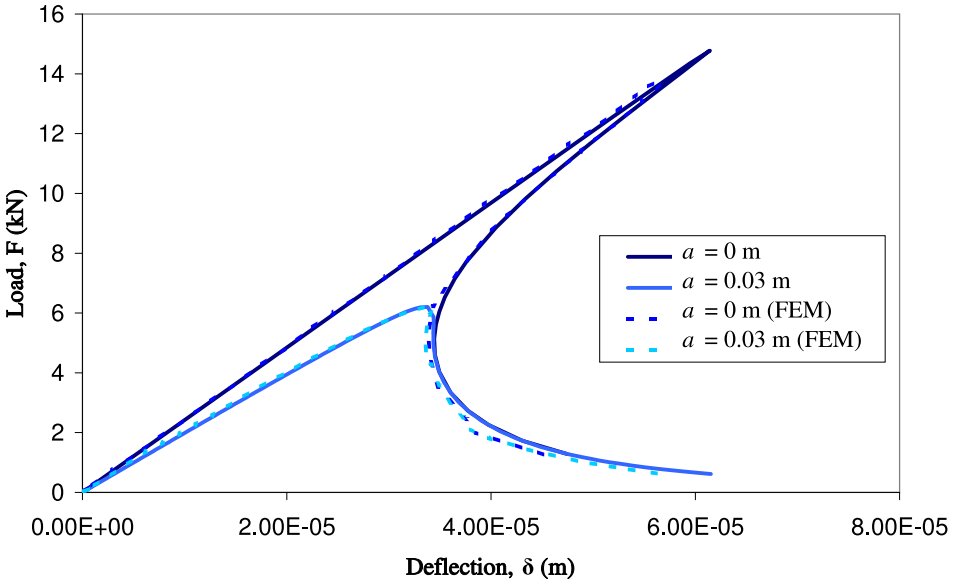

Figure 7.13: Three-point bending test BEM and FEM load-deflection plots for $G_{Ic} = 10\text{J/m}^2$.

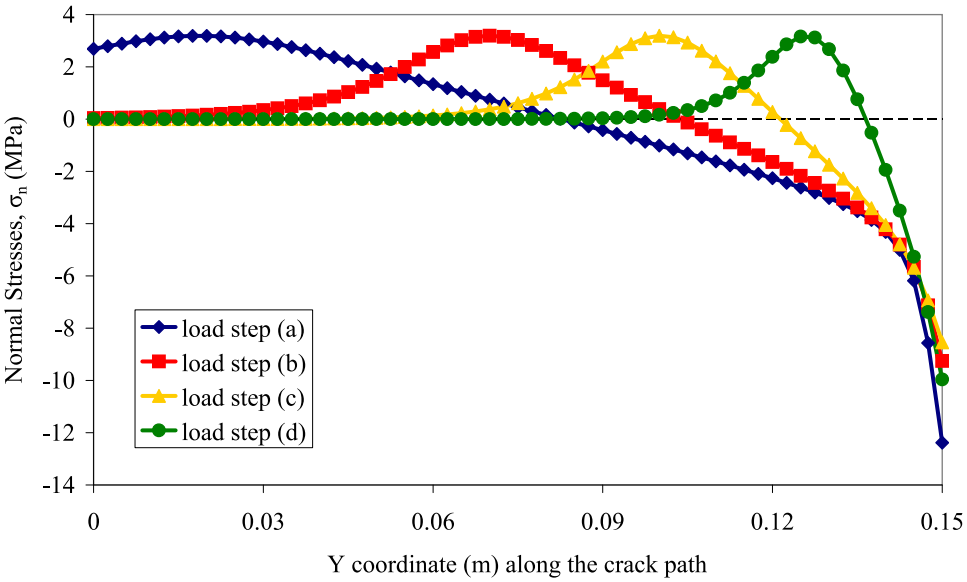

Figure 7.14: Normal stresses along the crack path for different load steps at the softening branch (a) $F = 17718N$ (peak load), (b) $F = 9144N$, (c) $F = 4328N$ and (d) $F = 1395N$ in the three-point bending test.

uncracked specimen reveals considerable instability and a nearly vertical drop in its loading capacity (a small snap-back is observed), whereas the cracked specimens appear much more “ductile". The last part of the softening branch appears as totally independent of the initial crack depth a, since all the plots superpose. The F-δ curves shown in Fig. 7.11 describe the specimen behavior when $G_{Ic} = 10\text{J/m}^2$. For $a \leq 0.02m$ a snap-back instability occurs, that is, a softening branch with positive slope is revealed.

Fig. 7.12 and Fig. 7.13 show a comparison between the present results obtained by the SGBEM code and those obtained in [36] by means of the Finite Element Method (FEM). Taking into account different cohesive laws, exponential herein and bi-linear in [36], and different meshes employed in both approaches, the achieved agreement of the results can be considered as very good.

One of the reasons for the good agreement of the SGBEM and FEM results is the use of the *Method* S [172] in the SGBEM implementation to impose point-supports for the removal of rigid body motions, thus employing identical boundary conditions in both approaches.

In Fig. 7.14 the normal stresses along the crack path for the same configuration and load steps as in Fig. 7.15 are shown. From the stresses along

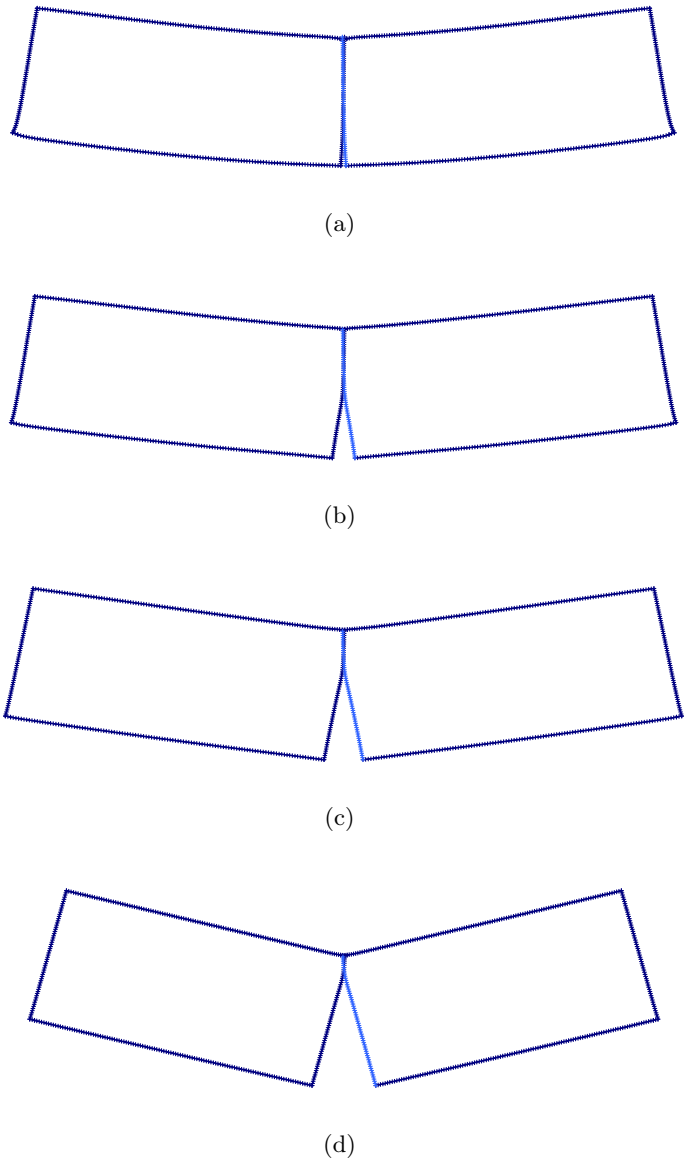

(a)

(b)

(c)

(d)

Figure 7.15: Deformed boundary element mesh (displacement multiplied by a factor of 500) for the initially uncracked specimen with $G_{Ic} = 50\text{J/m}^2$ for different load steps at the softening branch: (a) $F = 17718N$ (peak load), (b) $F = 9144N$, (c) $F = 4328N$ and (d) $F = 1395N$ in the three-point bending test.

the cohesive zone, it can be observed how the softening (process zone) develops at the different load steps. The advancing of the so called mathematical crack tip (where the critical stress is reached) can be observed, although not explicitly. Also, in Fig. 7.14 it can be observed that compressions appear in the part ahead of the crack tip due to an equilibrium of momentums. Thus, the use of the modification of the Ortiz-Pandolfi CZM proposed in Section 3.2 becomes important.

Fig. 7.15 shows the deformed boundary element mesh of the beam at various load steps for the initially uncracked specimen with $G_{Ic} = 50\text{J/m}^2$, the crack growth being clearly observable at those stages. Notice the ticks appearing in the graphic, which represent the nodes of the SGBEM mesh.

7.5 Concluding remarks

In the present chapter a symmetric boundary integral formulation for problems with cohesive cracks placed inside of homogeneous domains and between subdomains has been proposed and implemented. This new 2D SGBEM code is based upon a previous implementation of crack analysis in the LEFM framework [135] and also a cohesive zone formulation from [153, 154]. This approach is likely to be suitable for engineering applications involving isotropic materials, e.g. for an analysis of crack initiation and growth in composites modeled as piecewise homogeneous materials at the micro-scale (glass fibre).

The introduction of the cohesive zone requires an iterative solution procedure to solve the nonlinear equations resulting from the boundary integral formulation; the arc-length method with the normal flow procedure, as described in Section 6.3, has been implemented and used.

As shown by the numerical results, the cohesive zone formulation correctly modeled the experimentally observed crack growth behavior for the wedge split test [52] and agreed very well with a previous FEM crack growth analysis of the load-deflection behavior for the three-point bending test [36]. Although a different cohesive law is used in [36], the SGBEM results are consistent with the results presented therein. The SGBEM analysis was capable of following the instabilities produced by a nearly vertical drop in the loading capacity and also snap-back behaviors seen in some cases (three-point bending test).

To predict the real behavior of structures, the first step would be to determine parameters of the discrete model (σ_c and δ_c in the case of the Ortiz-Pandolfi model for Mode I), where the so-called inverse method could

be very useful [26].

As can be observed by the analysis of the three point bending test, when the initial crack depth a becomes larger the specimen becomes more "ductile", and at the same time it makes the problem more stable. It is also important to mention the influence of G_{Ic}, as shown by the results. When this value is small an unstable behavior is presented, especially for small initial crack depths a.

Chapter 8

Implementation and validation of the Linear Elastic-Brittle Interface Model in a 2D collocational BEM code

The Linear Elastic-Brittle Interface (LEBI) Model has been implemented in a 2D BEM code [71, 72, 131], whose original version allowed isotropic axisymmetric and anisotropic plane problems to be modeled, including multiple solids with perfect interfaces (perfectly bonded) or contact zones between them. The new feature incorporated in this code is the possibility of defining weak interfaces between the elastic solids. It is noteworthy that the BEM is a suitable tool for modeling a crack growing along the weak interface because the non-linearity introduced is associated only to the interface boundary. Another feature of the code is that the equilibrium and compatibility conditions, along contact zones and along perfect or weak interfaces, are imposed in a weak form allowing an easy use of non-conforming discretizations [20, 25, 71, 72]. Coupling BEM and LEBI Model is straightforward because the displacements and tractions at the interfaces are the primarily unknowns in BEM.

8.1 Linear Elastic-Brittle (Weak) Interface implementation in 2D BEM

The introduction of the Linear Elastic-Brittle Interface constitutive law described in Chapter 4, see Figure 4.4, requires a set of linear and non-linear equations to be applied. These equations complement the equations imposed in a weak manner for the interface conditions, see Section 5.4. Thus, if the interface is not broken at a point, the linear equations corresponding to the m-th load step are imposed at the nodes of one side of the undamaged interface, Γ_i^A, in the following form, see (4.9):

$$\triangle_m t_n^A(y) = k_n \triangle_m \delta_n^A(y), \qquad \triangle_m t_t^A(y) = k_t \triangle_m \delta_t^A(y), \tag{8.1}$$

where $t_n^A(y)$ are the normal tractions, $\delta_n^A(y)$ are the relative normal displacements (separations of Γ_i^A with respect to Γ_i^B), $t_t^A(y)$ are the tangential tractions, and $\delta_t^A(y)$ are the relative tangential displacements (sliding of the Γ_i^A with respect to Γ_i^B).

The sequentially linear analysis algorithm, Section 6.2, is used with the Linear Elastic-Brittle Interface formulation, introduced in Chapter 4. Thus, in the first load step all interface elements behave according to (8.1). Then, the interface failure criteria is applied, ψ_G being calculated in every interface point, with its corresponding $\sigma_c(\psi_G)$.

Non-linearity arises when the condition $G \leq G_c$ is violated, as G is directly related to σ in an undamaged interface point, $\sigma \leq \sigma_c(\psi_G)$ can also be used as the condition to be evaluated. Thus, when solving the m-th load step, the values $F_m^*(y)$ of the load factor that leads to the violation of the condition previously described are determined at each interface node y, and subsequently the limit load factor of the current step, $F_m = \min_y F_m^*(y)$, is defined. In the next load step the linear system is defined by replacing in the node that failed, the boundary conditions defined in (8.1) by the conditions:

$$\triangle_{m+1} t_n^A(y) = 0, \qquad \triangle_{m+1} t_t^A(y) = 0. \tag{8.2}$$

which means that in the following step this part of the interface is traction free. Except for the case that both sides of interface enter in contact in this interface point. In such a case two options could be taken into account: (i) allow the overlapping without producing contact stresses, which could be useful for solving problems where the overlapping can be neglected; (ii) the crack faces enter in linear friction-less contact as described in Section 4.2, thus the following conditions are used at the interface point, instead of

(8.2):

$$\triangle_{m+1} t_n^A(y) = k_n \triangle_{m+1} \delta_n^A(y), \qquad \triangle_{m+1} t_t^A(y) = 0. \tag{8.3}$$

Notice that if the overlapping disappears at this interface point the conditions in (8.3) will be changed again to (8.2). This fact allows that once a point is broken, it could enter in contact or become open again as many times as the problem needs it.

8.2 Adhesive layer between orthotropic half spaces

In order to validate the implementation of the linear elastic-brittle interface model, the problem of two half planes joined by a thin layer is solved. In this validation problem no crack growth is considered.

8.2.1 Governing integral equations

To solve the problem of two isotropic half-planes bonded by a thin adherent layer modeled by a weak interface including a crack and subjected to a far field tension, see Fig. 8.1(a), Lenci [102] deduced a governing integral equation for the problem of pressurized cracks, see Fig. 8.1(b), related to the original problem by superposition with a constant stress solution. The integral equation obtained was solved by a specific numerical procedure.

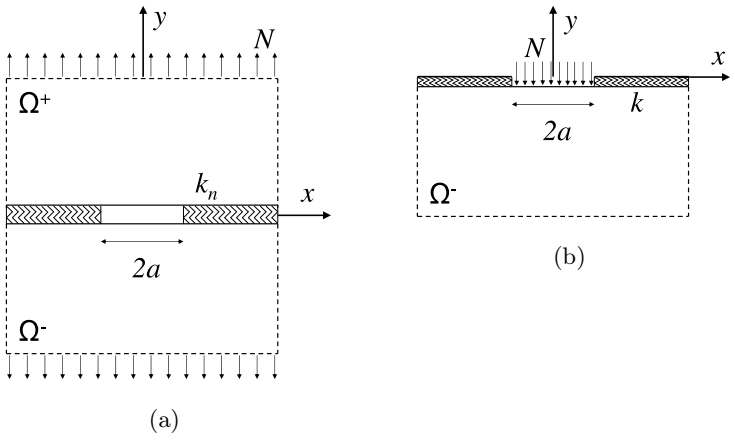

Figure 8.1: (a) Crack at a weak interface under far field tension, (b) simplified problem of a pressurized crack at a weak interface.

In this section Lenci's approach will be generalized to the case of identical orthotropic half-planes bonded by a weak interface including a crack and subjected to far field tension, see Fig. 8.1(a). Orthotropic axes of adherents are considered parallel and perpendicular to the interface.

Let $\sigma_y(x) = \sigma_y(x, y = 0)$ and $v(x) = v(x, y = 0)$ be the normal stress and the vertical displacement of the lower half-plane at the interface, respectively. By superposition with the constant stress solution $\sigma_y = N$ constant tension ($N > 0$), and by symmetry with respect to the x-axis we can limit the present analysis to Ω^- subjected to $\sigma_y(x) = -N$ in $|x| < a$, $\sigma_y(x) = -kv(x)$ in $|x| > a$ and $\tau_{xy}(x, y = 0) = 0$, defining the pressurized crack problem shown in Fig. 8.1(b); $k = 2k_n$ is defined to simplify the notation.

In the case of an isotropic material, by using the Flamant solution as a Green function, the normal stress and the vertical displacement at the upper boundary ($y = 0$) of Ω^- can be related by [102]:

$$v(x) = -\frac{\kappa + 1}{4\mu\pi} \int_{-\infty}^{+\infty} \sigma_y(t) \ln|t - x| dt, \tag{8.4}$$

where μ is the shear stiffness, $\kappa = 3 - 4\nu$ in the case of plane strain and $\kappa = (3 - \nu)/(1 + \nu)$ in the case of generalized plane stress and ν is the Poisson ratio. The function $\sigma_y(x)$ is even and given by

$$\sigma_y = \begin{cases} -N, & 0 < x < a, \\ G(x), & x > a, \end{cases} \tag{8.5}$$

where $G(x)$ is the unknown interface stress. The notation introduced by [102] has been kept herein for an easy comparison of the deduction introduced therein and the present analysis.

In the present case of orthotropic half planes, the strain-stress law for a generalized plane strain state can be expressed in the following way:

$$\begin{pmatrix} \varepsilon_{xx} \\ \varepsilon_{yy} \\ 2\varepsilon_{xy} \end{pmatrix} = \begin{pmatrix} s'_{11} & s'_{12} & 0 \\ s'_{12} & s'_{22} & 0 \\ 0 & 0 & s'_{66} \end{pmatrix} . \begin{pmatrix} \sigma_{xx} \\ \sigma_{yy} \\ \sigma_{xy} \end{pmatrix}, \qquad s'_{IJ} = s_{IJ} - \frac{s_{I3} s_{3J}}{s_{33}}, \tag{8.6}$$

where s'_{IJ} are the reduced elastic compliances. Applying the concept of the Airy stress function and using (8.6), the strain compatibility equation yields

the following characteristic equation of an orthotropic material [101, 165].

$$\ell_4(p) = s'_{11}p^4 + (2s'_{12} + s'_{66})p^2 + s'_{22} = 0, \tag{8.7}$$

whose complex conjugate roots p_α and $\overline{p}_\alpha$ ($\alpha = 1, 2$) can be expressed as [23, 114]:

$$p_\alpha = \frac{\pm s_- + i s_+}{\sqrt{2s'_{11}}}, \qquad s_\pm = \sqrt{\sqrt{s'_{11}s'_{22}} \pm (s'_{12} + 0.5s'_{66})}. \tag{8.8}$$

By particularizing a general expression for displacement solution in an orthotropic half-plane ($y \leq 0$) subjected to a normal point force (P_y) at its boundary, at the origin of cartesian coordinates ($x = y = 0$), deduced in [175], see also [101, 165], the following simple expression of normal displacements along the half-plane boundary ($y = 0$) originated by this force can be obtained:

$$v(x) = -\frac{s_+\sqrt{s'_{22}}P_y}{\pi} \ln|x|. \tag{8.9}$$

Thus, in a similar way as in (8.4), we can define for the case of an orthotropic half-plane bonded by a weak interface, as shown in Fig. 8.1(b), the vertical displacement of the bottom side of the interface as

$$v(x) = -\frac{s_+\sqrt{s'_{22}}}{\pi} \int_{-\infty}^{+\infty} \sigma_y(t) \ln|t - x| dt. \tag{8.10}$$

Then, using (8.5) and (8.10) and introducing dimensionless coordinates $r = t/a$ and $\xi = x/a$ yields:

$$v(\xi) = -\frac{s_+\sqrt{s'_{22}}}{\pi} aN \left\{ 2\ln a \int_1^\infty g(r)dr + \int_1^\infty g(r) \ln|r^2 - \xi^2| dr - 2\ln a + h(\xi) \right\}, \tag{8.11}$$

where

$$h(\xi) = -\ln\left|\xi^2 - 1\right| + \xi \ln\left|\frac{\xi - 1}{\xi + 1}\right| + 2, \tag{8.12}$$

and $g(r) = G(ar)/N = G(t)/N$ is the unknown dimensionless stress along the bonded interface part. In the problem illustrated in Fig. 8.1(b), the vertical displacement $v(x)$ vanishes when $x \to \infty$ and the sum of the forces applied to Ω^- is zero. Consequently, the global equilibrium condition takes

the form:

$$\int_1^\infty g(r)dr = 1. \tag{8.13}$$

Equation (8.11) can be simplified, by substituting (8.13), into the following form:

$$v(\xi) = -\frac{s_+\sqrt{s'_{22}}}{\pi} aN \left\{ \int_1^\infty g(r) \ln|r^2 - \xi^2| dr + h(\xi) \right\}. \tag{8.14}$$

In the bonded part $\xi > 1$, the vertical displacement satisfies the weak interface condition $\sigma_y(\xi) = -kv(\xi)$. This relationship and (8.14) finally give the integral equation which governs the problem:

$$g(\xi) = \delta \left\{ \int_1^\infty g(r) \ln|r^2 - \xi^2| dr + h(\xi) \right\}, \qquad \xi > 1, \tag{8.15}$$

where

$$\delta = \frac{s_+\sqrt{s'_{22}}ka}{\pi} \tag{8.16}$$

is a new dimensionless parameter governing the pressurized crack solution at a weak interface between orthotropic materials. It is a structural parameter because it relates adhesive-layer stiffness to the adherent stiffness, taking into account the crack length (the unique characteristic length of the geometry of the present problem).

Note that the present dimensionless form of the governing integral equation in (8.15) coincides with that obtained by Lenci [102] except for the present definition of δ for orthotropic half-planes bonded by a cracked weak interface parallel to one orthotropic axis of the half-planes. The present definition of δ is in fact a generalization of Lenci's original isotropic definition to this particular orthotropic case. It can be shown that (8.16) when written for isotropic materials reduces to Lenci's expression $\delta = ka(\kappa + 1)/(4\pi\mu)$.

8.2.2 Numerical solution

The numerical solution of the problem defined in the previous section, Fig. 8.1(a) is obtained here by using a collocational BEM code [72, 131], solving the Somigliana displacements identity for orthotropic materials. This code uses linear continuous elements [131] for elastic plane problems.

To solve the problem of pressurized cracks in a weak interface between two orthotropic half-planes, the problem symmetry with respect to the y-axis has been used. Each half-plane has been modeled by a square domain much larger than the crack size, trying to simulate a finite crack between infinite half-planes. The mesh used for each square domain has 518 elements. The height and width of each square domain is 100 times the size of the crack half-length a (taken as 1mm herein), see Fig. 8.1(a).

According to Subsection 8.2.1, using an appropriate material paremeter, the dimensionless form of the solutions of a pressurized crack at a weak interface between orthotropic and isotropic half planes are coincident if the crack is parallel to one of the orthotropic axes. The orthotropic material properties used in BEM calculations are those of an 8552/AS4 carbon fibre-epoxy composite, with the following orthotropic properties: E_x=135GPa, E_y=10GPa, E_z=10GPa, G_{xy}=5GPa, G_{xz}=5GPa, ν_{xy}=0.3, ν_{yz}=0.4 and ν_{xz}=0.3. Nevertheless, as the numerical results obtained are presented in dimensionless form, they are valid for any orthotropic material. Then, in order to obtain the different values of the dimensionless parameter δ shown, the value k was varied from 109.8 x 10^9 Pa/m to 109.8 x 10^{13} Pa/m.

As shown in the following, the numerical results for orthotropic materials obtained by the BEM code (when changed to dimensionless form and using the new characteristic parameter δ, defined in (8.16)) are in excellent agreement with those obtained for isotropic materials in [102] by a different numerical procedure.

The function $g(\xi)$ is reported in Fig. 8.2(a) for different values of δ. For relatively "soft" interfaces (i.e., low values of δ) $g(\xi)$ achieves very small and almost constant values, while in the opposite case of "stiff" interfaces the stresses are increasing significatively in the neighborhood of the crack tip. To better visualize the shape of the solution, the normalized function $g(\xi)/g(1)$ is shown in Fig. 8.2(b), which illustrates for example how slowly the solution spreads over the whole interface when δ tends to zero.

An important feature of the solution shown in [102] is its behavior near the crack tip, where interface tractions are bounded at the tip of a crack situated along a weak interface, in contrast with the singular (unbounded) tractions at the tip of an interface crack situated along a perfect interface, where no relative displacements of bonded surfaces are allowed. Thus, during crack growth along a weak interface, tractions are kept bounded. It appears that local normal tractions in the zone close to the interface crack tip follow the asymptotic law [102]:

$$\sigma \cong \sigma_0 + \sigma_1(\xi - 1)\left[\ln(\xi - 1) - 1\right], \quad \text{for} \quad \xi \to 1_+. \tag{8.17}$$

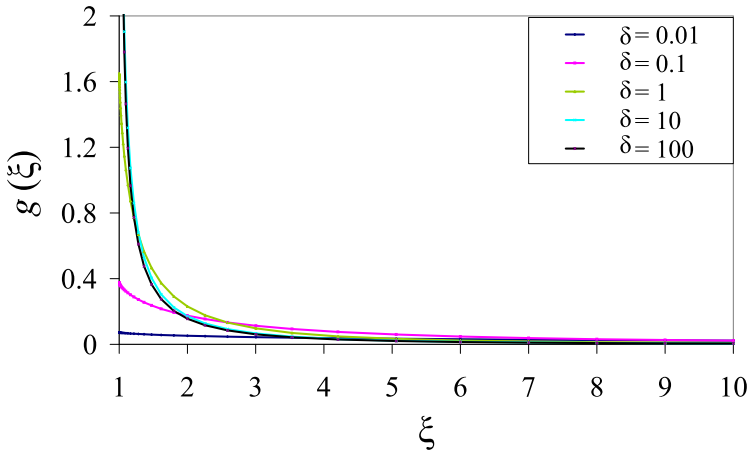

(a)

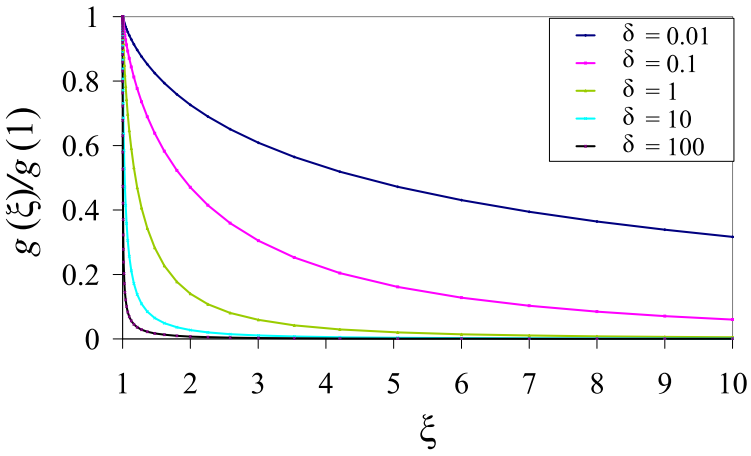

(b)

Figure 8.2: Pressurized crack at a weak interface between identical orthotropic half-planes. BEM solution for various values of the parameter δ: (a) function $g(\xi)$, (b) normalized solution $g(\xi)/g(1)$.

The vertical displacement $v(\xi)$ at the bottom side of the interface is depicted in Fig. 8.3. It has a minimum in the midpoint of the crack and it monotonically tends to zero when $\xi \to \infty$. For "soft" interfaces the displacement is large (tending to infinity as $\delta \to 0$), while for "stiff" interfaces it rapidly converges to the Griffith crack displacements. From observations

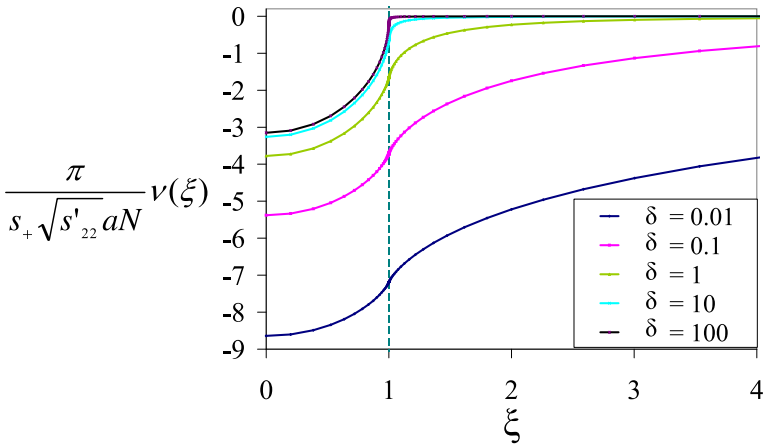

Figure 8.3: Pressurized crack at a weak interface between identical orthotropic half-planes. BEM solution for various values of the parameter δ of the normalized vertical displacement $v(\xi)$.

it can be concluded that for $\delta > 100$ the weak interface can be considered as a perfect bonding for practical purposes. An excellent agreement of the present results for particular orthotropic materials in their dimensionless form with those presented by [102] for isotropic materials has been obtained. Recall that Lenci [102] solved (8.15) for isotropic materials by a special numerical procedure, whereas in the present work the Somigliana displacement identities for the upper and bottom orthotropic adherents have been solved by the collocational BEM.

8.3 Concluding remarks

In the present chapter, some implementation details and validation of the Linear Elastic-Brittle Interface Model are presented.

The presence of a crack at a linear elastic-brittle interface, which represents a simple model of a thin adhesive layer, has been analyzed in the present chapter in detail. First the governing integral equation for a pressurized crack at the weak interface between identical orthotropic half planes has been deduced. A new dimensionless characteristic structural parameter δ was introduced in this governing integral equation . It relates adhesive-layer stiffness to the adherent stiffness, taking into account crack length. Then, the problem of a pressurized crack has been solved by the collocational BEM. An excellent agreement has been obtained between the numerical results by the present BEM code and those shown in [102].

An important novelty in the present thesis is that not only numerical solution of stresses and displacements for a crack at a weak interface can be computed, but also the crack growth along the weak interface can be modeled using a mixed mode fracture criterion for an adhesive thin layer modeled by linear elastic-brittle traction-displacement law. This capability will be tested to analyze different damage mechanisms in composite applications presented from Chapter 10 to 13.

It has been proved that with the use of adequate properties (a large value of the dimensionless parameter δ) the solution is analogous to the one obtained by LEFM, with the advantage that crack onset and propagation can be modeled in an easy manner, as will be shown in Chapters 10-13.

Chapter 9

Formulation, implementation and validation of new expressions of the integral kernels for transversely isotropic elastic materials in 3D BEM

Implementing a cohesive zone-like model in 3D BEM code will be part of a future development based on the present thesis. The objective of this work is to develop and efficient and accurate numerical tool for analysis of different mechanisms of damage in composite laminates taking into account 3D effects. Nevertheless, in order to study problems in composite materials by 3D BEM an efficient fundamental solution for transversely isotropic elastic materials in 3D is necessary. Thus, explicit closed-form real-variable expressions of a fundamental solution and its derivatives for three-dimensional problems in transversely linear elastic isotropic solids are developed first in the present chapter. The expressions of the fundamental solution in displacements U_{ik} and its derivatives, originated by a unit point force, should be valid for any combination of material properties and for any orientation of the radius vector between the source and field points. A compact expression of this kind for U_{ik} was introduced by Ting and Lee [167] in terms of the Stroh eigenvalues on the oblique plane normal to the

radius vector. Then, working from this expression of U_{ik}, and after a revision of the Ting and Lee [167] final formula, a new approach (based on the application of the rotational symmetry of the material) for deducing the first and second order derivative kernels, $U_{ik,j}$ and $U_{ik,j\ell}$ respectively, is developed in the present chapter. The new expressions of the fundamental solution and its derivatives do not suffer from the difficulties of some previous expressions, obtained by other authors in different ways, with complex valued functions appearing for some combinations of material parameters and/or with division by zero for the radius vector at the rotational symmetry axis. The expressions of U_{ik}, $U_{ik,j}$ and $U_{ik,j\ell}$ are presented herein in a form suitable for an efficient computational implementation in BEM codes.

9.1 BIE kernels

9.1.1 Introduction

An accurate and efficient evaluation of the integral kernels, typically represented by a *fundamental solution* (*free-space Green's function*) and its derivatives, is a key issue in the numerical solution of Boundary Integral equations (BIEs) by the Boundary Element Method (BEM) [5, 131, 10], the Method of Fundamental Solutions (MFS) [62] and other approaches.

Consider a homogeneous linearly elastic anisotropic material characterized by the fourth rank tensor of elastic stiffnesses $C_{ijk\ell}$ $(i,j,k,\ell = 1,2,3)$, verifying the symmetry relations $C_{ijk\ell} = C_{jik\ell} = C_{k\ell ij}$. Then, the constitutive law writes as

$$\sigma_{ij}(\boldsymbol{x}) = C_{ijk\ell}\varepsilon_{k\ell}(\boldsymbol{x}) = C_{ijk\ell}u_{k,\ell}(\boldsymbol{x}), \tag{9.1}$$

where σ_{ij}, $\varepsilon_{k\ell}$ and u_k, respectively, are the tensors of stresses and strains and the vector of displacements at a point $\boldsymbol{x} = (x_1, x_2, x_3)$. It is assumed that $C_{ijk\ell}$ is a positive definite tensor, *i.e.* $C_{ijk\ell}\varepsilon_{ij}\varepsilon_{k\ell} > 0$ for any nonzero strain tensor.

Let $\boldsymbol{U}(\boldsymbol{x})$ denote a fundamental solution for the above material given by a 3×3 matrix whose columns represent displacement vectors (at a point $\boldsymbol{x} \neq \boldsymbol{0}$) originated in the infinite anisotropic elastic medium ($\mathbb{R}^3$) by an application of the unit point forces at the origin of coordinates and oriented in the direction of coordinate axes. Thus, $U_{ik}(\boldsymbol{x})$ is the displacement originated at point $\boldsymbol{x}$ in direction i when a unit point force is applied at the origin of coordinates in direction k.

As the closed-form expressions $\boldsymbol{U}(\boldsymbol{x})$ do not exist for all classes of these

materials, and an efficient numerical procedure for evaluation of $\boldsymbol{U}(\boldsymbol{x})$, and even more of its derivatives, is not immediate, BEM is still not so popular for these materials as it is for isotropic materials and, thus, any progress in extending the scope of BEM applicability to these materials would be welcome.

For a better understanding of the context of the present work, the main contributions to the development of expressions of different kinds for $\boldsymbol{U}(\boldsymbol{x})$ suitable for implementation in 3D BEM codes will be briefly reviewed.

Fundamental solution for general anisotropic materials in 3D

With reference to general anisotropic elastic materials, working from the Fredholm expression of $\boldsymbol{U}(\boldsymbol{x})$ [65] obtained by the 3D Fourier transform, the next contributions were aimed at obtaining an expression of $\boldsymbol{U}(\boldsymbol{x})$ as explicit and simple as possible. Lifshitz and Rozentsveig [103] applied the Cauchy residue calculus to a 1D integral obtained from the 3D Fourier integral giving an explicit expression of $\boldsymbol{U}(\boldsymbol{x})$ in terms of the complex poles, roots of a sixth order algebraic equation (called the Stroh eigenvalues at present), degenerate cases with multiple poles being excluded from their calculation.

The application of the Stroh formalism to anisotropic elasticity (see Ting [165]) to evaluate $\boldsymbol{U}(\boldsymbol{x})$ and its derivatives in 3D has been shown to be a fruitful approach, leading to several substantial contributions in the 1970s, *e.g.* by Malén [110], expressing $\boldsymbol{U}(\boldsymbol{x})$ in terms of the normalized Stroh eigenvectors provided that all eigenvalues are distinct, and also more recently, without assuming the distinctness of the eigenvalues, by Nakamura and Tanuma [123] (expressing $\boldsymbol{U}(\boldsymbol{x})$ in terms of the Stroh eigenvalues and eigenvectors) and Ting and Lee [167] and Lee [98] (expressing $\boldsymbol{U}(\boldsymbol{x})$ in terms of the Stroh eigenvalues only). Also Wu's [181] generalization of the Stroh formalism to 3D elasticity has been shown to be fruitful in generating Green's functions of different kinds in a uniform way, its full potential still to be fully explored.

Recently, Lee [98] deduced new general analytic expressions of the first and second order derivatives of $\boldsymbol{U}(\boldsymbol{x})$ in terms of the Stroh eigenvalues only, which further develop expressions originally derived by Barnett [13].

Note, at this point, that the problem of finding a closed-form analytic expression of $\boldsymbol{U}(\boldsymbol{x})$ in terms of elastic stiffnesses for a general anisotropic elastic material appears to be equivalent to finding closed-form expressions for the roots of the above mentioned sextic equation. According to the work of Head [81], no general solution in radicals of this sextic equation is

possible, and therefore it seems that a fully closed-form expression of $\boldsymbol{U}(\boldsymbol{x})$ for general anisotropy will never be available.

BEM applications to anisotropic elastic materials started with the work of Wilson and Cruse [179], who implemented the expressions of $\boldsymbol{U}(\boldsymbol{x})$ and its first and second order derivatives in terms of a 1D integral over the unit circle [65, 103] and achieved an efficient numerical procedure by tabulating the values of $\boldsymbol{U}(\boldsymbol{x})$ and its derivatives (with respect to spherical angles) and finally by interpolating these values in BEM calculations. Although, apparently, for a long time this was the only satisfactory and widely used numerical procedure, *e.g.* Schclar [155], it requires large computer storage for tabulated values and it may not provide sufficient accuracy in materials with a high degree of anisotropy.

A new numerical procedure for a direct evaluation of $\boldsymbol{U}(\boldsymbol{x})$ and its derivatives, which is more accurate and more efficient (in terms of both computer storage and time), was developed by Gray and his co-workers [136, 137, 151] from expressions obtained by residue calculations [51], covering also the degenerate cases with multiple poles. Another 3D BEM implementation based on Wang's [173] residue calculations was developed by Tonon *et. al.* [168].

Finally, let us mention that, to the best of the authors' knowledge, the explicit expressions of $\boldsymbol{U}(\boldsymbol{x})$ for general anisotropic materials obtained using the concepts of the Stroh formalism in [98, 123, 167] have not yet been implemented and validated in the BEM context.

Fundamental solution for transversely isotropic materials in 3D

With reference now to transversely isotropic elastic materials, the above mentioned sextic equation can be solved in radicals [14, 163], and consequently the closed-form expressions of $\boldsymbol{U}(\boldsymbol{x})$ and its derivatives are possible. This feature represents a fundamental difference with respect to the above discussed general anisotropy case and will be further exploited in the present work.

Whereas numerical approaches, such as modulation function interpolation [155, 179] or numerical solution of the sextic equation for different relative orientations of the source and field points [136, 137, 151], are the unique option for generally anisotropic materials where closed-form expressions are not available, it is expected that using a closed-form expression of $\boldsymbol{U}(\boldsymbol{x})$ for transversely isotropic materials will result in significant computing time savings and a higher accuracy.

Let, without loss of generality, the x_3-axis be the rotational-symmetry axis, the x_1x_2-plane thus being the isotropy plane. Applying Voigt reduced

notation [165], the elastic stiffnesses are represented by a symmetric and positive definite matrix C_{IJ} $(I, J = 1, \ldots, 6)$. A transversely isotropic material is characterized by the following five elastic constants:

$$C_{1111} = C_{11},\ C_{3333} = C_{33},\ C_{1122} = C_{12},\ C_{1133} = C_{13},\ C_{2323} = C_{44} \quad (9.2)$$

It holds that $C_{1212} = C_{66} = (C_{11} - C_{12})/2$. Let $\triangle$ be defined as

$$\triangle = \sqrt{C_{11}C_{33}} - C_{13} - 2C_{44}. \quad (9.3)$$

The values of $\triangle$ form three different groups of transversely isotropic materials, obtained by different combinations of material properties. It should be mentioned that previous fundamental solution and its modifications [104, 129] are only available when $\triangle >$ and $\triangle = 0$, and different expressions are necessary for each case.

Consider a point $\boldsymbol{x} \neq \boldsymbol{0}$ and a pair of orthogonal unit vectors $\boldsymbol{n}(\boldsymbol{x})$ and $\boldsymbol{m}(\boldsymbol{x})$, $\boldsymbol{n} \perp \boldsymbol{m}$, situated on the plane perpendicular to (the position vector) $\boldsymbol{x}$ so that $(\boldsymbol{n}, \boldsymbol{m}, \boldsymbol{x}/r)$, $r = |\boldsymbol{x}|$, form a right-handed triad. Let ϕ, $0 \leq \phi \leq \pi$, be the angle between the x_3-axis and vector $\boldsymbol{x}$, shown in Fig. 9.1.

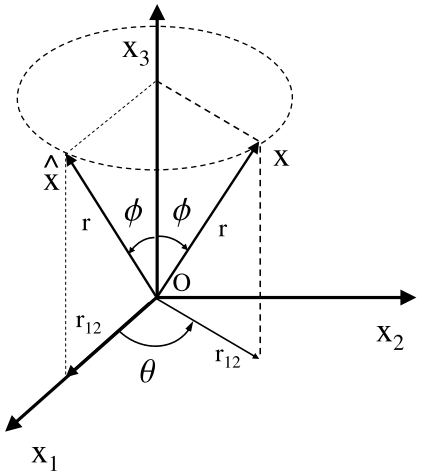

Figure 9.1: Points $\boldsymbol{x}$ and $\widehat{\boldsymbol{x}}$ in spherical coordinates associated to a transversely isotropic material.

Several closed-form expressions of $\boldsymbol{U}(\boldsymbol{x})$ for a transversely isotropic material presented in the past have been obtained in different ways. Whereas Lifshitz and Rozenzweig [103], Kröner [94], Willis [178], Lejček [100] and Hu

et al. [84] directly evaluated expressions obtained from the general formula of Fredholm [65]; Elliot [57], Chen [43], Pan and Chou [129], Fabrikant [60], Hanson [77] and Loloi [104] applied the potential function approach; and Nakamura and Tanuma [123], Ting and Lee [167] and Lee [98] combined the Fredholm's approach and Stroh formalism.

It will be instructive to relate, in what follows, the degeneracy cases (depending on the material properties and the direction of $\boldsymbol{x}$) observed in the expressions of $\boldsymbol{U}(\boldsymbol{x})$ for transversely isotropic materials obtained by the potential function approach with the classification of the fundamental elasticity matrix $\mathbf{N}(\mathbf{n}, \mathbf{m})$, in the framework of the Stroh formalism [165, 166].

The fundamental elasticity matrix $\mathbf{N}(\mathbf{n}, \mathbf{m})$ in the Stroh formalism is non-semisimple (having a double or a triple eigenvalue, and only two independent eigenvectors) if $\triangle = 0$ [14, 163]. It is not difficult to show that $\triangle = 0$ is equivalent to zero discriminant of the characteristic quadratic equation of the potential theory.

The cases of $\phi = 0$ or π also lead to a non-semisimple matrix $\mathbf{N}(\mathbf{n}, \mathbf{m})$ [14, 163]. In these cases the potential function approach may lead to division by zero in the expressions of $\boldsymbol{U}(\boldsymbol{x})$ and some specific arrangements have to be applied [77, 104, 129].

In the remaining cases, $\mathbf{N}(\mathbf{n}, \mathbf{m})$ is semi-simple (having a double eigenvalue for a specific combination of elastic stiffnesses with C_{44}/C_{66}, giving a solution of the characteristic quadratic equation of the potential theory) or simple (having three different eigenvalues), and has three independent eigenvectors in any case. In these cases, $\triangle > 0$ and $\triangle < 0$ respectively lead to real and complex solutions of the characteristic quadratic equation of the potential theory, which correspondingly produces real- and complex-variable expressions of $\boldsymbol{U}(\boldsymbol{x})$.

Note that the complex-variable expressions of $\boldsymbol{U}(\boldsymbol{x})$ obtained by using the potential theory in the case $\triangle < 0$ include complex functions, which are cumbersome for implementing in a BEM code and require very careful programming to keep their values in the same branch when multivaluedness arises [129]. Therefore, it is not a surprise that BEM results obtained by using these complex-variable expressions of $\boldsymbol{U}(\boldsymbol{x})$ for materials with $\triangle < 0$ have not been published so far.

From the above mentioned closed-form expressions of $\boldsymbol{U}(\boldsymbol{x})$, the expression deduced by Pan and Chou [129] is usually used in BEM codes, see Sáez *et al.* [150] and Loloi [104] for its BEM implementations and Ariza and Domínguez [8] for an expression of the hypersingular kernel in the trac-

tion BIE obtained from the second order derivatives of $\boldsymbol{U}(\boldsymbol{x})$.

As discussed above, this solution [129] has several features which make somewhat cumbersome its implementation covering all possible cases: *i)* expressions depending on the values of $\triangle$ (positive, negative or zero) and in particular its complex-variable character for $\triangle < 0$; *ii)* a loss of precision and/or a division by zero for $\phi = \pi$. Although the difficulty with the degeneracy problem at $\phi = \pi$ has been solved by Loloi [104] by means of an *ad hoc* approach (using the sign(x_3) function), the mentioned features may still cause some difficulties in using this expression in further analytic deductions and in BEM development.

The aim of the present chapter is to obtain, and numerically test, completely general and closed-form real-variable expressions of $U_{ik}(\boldsymbol{x})$, its derivatives $U_{ik,j}(\boldsymbol{x})$ and $U_{ik,jl}(\boldsymbol{x})$ and the corresponding stress Σ_{ijk} and traction $T_{ik}(\boldsymbol{x})$ solutions, as well as the hypersingular kernels Σ^{loop}_{ijkl} and S_{ijk} valid for any transversely isotropic material.

9.1.2 Displacement fundamental solution for anisotropic materials

According to Malén [110] and Lothe [105], $\boldsymbol{U}(\boldsymbol{x})$ can be expressed in terms of the Barnett-Lothe tensor $\boldsymbol{H}(\boldsymbol{x})$ as:

$$\boldsymbol{U}(\boldsymbol{x}) = \frac{1}{4\pi r}\boldsymbol{H}(\boldsymbol{x}). \tag{9.4}$$

Thus, in the context of BIEs, $\boldsymbol{H}(\boldsymbol{x})$ represents the *characteristic* (or *modulation*) function of the displacement fundamental solution $\boldsymbol{U}(\boldsymbol{x})$. It is well known that $\boldsymbol{H}(\boldsymbol{x})$ can be evaluated in several ways [165, 123, 167], one option being given by the integral:

$$\boldsymbol{H}(\boldsymbol{x}) = \frac{1}{\pi}\int_{-\infty}^{+\infty} \boldsymbol{\Gamma}^{-1}(p)\mathrm{d}p, \tag{9.5}$$

with the matrix

$$\boldsymbol{\Gamma}(p) = \boldsymbol{Q} + p(\boldsymbol{R} + \boldsymbol{R}^T) + p^2\boldsymbol{T} \tag{9.6}$$

expressed in terms of a the integration variable p and the matrices $\boldsymbol{Q}$, $\boldsymbol{R}$ and $\boldsymbol{T}$, defined for an $\boldsymbol{x} \neq \boldsymbol{0}$ as:

$$Q_{ij} = C_{ijk\ell}n_j n_\ell, \quad R_{ik} = C_{ijk\ell}n_j m_\ell, \quad T_{ik} = C_{ijk\ell}m_j m_\ell, \tag{9.7}$$

where superscript T denotes the matrix transpose. Note that the matrices $\boldsymbol{Q}$ and $\boldsymbol{T}$ are symmetric and positive definite matrices.

It can be shown that $\boldsymbol{H}(\boldsymbol{x})$ is independent of the choice of $\boldsymbol{n}$ and $\boldsymbol{m}$ on the plane perpendicular to $\boldsymbol{x}$ [165]. As follows from the above relations, $\boldsymbol{H}(\boldsymbol{x})$ is a symmetric and positive definite matrix depending only on the direction of $\boldsymbol{x}$ but not on its magnitude, *i.e.* $\boldsymbol{H}(\boldsymbol{x}) = \boldsymbol{H}(\frac{\boldsymbol{x}}{r})$, and fulfilling $\boldsymbol{H}(-\boldsymbol{x}) = \boldsymbol{H}(\boldsymbol{x})$. Hence, $\boldsymbol{U}(\boldsymbol{x})$ is also a symmetric positive definite matrix and $\boldsymbol{U}(-\boldsymbol{x}) = \boldsymbol{U}(\boldsymbol{x})$.

Lifshitz and Rozentsveig [103] obtained, by applying the Cauchy residue theory, an expression of the integral in (9.5) which can be arranged in the following form:

$$\boldsymbol{H}(\mathbf{x}) = 2i \sum_{v=1}^{3} \frac{\hat{\boldsymbol{\Gamma}}(p_v)}{|\boldsymbol{\Gamma}(p_v)|'}, \tag{9.8}$$

where i is the imaginary unit, $|\boldsymbol{\Gamma}(p)|$ is the determinant of $\boldsymbol{\Gamma}(p)$, $|\boldsymbol{\Gamma}(p)|' = d|\boldsymbol{\Gamma}(p)|/dp$, $\hat{\boldsymbol{\Gamma}}(p_v)$ is the adjoint matrix of $\boldsymbol{\Gamma}(p_v)$ defined by the relation $\boldsymbol{\Gamma}(p_v)\hat{\boldsymbol{\Gamma}}(p_v) = |\boldsymbol{\Gamma}(p_v)|I$, where I is the identity matrix, and $p_v = \alpha_v + i\beta_v$ ($v = 1, 2, 3$) are the three complex roots with the positive definite imaginary part ($\beta_v > 0$) of the sextic algebraic equation (sometimes called Stroh eigenvalues):

$$|\boldsymbol{\Gamma}(p)| = 0. \tag{9.9}$$

It should be noted that the expression of $\boldsymbol{H}(\mathbf{x})$ in (9.8) is not valid for mathematically degenerate cases with repeated roots p_v, *e.g.* $p_1 = p_2$ or $p_1 = p_2 = p_3$.

Ting and Lee [167], starting from (9.8) and writing $\hat{\boldsymbol{\Gamma}}(p)$ as a polynomial of fourth degree in p

$$\hat{\boldsymbol{\Gamma}}(p) = \sum_{n=0}^{4} p^n \hat{\boldsymbol{\Gamma}}^{(n)}, \tag{9.10}$$

achieved a new general expression of $\boldsymbol{H}(\mathbf{x})$ valid for any kind of linearly elastic material:

$$\boldsymbol{H}(\mathbf{x}) = \frac{1}{|\boldsymbol{T}|} \sum_{n=0}^{4} q_n \hat{\boldsymbol{\Gamma}}^{(n)}, \tag{9.11}$$

where the real coefficients q_n are expressed through fractions defined in terms of p_v, with no division by zero in the degenerate cases as happens with the expression of $\boldsymbol{H}(\boldsymbol{x})$ in (9.8).

A simplified expression of $\boldsymbol{H}(\boldsymbol{x})$ can be achieved for configurations, materials and some specific positions of $\boldsymbol{x}$ with respect to a material, for

which (9.9) is a cubic equation with real coefficients in p^2. In this case the determinant $|\boldsymbol{\Gamma}(p)|$ is expressed using (9.6) as

$$|\boldsymbol{\Gamma}(p)| = |\boldsymbol{T}|(p^2 - p_1^2)(p^2 - p_2^2)(p^2 - p_3^2), \tag{9.12}$$

which leads to the following form of the sextic equation (9.9):

$$[p^4 + (g^2 - 2h)p^2 + h^2][p^2 + \beta_3^2] = 0, \tag{9.13}$$

g, h and β_3 being real and positive. The two roots p_1 and p_2 are pure imaginary or complex numbers, whereas the root p_3 is always a pure imaginary number.

Then, applying (9.10) and (9.12) in (9.8) a simple expression in the form of (9.11) is obtained:

$$\boldsymbol{H}(\boldsymbol{x}) = \frac{1}{|T|\xi}\{\frac{\zeta}{h\beta_3}\hat{\boldsymbol{\Gamma}}^{(0)} + \hat{\boldsymbol{\Gamma}}^{(2)} + \delta\hat{\boldsymbol{\Gamma}}^{(4)}\}, \tag{9.14}$$

where the real and positive numbers ζ, δ and ξ defined as:

$$\zeta = -i(p_1 + p_2 + p_3) = g + \beta_3, \tag{9.15a}$$
$$\delta = -(p_1p_2 + p_2p_3 + p_3p_1) = h + g\beta_3, \tag{9.15b}$$
$$\xi = i(p_1 + p_2)(p_2 + p_3)(p_1 + p_3) = g(h + g\beta_3 + \beta_3^2), \tag{9.15c}$$

depend only on p_1+p_2, p_1p_2 and p_3. Thus, it is not necessary to evaluate individually all the roots of the sextic equation, and the final expression (9.14) is valid for both non-degenerate and degenerate cases. Explicit expressions for β_3, h and g can be determined from (9.9) and (9.13) determining first the pure imaginary root $p_3 = i\beta_3$ by an explicit formula for roots of cubic algebraic equations [167].

Finally, the following key results by Ting and Lee [167] (Section 4 therein) will be useful in the evaluation of $\boldsymbol{H}(\boldsymbol{x})$ presented in the next section. If $\boldsymbol{x}$ is situated on a plane of elastic symmetry then, without loss of generality, one can assume that this plane coincides with a coordinate plane (applying a suitable rotation of the coordinate system if necessary), which implies the reduction of (9.9) to (9.13) and the vanishing of some components of $\boldsymbol{H}(\boldsymbol{x})$ (*e.g.*, $H_{12}(\boldsymbol{x}) = 0$ and $H_{23}(\boldsymbol{x}) = 0$ if the plane $x_2 = 0$ is a plane of elastic symmetry).

9.1.3 Displacement fundamental solution for transversely isotropic materials

Consider a transversely isotropic material as specified in (9.2). Any plane that contains the x_3-axis is a plane of elastic symmetry and, according to [167], form (9.13) of the sextic equation and the completely explicit expression of $\boldsymbol{H}(\boldsymbol{x})$ from (9.14) could be applied for any point $\boldsymbol{x}$.

The following procedure leads to a relatively simple and general expression of $\boldsymbol{H}(\boldsymbol{x})$. Let us define a vector

$$\widehat{\boldsymbol{x}} = (r_{12}, 0, x_3), \qquad \text{where} \qquad r_{12} = \sqrt{x_1^2 + x_2^2}. \tag{9.16}$$

Let $c = \cos\phi = x_3/r$ and $s = \sin\phi = r_{12}/r$, the angle $0 \leq \phi \leq \pi$ being shown in Fig. 9.1. Then, defining $\boldsymbol{n} = (c, 0, -s)$ and $\boldsymbol{m} = (0, 1, 0)$, $[\boldsymbol{n}, \boldsymbol{m}, \widehat{\boldsymbol{x}}/r]$ forms a right-handed triad. Explicit expressions for the non-zero terms of

$$\boldsymbol{H}(\widehat{\boldsymbol{x}}) = \begin{pmatrix} H_{11} & 0 & H_{13} \\ 0 & H_{22} & 0 \\ H_{13} & 0 & H_{33} \end{pmatrix}, \tag{9.17}$$

can be obtained using (9.14)

$$\begin{aligned} H_{11} &= \frac{1}{C_{66}\beta_3} + \frac{C_{44}c^2 + C_{33}s^2}{C_{11}C_{44}gh} - \frac{f}{\xi}, \\ H_{22} &= \frac{1}{C_{11}g} + \frac{f}{\xi}, \\ H_{33} &= \frac{1}{gh}\left\{\frac{h + c^2}{C_{44}} + \frac{s^2}{C_{11}}\right\}, \\ H_{13} &= \tilde{H}_{13}s, \end{aligned} \tag{9.18}$$

where

$$
\begin{aligned}
\tilde{H}_{13} &= \frac{(C_{13}+C_{44})c}{C_{11}C_{44}gh},\\
\beta_3 &= \left\{\frac{C_{66}c^2+C_{44}s^2}{C_{66}}\right\}^{1/2},\\
h &= \left\{c^4+\frac{\eta s^2c^2}{C_{11}C_{44}}+\frac{C_{33}s^4}{C_{11}}\right\}^{1/2},\\
\eta &= C_{11}C_{33}-C_{13}^2-2C_{13}C_{44},\\
g &= \left\{2(h+c^2)+\frac{\eta s^2}{C_{11}C_{44}}\right\}^{1/2},\\
\xi &= g(h+g\beta_3+\beta_3^2),\\
f &= \frac{h+c^2}{C_{66}}+\frac{gh}{C_{66}\beta_3}+\frac{C_{33}s^2}{C_{11}C_{44}},
\end{aligned}
\tag{9.19}
$$

β_3, h, g and ξ being positive dimensionless functions of c and s.

A general expression of the tensor $\boldsymbol{H}(\boldsymbol{x})$ for any $\boldsymbol{x}$, in terms of cos and sin functions of spherical angles ϕ and θ of $\boldsymbol{x}$, can be obtained from (9.17) and (9.18) by the following transformation of components of $\boldsymbol{H}(\widehat{\boldsymbol{x}})$:

$$H_{ik}(\boldsymbol{x}) = \Omega_{ia}\Omega_{kb}H_{ab}(\widehat{\boldsymbol{x}}), \tag{9.20}$$

where the rotation matrix $\boldsymbol{\Omega}$ is defined as

$$\boldsymbol{\Omega} = \begin{pmatrix} \cos\theta & -\sin\theta & 0\\ \sin\theta & \cos\theta & 0\\ 0 & 0 & 1 \end{pmatrix}, \tag{9.21}$$

the angle $0 \le \theta < 2\pi$ being shown in Fig. 9.1. Note that transformation rule (9.20) with (9.21) for $\boldsymbol{H}(\boldsymbol{x})$ evaluation has been obtained by a small correction in the original formula given by Ting and Lee [167].

Finally, bringing together Equations (9.4) and (9.17-9.21) an explicit and completely general expression for the fundamental solution $\boldsymbol{U}(\boldsymbol{x})$ in a transversely isotropic material is obtained. The form of this expression suitable for a computational implementation obtained by performing explicitly the transforms indicated in (9.20) is given in the Appendix, see (A.18), where the presence of several zero components in $\boldsymbol{H}(\widehat{\boldsymbol{x}})$ and $\boldsymbol{\Omega}$ has provided simple and short expressions of the components of $\boldsymbol{H}(\boldsymbol{x})$.

9.1.4 Traction fundamental solution for transversely isotropic materials

Let $E_{ijk}(\boldsymbol{x})$ represent strains ε_{ij} at $\boldsymbol{x}$ originated in the infinite elastic medium subjected to a unit point force in the k-direction at the origin of coordinates. Then,

$$E_{ijk}(\boldsymbol{x}) = \frac{1}{2}\left(\frac{\partial U_{ik}}{\partial x_j}(\boldsymbol{x}) + \frac{\partial U_{jk}}{\partial x_i}(\boldsymbol{x})\right) = \frac{1}{2}\left(U_{ik,j}(\boldsymbol{x}) + U_{jk,i}(\boldsymbol{x})\right). \tag{9.22}$$

Derivatives of the displacement fundamental solution appearing in (9.22) can be expressed in a form analogous to (9.4):

$$U_{ik,j}(\boldsymbol{x}) = \frac{\widehat{U}_{ik;j}(\boldsymbol{x})}{4\pi r^2}, \tag{9.23}$$

where $\widehat{U}_{ik;j}(\boldsymbol{x})$ is the *characteristic* (or *modulation*) function, which depends only on the direction of $\boldsymbol{x}$ but not on its magnitude, *i.e.* $\widehat{U}_{ik;j}(\boldsymbol{x}) = \widehat{U}_{ik;j}\left(\frac{\boldsymbol{x}}{r}\right)$. While a comma between subscripts denotes a derivative with respect to a cartesian coordinate, a semicolon in a modulation function is used only (mnemotechnically) to represent that this function is associated to the corresponding derivative kernel. Notice that $\widehat{U}_{ik;j}(\boldsymbol{x}) = \widehat{U}_{ki;j}(\boldsymbol{x})$ and $\widehat{U}_{ik;j}(-\boldsymbol{x}) = -\widehat{U}_{ik;j}(\boldsymbol{x})$.

Starting from the expression of $U_{ik}(\boldsymbol{x})$ given by (9.4) and (9.17-9.21) and directly performing differentiation leads to somewhat large expressions for $\widehat{U}_{ik;j}(\boldsymbol{x})$, which additionally, when expressed in terms of coordinates of point $\boldsymbol{x}$, include terms of the type "zero divided by zero" when $\boldsymbol{x}$ is placed on the x_3-axis. To avoid this problem, a trick analogous to that proposed by Ting and Lee [167] can be used here.

First, $\widehat{U}_{ik;j}(\widehat{\boldsymbol{x}})$ is evaluated by the above described procedure. Then, considering that x_3 is the rotational symmetry axis of the material, a general expression of $\widehat{U}_{ik;j}(\boldsymbol{x})$, in terms of cos and sin functions of spherical angles ϕ and θ of a point $\boldsymbol{x}$, is simply obtained by a transformation analogous to (9.20):

$$\widehat{U}_{ik;j}(\boldsymbol{x}) = \Omega_{ia}\Omega_{kb}\Omega_{jc}\widehat{U}_{ab;c}(\widehat{\boldsymbol{x}}). \tag{9.24}$$

Analytic evaluation of $\widehat{U}_{ik;j}(\widehat{\boldsymbol{x}})$ has been performed with the aid of the computer algebra software Mathematica [180]. The completely general and closed-form expressions of $\widehat{U}_{ik;j}(\widehat{\boldsymbol{x}})$ obtained are presented in a compact form

suitable for computer implementation:

$$\begin{array}{lll}
\widehat{U}_{11;1} = H'_{11}c - H_{11}s, & \widehat{U}_{12;2} = \tilde{H}_{12}s, & \widehat{U}_{11;3} = -H'_{11}s - H_{11}c, \\
\widehat{U}_{22;1} = H'_{22}c - H_{22}s, & \widehat{U}_{23;2} = \tilde{H}_{13}, & \widehat{U}_{22;3} = -H'_{22}s - H_{22}c, \\
\widehat{U}_{33;1} = H'_{33}c - H_{33}s, & & \widehat{U}_{33;3} = -H'_{33}s - H_{33}c, \\
\widehat{U}_{13;1} = H'_{13}c - H_{13}s, & & \widehat{U}_{13;3} = -H'_{13}s - H_{13}c,
\end{array} \tag{9.25}$$

where

$$\begin{aligned}
H'_{11} &= -\frac{\beta'_3}{C_{66}\beta_3^2} - \frac{C_{44}c^2 + C_{33}s^2}{C_{11}C_{44}gh}\left(\frac{h'}{h} + \frac{g'}{g}\right) + \frac{2\left(C_{33} - C_{44}\right)cs}{C_{11}C_{44}gh} \\
&\quad - \frac{1}{\xi}\left(f' - \frac{\xi' f}{\xi}\right), \\
H'_{22} &= -\frac{g'}{C_{11}g^2} + \frac{1}{\xi}\left(f' - \frac{\xi' f}{\xi}\right), \\
H'_{33} &= -\frac{1}{gh}\left(\frac{2cs}{C_{11}} + \frac{h' - 2cs}{C_{44}}\right) - H_{33}\left(\frac{h'}{h} + \frac{g'}{g}\right), \\
H'_{13} &= \frac{C_{13} + C_{44}}{C_{11}C_{44}gh}\left(c^2 - s^2 - cs\left(\frac{h'}{h} + \frac{g'}{g}\right)\right).
\end{aligned}$$

$$\begin{aligned}
\tilde{H}_{12} &= \frac{C_{33}}{C_{11}C_{44}gh} - \frac{\eta c^2 + C_{33}C_{44}s^2}{C_{11}C_{44}\left(h + c^2\right)}\left(\frac{1}{C_{11}gh} + \frac{g}{C_{66}\beta_3\xi}\right) \\
&\quad + \frac{1}{\xi}\left(\frac{\eta - 2C_{33}C_{66}}{C_{11}C_{44}C_{66}} + \frac{C_{44}g}{C_{66}^2\beta_3}\right), \\
\beta'_3 &= \frac{\left(C_{44} - C_{66}\right)cs}{C_{66}\beta_3}, \\
h' &= \frac{1}{h}\left(-2c^3s + \frac{\eta cs}{C_{11}C_{44}}\left(c^2 - s^2\right) + \frac{2C_{33}cs^3}{C_{11}}\right), \\
g' &= \frac{1}{g}\left(h' - 2cs + \frac{\eta cs}{C_{11}C_{44}}\right), \\
\xi' &= g\left(h' + g'\beta_3 + g\beta'_3 + 2\beta_3\beta'_3\right) + \frac{g'\xi}{g}, \\
f' &= \frac{h' - 2cs}{C_{66}} + \frac{1}{C_{66}\beta_3}\left(hg' + h'g - \frac{\beta'_3 gh}{\beta_3}\right) + \frac{2C_{33}cs}{C_{11}C_{44}},
\end{aligned}$$

Functions $\beta'_3, h', g', \xi', f'$ and H'_{ik} represent the first order derivatives

with respect to the angle ϕ of the corresponding functions defined in (9.18-9.19).

The remaining components of $\widehat{U}_{ik;j}(\widehat{\boldsymbol{x}})$ vanish,

$$\widehat{U}_{12;1} = \widehat{U}_{23;1} = \widehat{U}_{11;2} = \widehat{U}_{13;2} = \widehat{U}_{22;2} = \widehat{U}_{33;2} = \widehat{U}_{12;3} = \widehat{U}_{23;3} = 0. \quad (9.26)$$

It should be mentioned that in the original expression of $\widehat{U}_{12;2}(\widehat{\boldsymbol{x}})$, directly obtained by differentiating (9.20), the term $(H_{11} - H_{22})/s$ appeared, which would lead to zero divided by zero for points at the x_3-axis. This term, which has a finite limit value for $\phi \to 0$ or π, has been rewritten in the form $\tilde{H}_{12}s$, which is well defined for any point with $r > 0$.

By applying the stress-strain constitutive law in matrix form, the stresses corresponding to the above fundamental solution are obtained as:

$$\begin{Bmatrix} \Sigma_{11k} \\ \Sigma_{22k} \\ \Sigma_{33k} \\ \Sigma_{23k} \\ \Sigma_{13k} \\ \Sigma_{12k} \end{Bmatrix} = \boldsymbol{C} \begin{Bmatrix} E_{11k} \\ E_{22k} \\ E_{33k} \\ 2E_{23k} \\ 2E_{13k} \\ 2E_{12k} \end{Bmatrix} = \boldsymbol{C} \begin{Bmatrix} U_{1k,1} \\ U_{2k,2} \\ U_{3k,3} \\ U_{2k,3} + U_{3k,2} \\ U_{1k,3} + U_{3k,1} \\ U_{1k,2} + U_{2k,1} \end{Bmatrix}, \quad (9.27)$$

$\Sigma_{ijk}(\boldsymbol{x})$ representing the stress tensor σ_{ij} at $\boldsymbol{x}$ originated in the infinite elastic medium subjected to a unit point force in the k-direction at the origin of the coordinates. Again, it will be useful to write the stress fundamental solution in the form analogous to (9.4) and (9.23):

$$\Sigma_{ijk}(\boldsymbol{x}) = \frac{\widehat{\Sigma}_{ijk}(\boldsymbol{x})}{4\pi r^2}, \quad (9.28)$$

where $\widehat{\Sigma}_{ijk}(\boldsymbol{x}) = \widehat{\Sigma}_{ijk}\left(\frac{\boldsymbol{x}}{r}\right)$. Notice that $\widehat{\Sigma}_{ijk}(\boldsymbol{x}) = \widehat{\Sigma}_{jik}(\boldsymbol{x})$ due to the symmetry of the stress tensor and $\widehat{\Sigma}_{ijk}(-\boldsymbol{x}) = -\widehat{\Sigma}_{ijk}(\boldsymbol{x})$.

By substituting expressions (9.23) and (9.28) into (9.27), it is easily seen that a relation analogous to (9.27) holds for the characteristic functions $\widehat{U}_{ik;j}(\boldsymbol{x})$ and $\widehat{\Sigma}_{ijk}(\boldsymbol{x})$ as well. Then, using expressions (9.25-9.26) gives directly the following closed-form expressions of $\widehat{\Sigma}_{ijk}(\widehat{\boldsymbol{x}})$:

$$
\begin{aligned}
\widehat{\Sigma}_{111} &= C_{12}\tilde{H}_{12}s + C_{11}\left(H'_{11}c - H_{11}s\right) + C_{13}\left(-H'_{13}s - H_{13}c\right),\\
\widehat{\Sigma}_{221} &= C_{11}\tilde{H}_{12}s + C_{12}\left(H'_{11}c - H_{11}s\right) + C_{13}\left(-H'_{13}s - H_{13}c\right),\\
\widehat{\Sigma}_{331} &= C_{13}\tilde{H}_{12}s + C_{13}\left(H'_{11}c - H_{11}s\right) + C_{33}\left(-H'_{13}s - H_{13}c\right),\\
\widehat{\Sigma}_{131} &= C_{44}\left(-H'_{11}s - H_{11}c\right) + C_{44}\left(H'_{13}c - H_{13}s\right),\\
\widehat{\Sigma}_{232} &= C_{44}\left(-H'_{22}s - H_{22}c\right) + C_{44}\tilde{H}_{13},\\
\widehat{\Sigma}_{122} &= C_{66}\tilde{H}_{12}s + C_{66}\left(H'_{22}c - H_{22}s\right)s,\\
\widehat{\Sigma}_{113} &= C_{13}\left(-H'_{33}s - H_{33}c\right) + C_{12}\tilde{H}_{13} + C_{11}\left(H'_{13}c - H_{13}s\right),\\
\widehat{\Sigma}_{223} &= C_{13}\left(-H'_{33}s - H_{33}c\right) + C_{11}\tilde{H}_{13} + C_{12}\left(H'_{13}c - H_{13}s\right),\\
\widehat{\Sigma}_{333} &= C_{33}\left(-H'_{33}s - H_{33}c\right) + C_{13}\tilde{H}_{13} + C_{13}\left(H'_{13}c - H_{13}s\right),\\
\widehat{\Sigma}_{133} &= C_{44}\left(H'_{33}c - H_{33}s\right) + C_{44}\left(-H'_{13}s - H_{13}c\right).
\end{aligned}
\tag{9.29}
$$

The remaining components of $\widehat{\Sigma}_{ijk}(\widehat{\boldsymbol{x}})$ vanish due to the fact that the plane $x_2 = 0$ is the symmetry or skew-symmetry plane of the elastic problem associated to a particular direction of the point force, namely:

$$
\widehat{\Sigma}_{121} = \widehat{\Sigma}_{231} = \widehat{\Sigma}_{112} = \widehat{\Sigma}_{222} = \widehat{\Sigma}_{332} = \widehat{\Sigma}_{132} = \widehat{\Sigma}_{123} = \widehat{\Sigma}_{233} = 0. \tag{9.30}
$$

Again, considering that x_3 is the rotational symmetry axis of the material, a general expression of $\widehat{\Sigma}_{ijk}(\boldsymbol{x})$, in terms of cos and sin functions of spherical angles ϕ and θ of a point $\boldsymbol{x}$, is obtained by a transformation analogous to (9.24):

$$
\widehat{\Sigma}_{ijk}(\boldsymbol{x}) = \Omega_{ia}\Omega_{jb}\Omega_{kc}\widehat{\Sigma}_{abc}(\widehat{\boldsymbol{x}}). \tag{9.31}
$$

The corresponding traction fundamental solution $T_{ik}(\boldsymbol{x})$, associated to the unit normal vector $\boldsymbol{n}(\boldsymbol{x})$ is directly obtained from $\Sigma_{ijk}(\boldsymbol{x})$ applying the Cauchy lemma:

$$
T_{ik}(\boldsymbol{x}) = \Sigma_{ijk}(\boldsymbol{x})\, n_j(\boldsymbol{x}) \tag{9.32}
$$

The main advantage of the above presented expressions for $U_{ik,j}(\boldsymbol{x})$, $\Sigma_{ijk}(\boldsymbol{x})$ and $T_{ik}(\boldsymbol{x})$ in comparison with the previous expressions of other authors [104, 129] is that they are completely general real-variable expressions, valid for any combination of material parameters and any position of the evaluation point.

For a direct and efficient computational implementation of the obtained expressions of $\widehat{U}_{ik,j}(\boldsymbol{x})$ and $\widehat{\Sigma}_{ijk}(\boldsymbol{x})$ for any point $\boldsymbol{x} \neq \boldsymbol{0}$, the transforms

indicated in (9.24) and (9.31) have been explicitly performed producing compact and general expressions presented in Appendix, which take advantage of the presence of many zero components in $\widehat{U}_{ik;j}(\widehat{\boldsymbol{x}})$ and $\widehat{\Sigma}_{ijk}(\widehat{\boldsymbol{x}})$. It has been numerically verified that in terms of computational time, the expressions in (A.20) and (A.21) are significantly more efficient than their counterparts (9.24) and (9.31).

Finally, it should be mentioned that the reason for presenting in an explicit way expressions of the derivatives of the displacement fundamental solution and not only of the stress fundamental solution is the fact that BEM programmers sometimes prefer to use the first one instead of the second, and also the fact that these expressions are applied in the deduction of the second order derivatives of the displacement fundamental solution in the deduction of the Somigliana stress identity.

9.2 HBIE kernels

9.2.1 Introduction

The present section deals with the evaluation of a evolution of the hypersingular integral kernel in the Somigliana stress identity for transversely isotropic materials.

For the sake of brevity only the main contributions in the development and application of different kinds of expressions for the second order derivative of fundamental solutions (or related kernels) will be briefly reviewed herein. See Subsection 9.1.1 for a comprehensive review of the history fundamental solutions evolution and its derivatives for general anisotropic materials, and in particular for the transversely isotropic materials in 3D.

Barnett [13] obtained integral representations of the first and second order derivatives of the fundamental solution for a general anisotropic material, $\boldsymbol{U}(\boldsymbol{x})$, by using Fourier transforms. Barnett used numerical schemes to evaluate his results. Recently, Lee [99] deduced new general analytical expressions of the second order derivatives of $\boldsymbol{U}(\boldsymbol{x})$ in terms of the Stroh eigenvalues.

The implementation in BEM of expressions of anisotropic fundamental solutions and its derivatives using the Stroh formalism as introduced by Lee [98], were recently developed by Shiah *et. al.* [157] and Tan *et. al.* [162]. Although the theory and formulation was obtained a few years before. Rungamornrat [149] transforms the hypersingular and strongly singular integrals appearing in the SGBEM formulation into line and surface integrals, which are at most weakly singular and consequently can be ana-

lytically or numerically evaluated without difficulty. Some extensions of the fundamental solutions and its derivatives for anisotropic piezoelectric [42] and magneto-electro-elastic materials [31] have been also obtained. Chen and Lin [42] evaluated numerically (from the integral solutions derived from Fourier transform methods) the first and second order derivative for linear piezoelectric materials. Recently, Buroni and Sáez [31] obtained the fundamental solution for fully magnetoelectro-elastic and general anisotropic materials. The first and second order derivatives are also obtained combining extended Stroh formalism, Radon transform and Cauchy's residue theory.

In the particular case for transversely isotropic materials, it is remarkable to mention that closed-form expressions for the hypersingular kernel in the traction BIE obtained from second order derivatives of $\boldsymbol{U}(\boldsymbol{x})$ were presented by Ariza and Domínguez [8]. These expressions were obtained using the potential theory and was based on previous works [104, 129]. To the best knowledge of the authors the expressions presented in [8] are the only ones that are presented in an explicit and closed-form manner for transversely isotropic materials. The aim of the present work is to deduce, and numerically test, completely general and closed-form real-variable expressions of the strongly singular and hypersingular kernels in the traction BIE, valid for any transversely isotropic material obtained using the concepts of the Stroh formalism.

9.2.2 Modulation functions of the fundamental solution and its derivatives

The fundamental solution and its derivatives can be expressed in terms of the so-called modulation functions depending only on spherical angles, see Fig. 9.1, in the following form:

$$U_{ik}(r,\theta,\phi) = \frac{1}{4\pi r}\widehat{U}_{ik}(\theta,\phi), \tag{9.33}$$

$$U_{ik,j}(r,\theta,\phi) = \frac{1}{4\pi r^2}\widehat{U}_{ik;j}(\theta,\phi), \tag{9.34}$$

$$U_{ik,j\ell}(r,\theta,\phi) = \frac{1}{4\pi r^3}\widehat{U}_{ik;j\ell}(\theta,\phi), \tag{9.35}$$

where 'widehat' symbol denotes the modulation functions of the fundamental solution, and also of its derivatives with respect to cartesian coordinates. The modulation functions are independent of the radius r in spherical coordinates. Again a comma between subscripts denotes a derivative with

respect to a cartesian coordinate, a semicolon in a modulation function is used only (mnemotechnically) to represent that this function is associated to the corresponding derivative kernel in (9.34) or (9.35).

The modular functions of the fundamental solution derivatives will be shown first in terms of the derivatives of $\boldsymbol{H}(\boldsymbol{x})$. By applying standard rules for differentiation with respect to cartesian coordinates in (9.34) and (9.35) we obtain

$$\widehat{U}_{ik;j}(\theta,\phi) = H_{ik,j}(r,\theta,\phi)r - H_{ik}(\phi,\theta)r_{,j} \tag{9.36}$$

$$\begin{aligned}\widehat{U}_{ik;j\ell}(\theta,\phi) =& H_{ik,j\ell}(r,\theta,\phi)r^2 - H_{ik,j}(r,\theta,\phi)r_{,\ell}r - H_{ik,\ell}(r,\theta,\phi)r_{,j}r \\ &- H_{ik}(\theta,\phi)\left(\delta_{j\ell} - 3r_{,j}r_{,\ell}\right)\end{aligned} \tag{9.37}$$

where $r_{,j}(\theta,\phi) = r_j(r,\theta,\phi)/r$.

By conveniently introducing new modulation functions obtained by derivatives of $H_{ik}(\theta,\phi)$ as follows,

$$H_{ik,j}(r,\theta,\phi) = r^{-1}\widehat{H}_{ik;j}(\theta,\phi) \tag{9.38}$$

$$H_{ik,j\ell}(r,\theta,\phi) = r^{-2}\widehat{H}_{ik;j\ell}(\theta,\phi) \tag{9.39}$$

the modulation functions of the derivatives of U_{ik} can be also expressed in terms of the modulation functions H_{ik}, $\widehat{H}_{ik;j}$ and $\widehat{H}_{ik;j\ell}$ as follows

$$\widehat{U}_{ik;j}(\theta,\phi) = \widehat{H}_{ik;j}(\theta,\phi) - H_{ik}(\theta,\phi)r_{,j} \tag{9.40}$$

$$\begin{aligned}\widehat{U}_{ik;j\ell}(\theta,\phi) =& \widehat{H}_{ik;j\ell}(\theta,\phi) - \widehat{H}_{ik;\ell}(\theta,\phi)r_{,j} - \widehat{H}_{ik;j}(\theta,\phi)r_{,\ell} \\ &- H_{ik}(\theta,\phi)(\delta_{j\ell} - 3r_{,j}r_{,\ell})\end{aligned} \tag{9.41}$$

Sometimes it is useful to express the *characteristic* (or *modulation*) function $\widehat{U}_{ik;j}(\boldsymbol{x})$ as a function of $\boldsymbol{x}$. Then, such modulation function depends only on the direction of $\boldsymbol{x}$ but not on its magnitude, *i.e.* $\widehat{U}_{ik;j}(\boldsymbol{x}) = \widehat{U}_{ik;j}\left(\frac{\boldsymbol{x}}{r}\right)$. The following symmetry relation hold $\widehat{U}_{ik;j}(\boldsymbol{x}) = \widehat{U}_{ki;j}(\boldsymbol{x})$ and $\widehat{U}_{ik;j}(-\boldsymbol{x}) = -\widehat{U}_{ik;j}(\boldsymbol{x})$.

As will be shown the modulation function $\widehat{U}_{ik;j\ell}$ have simple expressions in terms of the first and second order derivative of H_{ik} with respect to spherical angles θ and ϕ. These expressions are obtained for $\theta = 0$, as they will be enough to obtain final expressions of $U_{ij,kl}$ by applying a transformation introduced in [167] for U_{ik} and also used and extended in Subsection 9.1.4 for $U_{ik,j}$.

9.2.3 Strongly singular kernel D_{ijk} for the stress Somigliana identity

It is noteworthy to remind that the expressions for D_{ijk} coincide, except for a change of sign, with the stress tensor components Σ_{ijk} introduced in the previous section, see (9.31). The change of sign is due to the different differentiation point: integration point for the stress tensor and collocation point for the kernel D_{ijk}.

$$D_{ijk}(\boldsymbol{x}) = -\Sigma_{ijk}(\boldsymbol{x}) \tag{9.42}$$

9.2.4 Hyper-singular kernel S_{ijk} for the stress Somigliana identity

The tensor S_{ijk} is based on the related kernel of the second order derivative $U_{ik,jl}$ and the tensor Σ^{loop}_{ijkl} (the stress influence function in an infinitesimal dislocation loop [115]). The corresponding fundamental solution, tensor S_{ijk}, associated to the unit normal vector $\boldsymbol{n}(\boldsymbol{x})$ is directly obtained from $\Sigma^{loop}_{ijkl}(\boldsymbol{x})$ by:

$$S_{ijk}(\boldsymbol{x}) = \Sigma^{loop}_{ijkl}(\boldsymbol{x})\, n_l(\boldsymbol{x}) \tag{9.43}$$

Explicit expressions of S_{ijk} are shown in the Appendix. While explicit expression for the tensors $U_{ik,jl}$ and Σ^{loop}_{ijkl} will be obtained in the following.

Thus, first the second order derivative $U_{ik,jl}(\boldsymbol{x})$ is expressed in terms of the modulation function $\widehat{U}_{ik;jl}(\boldsymbol{x})$, see (9.35). Then, as will be shown expressions for $\widehat{U}_{ik;jl}(\widehat{\boldsymbol{x}})$, $\theta = 0$, are only necessary to correctly describe the behavior of any transversely isotropic material. Then, $\widehat{U}_{ik;jl}(\widehat{\boldsymbol{x}})$ is evaluated and considering that x_3 is the rotational symmetry axis of the material, a general expression of $\widehat{U}_{ik;jl}(\boldsymbol{x})$, in terms of cos and sin functions of spherical angles ϕ and θ of a point $\boldsymbol{x}$, is simply obtained by a transformation analogous to (9.20) and (9.31):

$$\widehat{U}_{ik;jl}(\boldsymbol{x}) = \Omega_{ia}\Omega_{kb}\Omega_{jc}\Omega_{ld}\widehat{U}_{ab;cd}(\widehat{\boldsymbol{x}}). \tag{9.44}$$

The reason to present this expressions explicitly is that some BEM programmers prefer to use them instead of using the expressions of tensor S_{ijk}.

Thus $\widehat{U}_{ik;jl}(\widehat{\boldsymbol{x}})$ expressions are expressed by:

$$
\begin{aligned}
\widehat{U}_{11;11} =& H''_{11}c^2 - 4H'_{11}cs - H_{11}c^2 + 2H_{11}s^2,\\
\widehat{U}_{11;13} =& - H''_{11}cs - 2H'_{11}(c^2 - s^2) + 3H_{11}cs,\\
\widehat{U}_{11;22} =& \tilde{H}_{11}c - 2\tilde{H}_{12} - H_{11},\\
\widehat{U}_{11;33} =& H''_{11}s^2 + 4H'_{11}cs + 2H_{11}c^2 - H_{11}s^2,\\
\widehat{U}_{12;12} =& (\tilde{H}_{11} - \tilde{H}_{22})c - \tilde{H}_{12} - H_{11} + H_{22},\\
\widehat{U}_{12;23} =& - H'_{11} + H'_{22} - \tilde{H}_{12}cs,\\
\widehat{U}_{13;11} =& H''_{13}c^2 - 4H'_{13}cs - H_{13}c^2 + 2H_{13}s^2,\\
\widehat{U}_{13;13} =& - H''_{13}cs - 2H'_{13}(c^2 - s^2) + 3H_{13}cs,\\
\widehat{U}_{13;22} =& - \tilde{H}_{13}\,(2s + \gamma c) - H_{13},\\
\widehat{U}_{13;33} =& H''_{13}s^2 + 4H'_{13}cs + 2H_{13}c^2 - H_{13}s^2,\\
\widehat{U}_{22;11} =& H''_{22}c^2 - 4H'_{22}cs - H_{22}c^2 + 2H_{22}s^2,\\
\widehat{U}_{22;13} =& - H''_{22}cs - 2H'_{22}(c^2 - s^2) + 3H_{22}cs,\\
\widehat{U}_{22;22} =& \tilde{H}_{22}c + 2\tilde{H}_{12} - H_{22},\\
\widehat{U}_{22;33} =& H''_{22}s^2 + 4H'_{22}cs + 2H_{22}c^2 - H_{22}s^2,\\
\widehat{U}_{23;23} =& - H'_{13} - \tilde{H}_{13}c,\\
\widehat{U}_{33;11} =& H''_{33}c^2 - 4H'_{33}cs - H_{33}c^2 + 2H_{33}s^2,\\
\widehat{U}_{33;13} =& - H''_{33}cs - 2H'_{33}(c^2 - s^2) + 3H_{33}cs,\\
\widehat{U}_{33;22} =& - H_{33} + \tilde{H}_{33}c,\\
\widehat{U}_{33;33} =& H''_{33}s^2 + 4H'_{33}cs + 2H_{33}c^2 - H_{33}s^2,
\end{aligned}
\tag{9.45}
$$

where

$$
\begin{aligned}
H''_{13} &= \frac{C_{13}+C_{44}}{C_{11}C_{44}hg}\left[\left(\frac{g'^2}{g^2}+\frac{h'^2}{h^2}-4\right)cs-\frac{g''cs+g'(c^2-s^2)}{g}\right.\\
&\quad\left.-\frac{h''cs+h'(c^2-s^2)}{h}\right]-H_{13}\gamma\\
H''_{33} &= -H_{33}\left(\frac{g''g-g'^2}{g^2}+\frac{h''h-h'^2}{h^2}\right)-H'_{33}\gamma-\frac{\gamma}{gh}\left(\frac{h'-2cs}{C_{44}}+\frac{2cs}{C_{11}}\right)\\
&\quad+\frac{1}{gh}\left(\frac{h''-2(c^2-s^2)}{C_{44}}+\frac{2(c^2-s^2)}{C_{11}}\right)\\
H''_{22} &= \frac{2g'^2-g''g}{C_{11}g^3}+\frac{1}{\xi}\left(f''-\frac{(\xi''f+\xi'f')\xi-f\xi'^2}{\xi^2}\right)+\frac{\xi'}{\xi^2}\left(\frac{f\xi'}{\xi}-f'\right)\\
H''_{11} &= \frac{2\beta_3'^2-\beta_3''\beta_3}{C_{66}\beta_3^3}+\frac{C_{44}c^2+C_{33}s^2}{C_{11}C_{44}gh}\left(\gamma^2-\frac{g''g-g'^2}{g^2}-\frac{h''h-h'^2}{h^2}\right)\\
&\quad-\frac{1}{\xi}\left(f''-\frac{(\xi''f+\xi'f')\xi-f\xi'^2}{\xi^2}\right)+\frac{2(C_{33}-C_{44})(c^2-s^2)}{C_{11}C_{44}gh}\\
&\quad-\frac{4(C_{33}-C_{44})cs\gamma}{C_{11}C_{44}gh}-\frac{\xi'}{\xi^2}\left(\frac{f\xi'}{\xi}-f'\right) \qquad (9.46)\\
\beta_3'' &= -\frac{\beta_3'^2}{\beta_3}+\frac{(C_{44}-C_{66})}{C_{66}\beta_3}\left(c^2-s^2\right)\\
h'' &= \frac{1}{h}\left[-h'^2-2h^2+2\left(3+\frac{3C_{33}}{C_{11}}-\frac{\eta}{C_{11}C_{44}}\right)c^2s^2+\frac{\eta\left(c^2-s^2\right)^2}{C_{11}C_{44}}\right]\\
g'' &= \frac{1}{g}\left[h''-g'^2+\left(\frac{\eta}{C_{11}C_{44}}-2\right)\left(c^2-s^2\right)\right]\\
\xi'' &= g\left(h''+\beta_3g''+\beta_3''g+2\beta_3'g'+\frac{2\left(C_{44}-C_{66}\right)\left(c^2-s^2\right)}{C_{66}}\right)\\
&\quad+\frac{g''\xi}{g}+2g'\left(\frac{\xi'}{g}-\frac{g'\xi}{g^2}\right)\\
f'' &= \frac{1}{C_{66}\beta_3}\left(h''g+hg''-\frac{\beta_3''gh+\beta_3'g'h+\beta_3'h'g}{\beta_3}+\frac{2gh\beta_3'^2}{\beta_3^2}+2h'g'\right)\\
&\quad-\frac{(hg'+h'g)\beta_3'}{C_{66}\beta_3^2}+\frac{2C_{33}(c^2-s^2)}{C_{11}C_{44}}+\frac{h''-2(c^2-s^2)}{C_{66}}
\end{aligned}
$$

Functions $H''_{ik}, \beta''_3, h'', g'', \xi'$ and f'' represent the second order derivatives with respect to the angle ϕ of the functions defined in (9.18) and (9.19).

It is also useful to define:

$$\begin{aligned} \beta_3' &= \tilde{\beta}_3 s, & h' &= \tilde{h} s, & g' &= \tilde{g} s, & \xi' &= \tilde{\xi} s, \\ f' &= \tilde{f} s, & H_{11}' &= \tilde{H}_{11} s, & H_{22}' &= \tilde{H}_{22} s, & H_{33}' &= \tilde{H}_{33} s \end{aligned} \tag{9.47}$$

In (9.47), 'tilde' functions are related to the first order derivatives functions defined in (9.19). These functions are presented in order to avoid the presence of divisions by s, leading eventually in divisions by 0 when $\phi = 0$.

Continuing with the deduction of the kernel S_{ijk}, the stress-strain constitutive law is applied twice to modulation function related to the second order derivative of the fundamental solution, obtaining:

$$\widehat{\Sigma}_{ijkl}^{loop}(\boldsymbol{x}) = C_{ijmn} C_{pqkl} \widehat{U}_{mp,nq}(\boldsymbol{x}). \tag{9.48}$$

where Σ_{ijkl}^{loop} is the stress influence function in an infinitesimal dislocation loop [115], which is defined by $b_k n_l$ (where b is the constituent Burgers vector and $\mathbf{n}$ is the normal vector to the infinitesimal area).

Considering that x_3 is the rotational symmetry axis of the material, a modulation function can be obtained from a general expression of $\widehat{\Sigma}_{ijkl}^{loop}(\boldsymbol{x})$, in terms of cos and sin functions of spherical angles ϕ and θ of a point $\boldsymbol{x}$, by a transformation analogous to (9.44):

$$\widehat{\Sigma}_{ijkl}^{loop}(\boldsymbol{x}) = \Omega_{ia}\Omega_{jb}\Omega_{kc}\Omega_{ld}\widehat{\Sigma}_{abcd}^{loop}(\widehat{\boldsymbol{x}}). \tag{9.49}$$

and

$$\Sigma_{ijkl}^{loop}(\boldsymbol{x}) = \frac{\widehat{\Sigma}_{ijkl}^{loop}(\boldsymbol{x})}{4\pi r^3}, \tag{9.50}$$

Thus, $\widehat{\Sigma}_{ijkl}^{loop}(\widehat{\boldsymbol{x}})$ expressions are defined as:

$$\begin{aligned} \widehat{\Sigma}_{1111}^{loop} = {} & C_{11}^2 \left[H_{11}'' c^2 - 4H_{11}' cs + H_{11}\left(2s^2 - c^2\right)\right] + 2C_{12}C_{13}\left[-H_{13}' - \tilde{H}_{13} c\right] \\ & + C_{13}^2\left[-H_{13}'' cs - 2H_{13}'\left(c^2 - s^2\right) + 3H_{13} cs\right] + C_{12}^2\left[2\tilde{H}_{12} + \tilde{H}_{22} c - H_{22}\right] \\ & + 2C_{11}C_{13}\left[-H_{13}'' cs - 2H_{13}'\left(c^2 - s^2\right) + 3H_{13} cs\right] \\ & + 2C_{11}C_{12}\left[\left(\tilde{H}_{11} - \tilde{H}_{22}\right) c - \tilde{H}_{12} - H_{11} + H_{22}\right] \end{aligned}$$

$$
\begin{aligned}
\widehat{\Sigma}^{loop}_{1122} &= C_{11}C_{12}\left[H''_{11}c^2 - 4H'_{11}cs + 2\tilde{H}_{12} + \tilde{H}_{22}c + H_{11}\left(2s^2 - c^2\right) - H_{22}\right] \\
&+ C_{11}C_{13}\left[-H''_{13}cs - 2H'_{13}\left(c^2 - s^2\right) - H'_{13} + \tilde{H}_{13}c + 3H_{13}cs\right] \\
&+ C_{12}C_{13}\left[-H''_{13}cs - 2H'_{13}\left(c^2 - s^2\right) - H'_{13} + \tilde{H}_{13}c + 3H_{13}cs\right] \\
&+ C_{11}^2\left[\left(\tilde{H}_{11} - \tilde{H}_{22}\right)c - \tilde{H}_{12} - H_{11} + H_{22}\right] \\
&+ C_{12}^2\left[\left(\tilde{H}_{11} - \tilde{H}_{22}\right)c - \tilde{H}_{12} - H_{11} + H_{22}\right] \\
&+ C_{13}^2\left[-H''_{13}cs - 2H'_{13}\left(c^2 - s^2\right) + 3H_{13}cs\right] \\
\widehat{\Sigma}^{loop}_{1113} &= +C_{12}C_{44}\left[-H'_{11} + H'_{22} - \tilde{H}_{12}cs - \tilde{H}_{13}\left(2s + \gamma c\right) - H_{13}\right] \\
&+ C_{11}C_{44}\left[H''_{13}c^2 - H''_{11}cs - 4H'_{13}cs - 2H'_{11}\left(c^2 - s^2\right) + H_{13}\left(2s^2 - c^2\right)\right. \\
&\left.+3H_{11}cs\right] + C_{13}C_{44}\left[H''_{13}s^2 - H''_{33}cs + 4H'_{13}cs - 2H'_{33}\left(c^2 - s^2\right)\right. \\
&\left.+H_{13}\left(2c^2 - s^2\right) + 3H_{33}cs\right] \\
\widehat{\Sigma}^{loop}_{1133} &= C_{13}C_{33}\left[H''_{33}s^2 + 4H'_{33}cs + H_{33}\left(2c^2 - s^2\right)\right] + C_{12}C_{33}\left[-H'_{13} - \tilde{H}_{13}c\right] \\
&+ C_{11}C_{13}\left[H''_{11}c^2 - 4H'_{11}cs + \left(\tilde{H}_{11} - \tilde{H}_{22}\right)c - \tilde{H}_{12} + H_{11}\left(2s^2 - c^2\right)\right. \\
&\left.-H_{11} + H_{22}\right] + C_{11}C_{33}\left[-H''_{13}cs - 2H'_{13}\left(c^2 - s^2\right) + 3H_{13}cs\right] \\
&+ C_{13}^2\left[-H''_{13}cs - 2H'_{13}\left(c^2 - s^2\right) - H'_{13} + \tilde{H}_{13}c + 3H_{13}cs\right] \\
&+ C_{12}C_{13}\left[\tilde{H}_{11}c + \tilde{H}_{12} - H_{11}\right] \\
\widehat{\Sigma}^{loop}_{1212} &= C_{66}^2\left[H''_{22}c^2 - 4H'_{22}cs + \left(3\tilde{H}_{11} - 2\tilde{H}_{22}\right)c - 4\tilde{H}_{12} + H_{22}\left(2s^2 - c^2\right)\right. \\
&\left.-3H_{11} + 2H_{22}\right] \\
\widehat{\Sigma}^{loop}_{1223} &= C_{44}C_{66}\left[-H''_{22}cs - 2H'_{22}\left(c^2 - s^2\right) - H'_{11} + H'_{22} - \tilde{H}_{12}cs\right. \\
&\left.-2\tilde{H}_{13}\left(2s + \gamma c\right) + 3H_{22}cs - 2H_{13}\right] \\
\widehat{\Sigma}^{loop}_{1313} &= C_{44}^2\left[H''_{11}s^2 - 2H''_{13}cs + H''_{33}c^2 + 4H'_{11}cs - 4H'_{13}\left(c^2 - s^2\right) - 4H'_{33}cs\right. \\
&\left.+H_{11}\left(2c^2 - s^2\right) + 6H_{13}cs + H_{33}\left(2s^2 - c^2\right)\right] \\
\widehat{\Sigma}^{loop}_{1322} &= C_{11}C_{44}\left[-H'_{11} + H'_{22} - \tilde{H}_{12}cs - \tilde{H}_{13}\left(2s + \gamma c\right) - H_{13}\right] \\
&+ C_{12}C_{44}\left[H''_{13}c^2 - H''_{11}cs - 4H'_{13}cs - 2H'_{11}\left(c^2 - s^2\right)\right. \\
&\left.+H_{13}\left(2s^2 - c^2\right) + 3H_{11}cs\right] + C_{13}C_{44}\left[H''_{13}s^2 - H''_{33}cs\right. \\
&\left.+4H'_{13}cs - 2H'_{33}\left(c^2 - s^2\right) + H_{13}\left(2c^2 - s^2\right) + 3H_{33}cs\right]
\end{aligned}
$$

$$
\begin{aligned}
\widehat{\Sigma}^{loop}_{1333} &= C_{13}C_{44}\left[-H'_{11}+H'_{22}-\tilde{H}_{12}cs-\tilde{H}_{13}\left(2s+\gamma c\right)-H_{13}\right]\\
&+C_{13}C_{44}\left[H''_{13}c^2-H''_{11}cs-4H'_{13}cs-2H'_{11}\left(c^2-s^2\right)\right.\\
&\left.+H_{13}\left(2s^2-c^2\right)+3H_{11}cs\right]+C_{33}C_{44}\left[H''_{13}s^2-H''_{33}cs\right.\\
&\left.+4H'_{13}cs-2H'_{33}\left(c^2-s^2\right)+H_{13}\left(2c^2-s^2\right)+3H_{33}cs\right]\\
\widehat{\Sigma}^{loop}_{2323} &= C^2_{44}\left[H''_{22}s^2+4H'_{22}cs-2H'_{13}-2\tilde{H}_{13}c-\tilde{H}_{33}c+H_{22}\left(2c^2-s^2\right)\right.\\
&\left.-H_{33}\right]\\
\widehat{\Sigma}^{loop}_{2222} &= C^2_{12}\left[H''_{11}c^2-4H'_{11}cs+H_{11}\left(2s^2-c^2\right)\right]+2C_{11}C_{13}\left[-H'_{13}-\tilde{H}_{13}c\right]\\
&+C^2_{13}\left[-H''_{13}cs-2H'_{13}\left(c^2-s^2\right)+3H_{13}cs\right]+C^2_{11}\left[2\tilde{H}_{12}+\tilde{H}_{22}c-H_{22}\right]\\
&+2C_{12}C_{13}\left[-H''_{13}cs-2H'_{13}\left(c^2-s^2\right)+3H_{13}cs\right]\\
&+2C_{11}C_{12}\left[\left(\tilde{H}_{11}-\tilde{H}_{22}\right)c-\tilde{H}_{12}-H_{11}+H_{22}\right]\\
\widehat{\Sigma}^{loop}_{2233} &= C_{12}C_{13}\left[H''_{11}c^2-4H'_{11}cs+\left(\tilde{H}_{11}-\tilde{H}_{22}\right)c-\tilde{H}_{12}+H_{11}\left(2s^2-c^2\right)\right.\\
&\left.-H_{11}+H_{22}\right]+C_{13}C_{33}\left[H''_{33}s^2+4H'_{33}cs+H_{33}\left(2c^2-s^2\right)\right]\\
&+C_{11}C_{13}\left[\tilde{H}_{11}c+\tilde{H}_{12}-H_{11}\right]+C_{11}C_{33}\left[-H'_{13}-\tilde{H}_{13}c\right]\\
&+C_{12}C_{33}\left[-H''_{13}cs-2H'_{13}\left(c^2-s^2\right)+3H_{13}cs\right]\\
&+C^2_{13}\left[-H''_{13}cs-2H'_{13}\left(c^2-s^2\right)-H'_{13}+\tilde{H}_{13}c+3H_{13}cs\right]\\
\widehat{\Sigma}^{loop}_{3333} &= C^2_{13}\left[2\left(\tilde{H}_{11}-\tilde{H}_{22}\right)c-\tilde{H}_{22}c-2H_{11}+H_{22}+H''_{11}c^2-4H'_{11}cs\right.\\
&\left.+H_{11}\left(2s^2-c^2\right)\right]+C^2_{33}\left[H''_{33}s^2+4H'_{33}cs+H_{33}\left(2c^2-s^2\right)\right]\\
&+2C_{13}C_{33}\left[-H''_{13}cs-2H'_{13}\left(c^2-s^2\right)-H'_{13}-\tilde{H}_{13}c+3H_{13}cs\right]
\end{aligned}
\tag{9.51}
$$

$$
\widehat{\Sigma}^{loop}_{1112}=\widehat{\Sigma}^{loop}_{1123}=\widehat{\Sigma}^{loop}_{1213}=\widehat{\Sigma}^{loop}_{1222}=\widehat{\Sigma}^{loop}_{1233}=\widehat{\Sigma}^{loop}_{1323}=\widehat{\Sigma}^{loop}_{2223}=\widehat{\Sigma}^{loop}_{2333}=0 \tag{9.52}
$$

$$
\widehat{\Sigma}^{loop}_{ijkl}=\widehat{\Sigma}^{loop}_{jikl}=\widehat{\Sigma}^{loop}_{ijlk}=\widehat{\Sigma}^{loop}_{klij} \tag{9.53}
$$

It must be mentioned that in terms of efficiency the authors suggests the use of the expressions of $\Sigma^{loop}_{ijkl}(\widehat{\boldsymbol{x}})$, due to the great amount of zeros and the full symmetry presented, and the short expressions obtained that makes easy the implementation in a computational code. Also for a direct and efficient computational implementation of the obtained expressions of

$\widehat{U}_{ij;kl}(\boldsymbol{x})$ and $\Sigma^{loop}_{ijkl}(\boldsymbol{x})$ for any point $x \neq 0$, the transforms indicated in (9.44) and (9.49) have been explicitly performed, producing compact and general expressions presented in the Appendix, which take advantage of the presence of many zero components in $\widehat{U}_{ij;kl}(\widehat{\boldsymbol{x}})$ and $\Sigma^{loop}_{ijkl}(\widehat{\boldsymbol{x}})$. It has been numerically verified that, in terms of computational time, expressions in Appendix are significantly more efficient than their counterparts (9.44) and (9.49).

It should be also stressed that independently of the hypersingular kernel selected (S_{ijk}, Σ^{loop}_{ijkl} or $U_{ij,kl}$) the expressions obtained are much more compact that the expressions based on Pan and Chou's solution and given by Ariza and Domínguez [8].

9.3 Validation of the BIE kernels

The primary means of providing confidence in the correctness of the expressions of the displacement fundamental solution U_{ik} and traction fundamental solution T_{ik} introduced in the present work and also of their implementation in the present 3D BEM code will be their application in the numerical solution of u-BIE (5.1) by this code.

Numerical results for problems in transversely isotropic elastic solids with known analytic solutions [101], coinciding with some problems solved by other authors [104, 179], except for the case with $\triangle < 0$ where no previous numerical results by other authors have been found in the literature, will be studied.

For the purpose of comparison with expressions of U_{ik} and T_{ik} studied in Section 9.2, the expression of U_{ik} due to Loloi [104] and an explicit expression of T_{ik} deduced, working from Loloi's expression of U_{ik} have also been implemented in the BEM code. It can be mentioned that no final explicit expression of T_{ik} was given in Reference [104]. Note also that 4-node linear boundary elements were used in Reference [104] whereas 9-node quadratic boundary elements have been used in the present BEM code.

Example 1

Let Ω be an elastic transversely isotropic cube whose sides of length ℓ are parallel to coordinate axes with the x_3-axis being the rotational-symmetry axis. Consider now this cube subjected to a simple tension. The elastic properties used in this example are shown in Table 9.1. The properties of Material 1 (with $\triangle > 0$) and Material 2 (with $\triangle = 0$) have been taken from Loloi [104] with the aim of comparing the numerical results obtained by

Table 9.1: Elastic stiffnesses considered in Example 1, values given in 10^6 psi.

Constants	Material No. 1 ($\triangle > 0$)	Material No. 2 ($\triangle = 0$)	Material No. 3 ($\triangle < 0$)
C_{11}	49.40	49.40	23.35
C_{12}	34.60	34.60	4.96
C_{13}	9.70	9.70	7.27
C_{33}	38.10	38.10	8.85
C_{44}	14.20	16.84	5.55

Table 9.2: Results of Example 1, Material No. 1($\triangle > 0$).

Load direction	Displacements	Analytic solution	Present solution	Solution [104]
x_3	u_1/u_3^e	-0.1154762	-0.1154762	-0.1154762
	u_2/u_3^e	-0.1154762	-0.1154762	-0.1154762
	u_3/u_3^e	1.0000000	1.0000000	1.0000000
x_1	u_1/u_1^e	1.0000000	0.9999998	0.9999998
	u_2/u_1^e	-0.6846397	-0.6846395	-0.6846395
	u_3/u_1^e	-0.0802886	-0.0802886	-0.0802886
x_2	u_1/u_2^e	-0.6846397	-0.6846395	-0.6846395
	u_2/u_2^e	1.0000000	0.9999998	0.9999998
	u_3/u_2^e	-0.0802886	-0.0802886	-0.0802886

using the expressions deduced from the original work of Pan and Chou [129] and those obtained here starting from the work of Ting and Lee [167], both implemented in the present BEM code. Material 3 (with $\triangle < 0$) is a hexagonal crystal of zinc.

In the BEM model used the cube boundary is discretized by six elements, one element per cube side. Three load cases with normal stresses in the coordinate axes directions have been solved with the symmetry boundary conditions applied at coordinate planes. Although an implicit symmetry can be applied for this example [104], the explicit symmetry was used here.

Numerical results in displacements for Materials 1 and 2 are shown in Tables 9.2 and 9.3 together with the results obtained using the expressions derived from Loloi [104] and implemented in the present BEM code. The

Table 9.3: Results of Example 1, Material No. 2 ($\triangle = 0$).

Load direction	Displacements	Analytic solution	Present solution	Solution [104]
x_3	u_1/u_3^e	-0.1154762	-0.1154762	-0.1154867
	u_2/u_3^e	-0.1154762	-0.1154762	-0.1154867
	u_3/u_3^e	1.0000000	1.0000000	1.0000306
x_1	u_1/u_1^e	1.0000000	0.9999998	0.9999943
	u_2/u_1^e	-0.6846397	-0.6846395	-0.6846325
	u_3/u_1^e	-0.0802886	-0.0802886	-0.0802905
x_2	u_1/u_2^e	-0.6846397	-0.6846395	-0.6846325
	u_2/u_2^e	1.0000000	0.9999998	0.9999943
	u_3/u_2^e	-0.0802886	-0.0802886	-0.0802905

Table 9.4: Results of Example 1, Material No. 3 ($\triangle < 0$).

Load direction	Displacements	Analytic solution	Present solution
x_3	u_1/u_3^e	-0.2567997	-0.2567997
	u_2/u_3^e	-0.2567997	-0.2567997
	u_3/u_3^e	1.0000000	0.9999999
x_1	u_1/u_1^e	1.0000000	1.0000000
	u_2/u_1^e	0.0582394	0.0582393
	u_3/u_1^e	-0.8693108	-0.8693107
x_2	u_1/u_2^e	0.0582394	0.0582393
	u_2/u_2^e	1.0000000	1.0000000
	u_3/u_2^e	-0.8693108	-0.8693107

differences between both numerical solutions and the analytic solution are almost negligible, as could be expected from the character of the analytic solution, linear in displacements and constant in stresses. An analogous conclusion is also valid for Material 3, results being shown in Table 9.4, where only the results obtained using the expressions of U_{ik} and T_{ik} introduced in Section 9.2 are shown, as complex-variable expressions of U_{ik} are given for materials with $\triangle < 0$ in Loloi [104].

Example 2

A prismatic rod subjected to an axial load, Fig. 9.2(a), is considered.

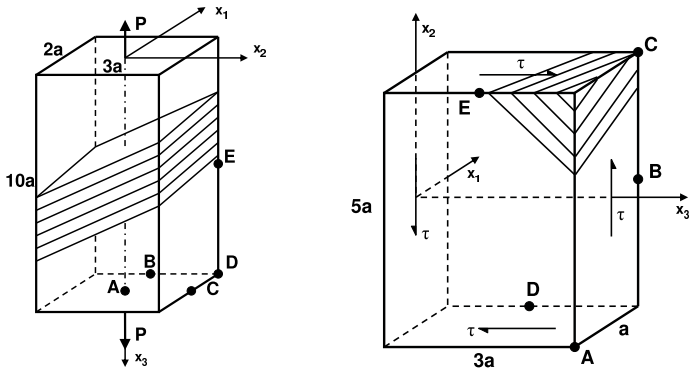

(a) (b)

Figure 9.2: Transversely isotropic problem configurations with an inclined plane of isotropy for Examples 2 and 3: (a) axial load, (b) shear load

The elastic properties in the material coordinate system are defined by:

$$E/E' = 2.0, \quad E/\mu' = 6.0, \quad \nu = 0.3, \quad \nu' = 0.4, \tag{9.54}$$

where E and ν are Young elastic modulus and Poisson ratio associated to the isotropy plane, E' is the Young modulus along the rotational-symmetry axis, and μ' and ν' are the shear modulus and Poisson ratio at the planes perpendicular to the plane of isotropy. The plane of isotropy is inclined 45° with respect to the plane x_1x_2 which coincides with one rod base, Fig. 9.2(a). A BEM model of one-fourth of the rod, symmetry boundary conditions having been considered at the planes x_1x_3 and x_2x_3, with 14 elements, 3

Table 9.5: Results of Example 2, transversely isotropic rod under axial tension.

Point	Solution	u_1/u_3^e	u_2/u_3^e	u_3/u_3^e	$\sigma_{33}/\sigma_{33}^e$
A	Analytic	0.0000000	0.0000000	1.0000000	1.0000000
$(0, 0, 10a)$	Present	0.0000000	0.0000000	1.0000091	1.0000091
	[104]	0.0000000	0.0000000	1.0000091	1.0000091
B	Analytic	-0.0170732	0.0000000	1.0000000	1.0000000
$(a, 0, 10a)$	Present	-0.0170740	0.0000000	1.0000094	1.0000094
	[104]	-0.0170740	0.0000000	1.0000094	1.0000094
C	Analytic	0.0000000	-0.0670588	1.0000000	1.0000000
$(0, 1.5a, 10a)$	Present	0.0000000	-0.0670600	1.0000008	1.0000008
	[104]	0.0000000	-0.0670600	1.0000008	1.0000008
D	Analytic	-0.0164706	-0.0670588	1.0000000	1.0000000
$(a, 1.5a, 10a)$	Present	-0.0164714	-0.0670579	0.9999987	0.9999987
	[104]	-0.0164714	-0.0670579	0.9999987	0.9999987
E	Analytic	-0.0318182	-0.1295455	1.0000000	1.0000000
$(a, 1.5a, 5a)$	Present	-0.0318332	-0.1295392	1.0000002	1.0000002
	[104]	-0.0318332	-0.1295392	1.0000002	1.0000002
Center	Analytic	0.0000000	0.0000000	1.0000000	1.0000000
$(0, 0, 5a)$	Present	0.0000000	0.0000000	1.0000107	1.0000107
	[104]	0.0000000	0.0000000	1.0000107	1.0000107

elements at each lateral side and 1 element at each extreme section, has been used. Tension has been applied at the extreme sections whereas the lateral sides have been traction free.

Numerical results in displacements and stresses at the points indicated in Fig. 9.2(a) are presented in Table 9.5 and compared with analytic values. Numerical solutions, in displacements and stresses, obtained by expressions of U_{ik} and T_{ik} from Section 9.2 and from Reference [104] are coincident up to all 8 digits presented. The maximum normalized errors are 0.00004 in stresses and 0.0004 in displacements.

Example 3

A transversely isotropic prismatic rod, with elastic properties defined by (9.54), subjected to a shear load is considered, see Fig. 9.2(b). The orientation of the coordinate system associated to the material is defined by the transformation matrix [104]:

$$\boldsymbol{Q} = \begin{pmatrix} +0.7500 & +0.4330 & +0.5000 \\ -0.2403 & +0.8827 & -0.4040 \\ -0.6162 & +0.1828 & +0.7660 \end{pmatrix}. \tag{9.55}$$

A BEM model of 10 elements, 2 at each lateral side and 1 at each extreme section, is applied. Due to the lack of symmetry and in order to avoid rigid body movements, displacements are prescribed at central points of each side except for the front ($x_1 = -\frac{a}{2}$) and back ($x_1 = \frac{a}{2}$)sides. Results in displacements at the points indicated in Fig. 9.2(b) are presented in Table 9.6. Both numerical solutions are coincident up to all 8 digits shown, the maximum normalized error, achieving the value 0.0009, which confirms the correctness of the theoretical formulas used.

Table 9.6: Results of Example 3, transversely isotropic rod under tangential stress.

Point	Result	u_1/u_3^e	u_2/u_3^e	u_3/u_3^e
A	Analytic solution	0.0990792	-0.1503137	1.0000000
$(-0.5a, -2.5a, 3a)$	Present solution	0.0990123	-0.1504005	1.0000161
	Solution using [104]	0.0990123	-0.1504005	1.0000161
B	Analytic solution	-0.5089075	-0.4758082	1.0000000
$(0.5a, 0, 3a)$	Present solution	-0.5084558	-0.4762378	1.0002009
	Solution using [104]	-0.5084558	-0.4762378	1.0002009
C	Analytic solution	0.1100334	-0.1669323	1.0000000
$(0.5a, 2.5a, 3a)$	Present solution	0.1101208	-0.1668616	0.9999395
	Solution using [104]	0.1101208	-0.1668616	0.9999395
D	Analytic solution	0.0679538	-0.1937795	1.0000000
$(0.5a, -2.5a, 1.5a)$	Present solution	0.0679590	-0.1937762	1.0000484
	Solution using [104]	0.0679590	-0.1937762	1.0000484
E	Analytic solution	0.0717356	-0.2045640	1.0000000
$(-0.5a, 2.5a, 1.5a)$	Present solution	0.0717414	-0.2045603	1.0000571
	Solution using [104]	0.0717414	-0.2045603	1.0000571

9.4 Validation of the HBIE kernels

The primary means of providing confidence in the correctness of the expressions of the Stress Integral Equation fundamental solutions, tensors D_{ijk} and S_{ijk}, deduced in the present work and also of their implementation in the present 3D BEM code will be their application in the numerical solution of σ-BIE (7.14) for internal points.

Numerical results for problems in transversely isotropic elastic solids having known analytic solutions [101], coinciding with some material properties solved by other authors [104, 179] except for the case with $\triangle < 0$ where no previous numerical results by other authors have been found in the literature, will be studied.

For the purpose of comparison with D_{ijk} and S_{ijk} expressions presented in Section 9.2, the expression of D_{ijk} due to Loloi [104] and an explicit expression of S_{ijk} deduced, starting from Loloi's expression of U_{ik} have also been implemented in the BEM code. Due to the results obtained using both solutions were exactly the same up to 8 digit considered in the different cases, the results are shown in form of normalized errors between the numerical and analytical solution given by (9.56) for displacements and stresses respectively.

$$err(u_i) = \frac{u_i^n - u_i^a}{u_N^a} \qquad err(\sigma_i) = \frac{\sigma_{ij}^n - \sigma_{ij}^a}{\sigma_N^a} \tag{9.56}$$

where u_i^n and u_i^a are numerical and analytical displacement in direction i, σ_{ij}^n and σ_{ij}^a are numerical and analytical ij stresses, and u_N^a and σ_N^a are nominal (maximum value in the domain of the problem) analytical displacement and stress respectively.

Example 4

A prismatic rod subjected to an axial load is considered. The elastic properties used in this example are shown in Table 9.7.

The plane of isotropy is inclined 45^o with respect to the plane x_1x_2 which coincides with one rod base. A BEM model of one-fourth of the rod, symmetry boundary conditions have been considered at the planes x_1x_3 and x_2x_3, with 10 elements, 2 elements at each lateral side and 1 element at each extreme section, has been used. Tension has been applied at the extreme sections whereas the lateral sides have been traction free, Fig. 9.3(a).

The numerical solution for some points obtained using the expressions deduced in the present work and those resulting from Loloi [104] imple-

Table 9.7: Elastic properties considered in Example 4, values given in 10^6 psi.

Constants	Material No. 1 ($\triangle > 0$)	Material No. 2 ($\triangle = 0$)	Material No. 3 ($\triangle < 0$)
C_{11}	15.73	49.40	23.35
C_{12}	6.50	34.60	4.96
C_{13}	4.44	9.70	7.27
C_{33}	7.78	38.10	8.85
C_{44}	2.00	16.84	5.55

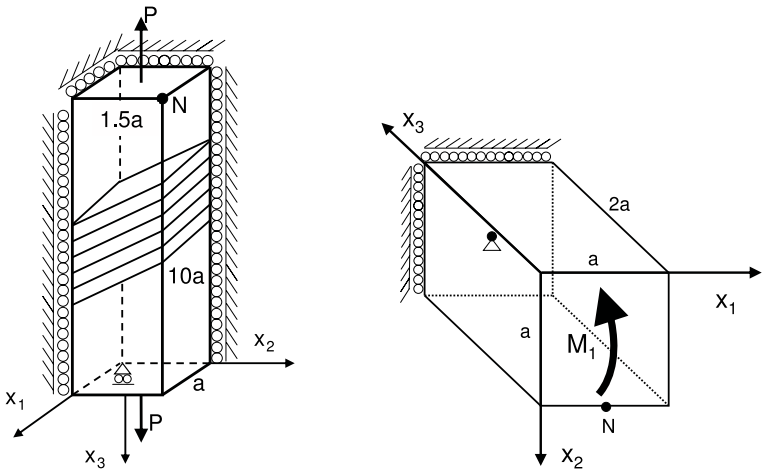

(a) (b)

Figure 9.3: Transversely isotropic problem configuration (a) with an inclined plane of isotropy for Example 4 and (b) with the plane of isotropy perpendicular to axis 3 for Example 5

mented in the present BEM code were coincident up to the 8 digits considered in the displacements and stresses solution. The differences between numerical results and analytic solution are almost negligible, as could be expected from the character of the analytic solution, linear in displacements and constant in stresses. The normalized errors are presented for the Materials 1 and 2 in Tables 9.8-9.11. An analogous conclusion is also valid for

Table 9.8: Normalized displacement errors of Example 4, transversely isotropic rod under axial tension. Material No. 1($\triangle > 0$)

Point (x,y,z)	$err(u_1)$	$err(u_2)$	$err(u_3)$
A (0.4a,0.5a,3a)	-3.89(-7)	-2.57(-6)	-3.42(-6)
B (0.4a,a,3a)	-9.17(-7)	-3.78(-6)	-2.69(-7)
C (0.6a,0.5a,3a)	-2.23(-7)	-2.29(-6)	-3.36(-6)
D (0.6a,a,3a)	-5.65(-7)	-3.41(-6)	-3.20(-7)

Table 9.9: Normalized stress errors of Example 4, transversely isotropic rod under axial tension. Material No. 1($\triangle > 0$)

Point (x,y,z)	$err(\sigma_{11})$	$err(\sigma_{22})$	$err(\sigma_{33})$	$err(\sigma_{23})$	$err(\sigma_{13})$	$err(\sigma_{12})$
A	2.42(-6)	-3.56(-5)	-1.18(-5)	4.43(-5)	-1.27(-5)	1.53(-5)
B	5.22(-6)	-5.77(-5)	-3.50(-5)	4.76(-5)	1.51(-5)	-2.10(-5)
C	1.02(-5)	-3.14(-5)	-8.68(-6)	4.21(-5)	5.23(-6)	1.57(-5)
D	1.35(-5)	-5.04(-5)	-3.02(-5)	4.51(-5)	-8.68(-6)	4.36(-6)

Table 9.10: Normalized displacement errors of Example 4, transversely isotropic rod under axial tension. Material No. 2($\triangle = 0$)

Point (x,y,z)	$err(u_1)$	$err(u_2)$	$err(u_3)$
A (0.4a,0.5a,3a)	-3.38(-5)	-5.57(-6)	6.37(-5)
B (0.4a,a,3a)	-4.43(-5)	-8.79(-6)	1.56(-5)
C (0.6a,0.5a,3a)	-4.12(-5)	-1.60(-6)	6.19(-5)
D (0.6a,a,3a)	-5.10(-5)	-3.71(-6)	1.59(-5)

Material 3, errors being shown in Tables 9.12 and 9.13, where only the results obtained using the expressions of D_{ijk} and S_{ijk} introduced in Section 9.2 are shown, as complex variable expressions of U_{ik} are given for materials with $\triangle < 0$ in Loloi [104].

Table 9.11: Normalized stress errors of Example 4, transversely isotropic rod under axial tension. Material No. 1($\triangle = 0$)

Point (x,y,z)	$err(\sigma_{11})$	$err(\sigma_{22})$	$err(\sigma_{33})$	$err(\sigma_{23})$	$err(\sigma_{13})$	$err(\sigma_{12})$
A	-2.33(-5)	-2.26(-5)	-1.78(-4)	-6.31(-5)	2.04(-5)	4.09(-5)
B	-3.34(-5)	-6.65(-5)	-7.32(-5)	-6.39(-5)	-1.59(-5)	-3.76(-5)
C	-2.34(-6)	-1.22(-5)	-1.75(-4)	-6.24(-5)	-5.04(-6)	4.71(-5)
D	-1.14(-5)	-4.79(-5)	-7.38(-5)	-6.24(-5)	9.66(-6)	-1.11(-5)

Table 9.12: Normalized displacement errors of Example 4, transversely isotropic rod under axial tension. Material No. 2($\triangle < 0$)

Point (x,y,z)	$err(u_1)$	$err(u_2)$	$err(u_3)$
A (0.4a,0.5a,3a)	-3.90(-6)	5.48(-5)	-8.55(-5)
B (0.4a,a,3a)	1.54(-5)	7.40(-5)	-8.64(-5)
C (0.6a,0.5a,3a)	-2.98(-6)	5.00(-5)	-8.51(-5)
D (0.6a,a,3a)	1.24(-5)	6.63(-5)	-8.60(-5)

Table 9.13: Normalized stress errors of Example 4, transversely isotropic rod under axial tension. Material No. 1($\triangle < 0$)

Point (x,y,z)	$err(\sigma_{11})$	$err(\sigma_{22})$	$err(\sigma_{33})$	$err(\sigma_{23})$	$err(\sigma_{13})$	$err(\sigma_{12})$
A	1.43(-4)	3.34(-4)	-7.01(-6)	-7.13(-5)	-1.64(-6)	3.01(-5)
B	-2.31(-5)	8.58(-4)	2.05(-4)	-2.63(-4)	-8.80(-5)	3.00(-4)
C	6.78(-5)	2.32(-4)	-4.19(-5)	-5.63(-5)	4.89(-5)	-1.98(-4)
D	-8.63(-5)	7.65(-4)	1.72(-4)	-2.44(-4)	2.50(-5)	-5.38(-5)

Example 5

A homogeneous bar in the form of a prism, Fig. 9.3(b), is deformed by a bending moment acting in the principal plane x_2x_3. The elastic properties in the material coordinate system are defined by:

$$E/E' = 2.0, \quad E/\mu' = 7.0, \quad \nu = 0.2, \quad \nu' = 0.3, \tag{9.57}$$

where E and ν are Young elastic modulus and Poisson ratio associated to the isotropy plane, E' is the Young modulus along the rotational-symmetry

axis, and μ' and ν' are the shear modulus and Poisson ratio at the planes perpendicular to the plane of isotropy. A BEM model of the beam, with 112 elements, 20 elements at each lateral side and 16 elements at each extreme section, has been used. The bending moment M_1 has been applied at one extreme section ($x_3 = 0$), whereas the other extreme was restricted in displacements ($u_3 = 0$ for $x_3 = 2a$) and the lateral sides have been considered as traction free.

Table 9.14: Normalized displacement errors of Example 5, transversely isotropic bar deformed by bending moments.

Point (x,y,z)	$err(u_1)$	$err(u_2)$	$err(u_3)$
A (0.25a,0.25a,0.1a)	-8.05(-7)	-4.68(-6)	-2.80(-5)
B (0.9a,0.9a,0.1a)	1.92(-6)	-6.07(-7)	-3.58(-5)
C (0.25a,0.25a,0.2a)	-8.17(-7)	-5.43(-6)	-2.94(-5)
D (0.9a,0.9a,0.2a)	2.26(-6)	-7.28(-7)	-3.92(-5)
E (0.25a,0.25a,a)	1.41(-6)	-2.39(-5)	-2.39(-5)
F (0.9a,0.9a,a)	9.10(-6)	-5.30(-6)	-9.54(-5)

Table 9.15: Normalized stress errors of Example 5, transversely isotropic bar deformed by bending moments.

Point (x,y,z)	$err(\sigma_{11})$	$err(\sigma_{22})$	$err(\sigma_{33})$	$err(\sigma_{23})$	$err(\sigma_{13})$	$err(\sigma_{12})$
A	-2.36(-6)	1.66(-5)	5.95(-5)	7.97(-5)	-6.13(-6)	1.73(-5)
B	1.83(-5)	-1.38(-5)	1.30(-4)	-8.31(-6)	-6.69(-5)	3.39(-6)
C	-3.44(-6)	2.13(-5)	5.86(-5)	9.52(-5)	-8.67(-6)	2.14(-5)
D	2.24(-5)	-1.74(-5)	1.47(-4)	-1.02(-5)	-8.00(-5)	4.39(-6)
E	-6.03(-5)	1.93(-4)	-2.54(-4)	5.14(-4)	-1.40(-4)	1.50(-4)
F	1.64(-4)	-1.22(-4)	5.24(-4)	-1.06(-4)	-4.58(-4)	5.36(-5)

The normalized errors from numerical results in both displacements and stresses for points indicated in Tables 9.14 and 9.15 are presented. Numerical solutions, in stresses, obtained by expressions of D_{ijk} and S_{ijk} from the present work and from the Reference [104] are coincident up to all 8 digits used.

Example 6

In the previous examples, the validity and accuracy of the fundamental solution and its derivatives for transversely isotropic materials has been established. The present example is an application where the present fundamental solution and the BEM can be used.

A three-dimensional model of the proximal tibia of the human knee is described. The geometry is generated via a wireframe structure constructed using three-dimensional reconstruction of Computarized Tomographies and Magnetic Resonance Imaging [121].

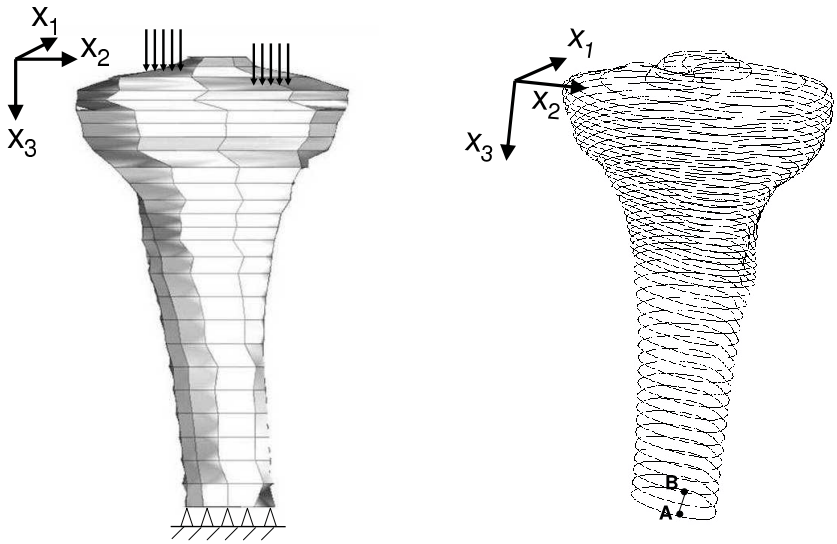

(a) (b)

Figure 9.4: BEM tibia model used in Example 6: (a) mesh and boundary conditions and (b) wireframe view.

The elastic properties in the material coordinate system are defined by:

$$E = 11.5, \quad E' = 17.0, \quad \mu' = 3.28, \quad \nu = 0.58, \quad \nu' = 0.31, \tag{9.58}$$

where E, E' and μ' are given in GPa [142]. The orientation of the coordinate system associated to the material is defined in a way that the axis x_3 coincide with the largest part of the bone Fig. 9.4(a). The described model cover a

portion up to 135 mm below the plateau of the tibia and is taken as a solid composed only of compact bone as solved by Müller *et. al.* [121].

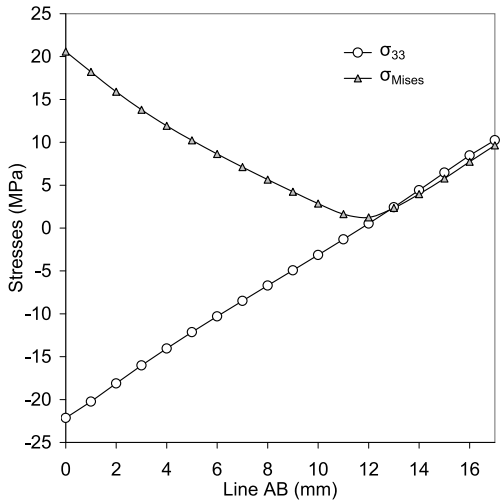

Figure 9.5: Stress progression in line AB show in Fig. 9.4.

A BEM model of 223 elements is used. The load condition applied occurs during normal gait at the stance phase in near full extension with a magnitude of 2450 N.The loaded nodal points covered areas approximately equal to the following contact areas of 468 mm^2 (medial condyle) and 297 mm^2 (lateral condyle). The compressive force was distributed over the nodes at the tibia condyles as a constant distributed force. The stress results indicate compressive and tensile stress developing from the anterior to the posterior part of the model, this behavior is represented in Fig. 9.5 where the stress progression obtained in line AB Fig. 9.4(b) it is shown, with $\sigma_{33} = -22.14$ MPa and $\sigma_{Mises} = 20.57$ MPa at A and $\sigma_{33} = 10.25$ MPa and $\sigma_{Mises} = 9.65$ MPa at B, all the points are positioned in a plane 3.5 mm above the distal end in x_3 direction and are distanced 1 mm among them. Point A and B are also distanced 1 mm from the lateral surface.

The compressive behavior of the anterior part of the tibia is shown in Fig. 9.6 where points distanced 1 mm from the lateral surface where taken starting from the point A mentioned above. Also the tensile progression of the posterior part of the model is shown in Fig. 9.7 there the points are distanced 1 mm from the lateral surface but starting from B. These results are in accordance to those obtained in [121]. Notice that, this example is just to show the capability of the 3D BEM code to solve application

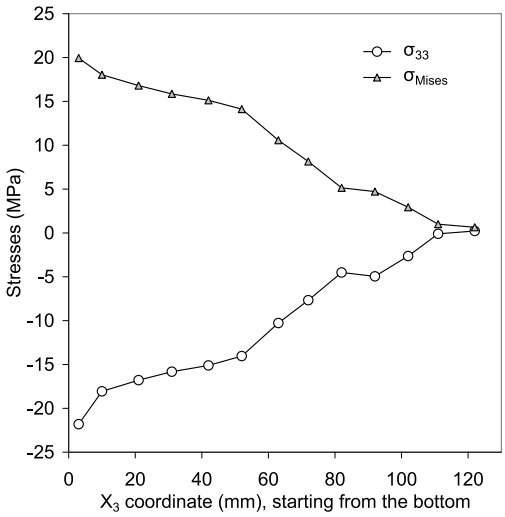

Figure 9.6: Compressive behavior at 1mm from the lateral surface starting from point A of the anterior part of the tibia trough its largest part.

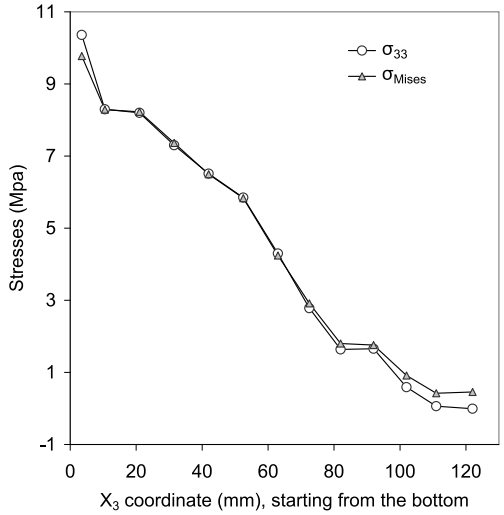

Figure 9.7: Tensile behavior at 1mm from the lateral surface starting from point B of the posterior part of the tibia trough its largest part.

problems, further studies are necessary in order to get an actual behavior of the human knee. Next steps could involve to consider the hole inside the bone and considering the bone to have different material properties.

9.5 Concluding remarks

The present chapter, introduces new closed-form expressions of the integral kernels $T_{ik}(\boldsymbol{x})$, $D_{ijk}(\boldsymbol{x})$ and $S_{ijk}(\boldsymbol{x})$ appearing in the Somigliana displacement and traction identity for transversely isotropic elastic materials, and also of the related integral kernels $U_{ik,j}(\boldsymbol{x})$, $U_{ik,jl}(\boldsymbol{x})$, $\Sigma_{ijk}(\boldsymbol{x})$ and $\Sigma^{loop}_{ijkl}(\boldsymbol{x})$.

The novel approach developed recently by Ting and Lee [167] gave as a result a closed-form expression of the fundamental solution $U_{ik}(\boldsymbol{x})$ for transversely isotropic materials with the following unique features: *i)* completely general and unique expressions valid for all possible configurations of material and relative positions of the source and field points; *ii)* given by means of real functions (no difficulties with using complex functions with complex arguments which may require keeping values in the same branch when multivaluedness arises as in the expressions obtained from the potential theory [104, 129] in the case $\triangle < 0$, see (9.3)); *iii)* continuous transition with respect to a variation of material properties (the expressions obtained from the potential theory approach [104, 129] require two distinct expressions for the cases $\triangle \neq 0$ and $\triangle = 0$); *iv)* continuous transition with respect to relative positions of the source and field points (the sign function was introduced in the $U_{ik}(\boldsymbol{x})$ expression obtained from the potential theory [104] to cover both cases where $\phi \to 0$ or π); *v)* a straightforward and efficient implementation in a BEM code. These features have been kept by the new closed-form expressions of $T_{ik}(\boldsymbol{x})$, $D_{ijk}(\boldsymbol{x})$ and $S_{ijk}(\boldsymbol{x})$, and its related kernels $U_{ik,j}(\boldsymbol{x})$, $U_{ik,jl}(\boldsymbol{x})$, Σ_{ijk} and Σ^{loop}_{ijkl} obtained in the present chapter working from the expression of $U_{ik}(\boldsymbol{x})$ due to Ting and Lee [167], after a revision of their final formula. These expressions of $U_{ik}(\boldsymbol{x})$, $T_{ik}(\boldsymbol{x})$, $D_{ijk}(\boldsymbol{x})$ and $S_{ijk}(\boldsymbol{x})$ have been implemented in a 3D collocational BEM code and verified numerically by solving several examples with known analytic solution, high accuracy results being obtained in all cases. All three cases with positive, zero and negative $\triangle$ have been solved, previous BEM results by other authors for the case $\triangle < 0$ not being known in the literature. This work also represents, the first numerical verification of the correctness of the novel expression of U_{ik} due to Ting and Lee [167]. It should also be pointed out that the new closed-form expressions for the tractions and stresses originated by a unit point force in the infinite transversal isotropic space, T_{ik} and Σ_{ijk}, can also be used in the context of the theory of dislocations [30, 86, 105, 178] where T_{ik} have a work-conjugated interpretation of the displacements originated by a unit infinitesimal dislocation loop in this space. Similarly, Σ^{loop}_{ijkl} can be interpreted as the stress tensor originated by a unit infinitesimal dislocation loop.

Chapter 10

Interlaminar fracture toughness test of composite materials

In the present chapter the interlaminar fracture toughness, G_{Ic}, test of composite materials is modeled by means of the Linear Elastic-Brittle Interface (LEBI) introduced in Chapter 4. The non-linear algorithm used is the sequentially linear analysis implemented in a 2D collocational BEM code. The LEBI model seems to reproduce very well the behavior of thin adhesive layers in a single model problem, as shown in Chapter 8. In this chapter, it will be shown that LEBI model is also able to simulate the behavior (and/or failure) of real structures.

10.1 Laboratory test and specimen description

The tests used in the aeronautical industry to evaluate the interlaminar fracture toughness in composite-composite joints are performed by well-known standard procedures [2, 87].

The specimen used is the Double Cantilever Beam (DCB) shown in Fig. 10.1(a). The DCB specimen is formed by two laminates joined by a thin adhesive layer. The laminates are processed according to EN 2565 standard, and the specimens are cut after the panel has been cured. The specimen is connected to the grips of a universal testing machine through small tabs bonded to laminates, as shown in Fig. 10.1(b). The load, P, and the relative displacement, d, of the wedge grips are continuously registered during crack propagation, Fig. 10.1(c).

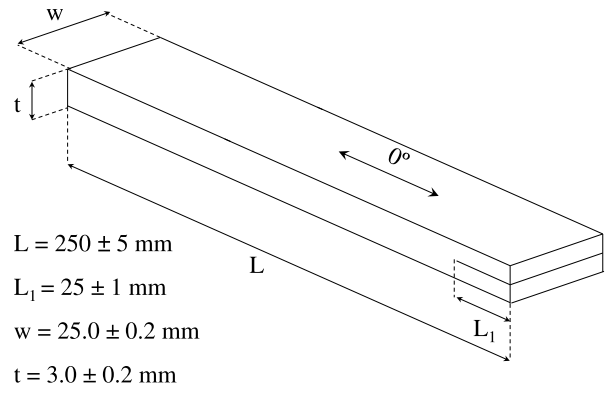

(a)

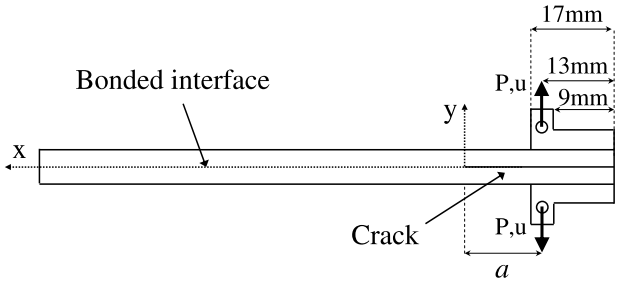

(b)

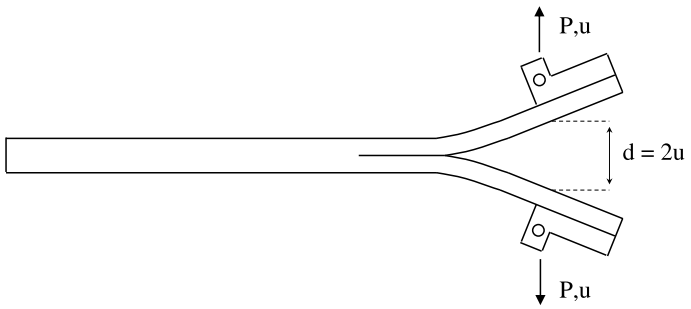

(c)

Figure 10.1: (a) Scheme of the DCB specimen, (b) DCB specimen with bonded tabs, (c) test configuration.

In a study of the experimental results obtained from G_{Ic} tests and fractographic analysis, using different kinds of adhesive, it was observed that some adhesives like FM 300K0.5 and EA 9695 K.05 presented jumps (non-smooth behavior) in the experimental load-displacement curve. This behavior seems to be explained by the presence of a polyester support in these adhesives [88, 89]

Figure 10.2: Fracture surface of a G_{Ic}-specimen tested with EA 9695 K.05 adhesive.

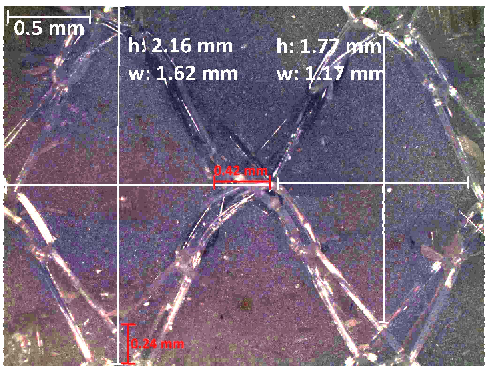

Figure 10.3: Detail of the polyester support of the EA 9695 K.05 adhesive, outer and inner dimensions of the rhombus-like mesh. Picture taken at 50x zoom.

In Fig. 10.2 the fracture surface of a tested G_{Ic} specimen with EA 9695 K.05 adhesive is shown. Clearly visible marks on the specimen fracture surface are related to the jumps appearing in the experimental load-displacement curve. At initial stages, the distance between marks is shorter than at further stages, resulting from larger jumps. In Fig. 10.3 a detailed picture, taken at 50x zoom, of the polyester support of the adhesive is shown.

10.2 Numerical results

In this example, a simulation of the interlaminar fracture toughness test according to ISO 15024 [87] is going to be carried out. In the present numerical study, a plane strain model has been solved assuming the hypothesis of small strains using the BEM code described in Subsection 5.5.1. The laminate considered is an 8552/AS4 carbon fibre - epoxy composite (having only 0^o plies), with the following orthotropic properties: E_x=135GPa, E_y=10GPa, E_z=10GPa, G_{xy}=5GPa, G_{xz}=5GPa, ν_{xy}=0.3, ν_{yz}=0.4 and ν_{xz}=0.3. The adhesive used is EA 9695 K.05, an epoxy adhesive with a polyester mesh support. The properties estimated for the LEBI constitutive law are: k_n=150GPa/m, σ_c =15MPa and δ_{nc}=0.1mm, corresponding to a value of G_{Ic} = 750 Jm^{-2}, see Fig. 4.4. Due to the symmetry of the problem there are not tangential relative displacements, thus the tangential part of the LEBI law does not play an important factor in this problem.

Load P was progressively applied at both laminates in the direction normal to the specimen boundary at a the distance of 13mm from the extreme where the initial crack is situated, see Fig. 10.1(b). Two point supports were defined at the left-hand extreme of the specimen, Fig. 10.1(b,c), to remove the rigid body motion in the displacement solution by the use of the method described in [22].

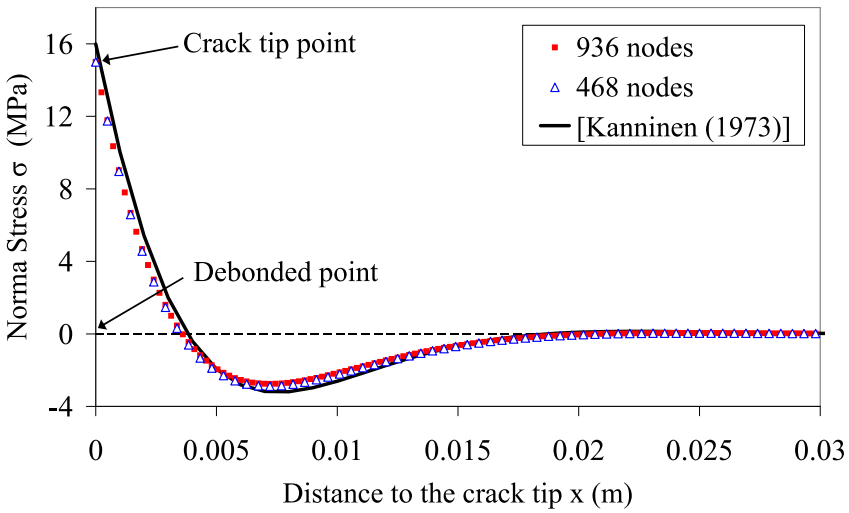

Figure 10.4: Normal stresses σ near the crack tip along the bonded zone, for a load step with P=29.7N, d=35.4mm and a=146.6mm.

The normal stresses along the bonded zone obtained in a load step corresponding to the decreasing part of the load-displacement curve with P=29.7N, d=0.0354m and a=146.6mm (using two different meshes), are shown in Fig. 10.4. The initial length of the adhesive layer (225 mm) is discretized by means of 468 (coarse mesh) or 936 (fine mesh) linear elastic-brittle interface elements placed on the upper and bottom sides of the interface. As can be observed in Fig. 10.4, a very accurate solution has already been obtained by the coarse mesh. The corresponding analytical solution of Strength of Materials for a beam on Winkler elastic-foundation deduced in [90][1] (Eq. 4 therein) has also been included in Fig. 10.4. The agreement between this analytic solution and the present BEM solution is good, significant differences being observed only in the zone close to the crack tip, as could be expected.

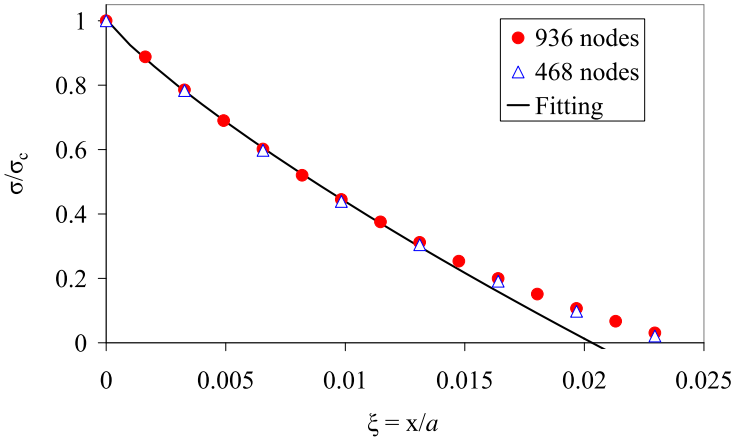

Figure 10.5: Fitting of the BEM normalized local stress solution by analytic expression (10.2), for a load step with P=29.7N, d=35.4mm and a=146.6mm.

In view of Lenci's [102] expression (8.17) for the local normal stresses along the bonded interface part close to the crack tip in a particular problem, and taking into account a general singularity analysis of a crack in presence of spring boundary conditions in [158], it appears that the first terms in the asymptotic expansion of the normal stresses take the form:

$$\frac{\sigma}{\sigma_c} = c_0 + c_1 \xi \left[\ln(\xi) + c_2\right], \quad \text{for} \quad \xi \to 0_+. \tag{10.1}$$

[1] In the present orthotropic case the parameter λ in [90] is defined as $\lambda^4 = \frac{6k_n}{E_x(t/2)^3}$.

Thus, these stresses are bounded, but their gradient has a logarithmic singularity at the crack tip. In this sense, it is noteworthy that the local numerical BEM solution for normal stresses in the present G_{Ic} specimen near the crack tip fits this expression very well. In Fig. 10.5, the normalized stresses σ/σ_c represented as a function of ξ are compared with the following fitted expression:

$$\frac{\sigma}{\sigma_c} = 1.0038 + 9.9132\xi\,[\ln(\xi) - 1.0991] \tag{10.2}$$

obtained from (10.1) by applying the least square method to the first nodes with $\xi < 0.012$. An excellent agreement between the BEM solution and the fitted asymptotic expression can be observed, and in addition to $c_0 \cong 1$ also $c_2 \cong -1$ in agreement with (8.17). Notice that this asymptotic behavior is applicable for the local solution near the crack tip only.

The deformed shape obtained for the same load step as defined before is depicted in Fig. 10.6(a). A detailed view of the deformed shape obtained with the BEM code is shown in Fig. 10.6(b). The different zones where the LEBI elements are broken, and where the elements are subjected to tensile or compressive normal stresses, are clearly indicated in the plot.

10.3 Experimental and numerical load - displacement diagrams

In Fig. 10.7 the load-displacement diagrams obtained experimentally (directly measured by the universal testing machine) and numerically (by means of BEM) at the points indicated in Fig. 10.1(c). G_{Ic} value employed in the numerical simulation ($G_{Ic} = 750$ Jm^{-2}) is obtained from the experimental test.

The most important result is that the model is able to catch the failure load as well as the energy dissipated during the debonding process, by means of a unique critical parameter (G_{Ic} or, equivalently, σ_c see (4.17)) together with the stiffness parameter k_n. As can be observed in Fig. 10.7, the numerical results obtained provide a good approximation of the experimental results. Therefore, the use of the LEBI formulation seems to be a promising approach to model composite adhesive joints. It is important to mention that in the experimental curve an unloading and a reloading are done because the laboratory standard required them; this behavior was not simulated due to its irrelevant effect on the numerical solution.

Changing the non-linear conditions node by node can make the crack

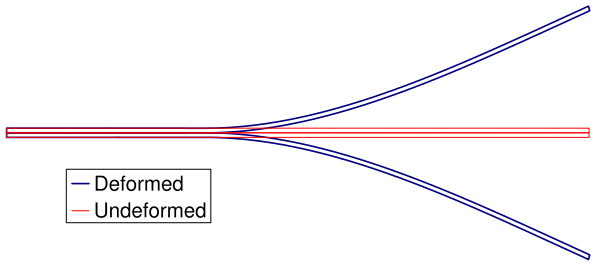

(a)

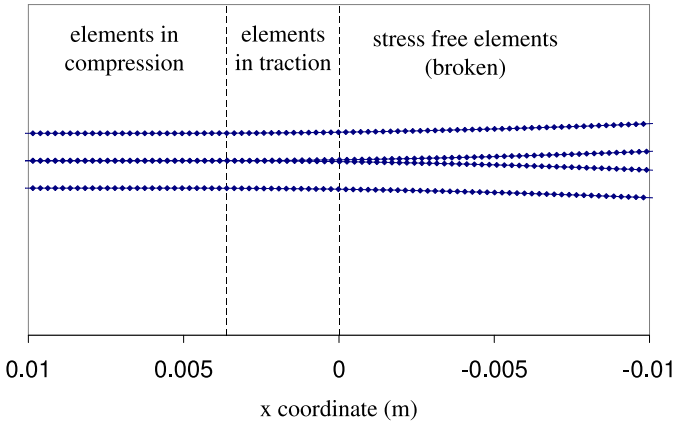

(b)

Figure 10.6: (a) Numerical deformed shape obtained, and (b) detail of the deformed shape at the vicinity of the crack tip of the modeled G_{Ic} test.

propagation very smooth (especially for fine meshes), in contrast with the experimental evidence found in some industrial adhesives that show crack growth by small but clearly finite jumps. For this specific kind of adhesive (especially the ones that have a "knife" kind of support, see Fig. 10.2) the end of a load step can be defined by a situation where the normal and tangential stiffnesses of a fixed number of consecutive nodes are set to zero. This number of nodes are related to the size of the rhombus-like mesh support of the adhesive, Fig. 10.3, and the marks observed in the experimental results, Fig. 10.2. In the results shown in Fig. 10.7, in the

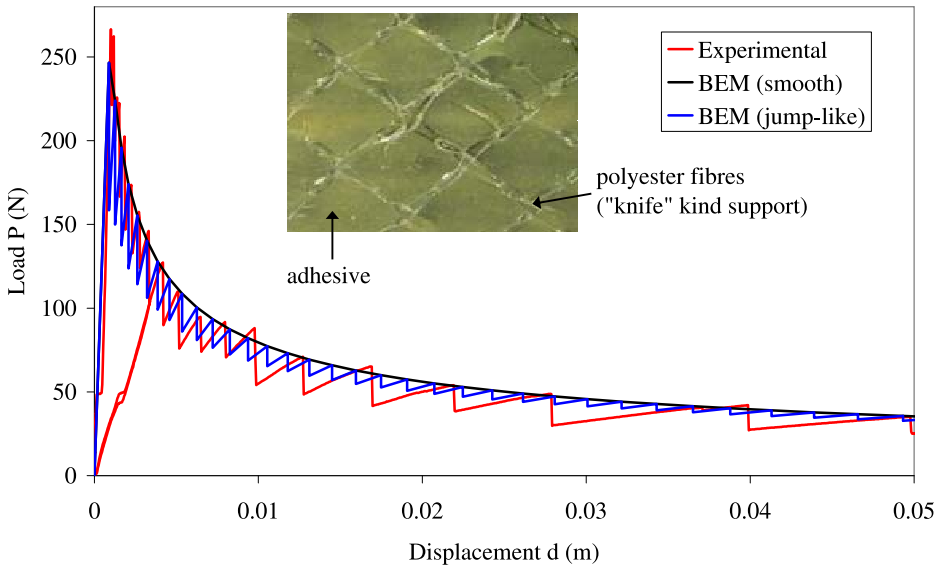

Figure 10.7: Comparison between the experimental and numerical load - displacement diagrams of the G_{Ic} test and a detail of the polyester support of the adhesive used.

jump-like curve obtained, 15 nodes were opened in each load step, which corresponds to approximately 5 times half of the width of a rhombus and also corresponds to the first distances between marks, Fig. 10.2. As can be seen from the BEM results, the jumps remain constant while the jumps in the experimental results become larger.

10.4 Non-symmetric DCB specimen

In order to see the capability of the mixed mode failure criterion proposed in Section 4.2, a non-symmetric DCB specimen has been studied numerically. The composite laminate and adhesive layer are assumed to have the same properties as in the previous section. The geometry of the specimen is almost the same as that depicted in Fig. 10.1, except for the thickness of the laminates taken as $t/2$ and t (one laminate two times thicker than the other). In Fig. 10.8 the global load - displacement response is shown, and compared with the previously studied symmetric DCB specimen. As can be seen, the failure load necessary to start the crack growth is a little higher.

In Fig. 10.9 the deformed shape obtained is shown for a load step with P=46.48N, d=45.8mm and a=134.6mm.

Although not shown in the plots, another important effect, resulting from the lack of symmetry, is the presence of tangential stresses along the interface, leading to values of the fracture mode mixity angle ψ_G in the following interval $7.15° < \psi_G < 9.01°$ for 12mm$< a <$ 208mm, when the fracture mode-sensitivity parameter $\lambda = 0$.

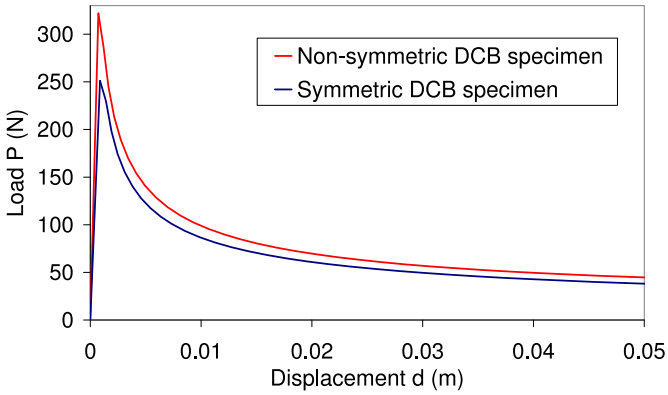

Figure 10.8: Numerical load - displacement diagrams for a symmetric and non-symmetric DCB specimen (bonded joint).

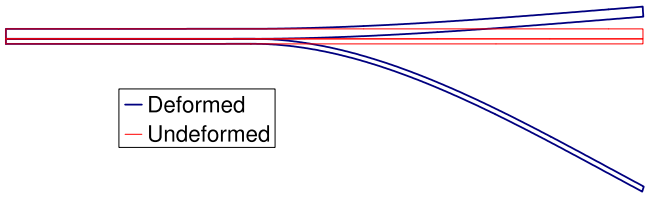

Figure 10.9: Numerical deformed shape obtained for a non-symmetric DCB specimen (bonded joint).

10.5 Concluding remarks

As shown by the numerical results presented in the previous section, the LEBI formulation modeled by a spring distribution correctly describes the behavior of adhesive joints used in the aeronautical industry. From laboratory tests and fractographic analysis it has been concluded that the jumps appearing in the experimental load - displacement curve are caused by the polyester support of the adhesive resin. The experimental and numerical

comparison presented in Section 10.3 corresponds to opening mode I due to symmetry configuration of the specimen. Nevertheless, the present implementation of the LEBI model allows for a similar analysis of non-symmetric configurations of bonded adhesive joints leading to a mixed fracture mode as studied numerically in Section 10.4. It has been proved that the real behavior of an adhesive layer with a polyester support that joins two unidirectional laminates can be approximated very well by means of BEM and a distribution of LEBI elements, by adjusting the parameters of the discrete model (k_n, σ_c, and the number springs that break in a load step). This fact will make it possible to predict the real behavior of structures that include similar adhesive joints by the model developed here.

Noteworthy, in accordance with the model used, is the bounded character of stresses along the LEBI interface, the maximum value of stresses being achieved at the crack tip. The interface constitutive law introduced and included in the incremental algorithm of the BEM code has the advantage of being independent of the number of elements used in the interface. An analytic expression for the local solution of normal tractions at the crack tip, deduced in the singularity analysis of the weak interface by Lenci [102] in a particular problem for isotropic half-planes, has been successfully compared with the present numerical solution for orthotropic laminates.

Chapter 11

Delamination cracks in [0/90] symmetric laminates

In the present chapter the problem of delamination cracks in [0/90] symmetric laminates of composite materials is modeled by means of the Linear Elastic-Brittle Interface (LEBI) model, introduced in Chapter 4. The non-linear algorithm used is the sequentially linear analysis, proposed in Section 6.2, and implemented in a 2D collocational BEM code.

11.1 Description of the problem

The problem analyzed in this chapter is shown in Fig. 11.1. It represents a [0/90]s laminate under tensile loading in the direction of the 0° fibres, that was solved previously by a means of the BEM and using the Virtual Crack Closure Technique (VCCT) to calculate the Energy Release Rate (ERR) by Blázquez *et. al.* [23, 24] and by París *et. al.* [130].

The first damage in this laminate is expected to be the nucleation and growth of cracks in the 90° ply transverse to the load. When one of these cracks approaches the interface with the 0° ply, it is accepted that it stops. New transverse cracks appear in the 90° ply with increasing load until the crack density reaches a critical value. Transverse matrix cracking in 90° ply leads to a load redistribution in the adjacent 0° plies and induces local stress concentrations at the neighborhood of the crack tips that, when the tips are near to the interface, can involve significant interlaminar delamination, [17, 130].

For the case analyzed in this work, the material systems is a carbon–epoxy (AS4/8552 Hexcel) laminate $[0_3/90_3]_S$, direction 1 being considered the fi-

bre direction: $E_{11} = 45.6$ GPa, $E_{22} = E_{33} = 16.2$ GPa, $\nu_{12} = \nu_{13} = 0.278$, $\nu_{23} = 0.4$, $G_{12} = G_{13} = 5.83$ GPa, $G_{23} = 5.786$ GPa. The half-thickness of the set of 90° plies, t, and the thickness of each of the set of 0° plies is 0.55 mm. The average separation between transverse cracks is taken to be $2L = 4$ mm.

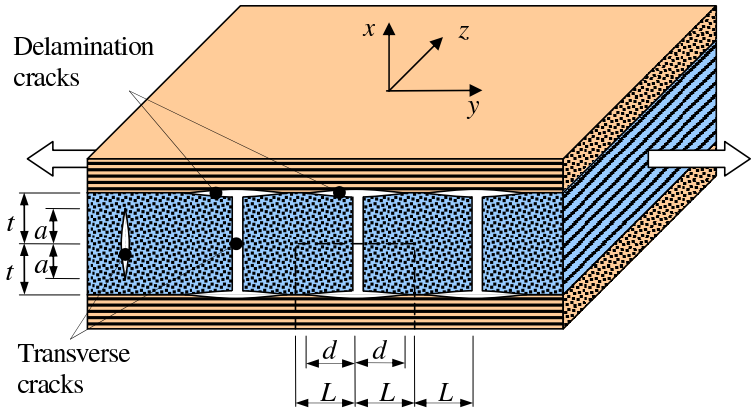

Figure 11.1: Transverse and delamination cracks in [0/90]s laminate, taken from [130].

11.2 Model of the problem

The previously described problem that will be studied, has some usually accepted damage patterns [130], see Fig. 11.2. One having only a transverse crack Fig. 11.2(a) and (b), the second having a transverse crack that has reached the interface with the 0° lamina and has deflected, starting a symmetric delamination Fig. 11.2(c). The third damage pattern shown Fig. 11.2(d) indicates that delamination will start to appear before the transverse crack reaches the interface. This scheme represented in Fig. 11.2(d) is known in Fracture Mechanics as the Cook-Gordon mechanism [44].

As mentioned before, the LEBI model is used to study the present problem. The cases shown in Fig. 11.2 exhibit symmetry (with respect to the horizontal middle plane in the figure), this fact allows us to study the delamination crack growth either using the configuration shown in Fig. 11.3(a) or Fig. 11.3(b). Nevertheless, if we want to study the onset and growth of the transversal crack (modeled using the LEBI model), it is necessary the use

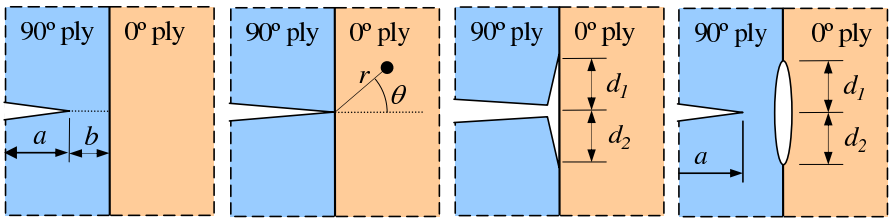

Figure 11.2: Damage configurations considered with a transverse crack: (a) not reaching the interface, (b) terminated at the interface, (c) deflected at the interface, and (d) approaching a damaged interface (mechanism of Cook-Gordon). Slightly modified version of a picture from [130].

of the configuration presented in Fig. 11.3(a) because of the use of interface elements that, in the present implementation, needs the presence of both solids adjacent to the interface.

In the BEM model used to simulate the geometry shown in Fig. 11.3(a) the uniform boundary element mesh has 3860 linear elements, while in the other case (Fig. 11.3(b)) the mesh is formed by 2040 linear elements. In both cases the constant element size is 5μm.

11.3 Numerical results for transverse and delamination cracks

11.3.1 Transverse cracks

As mentioned before, to study the onset and growth of the transverse crack, the geometry shown in Fig. 11.3(a) is used. The LEBI elements have been included at the interface between the 0° ply and 90° ply, and also in the assumed crack path of the transverse crack that could appear in the 90° ply (shown in Fig. 11.3(a) with a dashed line).

The properties of the interfaces at the two positions (transversal or delamination) were considered to be different, see Table 11.1. Two different combinations were used in order to see the influence of the interface properties in the overall behavior of the problem.

Notice that in the first combination the fracture toughness in mode I, G_{Ic}, is considered to be the same in both positions, but the critical stress, $\bar{\sigma}_c$, varies leading to different values of k_n. From Table 11.1, it can be seen

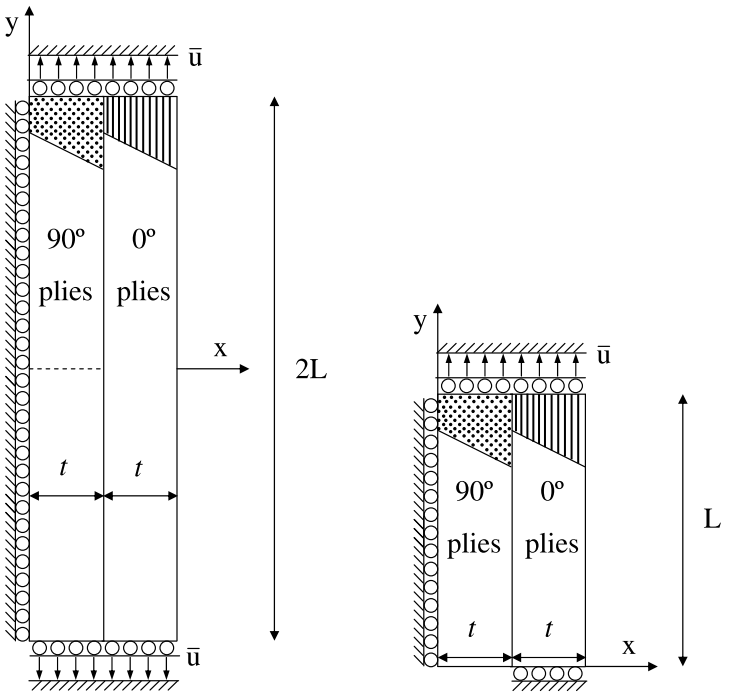

Figure 11.3: Geometry and boundary conditions for the delamination problem in [0/90] symmetric laminates.

Table 11.1: Considered combinations of the interface properties in the delamination problem of [0/90] symmetric laminates.

N°	Position	G_{Ic}(Jm^{-2})	$\bar{\sigma}_c$(MPa)	k_n (MPa/μm)	k_t (MPa/μm)
1	transversal	75	61	24.807	8.269
	delamination	75	90	54	18
2	transversal	75	61	24.807	8.269
	delamination	34.454	61	54	18

that the ratio $k_n/k_t = 3$ is defined for all cases considered. In the second combination G_{Ic} values are considered to be different, but having the same value of $\bar{\sigma}_c$.

In Fig. 11.4 the actual applied average (longitudinal) strain, $\varepsilon = \bar{u}/L$,

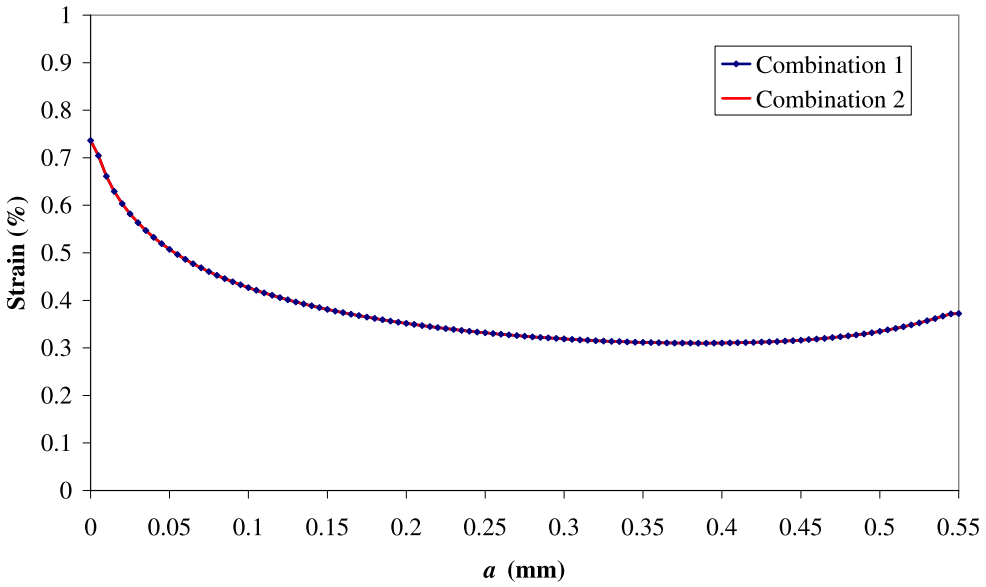

Figure 11.4: Applied strain versus the length of the transverse crack a.

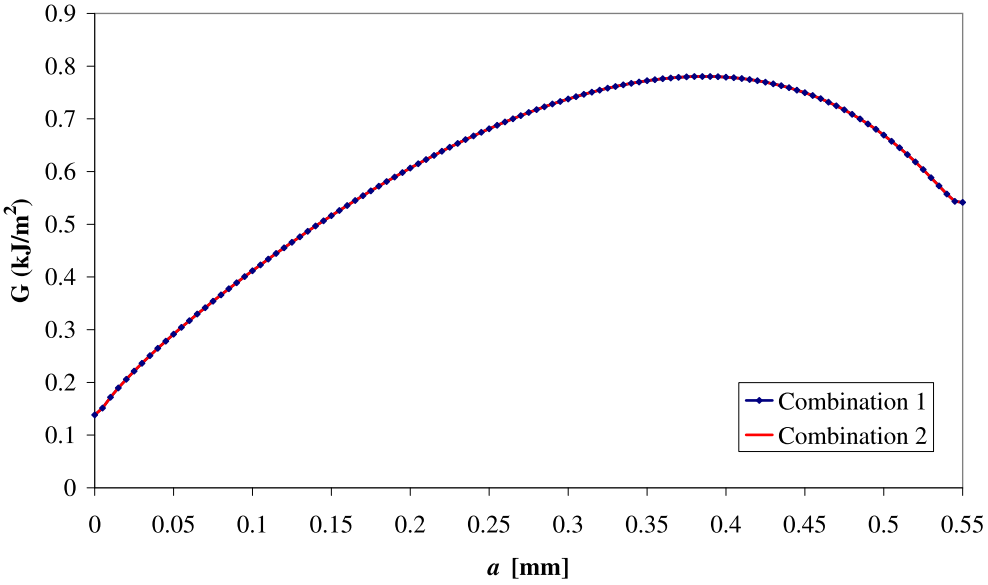

Figure 11.5: Predictions of the ERR (G), for a fixed applied strain of 1%, versus the length of the transverse crack a.

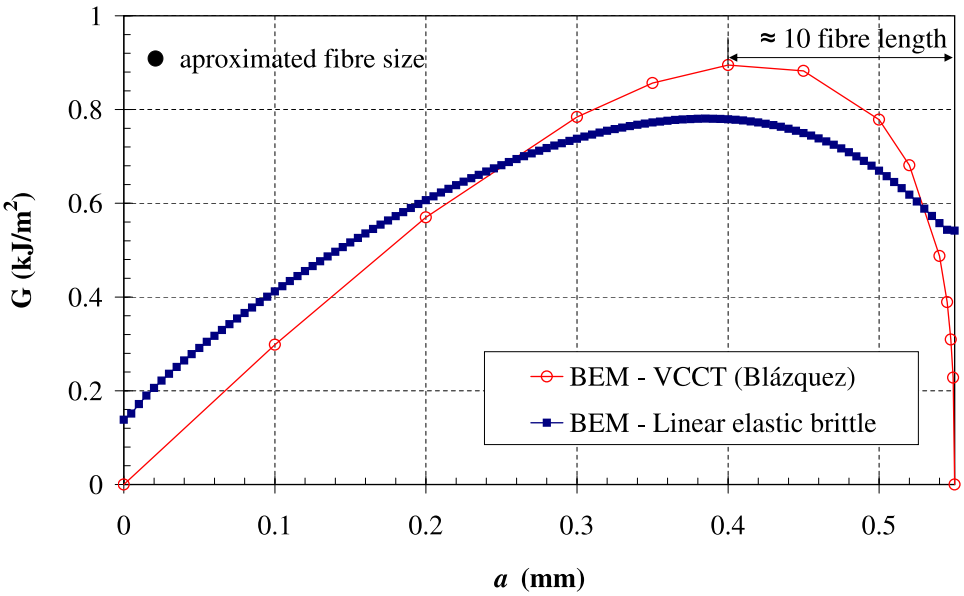

Figure 11.6: Comparison of the predictions of the ERR (G) obtained by VCCT [21] and the linear elastic-brittle formulation, for a fixed applied strain of 1%

versus the length of the transverse crack a is plotted. It can be seen that once a critical strain is applied the crack grows in an unstable manner (less applied strain is needed) until it reaches the interface between the 0° ply and 90° ply.

Although is not shown in the above mentioned figure the fracture energy G_c was always equal to $G_{Ic} = 75\text{Jm}^{-2}$, due to the mode I behavior of the transversal crack and according to Table 11.1.

Fig. 11.5 represents the distribution of the values of the ERR at the crack tip of the growing transverse crack versus the length a, for a fixed applied strain of 1%.

Notice that in both combinations the results are the same, this fact leads to the conclusion that the properties of the interface between the 0° ply and 90° ply ($\bar{\sigma}_c$ and G_{Ic}), has no significant influence on the behavior of the transversal crack, while k_n and k_t values keep the same for both combinations and the delamination crack has not onset yet.

In Fig. 11.6 the distribution of the values of the ERR of the transverse crack versus the length a, for a fixed applied strain of 1% obtained by means of the VCCT [21] is compared with the results obtained with the LEBI formulation proposed. A reasonable general agreement, from a qualitatively

point of view, from the obtained results can be observed. Nevertheless some differences can also be seen, especially in the zone where the transversal crack has onset and in the zone just before the transversal crack reaches the 0° ply and 90° ply interface. These differences are basically caused because the LEBI model allows an opening and tangential relative displacements at the crack tip and ahead of it, while in the VCCT these relative displacements are zero.

11.3.2 Delamination cracks

In the following, the onset and growth of the delamination crack is studied. In particular the effects of the variation of the geometry to be used, the consideration or not of an elastic contact algorithm, as defined in Section 4.2, and also the variation of the interface properties, are elucidated in the following section.

Different geometries

To study the onset and growth of the delamination crack, the geometries shown in Fig. 11.3(a) and (b) are used. The properties correspond to Combination 1 in Table 11.1. The contact algorithm is also activated.

In Fig. 11.7 a comparison of the actual applied strain versus the length of the delamination crack d is plotted, for the two geometries shown in Fig. 11.3. In fact, the value of d represents, half of the total length of the delamination crack. For the geometry shown in Fig. 11.3(b) is $d = d_1$, while for Fig. 11.3(a) d is defined as $d = (d_1 + d_2)/2$. The reason for this definition is that d_1 is not necessarily equal to d_2, as sometimes in modeling a crack growth it is possible to obtain non-symmetric solutions of originally symmetric problems. The growth of the delamination crack is an example of this behavior.

Fig. 11.8 represents a comparison of the distribution of the fracture energy necessary to cause the crack growth versus the length d; while Fig. 11.9 shows a comparison of the distribution of the values of the ERR of the transverse crack versus the length a, for a fixed applied strain of 1%, for the two geometries shown in Fig. 11.3.

In Figs. 11.7-11.9 comparisons of the results for the onset and growth of the delamination crack obtained by using the two geometries shown in Fig. 11.3 are presented. As can be seen from these figures, the results for geometry shown Fig. 11.3(a) presents some spurious oscillations. This fact is caused because although the problem is symmetric the geometry shown

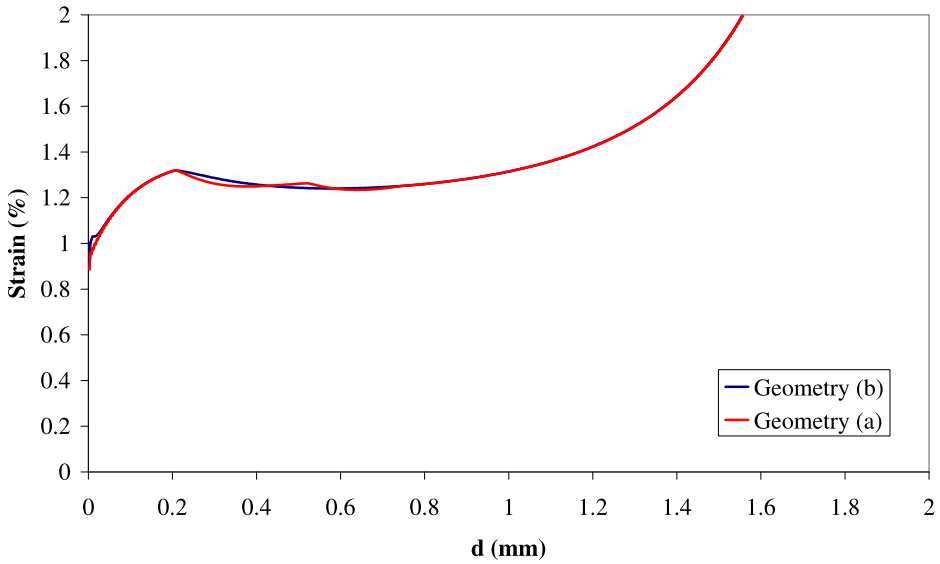

Figure 11.7: Comparison of the applied strain versus the length of the delamination crack d, for the geometries shown in Fig. 11.3.

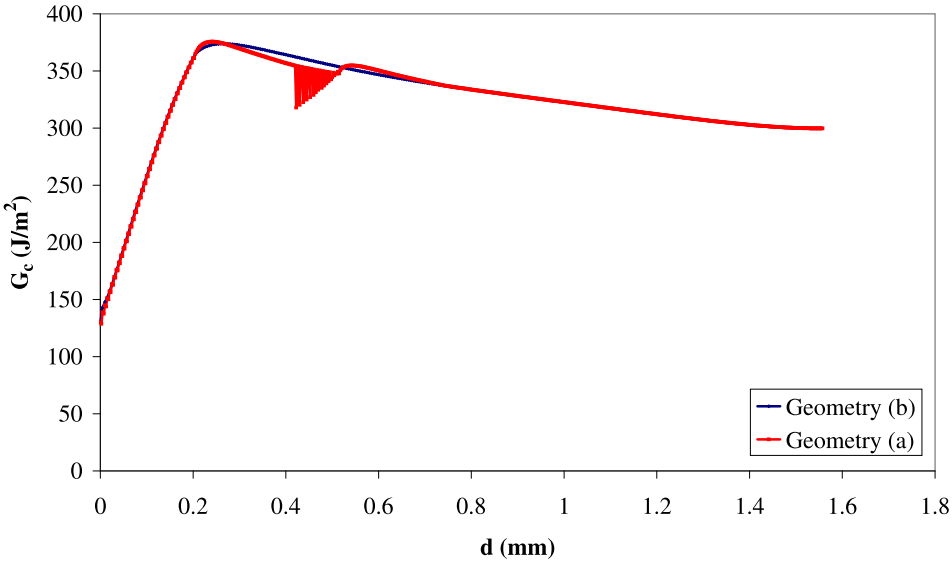

Figure 11.8: Comparison of the distribution of the fracture toughness necessary to cause the crack growth versus the length d, for the geometries shown in Fig. 11.3.

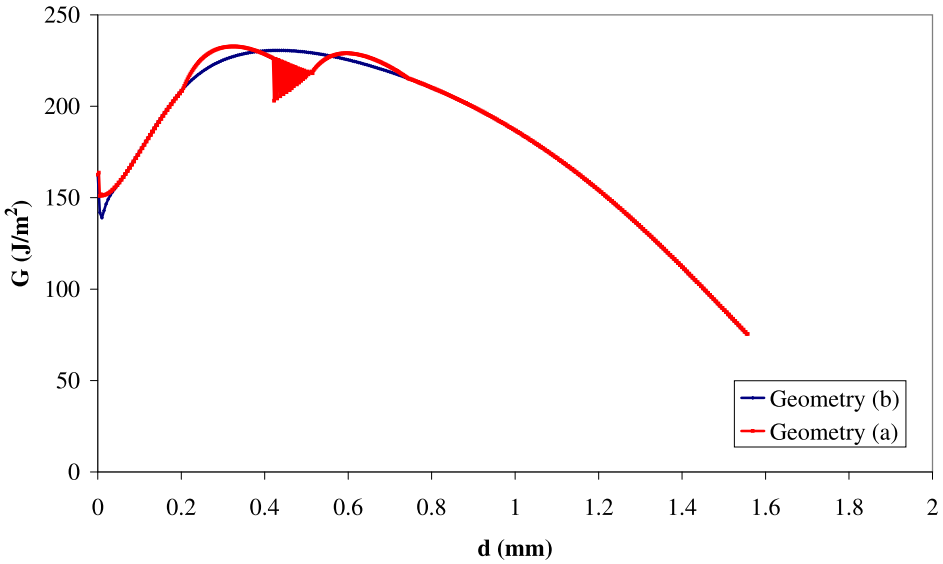

Figure 11.9: Comparison of the predictions of the ERR (G), for a fixed applied strain of 1%, versus the length of the delamination crack d, for the geometries shown in Fig. 11.3.

in Fig. 11.3(a) and the sequentially linear analysis (Section 6.2) allow for a non-symmetric crack growth, while in the geometry shown in Fig. 11.3(b) a symmetric crack growth is assumed. In this manner, once one crack branch (top or bottom) initiates an unstable growth (less applied strain is necessary for crack growing) the crack grows only trough this branch, leading to $d_1 \neq d_2$. Before a continuos unstable growth initiates in the second branch, some spurious behavior is obtained caused because the crack grows in both branches alternating small advances in both crack branches, see Figs. 11.8-11.9. In particular, picks and valleys obtained in Fig. 11.7 for the geometry shown in Fig. 11.3(a) are related to the unstable growth of one branch followed by the unstable growth of the other branch. Nevertheless, this behavior is observed along the unstable growth zone only, and once the crack growth becomes stable the symmetry of the problem is recovered. Thus, in the following to avoid this spurious behavior (with no clear physically meaning), with the aim to reduce computing time and because the obtained results are ver similar, only the geometry shown in Fig. 11.3(b) will be used in the following. In any case the observed alternating crack growth will require a further and more extensive study in the future.

Contact influence

The delamination crack starts being an open crack and, after a certain crack length size is reached, it starts to be partially in contact. Thus, the influence of contact in this specific problem is studied. In one case, once the LEBI element is broken it may enter in frictionless contact according to (4.9). In the other case interpenetration is allowed without causing any contact stresses. Again the properties taken where the ones for Combination 1, see Table 11.1 and the geometry used is the one shown in Fig. 11.3(b).

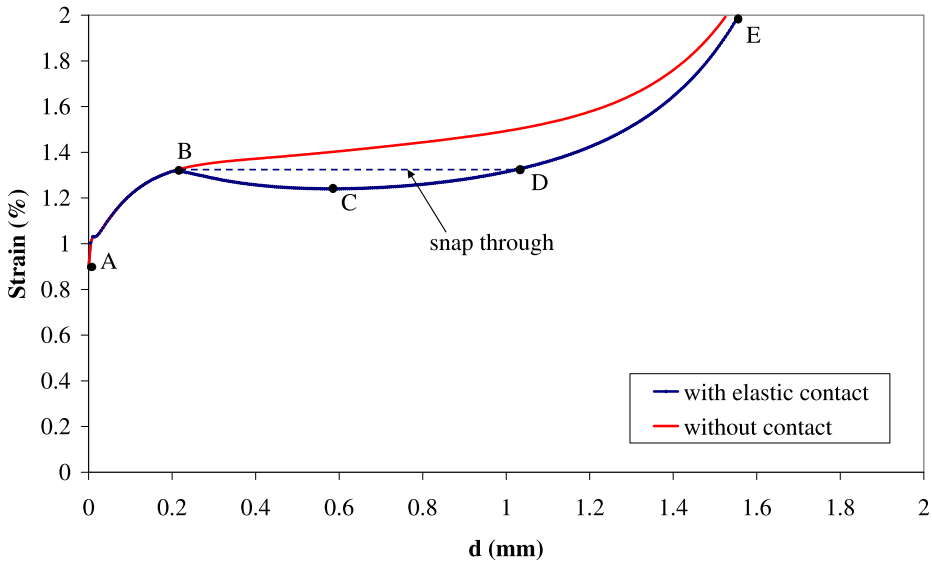

Figure 11.10: Comparison of the applied strain versus the length of the delamination crack d, considering contact or not.

In Fig. 11.10 a comparison of the actual applied strain versus the length of the delamination crack d is plotted, considering contact or not. Notice that when contact is considered the delamination crack initially behaves in a stable manner, then a relatively large unstable growth appears where an instability phenomenon called snap-through takes place, and finally a stable growth is reached again. If contact is not considered, allowing overlapping of delamination crack faces, the crack growth is always stable.

Fig. 11.11 represents a comparison of the mixity angle ψ_σ, see (4.15), obtained at the crack tip versus the length of the delamination crack d. In a first stage a stable crack growth in mixed mode ($\psi_\sigma \leq 90°$) is observed

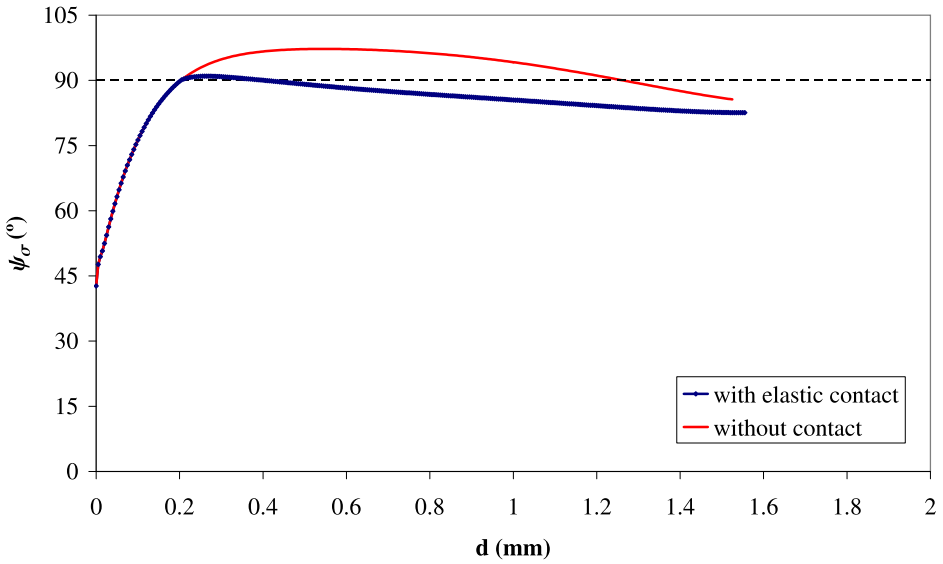

Figure 11.11: Mixity angle ψ_σ obtained at the crack tip versus the length of the delamination crack d, considering contact or not.

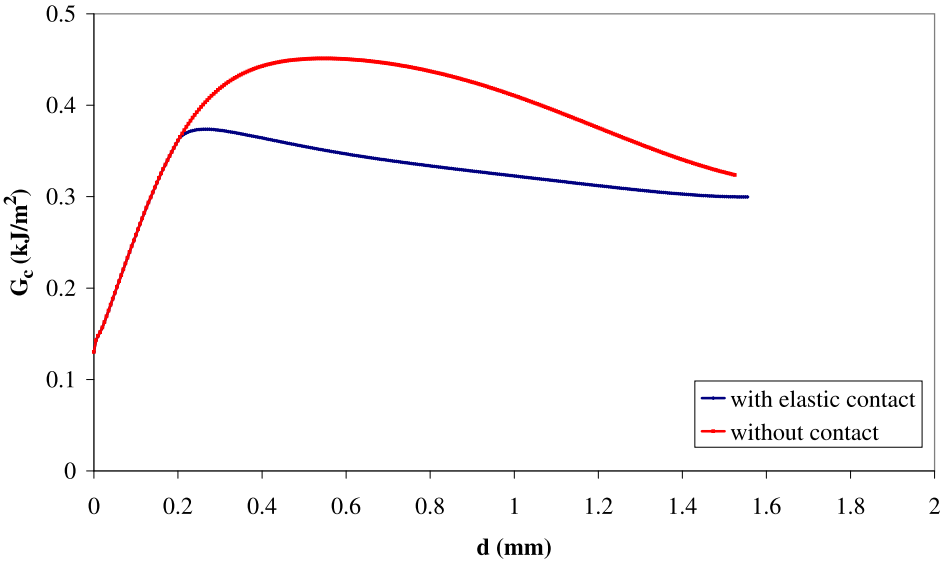

Figure 11.12: Comparison of the distribution of the fracture toughness necessary to cause the delamination crack growth versus the length d, considering contact or not.

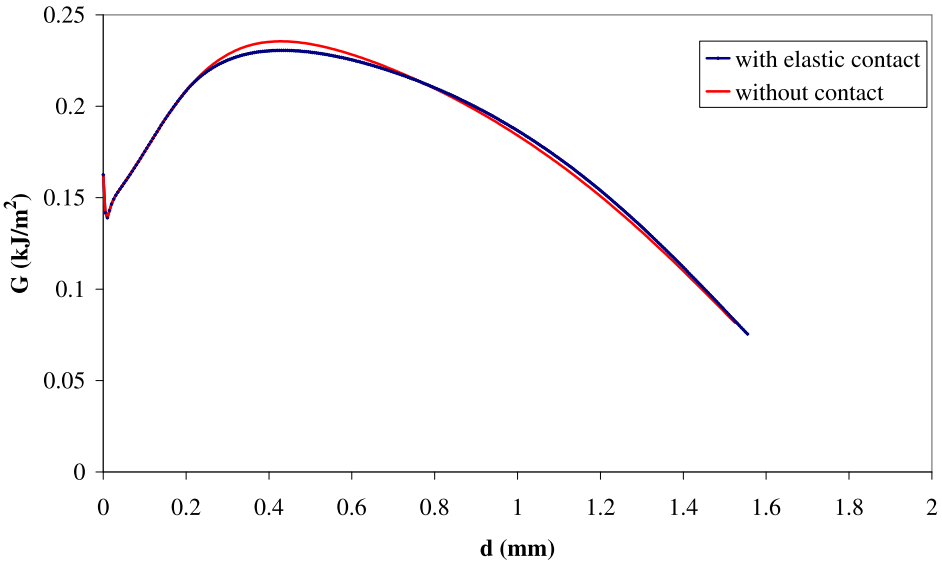

Figure 11.13: Comparison of the predictions of the ERR (G), for a fixed applied strain of 1%, versus the length of the delamination crack d, considering contact or not.

for two cases. After this stage a great difference of ψ_σ values is obtained. When contact is considered, a small stage of crack growth with the crack tip closed appears, and after this small stage the crack grows in mixed mode again, with the crack tip opened forming a "bubble" near the crack tip. On the other hand, when contact is not considered, the stage of crack growth with the crack tip closed is very large.

Fig. 11.12 represents a comparison of the distribution of the fracture energy necessary to cause the crack growth versus the length d. In this case it is noteworthy that when contact is considered the fracture energy necessary to growth is less than when contact is not considered. Thus, contact makes easier crack propagation. This fact could be explained because of the failure criteria used. As can be seen in Fig. 4.7, when the crack tip is in compression it needs more energy (bigger tangential stresses which controle the failure in this problem) to growth.

Fig. 11.13 shows a comparison of the distribution of the values of the ERR of the delamination crack versus the length d, for a fixed applied strain of 1%. It can be seen that, the differences of the values of the ERR of the delamination crack are almost negligible if contact is considered or not.

In Fig. 11.14 and Fig. 11.15 the normal and tangential stresses at the 0° ply and 90° ply interface are plotted for different load steps shown in

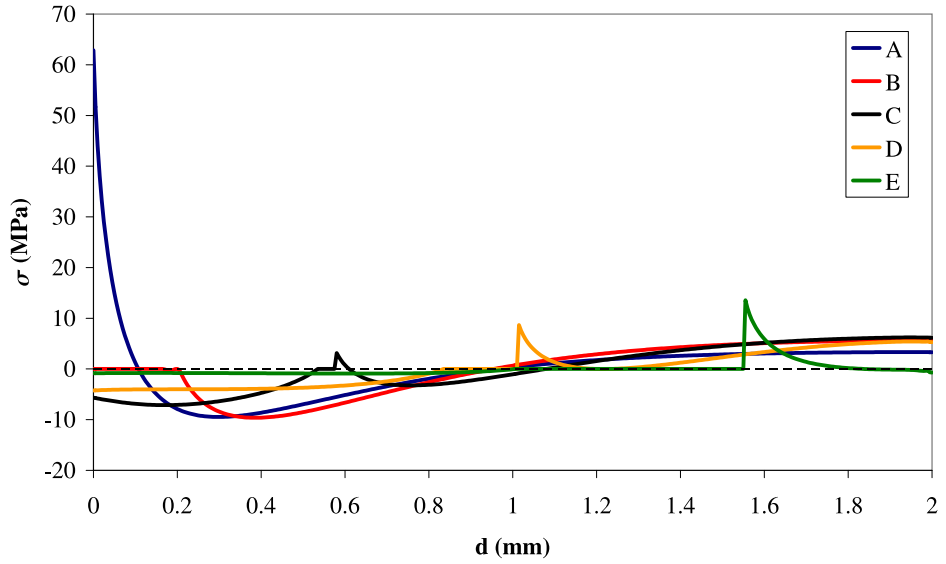

Figure 11.14: Normal stresses obtained at 0° ply and 90° ply interface for the different loads steps shown in Fig. 11.10.

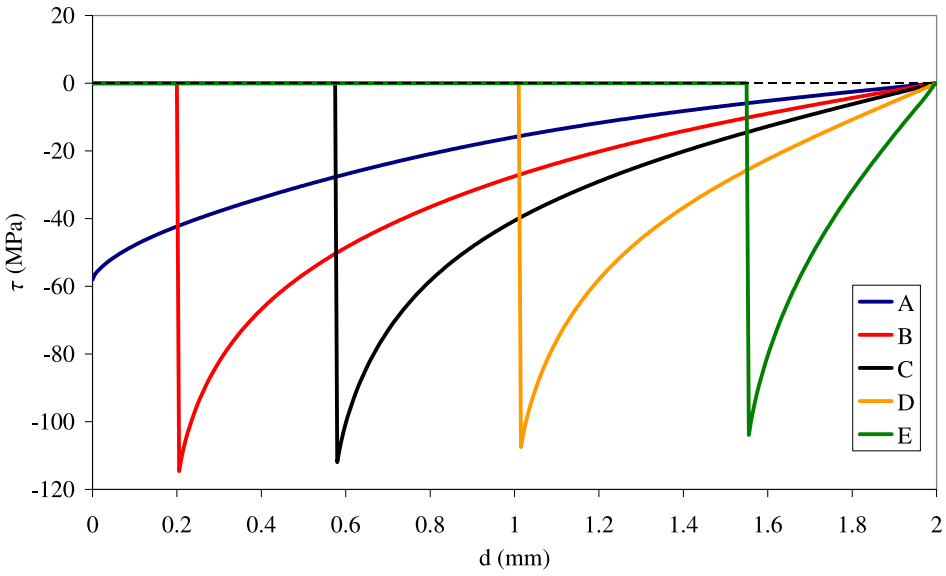

Figure 11.15: Tangential stresses obtained at 0° ply and 90° ply interface for the different loads steps shown in Fig. 11.10.

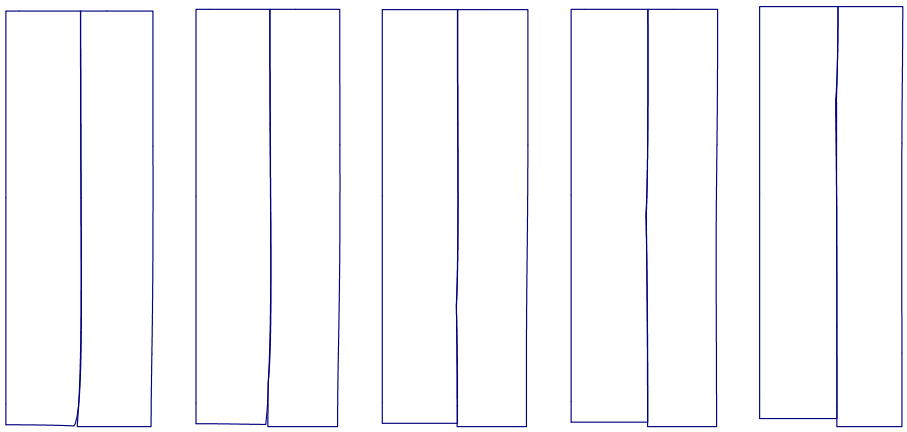

Figure 11.16: Deformed shapes obtained for the different loads steps shown in Fig. 11.10, multiplied by 20 in x-direction only.

Fig. 11.10 when elastic contact is considered. As can be seen from these figures the tangential stresses are much larger than the normal stresses during the delamination crack growth. In particular in Fig. 11.14, the "bubble" formed near the crack tip can be observed ($\sigma = 0$).

In Fig. 11.16 the deformed shapes of the same load steps considered in Fig. 11.14 and Fig. 11.15 are shown. These deformed shapes are multiplied by 20 only in x-direction.

Different interface properties

As can be concluded from the previous analysis, the use of contact seems to be reasonable. Thus, taking into account the contact algorithm the two combinations of interface properties are considered according to Table 11.1. Again the geometry used is that shown in Fig. 11.3(b).

In Fig. 11.17 a comparison of the actual applied strain versus the length of the delamination crack d is plotted, for the two combinations considered in Table 11.1. Notice that combination 2 with the same applied strain causes a larger delamination crack size. It is also noticeable, the fact that both curves are very similar in form but with very different values, this could be caused because although $\bar{\sigma_c}$ and G_{Ic} values are different the values of k_n and k_t are the same in both configurations.

Fig. 11.18 represents a comparison of the distribution of the fracture

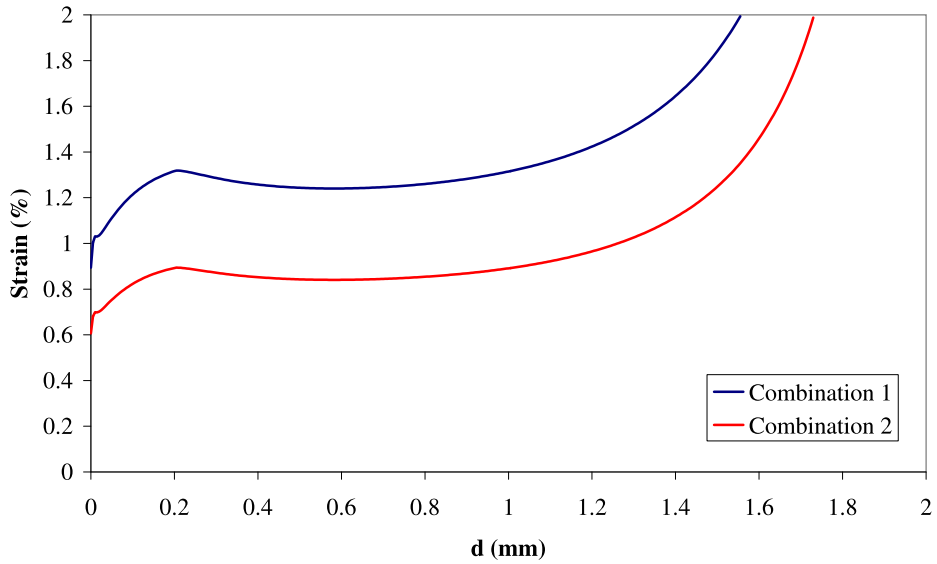

Figure 11.17: Comparison of the applied strain versus the length of the delamination crack d, for the two combinations considered in Table 11.1.

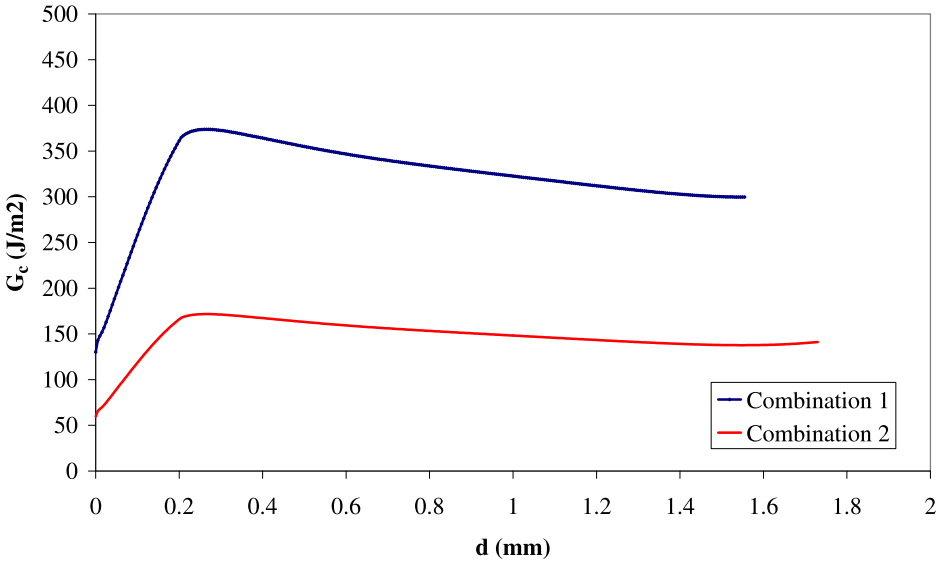

Figure 11.18: Comparison of the distribution of the fracture toughness necessary to cause the crack growth versus the length d, for the two combinations considered in Table 11.1.

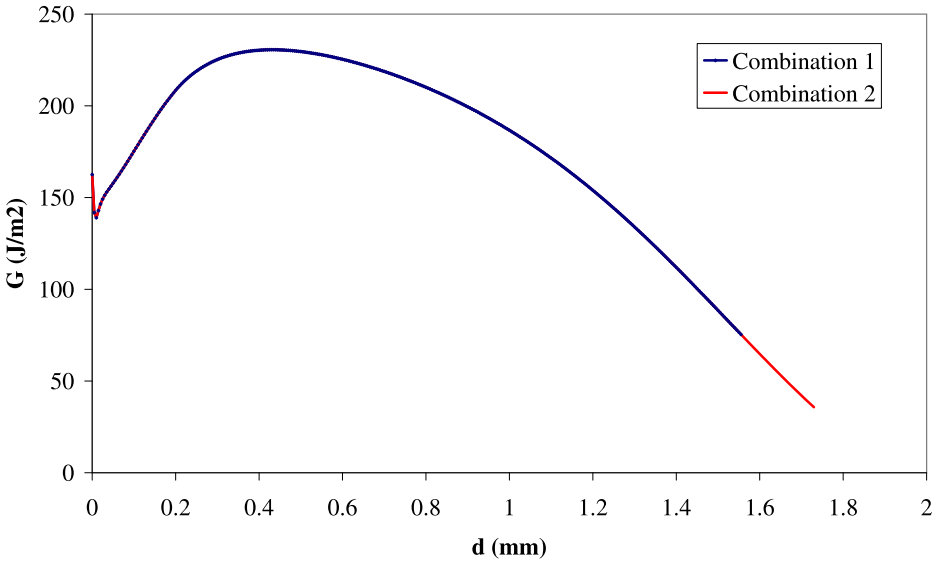

Figure 11.19: Comparison of the predictions of the ERR (G), for a fixed applied strain of 1%, versus the length of the delamination crack d, for the two combinations considered in Table 11.1.

energy necessary to cause the crack growth versus the length d. As in combination 2 the G_{Ic} associated to the interface is lower, the obtained results are in accordance to this fact. It can be observed that the delamination crack for combination 2 grows easier. Also ψ_σ values are exactly the same for both combinations.

Fig. 11.19 shows a comparison of the distribution of the values of the ERR of the delamination crack versus the length d, for a fixed applied strain of 1%. It can be seen that, there are no differences of the values of the ERR of the transverse crack for the two combinations considered in Table 11.1.

Comparison with other previous results

In a similar way as it was done for transversal cracks, in Fig. 11.20 the ERR (G) obtained by Blázquez [21], O'Brien [126], McCartney [118] and the the ERR obtained using the present LEBI formulation, for a fixed applied strain of 1%, are compared. Notice that the present results seem to be in a good qualitative agreement with those obtained by means of the VCCT [21].

Finally in Fig. 11.21 the ERR components (G_I, G_{II} and G) obtained by the VCCT [21] and the present LEBI formulation, for a fixed applied strain of 1% are plotted. Notice that the contribution of mode I and II are

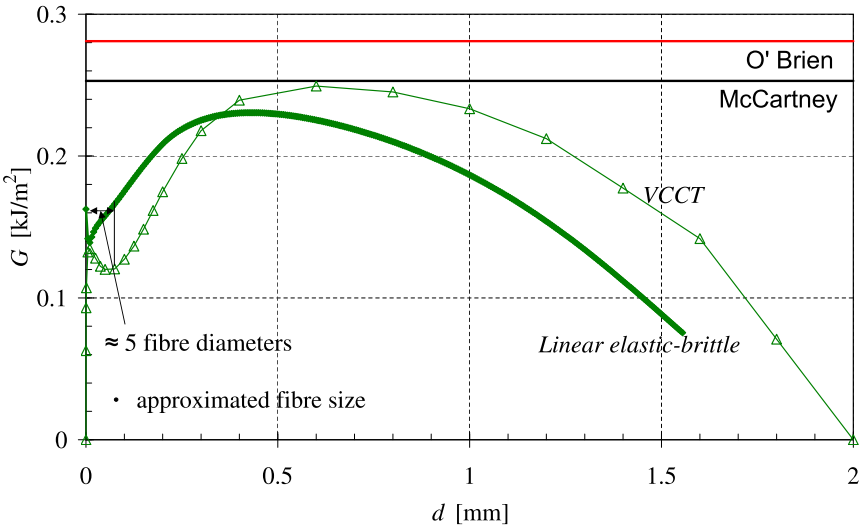

Figure 11.20: Comparison of the predictions of the ERR (G) for the delamination crack obtained by different authors and the linear elastic-brittle interface formulation, for a fixed applied strain of 1%.

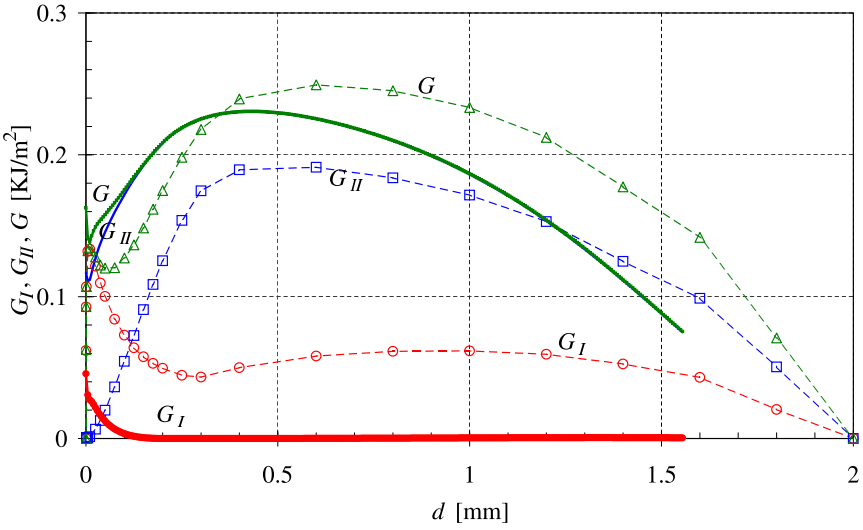

Figure 11.21: Comparison of the predictions of the ERR (G) obtained by the VCCT [21] (dashed lines) and the linear elastic-brittle formulation (continuous lines), for a fixed applied strain of 1% versus the length of the delamination crack d.

in accordance qualitatively by the two methods presented. In fact, it can be said that the larger contribution in mode I obtained by means of the VCCT is caused by the use of a very small value of the virtual crack step length, $\triangle a$. It can be expected that the results obtained by means of the VCCT and a larger value (more realistic) of $\triangle a$ will be in more accordance with the results obtained by means of the present LEBI formulation.

Cook-Gordon mechanism

By using the geometry shown in Fig. 11.3(a) and taking the combination for the interface properties shown in Table 11.2, the LEBI formulation was able to model the Cook-Gordon mechanism [44], see Fig. 11.2(d).

Table 11.2: Interface properties used to obtain a behavior similar as the Cook-Gordon mechanism [44], see Fig. 11.2(d).

Position	$G_{Ic}(\mathrm{Jm}^{-2})$	$\bar{\sigma}_c$(MPa)	k_n (MPa/μm)	k_t (MPa/μm)
transversal	75	61	24.807	8.269
delamination	15	61	124.034	41.345

Notice that the values of k_n and k_t between the two crack paths has a ratio of 5. Using these properties the transversal crack stopped around $a = 0.525$ mm and originated a delamination crack of a size of $d = d_1 = d_2 = 0.02$ mm. Then, the transversal crack starts its growing again and reaches the interface. It should be mentioned that this fact only shows that the LEBI formulation is capable to model this behavior, nevertheless a deeper study regarding this topic is necessary.

11.4 Concluding remarks

As shown by the numerical results presented in this chapter, the LEBI formulation seems to be a promising tool to describe the behavior of the transversal and delamination cracks in [0/90] symmetric laminates. As shown by the realistic results presented, the BEM tool developed can be considered a useful tool, due to the crack propagation can be modeled by using always the same uniform mesh. While for the VCCT [21, 130] a refined mesh is necessary near the crack tip, thus for a different load steps, different meshes are needed. Although it was not studied deeply in this chapter the

LEBI formulation is capable of reproducing the Cook-Gordon mechanism [44], see Fig. 11.2(d), by using an adequate combination of properties at the 0° ply and 90° ply interface and the properties used for the crack path of the transversal crack.

Chapter 12

Single Fibre Fragmentation Test

In the present chapter the Single Fibre Fragmentation Test (SFFT) of composite materials is modeled by means of the Linear Elastic-Brittle Interface (LEBI) model introduced in Chapter 4. The non-linear algorithm used is the sequentially linear analysis, described in Section 6.2, implemented in a 2D axisymmetric BEM code.

12.1 Description of the test

As mentioned in Section 2.3, the SFFT has been extensively used for fibre–matrix interface characterization in fibre reinforced composites. In the present study, a sample made of E-glass fibre and epoxy matrix is considered. SFFT specimens consist of a long fibre embedded in a large block of resin matrix, subjected to tensile load in the fibre direction, applied as a uniform strain at the ends of the specimen. Since strain to failure in the fibre is much lower than in the matrix, after reaching a certain load, successive fragmentation of the fibre is observed. Once the fragmentation process, which reflects the statistical fibre strength distribution, starts, tensile load is transferred to the fibre fragments through shear stresses at the fibre–matrix interface, thus allowing for the appearance of new fragments.

A specific numerical tool based on the Boundary Element Method and the LEBI formulation has been developed and employed for the numerical simulation of the problem. This approach has been chosen for the numerical analysis of the SFFT since it offers clear advantages if compared with other alternative numerical methods (for example, the Finite Element Method).

Firstly, taking into account the axial symmetry with respect to the fibre axis, only a 1D mesh is needed for the analysis of the 2D axi-symmetric problem with BEM. Secondly, since the debonding crack grows along the fibre–matrix interface, the displacements and tractions needed for the study of debond propagation are the actual primary unknowns in the nodes of the BEM mesh.

Isotropic linear elastic material behavior, repetitive solutions in the vicinity of all fragment ends and local symmetry with respect to the fibre crack is assumed in order to simplify the BEM model, as in [71, 72, 73]. Thus, the geometry and boundary conditions employed for the analysis are those shown in Fig. 12.1. Material properties, corresponding to typical E-glass fibre and epoxy matrix, are listed in Table 12.1. The outer radius of the resin cylinder is taken as $r_m = 1000\mu$m. In this preliminary analysis, the effect of the residual stresses, originated by the curing of the specimen and the friction contact between the crack faces in closed cracks has been neglected.

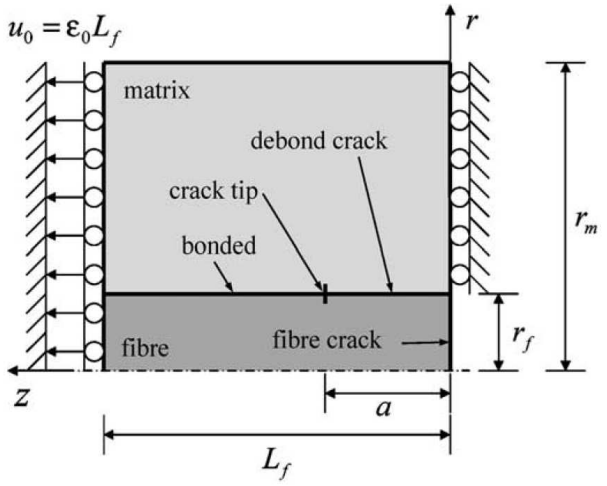

Figure 12.1: Single fibre fragmentation test geometry and boundary conditions, taken from [73].

The BEM mesh used has 820 continuous linear elements modeling the fibre, 800 elements in the fibre-matrix interface (the uniform element size is 0.5 μm), notice that is not necessary to mesh the nodes in the axisymmetric axis. The matrix is modeled with 892 continuous linear elements, where

again 800 elements are used in the interface, while 30 elements are used in the outer face of the matrix and 36 elements in each lateral face.

Table 12.1: Single fibre fragmentation test: material properties (m-epoxy matrix and f-glass fibre).

Mat.	Poisson ratio	Young's modulus	Outer radius
m	$\nu_m = 0.3$	$E_m = 3.5$ GPa	r_m= 1000 μm
f	$\nu_f = 0.2$	$E_f = 70$ GPa	r_f= 5 μm

12.2 Crack propagation along the fibre-matrix interface

The geometry and material properties used are those described previously in Section 12.1. Since there is not a unique accepted value for the Fracture Energy in mode II for the fibre matrix interface, three values of G_{IIc} were assumed, $G_{IIc} = 10, 20, 40$ J/m^2. The present problem is solved by means of the LEBI model. In the present application, the linear contact part of the LEBI formulation, once an element is broken, is deactivated, see Section 4.2; thus overlapping of crack faces is allowed. The interface properties are taken as: $k_n/k_t = 4$ and $\lambda = 0.3$ for the three values of G_{IIc} mentioned and shown in Table 12.2.

Table 12.2: Single fibre fragmentation test: fibre-matrix interface properties.

G_{IIc}	$\bar{\tau}_c$	δ_{tc}	G_{Ic}	$\bar{\sigma}_c$	δ_{nc}
10 J/m^{-2}	66.666 MPa	0.3 μm	2.061 J/m^{-2}	60.53 MPa	0.0681 μm
20 J/m^{-2}	133.332 MPa	0.3 μm	4.122 J/m^{-2}	121.06 MPa	0.0681 μm
40 J/m^{-2}	266.664 MPa	0.3 μm	8.244 J/m^{-2}	242.12 MPa	0.0681 μm

Notice that the values of G_{Ic}, $\bar{\sigma}_c$ and $\bar{\delta}_{nc}$ were calculated with the formulation and relations described in Section 3.2.

In Fig. 12.2, BEM results for the three values of G_{IIc} are shown. Also some FEM results using a Cohesive Zone Model are plotted, the model used is a linear CZM as described in Section 3.1, that is included in the comercial FEM code MSC.MARC. Notice that the BEM results are always above the FEM results. This fact could be explained by the different values of the total fracture energy, G_c at the crack tip during its growth. In the FEM

analysis the problem behaves in pure mode II, therefore $G_c = G_{IIc}$. In the BEM analysis the mixed mode formulation of the LEBI model allow a mixed mode (where a compression in mode I affects the value of G_c, $\psi_\sigma > 90°$), see Fig. 4.7. The values of G_c obtained in this problem are shown in Fig. 12.3 were it can be clearly seen that at initial steps the values of G_c are higher and then an almost constant value, although still higher than G_{IIc}, is reached. In spite of the significant differences in the FEM and BEM models used, an excellent agreement between the results of these models is achieved, see Fig. 12.2, when taking into account the different G_c values as shown in Fig. 12.3

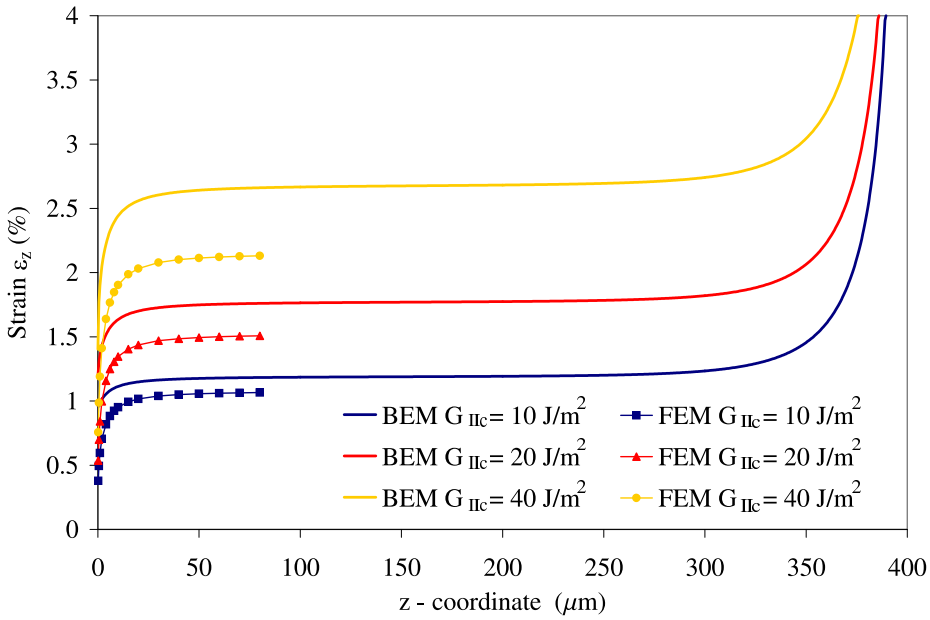

Figure 12.2: BEM results for the interface crack growth in SFFT with $\lambda = 0.3$ and $k_n/k_t = 4$ compared with FEM results.

In order to see the capabilities of the present LEBI model, the problem was solved again but changing the value of the parameter λ, with $\lambda = 0.2$, as can be seen in Fig. 12.4. Notice that the model just need the values of G_{Ic}, $\bar{\sigma}_c$ and $\bar{\delta}_{nc}$, this fact will lead to a different value of G_{IIc} determined by the LEBI model.

Notice that in Fig. 12.4 for $G_{Ic} = 8.244$ J/m^{-2} the final crack size is very small, due to the very high value of G_c. This behavior is led by the value of

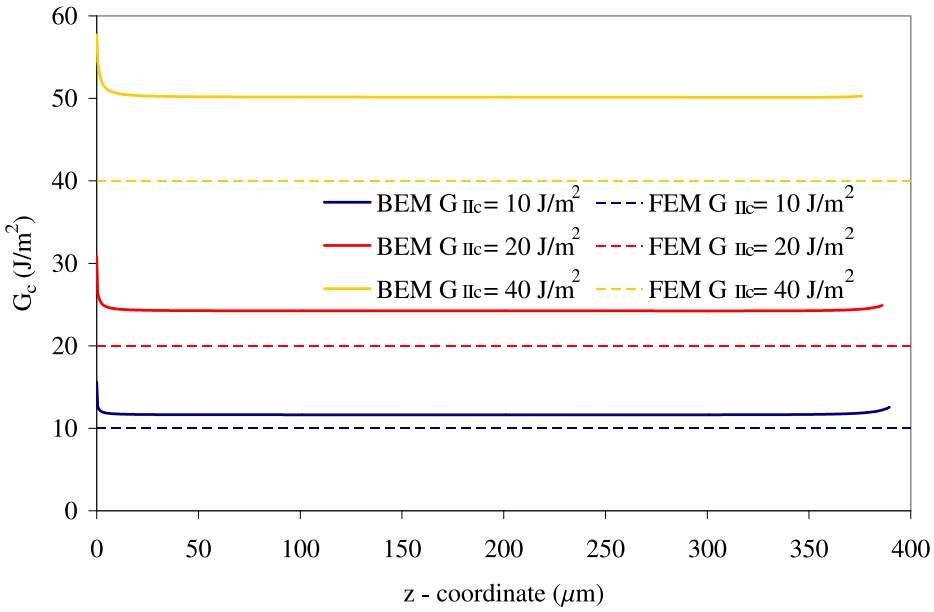

Figure 12.3: G_c values for the SFFT studied problem in Fig. 12.2.

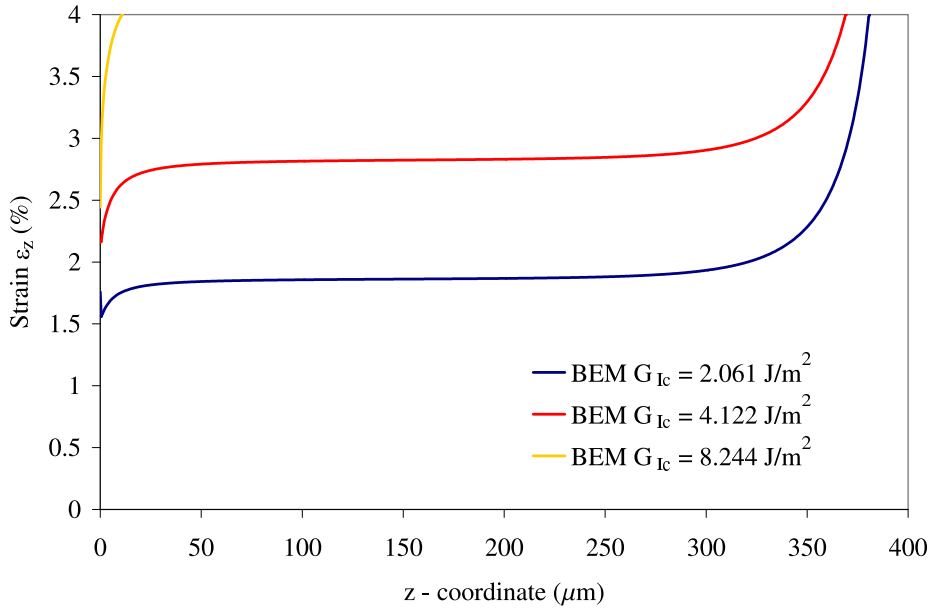

Figure 12.4: BEM results of SFFT with $\lambda = 0.2$ and $k_n/k_t = 4$.

λ. As this parameter becomes lower the value of G_c, when a compression is acting in mode I, becomes higher more quickly because of the different slope, see Fig. 4.7.

A second study was done in order to see the effect of the value of the ratio k_n/k_t. Thus, keeping constant all the other interface properties with $\lambda = 0.3$, the problem was solved with $k_n/k_t = 3, 5$, see Figs. 12.5-12.6 respectively.

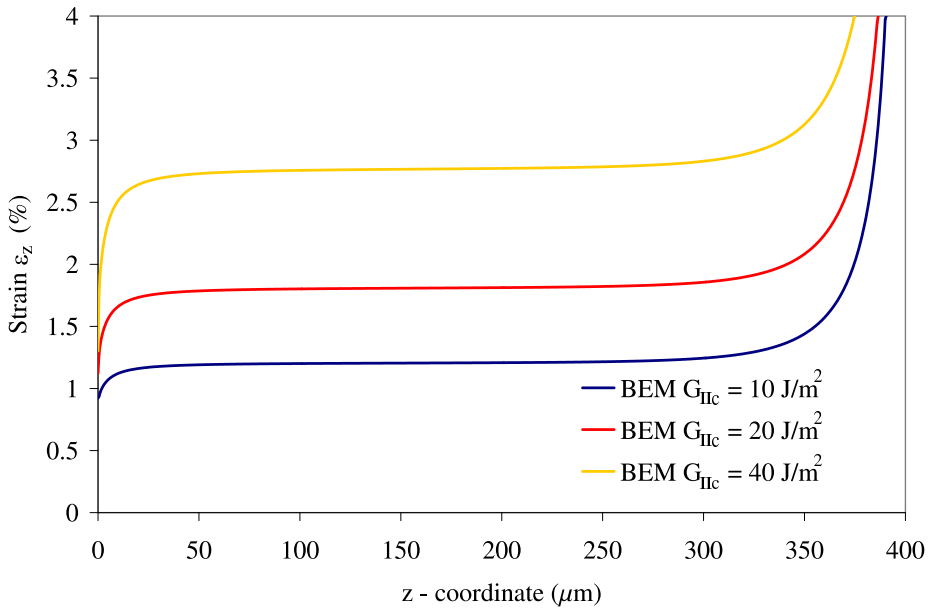

Figure 12.5: BEM results of SFFT with $\lambda = 0.3$ and $k_n/k_t = 3$.

As can be observed from Figs. 12.5-12.6 the value of the ratio k_n/k_t has a small effect on the SFFT problem. For lower values of k_n/k_t the G_c increases a little bit, while for higher values k_n/k_t the G_c decreases, this effect can be observed as a small shifting of the curves in Figs. 12.5-12.6.

An important effect that is shown by all the above figures (and the different parametric studies) is that in the initial stage a stable growth of the interface crack is reached. Followed by a long stage with a crack growth close to neutral equilibrium (almost unstable growth with a similar strain) and finally a crack arrest is presented, as a considerably amount of strain is necessary to continue with the crack growth.

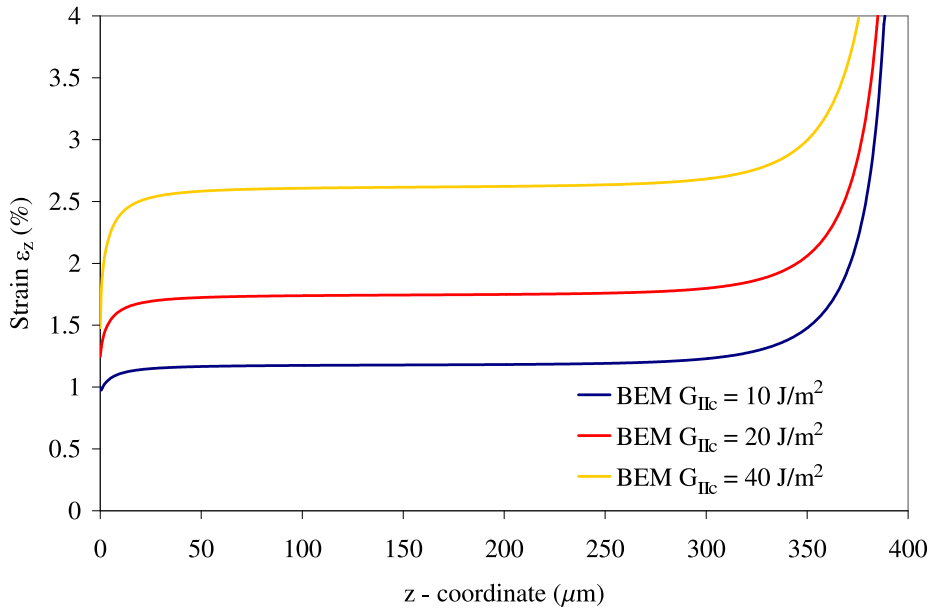

Figure 12.6: BEM results of SFFT with $\lambda = 0.3$ and $k_n/k_t = 5$.

12.3 Concluding remarks

As shown by the numerical results presented in this chapter, the LEBI formulation seems to correctly describe the behavior of the debond crack growth in the Single Fibre Fragmentation Test.

Although this is an initial study the LEBI model seems to be a promising tool, where the influence of the linear contact between crack faces after an element is broken can be take into account for further studies.

Chapter 13

Interface cracks between matrix and fibre under transversal loads

In the present chapter the onset and growth of interface cracks between matrix and fibre of composite materials subjected to far field transversal loads is studied by means of the Linear Elastic-Brittle Interface (LEBI) model introduced in Chapter 4. The non-linear algorithm used is the sequentially linear analysis implemented in a 2D collocational BEM code.

First the problem of an isolated fibre embedded in a large matrix is deeply studied under different combinations of transversal loads and then a cluster of fibres (three) is modeled.

13.1 Single fibre model

The problem of an elastic cylindrical inclusion (representing a fibre) inside an elastic matrix with and without a partial debond along its interface subjected to a remote uniform tension perpendicular to the debond has been studied in depth by many researchers, see references in [45, 112, 132].

In the present study an infinitely long cylindrical inclusion is considered, with circular section of radius a, inside an infinite matrix, Figure 13.1. Both the inclusion and the matrix are considered as linear isotropic materials. Let (x, y, z) and (r, θ, z) be the cartesian and cylindrical coordinates, the z-axis being the longitudinal axis of the inclusion, and the x-axis the one parallel to the direction of the load. A uniform remote tension $\sigma_x^\infty > 0$ and $\sigma_y^\infty = 0$

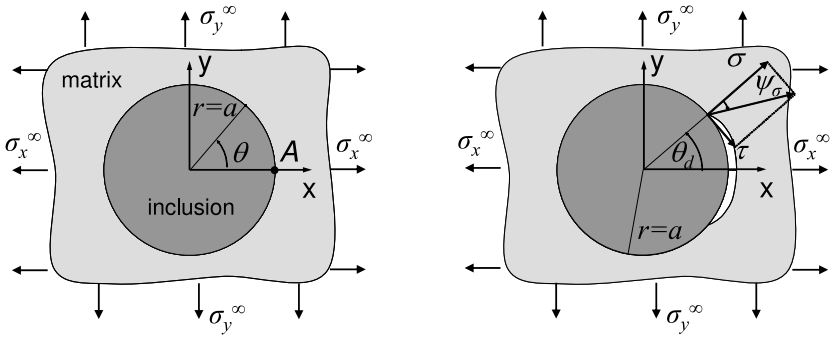

(a) (b)

Figure 13.1: Inclusion problem configuration under remote transverse tension (a) without and (b) with a partial debond.

is applied for uniaxial loading problems. For biaxial problems $\sigma_x^\infty > 0$ and $-\sigma_x^\infty \leq \sigma_y^\infty \leq \sigma_x^\infty$ is used. The semidebond angle is denoted as θ_d. A plane strain state is assumed in the system.

13.1.1 Fibre-matrix debond initiation and growth under uniaxial tension

Analytical solution for undamaged interface

Gao [66] developed closed-form solutions for circular inclusion problems with a general linear elastic (spring) layer interface condition with a constant eigenstrain in the inclusion and a tension at infinity. The materials are assumed to be isotropic with μ_i and κ_i, and μ_m, and κ_m as the material properties of inclusion (i) and matrix (m) respectively. Herein, μ is the shear modulus, $\mu = E/2(1+\nu)$, and $\kappa = 3 - 4\nu$ for plane strain, where ν is the Poisson's ratio. From the Airy stress function presented in [66], a closed-form expression has been obtained in the present thesis for the stresses at the interface under a uniform tension σ_x^∞ at infinity and zero eigenstrain.

$$\sigma(x = a, \theta) = \frac{\sigma_x^\infty k_n a(1+\kappa_m)[A + BC\cos(2\theta)]}{2AC}, \tag{13.1}$$

$$\tau(x = a, \theta) = \frac{\sigma_x^\infty k_t a(1+\kappa_m)[B\sin[2\theta]]}{2A}, \tag{13.2}$$

where

$$A = 12\mu_m^2 + a^2 k_n k_t(\kappa_m + t)(1 + \kappa_i t) + a\mu_m(k_n + k_t)(1 + 3\kappa_m + (3 + \kappa_i)t), \quad (13.3)$$

$$B = 6\mu_m + ak_n(1 + \kappa_i t), \quad (13.4)$$

$$C = 4\mu_m + ak_n(2 + (\kappa_i - 1)t), \quad (13.5)$$

with $t = \mu_m/\mu_i$.

According to Gao [66] a necessary and sufficient condition for having a constant stress inside the inclusion is that $k_n/k_t = 1$. Recall that, according to Section 4.1, this ratio can not correspond to an isotropic elastic layer, see equation (4.7).

Numerical solution and parametric studies

Consider an inclusion bonded to the matrix along its lateral surface through a continuous distribution of springs that behave according to the LEBI model introduced in Chapter 4. It is assumed that, although strictly speaking there might be no material between the fibre and matrix, the above interface model can still be used to simulate the behavior of this system. An important feature of this model is, as will be shown, the possibility of studying not only the fibre-matrix debond (interface crack) propagation but also the debond (interface crack) onset.

It is noticeable that although the problem is symmetric (geometry and loads) the onset and growth of the interface crack is non-symmetric, as can be observed from experimental evidence, see Fig. 2.4. Thus, although some researchers makes use of the symmetry to study this problem, in the present chapter the whole inclusion is modeled in order to see the capability of the model to represent the non-symmetric behavior.

BEM model. A typical bi-material system among fibre reinforced composite materials is chosen for this study: glass fibre and epoxy matrix. The elastic properties of these materials, the Dundurs' bi-material parameters, α and β, and the harmonic mean of the effective elasticity moduli E^* in plane strain, defined e.g. in [112, 113, 132], are detailed in Table 13.1.

The BEM model represents a cylindrical inclusion with a radius a =7.5 μm inside a relatively large square matrix with a 1 mm side. 1472 continuous linear boundary elements are used: 32 elements for the external boundary of the matrix and two uniform meshes of 720 elements to model the fibre-matrix interface (therefore, the polar angle of each element is 0.5°).

Table 13.1: Isotropic bi-material constants (m-epoxy matrix and f-glass fibre).

Mat.	Poisson ratio	Young's modulus	α	β	E^*
m	$\nu_m = 0.33$	$E_m = 2.79$ GPa	0.919	0.229	6.01 GPa
f	$\nu_f = 0.22$	$E_f = 70.8$ GPa			

Effect of the interface properties G_{Ic}, $\bar{\sigma}_c$ and λ. Due to the absence of a widely accepted value of the fibre-matrix interface fracture toughness in mode I, G_{Ic}, and of the critical tension of this interface, $\bar{\sigma}_c$, a parametric study is presented. The problem has been solved for different combinations of the estimations of their maximum and minimum values found in the literature [1, 112, 170, 184], see Table 13.2.

Table 13.2: Considered combinations of the fibre-matrix interface properties.

N°	G_{Ic}(Jm^{-2})	$\bar{\sigma}_c$(MPa)	k_n (MPa/μm)	k_t (MPa/μm)	$a_0(\mu$m)	γ
1	2	60	900	300	3.34	0.67
2	10	60	180	60	16.7	1.5
3	2	90	2025	675	1.48	0.44
4	10	90	405	135	7.42	0.99

A bimaterial characteristic length

$$a_0 = \frac{G_{Ic}E^*}{\bar{\sigma}_c^2}, \tag{13.6}$$

and the dimensionless structural parameter characterizing the interface brittleness,

$$\gamma = \frac{1}{\bar{\sigma}_c}\sqrt{\frac{G_{Ic}E^*}{a}} = \sqrt{\frac{a_0}{a}}, \tag{13.7}$$

introduced in [112], are also included in Table 13.2. The values of k_n in Table 13.2 are computed by the formula $k_n = \bar{\sigma}_c^2/(2G_{Ic})$ obtained from (4.19). The constant relation between k_n and k_t ($k_t = k_n/3$) chosen in Table 13.2 requires an explanation. This value is obtained assuming a fictitious material, a very thin layer between the fibre and matrix, modeled by the

present interface model whose Poisson ratio is somewhat arbitrarily defined as $\nu = 0.25$ according to (4.7).

Different values of the sensitivity parameter λ (λ=0, 0.2 and 0.3) appearing in the empirical fracture energy law (4.18) are chosen in Fig. 13.2, Fig. 13.3 and Fig. 13.4 respectively.

In part (a) of Figs. 13.2-13.4 the applied remote stress, σ_x^∞, is plotted as a function of the normal relative displacement (opening), δ_n, evaluated at point A$(a, 0)$ as defined in Fig. 13.1(a). The (minimum) remote stress value that is needed to initiate crack growth (in simple terms, the stress that is needed to break the first point, the first spring, in the present interface discrete model) is called critical stress, σ_c^∞, and corresponds to the local maximum of the functions shown in the above mentioned figures. It can be also observed in these figures that after reaching the critical stress, σ_c^∞, the crack growth becomes unstable, requiring smaller values of the remote tension that causes the further crack growth, thus an instability phenomenon called snap-through takes place.

In part (b) of Figs. 13.2-13.4 the (minimum) remote stress, σ_x^∞, needed to cause crack growth is plotted versus the semidebond angle θ_d (defined in Fig. 13.1(b)). It should be noted that from these figures it is possible to obtain an estimation of the value, θ_c, reached by the semidebond angle θ_d after the initial unstable crack growth, and also of the load, σ_c^∞, which produced the growth.

As expected (from the values of γ calculated), Combination 3, which has the highest critical normal stress value in mode I, $\bar{\sigma}_c$, and the lowest fracture toughness, G_c, presents the most brittle behavior (the lowest γ value), thus resulting in the highest value of θ_c and the lowest value of $\sigma_x^\infty/\bar{\sigma}_c$ of all the combinations studied.

The formulation of the LEBI constitutive law employed in this particular example is different to the one shown in Fig. 4.4 (developed later) and it does not allow crack growth when compressions are present at the crack tip. In such situations no further increment of load is applied, as can be observed in some curves in Figures 13.3(a)-13.5(a).

Table 13.3 summarizes the values of the σ_x^∞, $\sigma_x^\infty/\bar{\sigma}_c$ and θ_c for the different combinations studied.

The influence of λ on crack propagation should also be noticed. As can be checked from Figs. 13.2-13.4, the value of σ_c^∞ is independent of the value of λ. This fact is due to the problem configuration symmetry implying that the first point which reaches the critical load and fails works in pure mode I, causing the no influence of λ value on σ_c^∞. Nevertheless, changing the

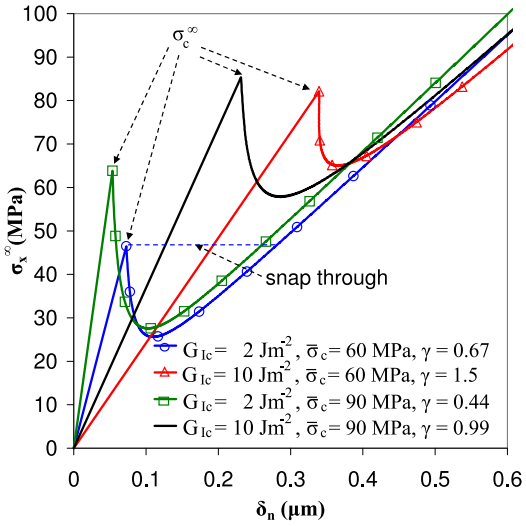

(a)

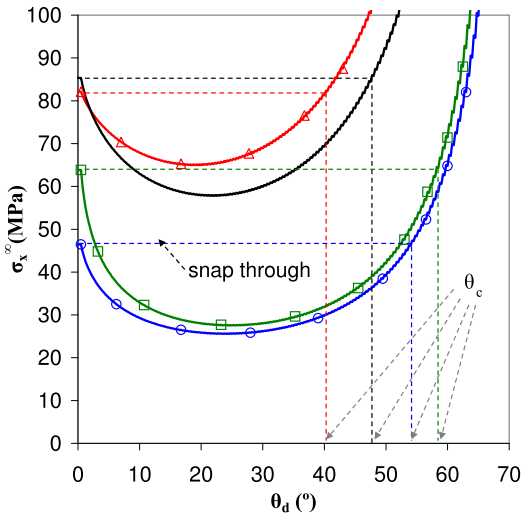

(b)

Figure 13.2: BEM results. (a) Applied stress with respect to the normal relative displacements at point A(a,0) and (b) applied stress with respect to the semidebond angle for different interface properties and $\lambda = 0$.

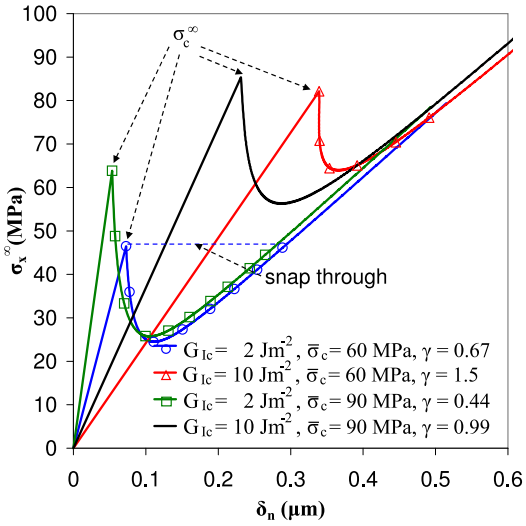

(a)

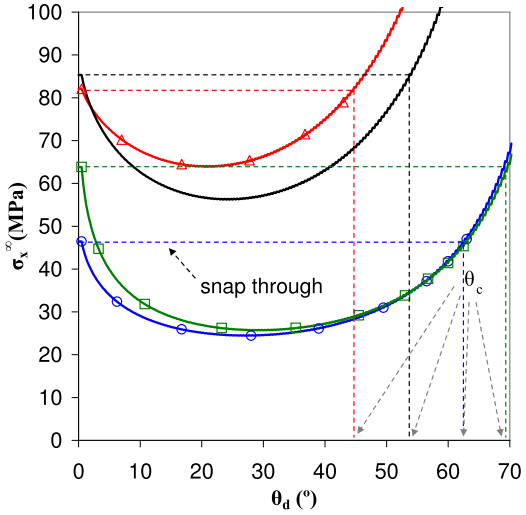

(b)

Figure 13.3: BEM results. (a) Applied stress with respect to the normal relative displacements at point A(a,0) and (b) applied stress with respect to the semidebond angle for different interface properties and $\lambda = 0.2$.

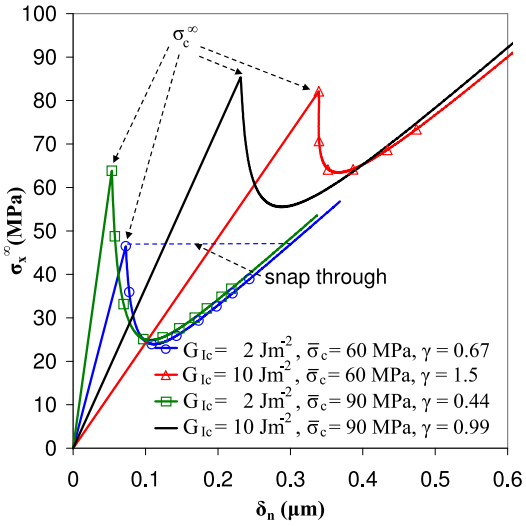

(a)

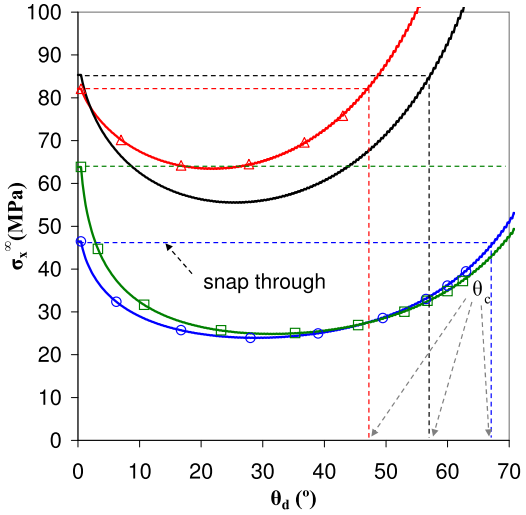

(b)

Figure 13.4: BEM results. (a) Applied stress with respect to the normal relative displacements at point A(a,0) and (b) applied stress with respect to the semidebond angle for different interface properties and $\lambda = 0.3$.

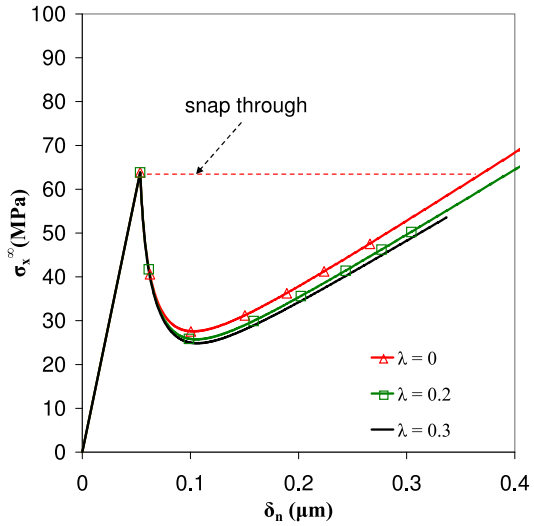

(a)

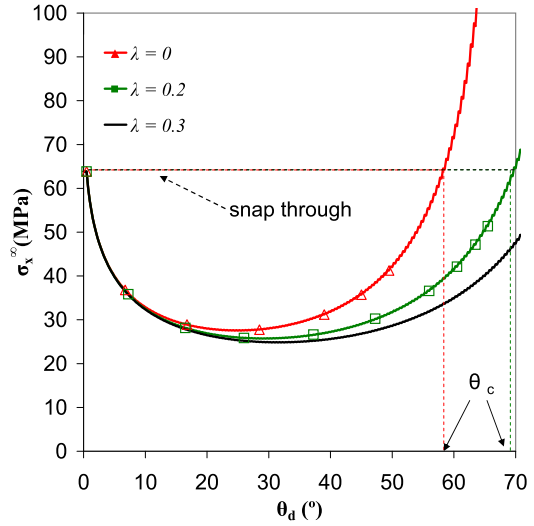

(b)

Figure 13.5: BEM results. (a) Applied stress with respect to the normal relative displacements at point A(a,0) and (b) applied stress with respect to the semidebond angle for different values of λ with $G_{Ic} = 2\text{Jm}^{-2}$, $\bar{\sigma}_c = 90$ MPa and $k_n/k_t = 3$.

Table 13.3: Critical remote load which produces the crack onset, σ_c^∞, and critical semidebond angle, θ_c, for different values of λ and the different considered combinations of the fibre-matrix interface properties.

N°	σ_c^∞ (MPa)	$\sigma_c^\infty/\bar{\sigma}_c$	θ_c (°)		
			$\lambda = 0$	$\lambda = 0.2$	$\lambda = 0.3$
1	46.5	0.775	54.25	62.75	67.75
2	82.1	1.368	40.25	44.75	47.25
3	63.9	0.710	58.25	69.75	> 70
4	85.3	0.948	47.75	53.75	57.25

way the load is applied and/or the modeling two or more inclusions could make σ_c^∞ become dependent on the value of λ.

The fact that σ_c^∞ is independent of λ in the present problem will also be reflected throughout the numerical results presented herein after in the different parametric studies.

Nevertheless, the value of θ_c is highly affected by λ. As can be observed in the above-mentioned figures and in Table 13.3, the semiangle θ_c increases when the value of λ becomes higher, which corresponds to decreasing fracture energy G_c with increasing λ as shown in Figure 4.6. The above-mentioned influence of λ is also clearly seen in Figure 13.5 where the following properties are assumed: $G_{Ic} = 2\text{Jm}^{-2}$, $\bar{\sigma}_c = 90$ MPa and $k_n/k_t = 3$ and only the value of λ is varied.

Effect of the relation between k_n and k_t. A second study determines the influence of the value of k_t in relation with k_n. For this study the properties defined previously for Combination 3 ($G_{Ic} = 2\text{Jm}^{-2}$ and $\sigma_c = 90$ MPa) are assumed. These values correspond to the combination which presented the most brittle interface behavior, making the hypothesis of the present interface model represent appropriately a possible real composite material behavior.

As assumed in (4.7), the ratio k_n/k_t is directly related to the value of the Poisson ratio of the interface elastic layer. Thus, for this study we will consider 3 different cases: $k_n/k_t = 1$, $k_n/k_t = 2.66$ and $k_n/k_t = 3$, the last two cases implying a value of the Poisson ratio of the interface $\nu = 0.2$ and $\nu = 0.25$ respectively. The first case, chosen for its simplicity, is not physically possible (there is no corresponding value of ν), at least if we consider isotropic elastic properties of the interface layer as we have presented in this

section. Nevertheless, if we consider that the layer has orthotropic elastic properties, the case $k_n/k_t = 1$ may have a physical meaning.

Table 13.4: Loads which produce the crack onset, σ_c^∞, and critical semidebond angle, θ_c, for different values of λ and for different values of the ratio k_n/k_t.

k_n/k_t	σ_c^∞ (MPa)	$\sigma_c^\infty/\bar{\sigma}_c$	θ_c (°)		
			$\lambda = 0$	$\lambda = 0.2$	$\lambda = 0.3$
1	69.2	0.769	54.25	68.25	> 70
2.66	64.5	0.717	57.75	69.50	> 70
3	63.9	0.710	58.25	69.75	> 70

In part (a) of Figures 13.6-13.8 the applied remote stress, σ_x^∞, is plotted as a function of the normal relative displacement (opening), δ_n, obtained at point A.

In part (b) of these figures the (minimum) remote stress, σ_x^∞, needed to cause crack growth is plotted versus the semidebond angle θ_d (defined in figure 13.1(b)). Again from these figures it is possible to obtain an estimation of the value, θ_c, reached by the semidebond angle after the initial unstable crack growth, and also of the load, σ_c^∞, which produced the growth.

Table 13.4 summarizes the values of the σ_x^∞, $\sigma_x^\infty/\bar{\sigma}_c$ and θ_c for the different values of the ratio k_n/k_t considered.

From Figs. 13.6-13.8 it can be observed that the variation of the tangential stiffness of the interface, k_t, does not significantly affect the values of the critical stress σ_c^∞ or the semiangle θ_c. Larger values of k_t implying larger values of σ_c^∞ and smaller values of θ_c. In Figure 13.8(b), θ_c values are larger than 70° and they are not shown.

As expected, due to results of the parametric study of the previous subsection, the value of the semiangle θ_c increases when the value of λ becomes higher.

Effect of the inclusion size. The last parametric study has been carried out to determine the influence of the size of the inclusion on the onset and growth of the debond crack, as discussed in [112]. Again the interface properties defined previously for Combination 3 in Table 13.2 ($G_{Ic} = 2\text{Jm}^{-2}$, $\sigma_c = 90$ MPa and $k_n/k_t = 3$) are assumed. The problem is solved for different inclusion radii, see Table 13.5.

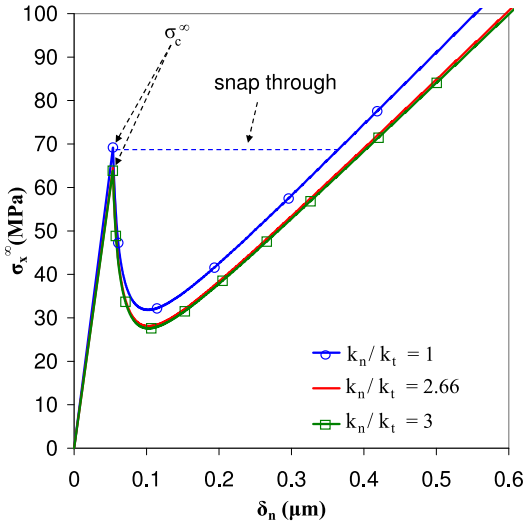

(a)

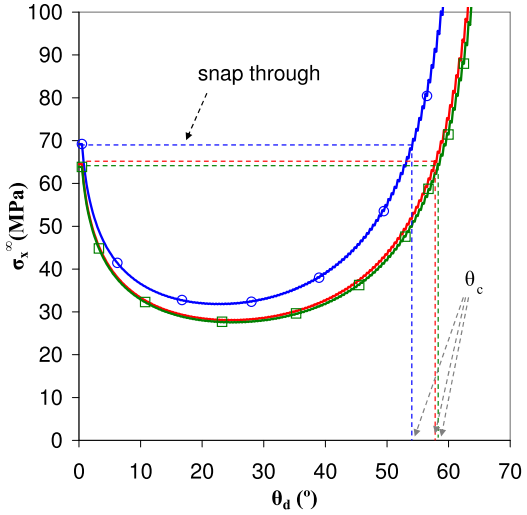

(b)

Figure 13.6: BEM results (a) Applied stress with respect to the normal relative displacements δ_n at point A, see Fig. 13.1, and (b) applied stress with respect to semidebond angle θ_d for different values of the ratio k_n/k_t and $\lambda = 0$.

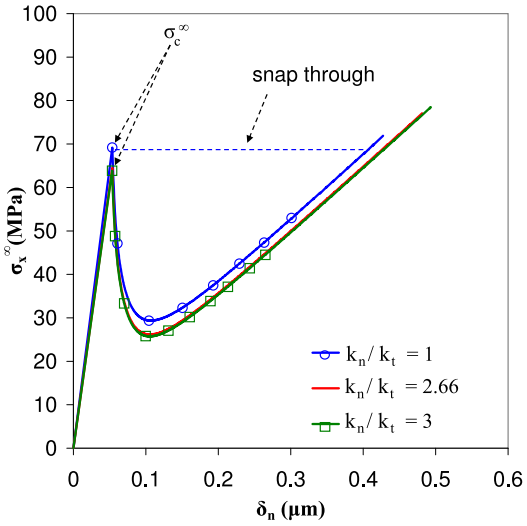

(a)

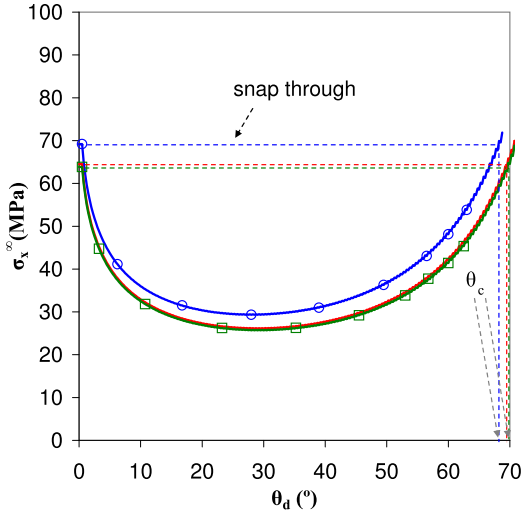

(b)

Figure 13.7: BEM results (a) Applied stress with respect to the normal relative displacements δ_n at point A, see Fig. 13.1, and (b) applied stress with respect to semidebond angle θ_d for different values of the ratio k_n/k_t and $\lambda = 0.2$.

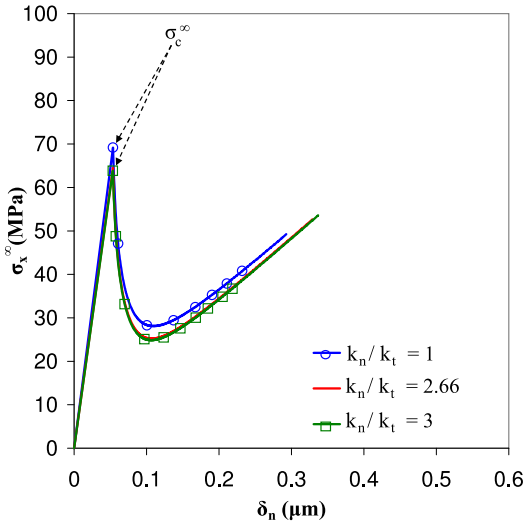

(a)

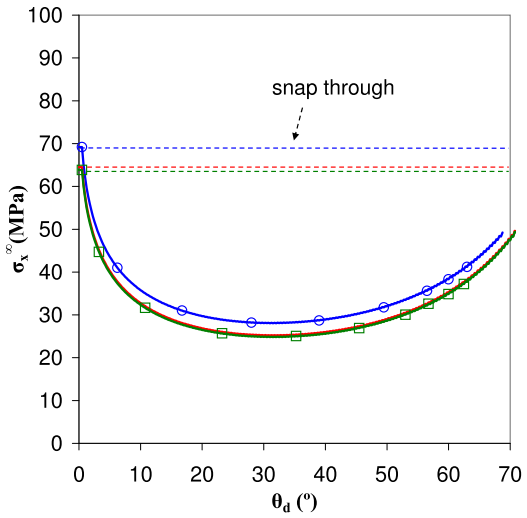

(b)

Figure 13.8: BEM results (a) Applied stress with respect to the normal relative displacements δ_n at point A, see Fig. 13.1, and (b) applied stress with respect to semidebond angle θ_d for different values of the ratio k_n/k_t and $\lambda = 0.3$.

Table 13.5: Considered inclusion radii with $G_{Ic} = 2\text{Jm}^{-2}$, $\sigma_c = 90$ MPa and $k_n/k_t = 3$.

$a(\mu\text{m})$	0.375	0.75	3.75	7.5
γ	1.99	1.4	0.62	0.44

Table 13.6: Loads which produce the crack onset, σ_c^∞, and critical semidebond angle, θ_c, for different values of λ and for different inclusion sizes.

a (μm)	σ_c^∞ (MPa)	$\sigma_c^\infty/\bar{\sigma}_c$	θ_c (°)		
			$\lambda = 0$	$\lambda = 0.2$	$\lambda = 0.3$
0.375	177.0	1.967	35.25	39.25	40.75
0.75	115.6	1.284	41.25	45.75	48.25
3.75	68.4	0.760	54.75	63.75	69.25
7.5	63.9	0.710	58.25	69.75	> 70

In a similar way as in the previous sections, in part (a) of Figures 13.9-13.11 the applied remote stress, σ_x^∞, is plotted as a function of the opening, δ_n, obtained at point A. In part (b) of Figures 13.9-13.11 the (minimum) remote stress, σ_x^∞, needed to cause crack growth is plotted versus the semidebond angle θ_d. From these figures it is possible to obtain an estimation of θ_c and σ_c^∞. Table 13.6 summarizes the values of the σ_c^∞, $\sigma_c^\infty/\bar{\sigma}_c$ and θ_c for the different values of a studied.

The results obtained are very similar to those obtained in a different way in [112]: as the inclusion radius, a, decreases, the value of the critical stress increases. It can also be seen that the value of the critical semidebond angle, θ_c, decreases when the radius of the inclusion decreases.

In Figure 13.12 the effect of inclusion size on the critical load that produces the debond onset, σ_c^∞, is shown. The marked points on one curve represent cases solved by BEM, and the continuous lines are obtained by the analytical solution developed in Section 4, expression (13.1). As mentioned before, λ does not affect the value of σ_c^∞, the same curve then being obtained in Figure 13.12 for different values of λ. Nevertheless, it is shown from the analytical solution for σ_c^∞, obtained from (13.1), that the ratio k_n/k_t slightly affects the behavior of the fibre-matrix system. As can be observed from (13.1), $\sigma_c^\infty \sim \frac{1}{a}$ for vanishing values of a, whereas it approaches

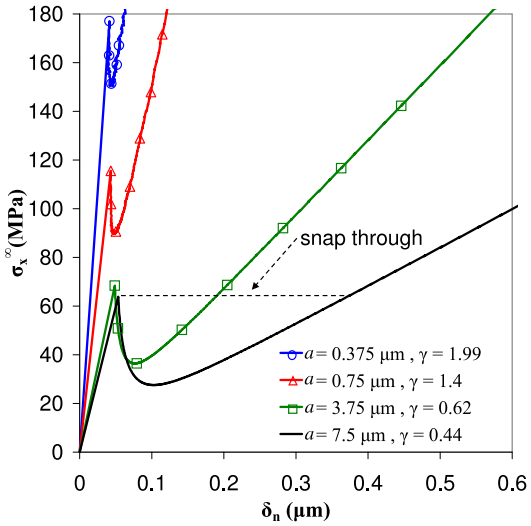

(a)

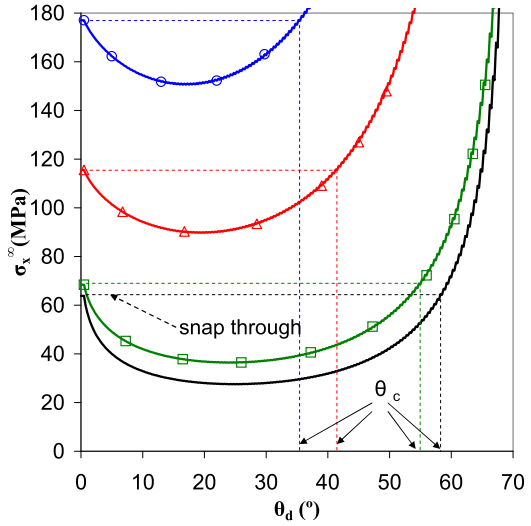

(b)

Figure 13.9: BEM results (a) Applied stress with respect to the normal relative displacements δ_n at point A, see figure 13.1, and (b) applied stress with respect to the semidebond angle θ_d for different inclusion sizes and $\lambda = 0$.

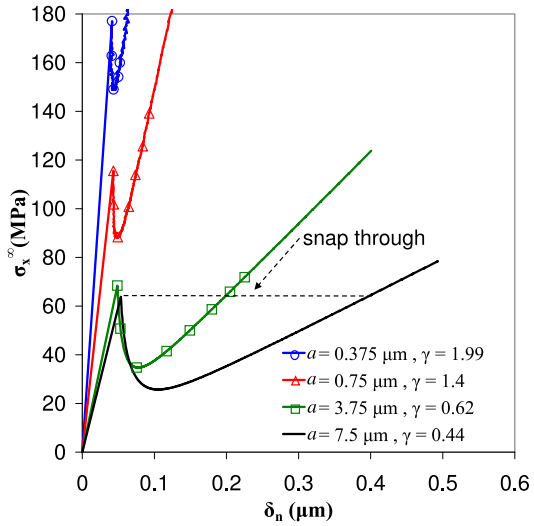

(a)

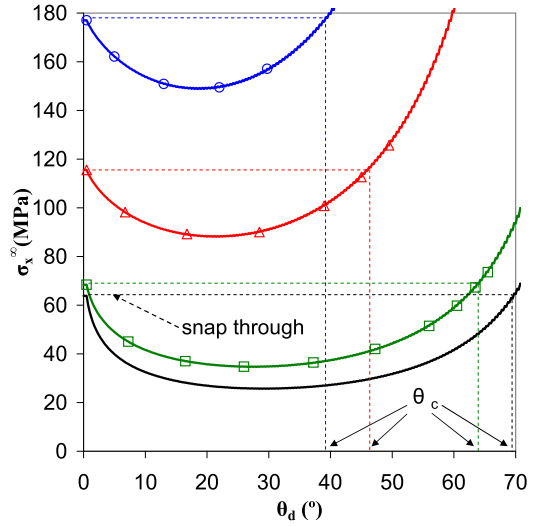

(b)

Figure 13.10: BEM results (a) Applied stress with respect to the normal relative displacements δ_n at point A, see figure 13.1, and (b) applied stress with respect to the semidebond angle θ_d for different inclusion sizes and $\lambda = 0.2$.

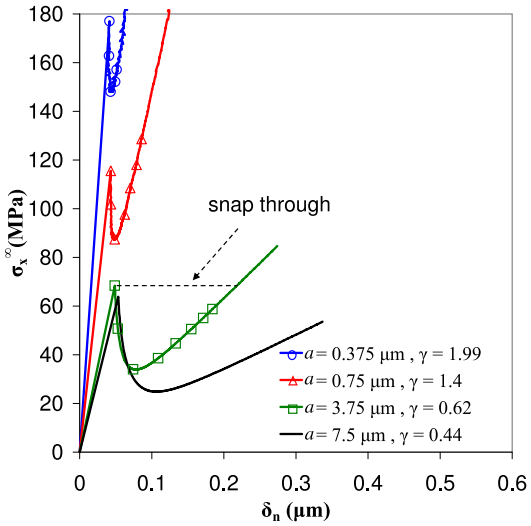

(a)

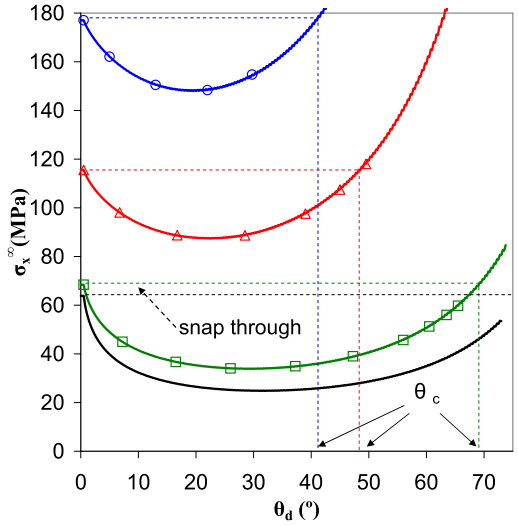

(b)

Figure 13.11: BEM results (a) Applied stress with respect to the normal relative displacements δ_n at point A, see figure 13.1, and (b) applied stress with respect to the semidebond angle θ_d for different inclusion sizes and $\lambda = 0.3$.

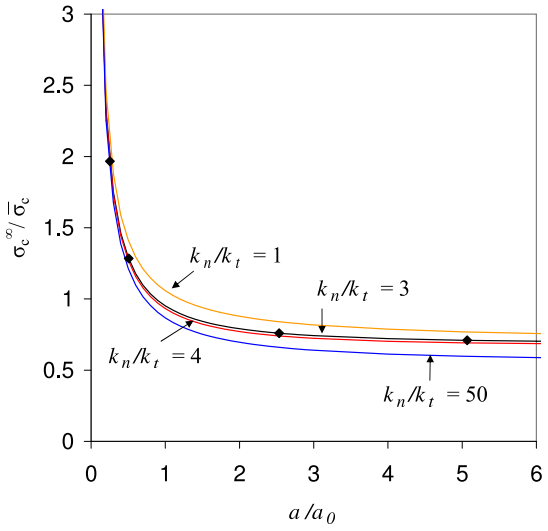

(a)

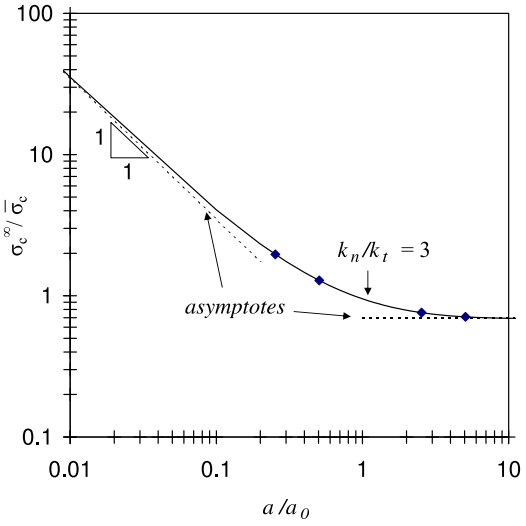

(b)

Figure 13.12: Comparison of BEM and analytical results. Inclusion size effect on the critical remote tension that produces the growth, σ_c^∞, as function of a/a_0.

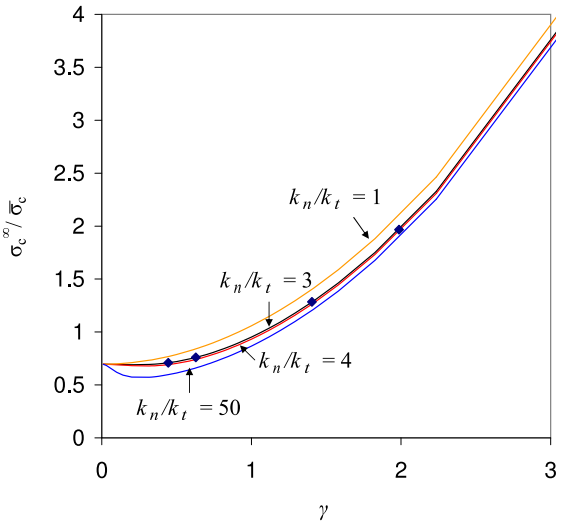

(a)

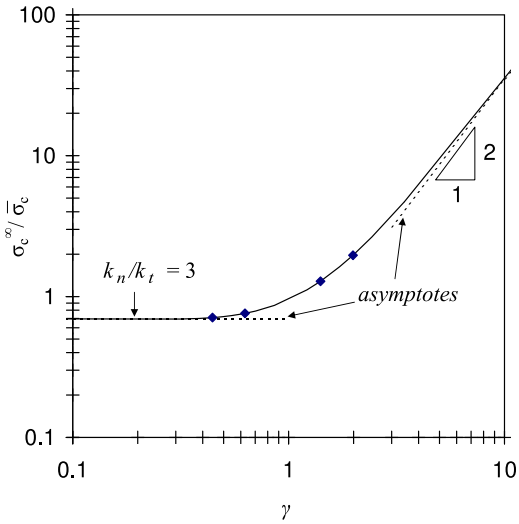

(b)

Figure 13.13: Comparison of BEM and analytical results. Inclusion size effect on the critical remote tension that produces the growth, σ_c^∞, as function of γ and a ratio $k_n/k_t = 3$.

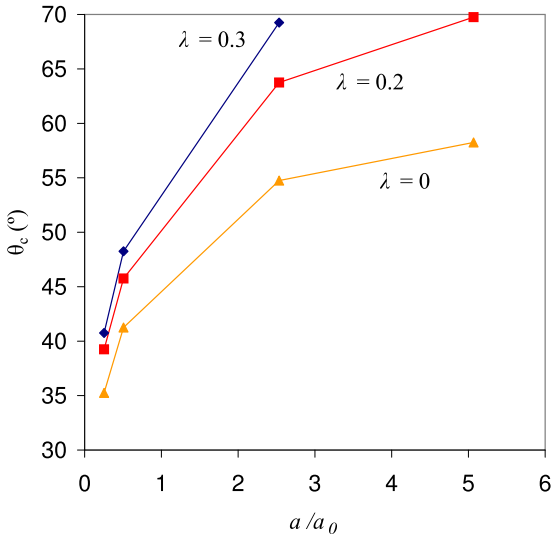

(a)

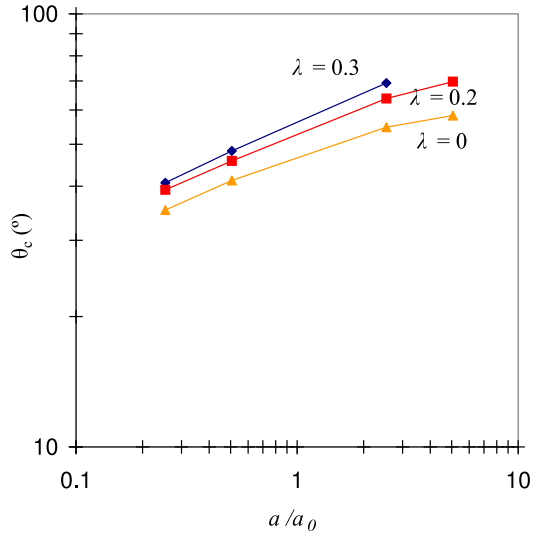

(b)

Figure 13.14: BEM results. Inclusion size effect on the critical semidebond angle, θ_c, for different values of λ and a ratio $k_n/k_t = 3$.

a constant value for $a \to \infty$, see asymptotes indicated in Figure 13.12(b). In Figure 13.13 the dependence of σ_c^∞ on the structural dimensionless parameter γ is depicted, the corresponding asymptotes also being indicated in Figure 13.13(b).

It is clear from the numerical results presented that the interface crack (debond) onset begins at the point A($r = a$, $\theta = 0$). Thus, in order to clarify which variables are governing the critical value of the remote tension σ_c^∞, it is instructive to rewrite equation (13.1) in terms of two dimensionless parameters, ξ:

$$\xi = k_t/k_n \tag{13.8}$$

and γ (13.7). Applying the failure criteria for pure fracture mode I at point A, $\sigma(A) = \bar{\sigma}_c$ and using (13.1) leads to the following expressions of σ_c^∞ normalized by $\bar{\sigma}_c$:

$$\frac{\sigma_c^\infty}{\bar{\sigma}_c} = \frac{\gamma^2}{(1+\kappa_m)E^*} \cdot \frac{4AC}{A+BC}, \tag{13.9}$$

where

$$A = 12\mu_m^2 + \frac{\xi(\kappa_m + t)(1+\kappa_i t)E^{*2}}{(2\gamma^2)^2} + \frac{\mu_m(1+\xi)(1+3\kappa_m+(3+\kappa_i)t)E^*}{2\gamma^2}, \tag{13.10}$$

$$B = 6\mu_m + \frac{(1+\kappa_i t)E^*}{2\gamma^2}, \tag{13.11}$$

$$C = 4\mu_m + \frac{(2+(\kappa_i - 1)t)E^*}{2\gamma^2}, \tag{13.12}$$

From equation (13.9) it can be seen that σ_c^∞ depends only on $\bar{\sigma}_c$, γ and ξ, once the elastic properties of a bimaterial system are defined. Additionally, as follows from the parametric study shown in Figures 13.12(a) and 13.13(a), the dependence of σ_c^∞ on ξ is relatively weak.

The inclusion size effect on the critical semidebond angle, θ_c, is shown in Figure 13.14. It can be seen that the fracture mode sensitivity parameter λ affects the value of θ_c, obtaining different curves for different values of λ while keeping constant the ratio $k_n/k_t = 3$.

Detailed study of a particular case. Among all the parametric studies carried out, a particular case is chosen to analyze in detail the behavior of the displacements and stresses along the interface. The material properties taken are $G_{Ic} = 2\text{Jm}^{-2}$, $\bar{\sigma}_c = 90$ MPa $k_n/k_t = 3$ and $\lambda = 0.2$. A radius a=7.5μm is also considered.

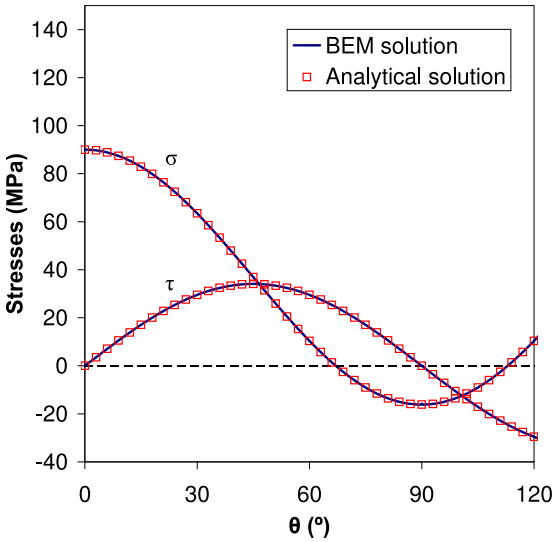

(a)

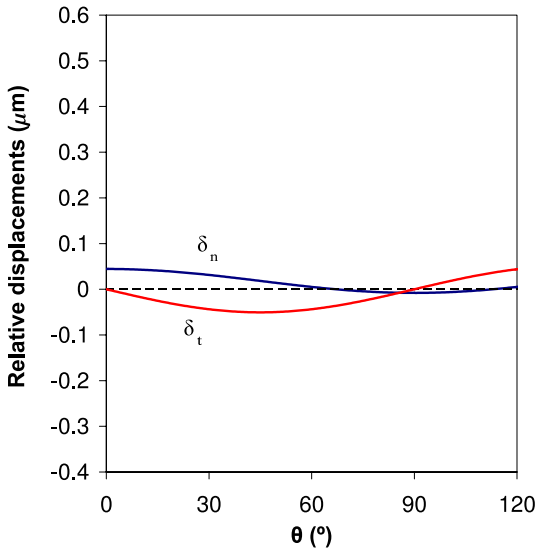

(b)

Figure 13.15: (a) Comparison of BEM and analytical solution for stresses, and (b) BEM solution for relative displacements along the fibre-matrix interface for the initial load step (before crack onset).

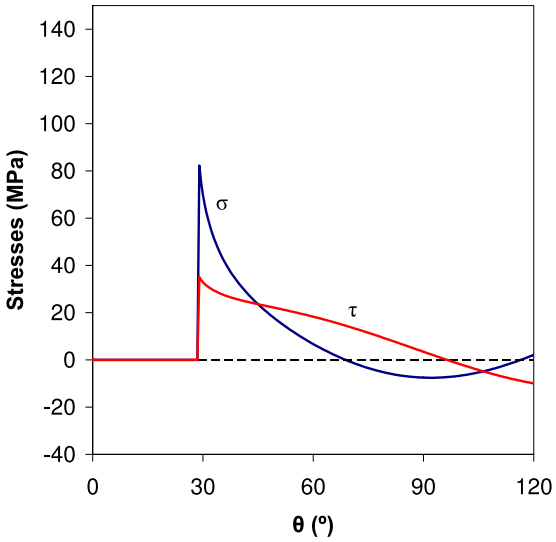

(a)

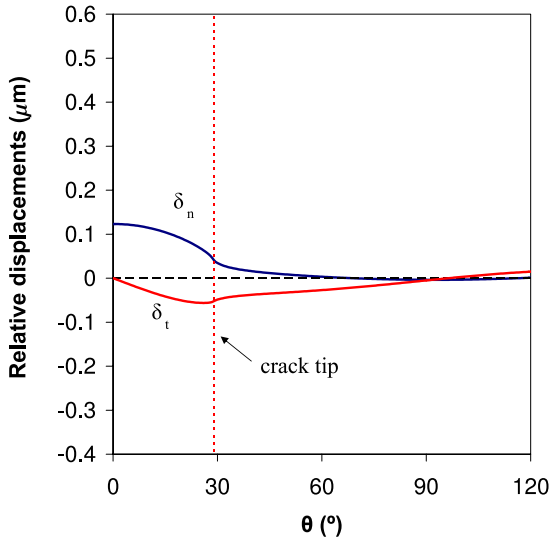

(b)

Figure 13.16: BEM solution for (a) stresses and (b) relative displacements along the fibre-matrix interface for a load step with semidebond angle $\theta_d = 29°$.

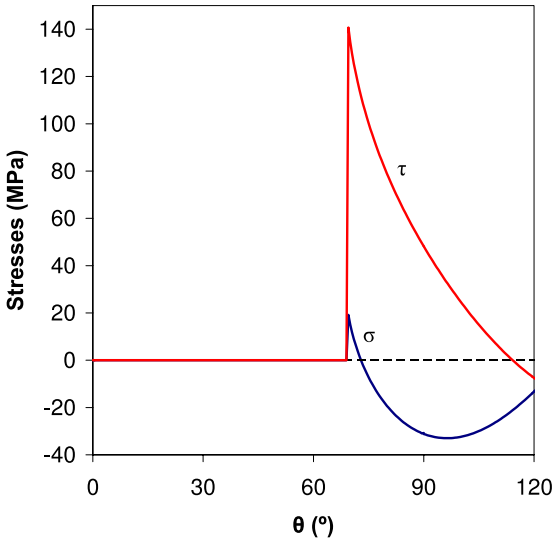

(a)

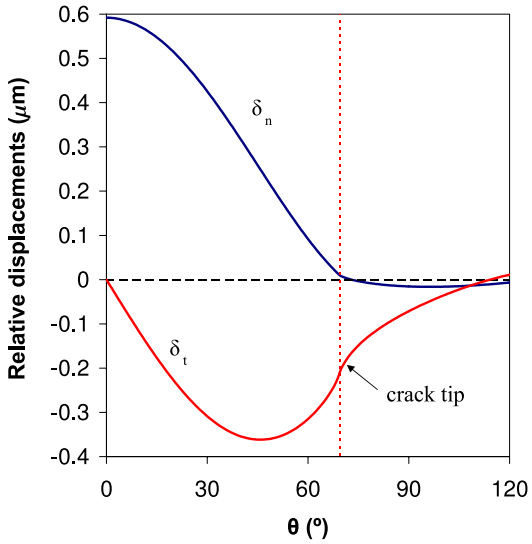

(b)

Figure 13.17: BEM solution for (a) stresses and (b) relative displacements along the fibre-matrix interface for a load step with semidebond angle $\theta_d = \theta_c = 69.5°$.

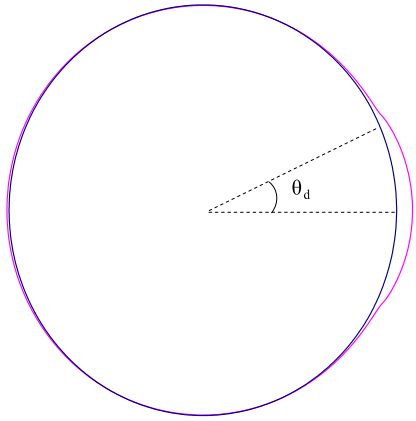

(a)

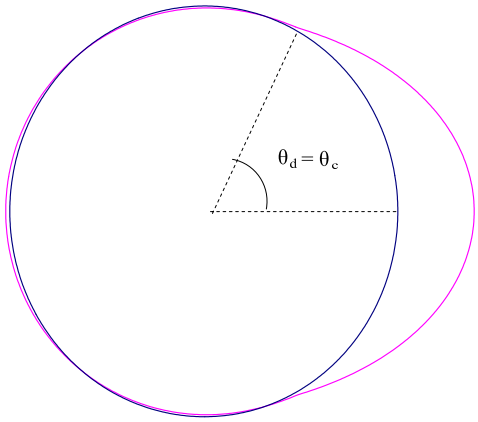

(b)

Figure 13.18: Deformed shape multiplied by 5 obtained when (a) $\theta_d = 29°$ and (b) $\theta_d = 69.5°$.

The results shown in Fig. 13.15 correspond to the applied load which causes the failure of the first interface point, A(a,0).

The values of the normal and tangential stresses along the fibre-matrix interface obtained by BEM and the analytical solution introduced in [66] and developed in Section 4 are shown in Fig. 13.15(a). The excellent agreement between the BEM solution and the analytical solution (13.1) is noteworthy.

The normal and tangential relative displacements along the interface obtained by BEM are plotted in Fig. 13.15(b).

An intermediate load step is shown in Fig. 13.16, corresponding to the local minimum value of σ_x^∞ in Figs. 13.3, 13.7 and 13.10. This step is reached when $\theta_d = 29^\circ$. In Fig. 13.16(a) of the figure the values of the normal and tangential stresses along the fibre-matrix interface obtained by BEM are shown. In part Fig. 13.16(b) the normal and tangential relative displacements are plotted. In this situation, the applied load σ_x^∞ is lower than the load needed to initiate the crack, and therefore it corresponds to the period of unstable growth.

Finally the solution for the load step in which the crack stops its unstable growth is shown in Fig. 13.17. In this load step $\theta_d = \theta_c = 69.5^\circ$. In Fig. 13.17(a) of this figure the values of the normal and tangential stresses are shown while in Fig. 13.17(b) the normal and tangential relative displacements are plotted.

From Figs. 13.15-13.17 it is interesting to notice how the tangential stresses become more important as the crack length becomes longer, since the orientation of the crack tip changes as the crack propagates.

The deformed shape obtained for the fibre-matrix system is shown in Figure 13.18 for the above described load steps with $\theta_d = 29^\circ$ and $\theta_d = 69.5^\circ$.

13.1.2 Fibre-matrix debond initiation and growth under biaxial (tension-tension or tension-compression) loads

In this subsection the same material properties and BEM model as in the previous subsection has been considered. The present study is focused in the crack onset and evolution when a constant remote biaxial load is applied. Considering $\sigma_x^\infty > 0$ as the dominant load and a secondary transversal load in y-direction verifying $|\sigma_y^\infty| \leq \sigma_x^\infty$. Again plane strain state is considered.

The LEBI properties considered are $G_{Ic} = 2\text{Jm}^{-2}$, $\bar{\sigma}_c = 90$ MPa, $k_n/k_t = 4$ and the inclusion radius is a=7.5μm. The parameter λ takes the following values: 0, 0.2 and 0.3.

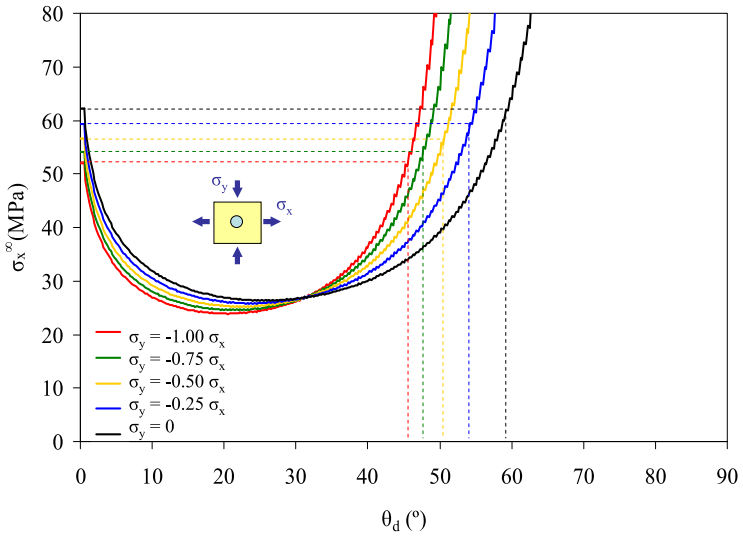

(a)

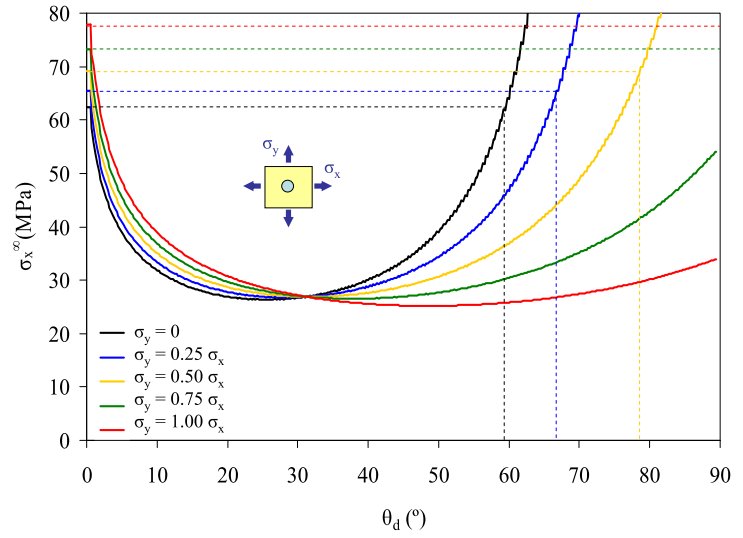

(b)

Figure 13.19: BEM results, applied stress with respect to semidebond angle for different values of σ_y^∞ and $\lambda = 0$.

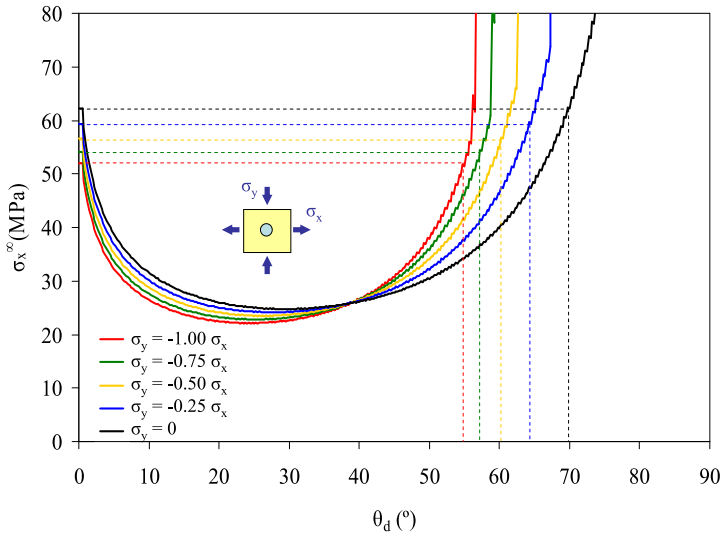

(a)

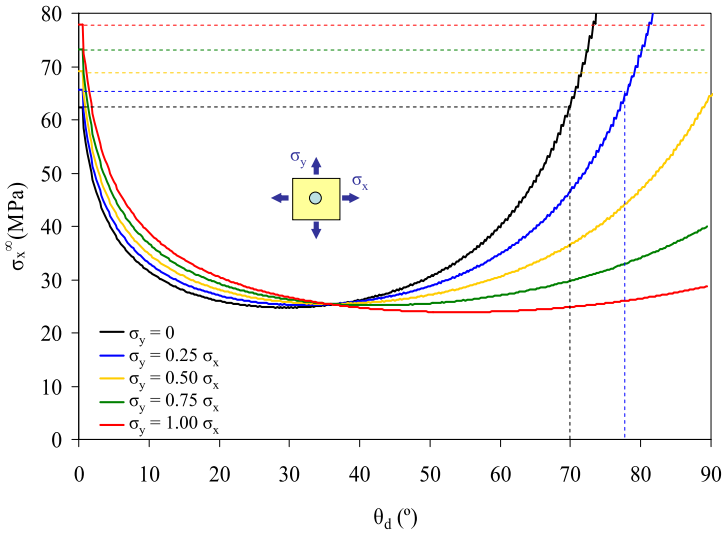

(b)

Figure 13.20: BEM results, applied stress with respect to semidebond angle for different values of σ_y^∞ and $\lambda = 0.2$.

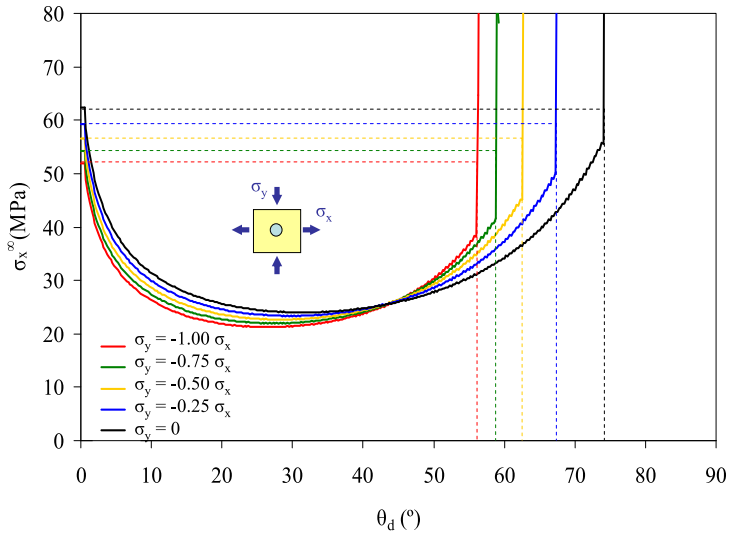

(a)

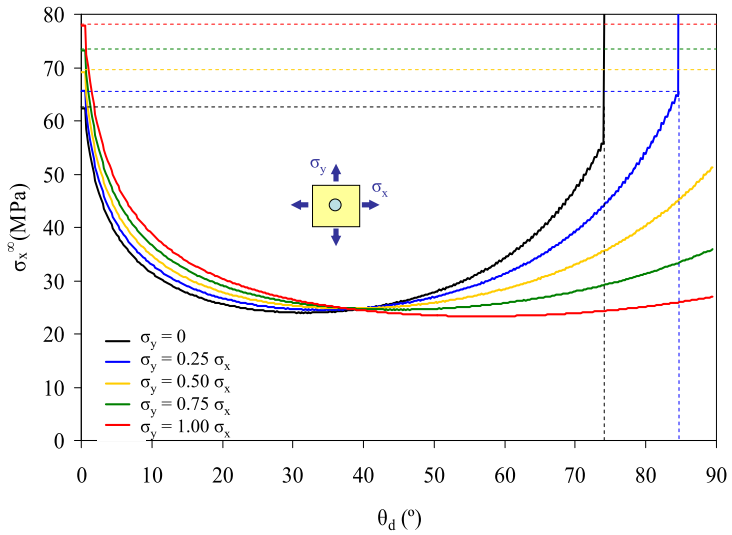

(b)

Figure 13.21: BEM results, applied stress with respect to semidebond angle for different values of σ_y^∞ and $\lambda = 0.3$.

From Figs. 13.19-13.21 the (minimum) remote stress, σ_x^∞, needed to cause crack growth is plotted versus the semidebond angle θ_d (defined in Fig. 13.1(b). It should be noted that from these figures it is possible to obtain an estimation of the value, θ_c, reached by the semidebond angle θ_d after the initial unstable crack growth, and also of the load, σ_c^∞, which produced the growth for different combinations of biaxial loads and different values of the parameter λ. As mentioned before the load applied in x-direction is considered dominant while the loads in y-direction are varied in order to obtain the desired combinations. In Figs. 13.19-13.21(a) the traction-compression combinations are shown while in Figs. 13.19-13.21(b) the traction-traction combinations can be observed.

As can be seen from these results, when the compression load in y-direction is larger the load necessary for crack debonding is smaller. In a similar way θ_c becomes lower when the compression load increases.

On the other hand, when the traction load in y-direction is larger the load necessary for crack debonding is also larger. Also, θ_c becomes higher when the traction load increases, eventually producing a very large debond of the fibre (unstable growth for $\theta_d > 90°$) for the highest loads of traction.

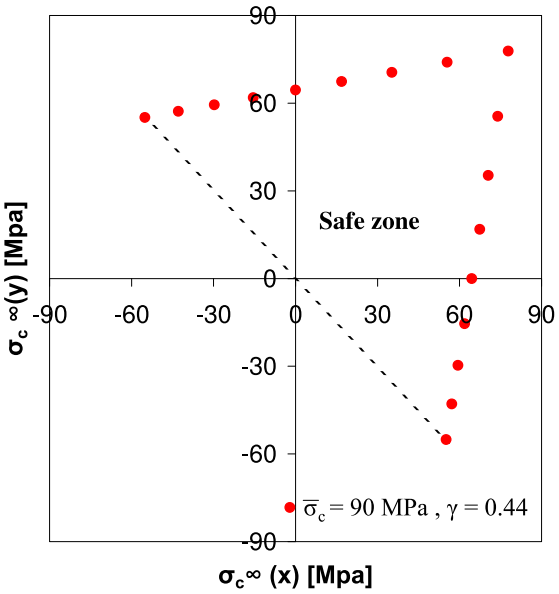

Figure 13.22: Failure curve of a circular inclusion under biaxial transversal loads with $\bar{\sigma}_c = 90$MPa and $k_n/k_t = 4$.

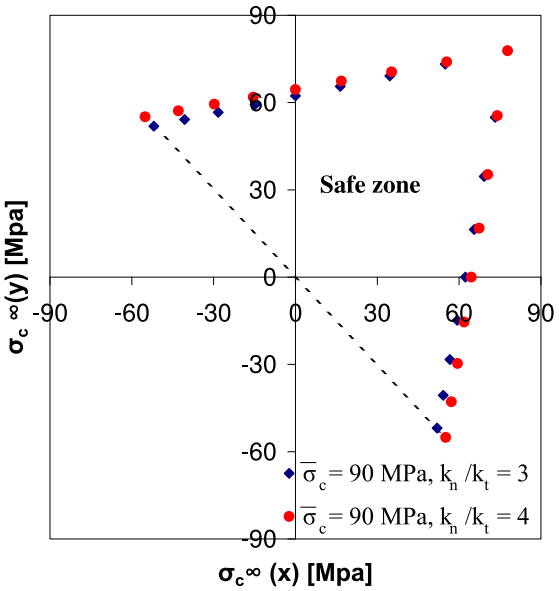

Figure 13.23: Failure curve of a circular inclusion under biaxial transversal loads with $\bar{\sigma}_c = 90$MPa and two values of k_n/k_t.

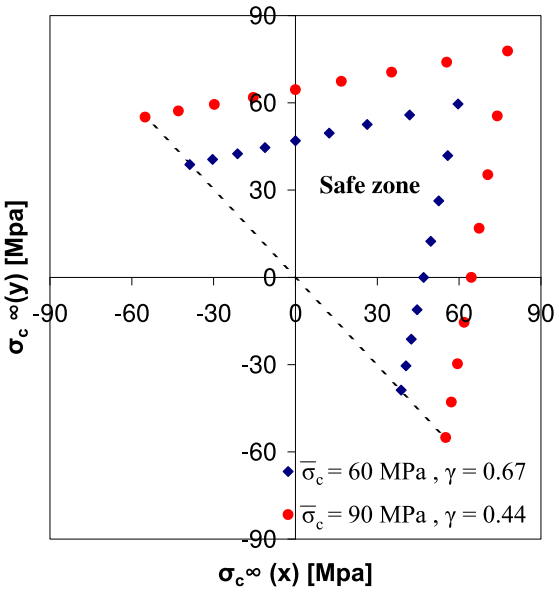

Figure 13.24: Failure curve of a circular inclusion under biaxial transversal loads with $\bar{\sigma}_c = 90$MPa, $\bar{\sigma}_c = 60$MPa and $k_n/k_t = 4$.

From all the cases solved it is possible to obtain a failure curve of a circular inclusion under biaxial transversal loads, see Fig. 13.22. It can be assumed that the triangular area defined by the points is a safe zone.

In a similar way as in previous sections the influence of k_n/k_t is studied, see Fig. 13.23. The interface properties taken to obtain the second curve are $G_{Ic} = 2\text{Jm}^{-2}$, $\bar{\sigma}_c = 90$ MPa and $k_n/k_t = 3$.

As can be seen in Fig. 13.23 the k_n/k_t ratio has only a slightly influence on the failure curve, this behavior was expected due to the previous results shown in the previous section for a uniaxial load.

In Fig. 13.23 the following interface properties were taken to obtain the second curve $G_{Ic} = 2\text{Jm}^{-2}$, $\bar{\sigma}_c = 60$ MPa, $k_n/k_t = 4$ ($\bar{\sigma}$ value is varied only).

The obtained results are in accordance with some experimental evidence. Paris *et. al.* [133] and Correa [45] carried out biaxial tests, where increasing compressions loads (as secondary loads) led to decreasing failure load (dominant).

13.2 Multi fibre model

The LEBI model seems to be an adequate model to study the behavior of fibre-matrix interfaces, as shown in the previous section for the case of the single fibre model. Nevertheless, in actual composites the fibres are embedded in a matrix forming clusters of cylindrical inclusions. Thus, the interaction among fibres as well as the distances among them play an important role, see Fig. 13.25.

In the present section an initial study of this problem is done to illustrate the capabilities of the BEM code developed. Three fibres inside a continuous surrounding matrix were modeled by means of the LEBI model, see Fig. 13.26. The material properties considered are the same as in the previous section and the interface properties are $G_{Ic} = 2\text{Jm}^{-2}$, $\bar{\sigma}_c = 90$ MPa, $k_n/k_t = 4$, with $\lambda = 0.3$. It should also be mentioned that the linear contact part of the LEBI formulation, see Section 4.2, is deactivated.

The radius of the fibres has been taken as 7.5 μm and the matrix that surround the fibres is a square of size 1mm. 2192 continuous linear boundary elements are used: 32 elements for the external boundary of the matrix and two uniform meshes of 360 elements, per fibre, to model the fibre-matrix interface (therefore, the polar angle of each element is 1°).

As can be seen in Fig. 13.27, an unstable onset on an interface crack is obtained in the multifibre model, in a similar way as in the single fibre

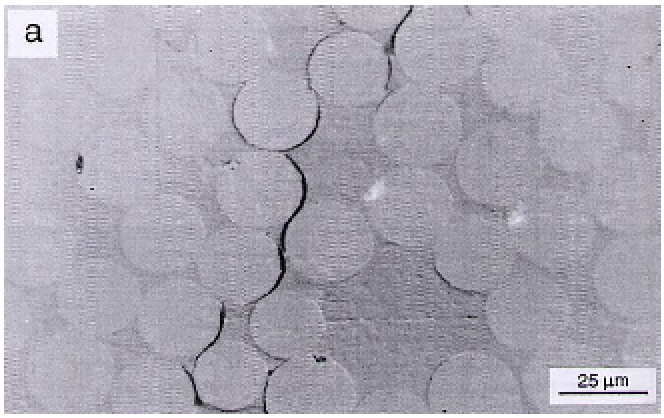

Figure 13.25: Example of a typical distribution of glass fibres in a glass-epoxy composite material.

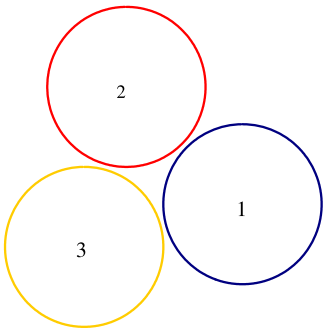

Figure 13.26: Multifibre model studied by means of BEM

model. After the initial crack onset (ending up at point A in Fig. 13.27) is followed by a stable interface crack growth (higher loads are needed to reach point B). Then, a second unstable crack onset in a different inclusion is obtained (ending up at point C), followed by stable growth of the second crack to reach point D. It is remarkable to comment that the spurious behavior shown between points C and D, are caused because some interface points are becoming in contact and also because the crack growth is being achieved in both cracks. Point E shows a third unstable onset, this time in the third fibre. Although the model is able to represent more debondings along the matrix-fibre interfaces further than point F, an actual behavior would probably be a crack kinking into the matrix followed by a coalescence of cracks. In fact it is possible that the actual behavior do not reach point D.

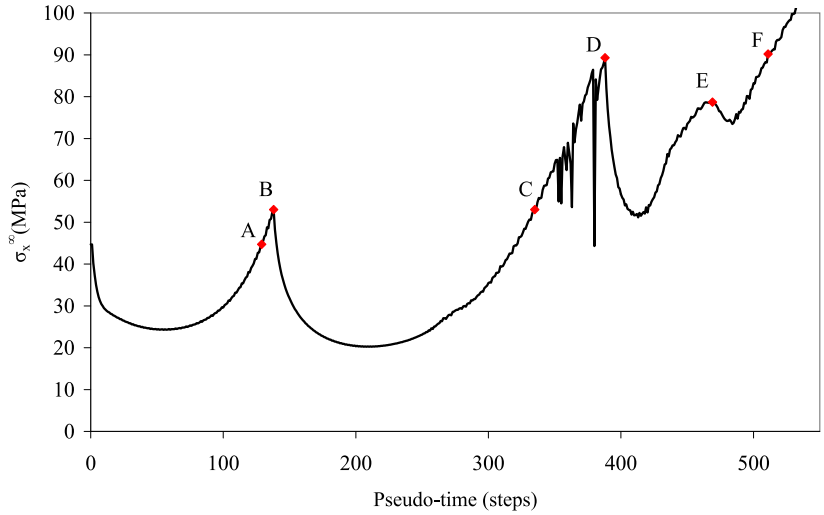

Figure 13.27: BEM results, applied stress with respect to a pseudo-time (load steps) in the multifibre model.

In Fig. 13.28, the different deformed shapes obtained at the points marked on Fig. 13.27 are presented. There it can clearly be seen the crack onset produced at those moments.

Although this is only a preliminary result, the capability of the numerical tool developed to capture a more complex debonding mechanism in fibre clusters has clearly been demonstrated.

13.3 Concluding remarks

The LEBI formulation has proved to be an adequate tool to represent the crack onset and growth of interface cracks between fibre and matrix under remote transversal loads.

A deep study of an isolated fibre has been carried out in this chapter. An analytical solution for the stresses along the undamaged interface for a circular inclusion under uniform transverse tension has been obtained from the work of Gao [66]. The problem of a circular inclusion under transverse tension assuming material properties of a common composite material (glass fibre and epoxy matrix) and the LEBI model has been solved, by the collocational BEM. An excellent agreement between the present BEM results and the analytical expressions for undamaged linear elastic interface has been obtained.

An important point is that not only the numerical solution of stresses

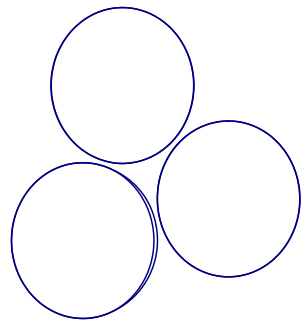

(a) Point A

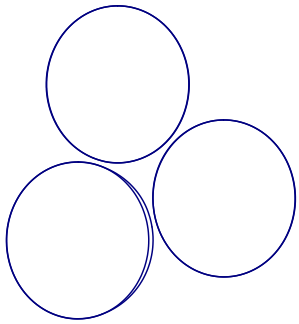

(b) Point B

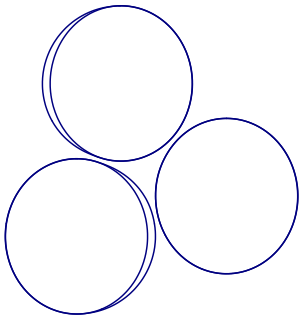

(c) Point C

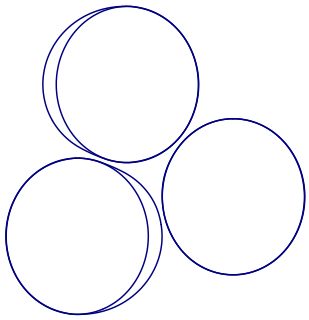

(d) Point D

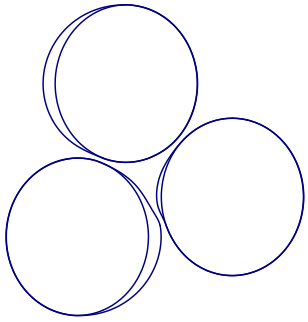

(e) Point E

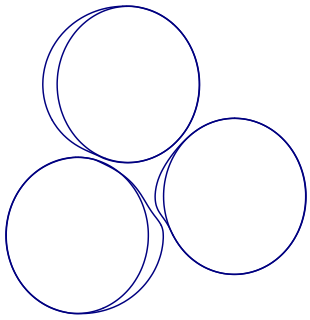

(f) Point F

Figure 13.28: Deformed shapes obtained at different load steps shown in Fig. 13.27.

and displacements for a crack at a linear elastic interface is presented, but also the crack onset and growth along the fibre-matrix interface is modeled using the new constitutive law of the LEBI model proposed.

The analytical solution obtained from Gao's work [66] has led to a new analytical expression (13.9) for the critical remote tension σ_c^∞. It has been shown that for fixed elastic bi-material properties, σ_c^∞ normalized by the interface strength in pure fracture mode I, $\bar{\sigma}_c$, depends only on two dimensionless parameters: structural parameter γ (13.7), introduced previously in [112], and ξ (13.8) representing the ratio of shear and normal stiffnesses of the continuous spring distribution in reference to a (fictitious) elastic layer.

From the analytical and numerical parametric studies it can be concluded, as expected, that the interface parameters σ_c and G_{Ic} (which appear in the definition of γ) have a great influence on σ_c^∞, as well as on the critical semidebond angle θ_c. The relation k_n/k_t does not seem to have a great influence on σ_c^∞ and θ_c. The parameter λ introduced in the failure criterion has a great influence on θ_c but none in σ_c^∞. It is important to note that the non-influence of λ over σ_c^∞ is caused by the geometry and the way the load is applied in the problem (the first failure point is always acting in pure fracture mode I).

From the numerical results it can be seen that after reaching σ_c^∞, the crack growth becomes unstable. And thus an instability phenomenon called snap-through takes place.

The inclusion size effect on the onset of debonding is observed: as the value of inclusion radius, a, becomes lower, the value of σ_c^∞ becomes higher, similarly to previous results in [112], although with different asymptotic behavior for small inclusion radii. It can also be seen that the value of the critical semidebond angle θ_c decreases when the radius of the inclusion becomes smaller.

The LEBI formulation introduced here for mixed mode crack growth along an interface is also useful for the analysis of fibre-matrix debonding under bi-axial transverse loads [133] as shown in Subsection 13.1.2. A failure curve for a cylindrical inclusion under transversal biaxial loads has been obtained.

Finally, the capability of the LEBI model to predict the onset and growth of debonds in a fibre cluster has been demonstrated.

Chapter 14

Conclusions and future developments

14.1 Conclusions

The work carried out in this thesis has been focused on the two research lines, corresponding to Part 2 and Part 3 of this thesis as defined in the Introduction, respectively:

(i) The development and implementation of a cohesive zone model and a linear elastic-brittle (weak) interface model, both representing non-singular fracture mechanics models, in Boundary Element Method (BEM) codes, as a numerical tool to solve elastic problems; and

(ii) the numerical study of different damage mechanisms in fibre reinforced composites and their joints at macro, meso and micro scales, that may provide support to a subsequent development of physically based failure criteria for these materials in future.

In the following the main contributions of the present thesis grouped in the above mentioned two research lines are detailed. In this sense, first, the contributions to the developments of the models and numerical tools, and, then, to the analysis of some damage mechanisms at composites are listed.

14.1.1 Development of models and numerical tools

In Part 2 of the thesis, two different non-singular fracture mechanics models have been studied. Also different numerical tools have been developed in order to obtain an effective implementation of these models.

Thus, in Chapter 3, a modification of the Ortiz-Pandolfi cohesive model [128] has been proposed. The objective of this proposal has been to model in a more realistic way (from a physical point of view) the compressive behavior in mode I. A good modeling of the compressive behavior allows us the study of different problems in composite materials with crack growing, since a compressive zone ahead of the crack tip is usually presented.

Then, a new Linear Elastic-Brittle Interface (LEBI) Model (continuous spring distribution model) has been introduced and analyzed in Chapter 4. This LEBI formulation allows to study not only of the stress and displacement fields along the zone ahead of the crack tip, but also the crack growth along a priori known crack path, defined usually as an interface or bonded surface. Another important feature of the LEBI model is the capability of modeling mixed mode problems and the possibility to model an elastic contact behavior in an interface point after it breaks. This interface model has been used in Part 3 of the thesis to study different problems in composite materials.

The use of the above mentioned non-singular fracture mechanics models required the development and implementation of suitable algorithms to solve non-linear problems. Two algorithms have been introduced in Chapter 6. A sequentially linear analysis has been developed and implemented to solve problems involving LEBI formulation, presented in Chapter 4. Three variants of the arc-length method (Riks, Ramms and Normal flow procedures) have been developed and implemented for the use in the Cohesive Zone Model (CZM) and Symmetric Galerkin BEM (SGBEM). A successful implementation of the non-linear solving algorithms is critical for capturing instability phenomenons in different damage mechanisms in composite materials.

A SGBEM formulation for problems with cohesive cracks placed inside homogeneous domains and between subdomains has been proposed and implemented. These new capabilities have been implemented in an existing 2D SGBEM code. This SGBEM approach is likely to be suitable for engineering applications involving isotropic elastic materials, e.g. for an analysis of crack initiation and growth in composites modeled as piecewise homogeneous materials at the micro-scale.

As shown by the numerical results in Chapter 7, the cohesive zone formulation correctly modeled the experimentally observed crack growth behavior for the wedge split test. It also agreed very well with a previous FEM crack growth 2D analysis of the load-deflection behavior for the three-point bending test. The SGBEM analysis with cohesive elements has been ca-

pable to follow the instabilities produced by a nearly vertical drop in the loading capacity and snap-back behaviors observed in some cases. All the approaches included and tested in this 2D SGBEM code, give as result an excellent numerical tool, that will allow the study of different instability phenomenons present in some damage mechanisms in composite materials.

The presence of a crack at a linear elastic brittle (weak) interface, which represents a simple model of a thin adhesive layer, has been studied in Chapter 8. First, the governing integral equation for a pressurized crack at the weak interface between identical orthotropic half planes has been deduced. A new dimensionless characteristic structural parameter δ was introduced in this governing integral equation. It relates the adhesive-layer stiffness to the adherent stiffness, taking into account the crack length. Then, the problem of a pressurized crack has been solved by the collocational 2D BEM. An excellent agreement has been obtained between the numerical results by the present BEM code and those shown in [102]. The results provided by this example have been used for a better understanding of the LEBI formulation. These results were useful to verify and improve the LEBI implementation in 2D BEM.

In Chapter 9, closed-form expressions of the integral kernels $U_{ik}(\boldsymbol{x})$, $T_{ik}(\boldsymbol{x})$, $D_{ijk}(\boldsymbol{x})$ and $S_{ijk}(\boldsymbol{x})$ appearing in the 3D Somigliana displacement and traction identities for transversely isotropic elastic materials, and also of the related integral kernels $U_{ik,j}(\boldsymbol{x})$, $U_{ik,jl}(\boldsymbol{x})$, $\Sigma_{ijk}(\boldsymbol{x})$ and $\Sigma^{loop}_{ijkl}(\boldsymbol{x})$, have been obtained. The correctness and validity of the expressions obtained have been proved by solving some examples with known analytical solution. All the expressions obtained have advantageous features as they are expressed in real-variable and they are unique for every material combination. The objective of working on this expressions is that in BEM, efficient expressions of the integral kernels play a very important role. The implementation of these expressions in a 3D BEM code has resulted in an efficient computational code. This code will be used in the future to study composite laminates, that may be considered as transversely isotropic materials, in configurations where 3D effects can not be neglected.

14.1.2 Study cases of damage and failure in composite materials at micro, meso and macro scale

In Part 3 of this thesis, some important problems that include damage and failure in composite materials are dealt with. Numerical studies have been carried out in order to study several aspects of crack onset and growth in these problems. The LEBI model implemented in the collocational 2D

BEM code using the sequentially linear analysis has been used in all these problems.

The interlaminar fracture toughness test for composite materials using the DCB specimen has been studied in Chapter 10. It has been proved that the real behavior of an adhesive layer with a polyester support that joins two unidirectional laminates can be approximated very well by means of the BEM and a distribution of springs which follow a LEBI constitutive law, by adjusting the parameters of the discrete model (G_{Ic}, σ_c, and eventually the number springs that break in a load step). A good agreement of the global load-displacement curve obtained from the laboratory experiments and the present numerical model has been achieved, even in the softening branch of the curve. The symmetric DCB specimen has tested the capability of the LEBI model to study a crack growth in fracture mode I. A problem of a crack growth in a non-symmetrical DCB specimen has also been solved in order to see the influence of the fracture mode mixity.

The behavior of the transversal and delamination cracks in a [0/90] symmetric laminate has been studied in Chapter 11. The predictions obtained with the LEBI model are qualitatively in accordance with those obtained by means of the VCCT [130] applying the framework of classical fracture mechanics. It is remarkable that the onset and unstable growth of the transversal crack requires a significatively lower load (applied strain) than the one needed to the onset of the delamination crack. In most of the analyzed cases, the transversal crack reached the interface between 0° and 90° plies before the delamination crack onset. Once the delamination crack starts to growth three stages can be clearly identified: (i) initial stage - initially a relatively short stable growth of the delamination crack takes place with open traction-free crack faces; (ii) intermediate stage - the delamination crack growth becomes unstable and there is contact between the crack faces, except for the zone close to the crack tip where a kind of bubble appears; (iii) final stage - the delamination crack growth becomes stable again. It is interesting to notice that although the problem configuration (geometry, material and boundary conditions) is symmetric its solution including a transversal and delamination crack may be non-symmetric. This fact was observed in the second stage of the delamination crack growth (unstable), where an non-symmetric growth can be observed in the two branches of the delamination crack. It was also observed that by using some suitable interface properties in the LEBI model for the transversal crack and the delamination crack, the Cook-Gordon mechanism can be obtained in the present numerical model. This fact proves that the formulation and the al-

gorithm used are able to capture this behavior, nevertheless a deeper study regarding this topic is necessary.

The Single Fibre Fragmentation Test (SFFT) has briefly been studied in Chapter 12 using the LEBI model. The results obtained for the SFTT are in agreement, from a qualitatively point of view, with similar results previously obtained by means of a Cohesive Zone Model and the Finite Element Method. From the obtained results an initial stage with a stable crack growth is observed, followed by an almost neutral (slightly stable) crack growth. It should be mentioned that the present problem has been solved without taking into account the elastic contact (interpenetrations of crack faces are allowed). The numerical results obtained may be compared with the results of laboratory tests in order to obtain an estimation of important parameters as it is the case of the fracture energy in mode II, G_{IIc}, of the fibre-matrix interface.

In Chapter 13 the onset and growth of debonds between fibre and matrix in a unidirectional composite lamina under transversal loads have been numerically studied by means of the LEBI formulation. First, the problem of an isolated fibre embedded in a large matrix subjected to far field uni-axial transversal tension has been studied. Then, the effect of biaxial transversal loads in the isolated fibre have been analyzed. Finally, an initial study of onset and growth of debonds in a fibre cluster embedded in a large matrix has also been presented. From the numerical results for the first problem of the isolated fibre under uniaxial transversal load, it can be concluded that values of the ratio between the critical stress needed to cause the crack onset and the critical tension of the interface in mode I, $\sigma_c^\infty/\bar{\sigma}_c$, are in the interval: $0.78 \leq \sigma_c^\infty/\bar{\sigma}_c \leq 1.37$. These values of the ratio have been obtained for different combinations of interface properties. It has also been observed that after the crack onset the initial crack growth is unstable until a critical semidebond angle, θ_c, is reached. θ_c values are highly affected by the fracture mode sensitivity parameter, λ. Thus, for $\lambda = 0$, θ_c values are in the interval $40^\circ \leq \theta_c \leq 58$, while, for example, for $\lambda = 0.2$, θ_c values are in the interval $45^\circ \leq \theta_c \leq 70$, for different combinations of interface properties. The inclusion size effect on the onset of debonding has also been studied numerically and analytically. An analytic expression for the asymptotic study of the size effect on σ_c^∞ has been developed. As the value of the inclusion radius, a, becomes lower, the value of σ_c^∞ becomes higher, similarly to previous results in [112], although with different asymptotic behavior for small inclusion radii. For large inclusion radii σ_c^∞ value is approximately constant. It has also been seen that the value of the critical

semidebond angle θ_c decreases when the radius of the inclusion becomes smaller. The analysis of fibre-matrix debonding under bi-axial transverse loads seems to confirm the idea proposed in [133]. Thus, the presence of a compressive transversal load σ_y^∞ perpendicular to the dominant transversal tension load σ_x^∞ decreases the critical stress, $\sigma_c^\infty = \sigma_x^\infty$, needed to cause the crack growth. With these numerical results a failure curve for a cylindrical inclusion under transversal biaxial loads has been obtained. Finally, the capability of the LEBI formulation to predict the crack onset and growth in a fibre cluster with several fibres (located very close each other) has been shown.

From all the numerical results obtained in the above analysis of different damage mechanisms, it can be concluded that the LEBI formulation is a promising tool to model crack onset and growth in composite materials at all the three levels: macro, meso and micro. Taking into account that, the LEBI model is a non-singular fracture mechanic model with traction concentration at the crack tip, a mesh refinement close to the advancing crack tips is not necessary. This fact, simplifies substantially the problem discretization in the presence of crack propagation since the initial, usually (quasi) uniform, mesh can be used during the crack propagation, where the crack path is known or assumed a priori.

14.2 Future developments

The work carried out in the present thesis will further continue as a more extensive study exploring the possibilities of the two non-singular fracture mechanics models, the Cohesive Zone Model (CZM) and the Linear Elastic Brittle-Interface (LEBI) model, implemented in the BEM codes, in analysis of different damage mechanisms of composite materials. The objective of this analysis will be to contribute to the development of physically based failure criteria of composite materials. This analysis will require to determine the governing parameters of the numerical models comparing their predictions with the experimental results. For this purpose, the solution of inverse problems using experimental results, for the different problems studied, can be carried out in order to obtain the needed parameters of the models (CZM and LEBI model).

With reference to the present implementation of the CZM, the next step in its development will be the modeling of crack growth with a priori unknown crack path. The CZM implementation for cracks in a homogeneous media presented in this thesis assumes a known crack path. However, a

CZM formulation and implementation where the crack path is a priori unknown is required in analysis of some damage mechanisms. Once this formulation and implementation is ready it can be combined with the cohesive interface formulation to solve problems where an interface crack kinks to homogeneous media. This situation is expected to appear, for example, in fibre-matrix debond growth under transverse loads, where kink cracks may coalesce resulting in large cracks.

The inclusion of the effect of friction in the CZM could be also very useful for some applications in composites. In particular, in contact between the crack faces in the delamination problem of cross-plies and in the single fiber fragmentation test, and possibly also in the inter-fibre failure under transversal loads.

The present thesis will also be a starting point to explore the possibilities of different Cohesive Zone Models (CZM) presented in literature, as well as different arc-length solver schemes applied in a SGBEM setting for the above mentioned applications in composite materials.

All the composite problems solved in the present thesis by means of the Linear Elastic-Brittle Interface (LEBI) model will be solved by means of the developed code for CZM and SGBEM and the results will be compared. Such a comparison will be very interesting to judge the adequacy of each model, and it will require also some experimental results. On one hand, the CZM is more general and complex model, it considers a damage zone where a softening takes place. It requires, however, sophisticated non-linear solvers. On the other hand, the LEBI model is substantially simpler, nevertheless able to provide numerical predictions in a good agreement with experiments, as in the case of the interlaminar fracture toughness test.

With reference to LEBI, some further improvements are expected as well. For example, the LEBI formulation can be changed in the compression part, by considering that the critical tangential stress do not vary in presence of contact (the value of $\tau_c(\sigma \leq 0) = \tau_c(90^\circ)$ remaining constant for compressions), also other behaviors should be explored.

The extension of the CZM and the LEBI model to 3D will provide a useful numerical tool that could be implemented in the 3D BEM code to solve problems in composite materials where the 3D effects can not be neglected.

In general all the initial study cases presented in Part 3 of this thesis should be complemented with extensive parametric studies.

In the following a few comments about further possibilities of the CZM and LEBI model in the study of the problems analyzed in Chapter 10 to 13

will be given.

The preliminary study of the interlaminar fracture toughness test of adhesively bonded joints using DCB specimens presented in Chapter 10 will continue with the analysis of adhesively bonded joints used in the aeronautical industry. A good modeling of the behavior of these joints could solve some problems of actual structures that include these kind of joints. An extensive research of adhesively bonded joints where the mode mixity is present (caused by non-symmetrical geometries or due to different properties of the adherents) seems to be straightforward with the LEBI formulation. A comparison with experimental data obtained in the standard tests will be fundamental in properties determination and fitting parameters of the numerical models.

The study of symmetric problems with non-symmetric solutions in presence of crack onset and growth is still an open topic. In the present thesis it has been shown that the LEBI formulation implemented using the sequentially linear analysis is able to capture this phenomena. Nevertheless, an extensive study regarding this topic, using the CZM and the LEBI model, could be performed for the delamination problem in [0/90] symmetric laminates as well as in the isolated fibre or a symmetric fibre cluster embedded in a matrix under transversal loads.

A deeper study of the delamination problem in [0/90] symmetric laminates, studied in Chapter 11, will be done. A parametric study of the influence of the interface properties on the transversal crack as well as on the delamination crack could help to understand this damage mechanism.

In the Single Fibre Fragmentation Test it will be interesting to study the influence of contact between crack faces of the fibre-matrix interface. All the results showed in the Chapter 12 neglected the effect of contact. The influence of residual stresses caused by the curing procedure should also be studied.

In the study of the failure of fibre-matrix interface in an isolated fibre embedded in a matrix, the effect of uniaxial compressive transversal loads could be analyzed. The analysis of fibre-matrix debonding under bi-axial transverse loads will be extended for problems with dominant transversal compressive loads. These numerical results will allow us to extend the obtained failure curves for a cylindrical inclusion under transversal biaxial loads.

In the same sense, the effect of the presence of contiguos fibres will be studied, starting with the effect of two fibres (influence of the distance between them and their relative positions with respect to the remote load).

Then, clusters of fibres with more than 10 fibres will be studied trying to understand from a more realistic point of view the problem of damage initiation in composite materials subjected to transverse loads. All the load patterns used for the isolated fibre will be used in the multifibre models.

A study of spherical inclusions will also be carried out, by the use of the axisymmetric formulation and the LEBI model, which could help to understand the debonding problem in particulate composites.

In all the above mentioned problems, perhaps with the exception of SFTT, the three dimensional effects could play a relevant role and should be investigated in-depth. In particular, they could help to clarify the adequacy of the simplified 2D or axisymmetric models for analysis of some damage mechanisms in composites.

Appendix A

Explicit expressions of the integral kernels in 3D BIEs for transversely isotropic elastic materials

A.1 Modular functions of the fundamental solution and its derivatives

In order to achieve expressions of modulations functions $\widehat{U}_{ik}$, $\widehat{U}_{ik;j}$ and $\widehat{U}_{ik;j\ell}$ suitable for implementation in BEM codes we need to deduce general and as simple and compact as possible expressions of modular functions H_{ik}, $\widehat{H}_{ik;j}$ and $\widehat{H}_{ik;j\ell}$. In fact, as it was shown for transversely isotropic materials, simple and compact expressions of these modulation functions are only needed for a particular coordinate plane including the x_3-axis, the plane $x_2 = 0$ being used herein.

With reference to the plane $x_2 = 0$ (i.e. $\theta = 0$) it will be useful to evaluate the particular expressions of $\mathbf{\Omega}(\theta)$ and its derivatives with respect to $\theta = 0$:

$$\mathbf{\Omega}(\theta)|_{\theta=0} = \begin{pmatrix} 1 & 0 & 0 \\ 0 & 1 & 0 \\ 0 & 0 & 1 \end{pmatrix}, \qquad \mathbf{\Omega}'(\theta)|_{\theta=0} = \begin{pmatrix} 0 & -1 & 0 \\ 1 & 0 & 0 \\ 0 & 0 & 0 \end{pmatrix}, \tag{A.1}$$

$$\boldsymbol{\Omega}''(\theta)|_{\theta=0} = \begin{pmatrix} -1 & 0 & 0 \\ 0 & -1 & 0 \\ 0 & 0 & 0 \end{pmatrix},$$

The expressions of the derivatives with respect to cartesian coordinates of a modulation function $f(\theta, \phi)$ for $\theta = 0$ take the simple form:

$$f_{,1} = r^{-1} c \partial_\phi f, \quad f_{,2} = r^{-1} s^{-1} \partial_\theta f, \quad f_{,3} = -r^{-1} s \partial_\phi f, \tag{A.2}$$

and the components of the unit vector $\widehat{\boldsymbol{x}}$ are:

$$r_{,1} = s, \quad r_{,2} = 0, \quad r_{,3} = c. \tag{A.3}$$

A.1.1 Modular function $\widehat{U}_{ik}$

Explicit expressions for the non-zero terms of the modulation function $\widehat{U}_{ik}(\theta = 0, \phi) = H_{ik}(\theta = 0, \phi)$ in the plane $x_2 = 0$:

$$\boldsymbol{H}(\widehat{\boldsymbol{x}}) = \begin{pmatrix} H_{11} & 0 & H_{13} \\ 0 & H_{22} & 0 \\ H_{13} & 0 & H_{33} \end{pmatrix}, \tag{A.4}$$

were shown in (9.17).

A.1.2 Modular function $\widehat{U}_{ik;j}$

Expression of $\widehat{U}_{ik;j}(\theta = 0, \phi)$ are calculated by (9.36). Thus, the derivatives of the Barnett-Lothe tensor, H_{ik}, appearing in (9.36) are evaluated. Using formulas in (A.2) applied to (A.4) ((9.17)) the following expressions of $\widehat{H}_{ik;j}(\theta = 0, \phi)$ are easily obtained:

$$\begin{aligned} \widehat{H}_{ik;1} &= c \partial_\phi H_{ik}, \\ \widehat{H}_{ik;2} &= s^{-1} \partial_\theta H_{ik}, \\ \widehat{H}_{ik;3} &= -s \partial_\phi H_{ik}, \end{aligned} \tag{A.5}$$

The expressions of the first order partial derivatives of $H_{ik}(\theta, \phi)$ with respect to angles θ and ϕ can be obtained as follows:

$$\partial_\phi H_{ik}(\theta, \phi) = \Omega_{im}(\theta) \Omega_{jn}(\theta) H'_{mn}(\phi), \tag{A.6}$$

$$\partial_\theta H_{ik}(\theta, \phi) = \Omega'_{im}(\theta) \Omega_{jn}(\theta) H_{mn}(\phi) + \Omega_{im}(\theta) \Omega'_{jn}(\theta) H_{mn}(\phi). \tag{A.7}$$

Then, these expressions can be easily computed for the particular case of $\theta = 0$ and in view of (A.1), giving;

$$\begin{aligned}\partial_\phi H_{ik}(\theta,\phi)|_{\theta=0} =&[\Omega_{im}\Omega_{jn}H'_{mn}]|_{\theta=0}\\ =&\begin{pmatrix} H'_{11} & 0 & H'_{13}\\ 0 & H'_{22} & 0\\ H'_{13} & 0 & H'_{33}\end{pmatrix},\end{aligned} \tag{A.8}$$

$$\begin{aligned}\partial_\theta H_{ik}(\theta,\phi)|_{\theta=0} =&[\Omega'_{im}\Omega_{jn}H_{mn} + \Omega_{im}\Omega'_{jn}H_{mn}]|_{\theta=0}\\ =&\begin{pmatrix} 0 & H_{11}-H_{22} & 0\\ H_{11}-H_{22} & 0 & H_{13}\\ 0 & H_{13} & 0\end{pmatrix},\end{aligned} \tag{A.9}$$

A.1.3 Modular function $\widehat{U}_{ik;j\ell}$

Expressions of $\widehat{U}_{ik;j\ell}(\theta = 0,\phi)$, are calculated by (9.37). The second order derivatives of H_{ik} appearing in (9.37) are evaluated. Using formulas in (A.2) applied to (A.5). The following expressions of $\widehat{H}_{ik;j\ell}(\theta = 0,\phi)$ are obtained:

$$\begin{aligned}\widehat{H}_{ik;11} &= c^2\partial^2_{\phi\phi}H_{ik} - 2cs\partial_\phi H_{ik},\\ \widehat{H}_{ik;22} &= s^{-2}\partial^2_{\theta\theta}H_{ik} + cs^{-1}\partial_\phi H_{ik},\\ \widehat{H}_{ik;33} &= s^2\partial^2_{\phi\phi}H_{ik} + 2cs\partial_\phi H_{ik},\\ \widehat{H}_{ik;12} &= cs^{-1}\partial^2_{\phi\theta}H_{ik} - s^{-2}\partial_\theta H_{ik},\\ \widehat{H}_{ik;13} &= -cs\partial^2_{\phi\phi}H_{ik} - (c^2-s^2)\partial_\phi H_{ik},\\ \widehat{H}_{ik;23} &= -\partial^2_{\phi\theta}H_{ik}.\end{aligned} \tag{A.10}$$

The following symmetry relations, due to interchange of partial derivatives, it holds

$$\widehat{H}_{ik;j\ell} = \widehat{H}_{ik;\ell j}. \tag{A.11}$$

Then, the expressions of the second order partial derivatives of $H_{ik}(\theta,\phi)$

with respect to the angles θ and ϕ are obtained:

$$\partial_\phi H_{ik}(\theta,\phi) = \Omega_{im}(\theta)\Omega_{jn}(\theta)H''_{mn}(\phi) \tag{A.12}$$

$$\partial_\theta H_{ik}(\theta,\phi) = \Omega'_{im}(\theta)\Omega_{jn}(\theta)H'_{mn}(\phi) + \Omega_{im}(\theta)\Omega'_{jn}(\theta)H'_{mn}(\phi) \tag{A.13}$$

$$\begin{aligned}\partial_\theta H_{ik}(\theta,\phi) =& \Omega''_{im}(\theta)\Omega_{jn}(\theta)H_{mn}(\phi) + 2\Omega'_{im}(\theta)\Omega'_{jn}(\theta)H_{mn}(\phi) \\ &+ \Omega_{im}(\theta)\Omega''_{jn}(\theta)H_{mn}(\phi).\end{aligned} \tag{A.14}$$

Then, for the particular case of $\theta = 0$, and in view of (A.1), these expressions can be easily expressed as:

$$\begin{aligned}\partial^2_{\phi\phi} H_{ik}(\theta,\phi)|_{\theta=0} =& [\Omega_{im}\Omega_{jn}H''_{mn}]|_{\theta=0} \\ =& \begin{pmatrix} H''_{11} & 0 & H''_{13} \\ 0 & H''_{22} & 0 \\ H''_{13} & 0 & H''_{33} \end{pmatrix},\end{aligned} \tag{A.15}$$

$$\begin{aligned}\partial^2_{\phi\theta} H_{ik}(\theta,\phi)|_{\theta=0} =& [\Omega'_{im}\Omega_{jn}H'_{mn} + \Omega_{im}\Omega'_{jn}H'_{mn}]|_{\theta=0} \\ =& \begin{pmatrix} 0 & H'_{11} - H'_{22} & 0 \\ H'_{11} - H'_{22} & 0 & H'_{13} \\ 0 & H'_{13} & 0 \end{pmatrix},\end{aligned} \tag{A.16}$$

$$\begin{aligned}\partial^2_{\theta\theta} H_{ik}(\theta,\phi)|_{\theta=0} =& [\Omega''_{im}\Omega_{jn}H_{mn} + 2\Omega'_{im}\Omega'_{jn}H_{mn} + \Omega_{im}\Omega''_{jn}H_{mn}]|_{\theta=0} \\ =& \begin{pmatrix} -2(H_{11} - H_{22}) & 0 & -H_{13} \\ 0 & 2(H_{11} - H_{22}) & 0 \\ -H_{13} & 0 & 0 \end{pmatrix}.\end{aligned} \tag{A.17}$$

A.2 Explicit expressions of $H_{ik}(\boldsymbol{x})$, $\widehat{U}_{ik;j}(\boldsymbol{x})$ and $\widehat{\Sigma}_{ijk}(\boldsymbol{x})$

In this section the explicit expressions corresponding to (9.20), (9.24) and (9.31) which are suitable for a direct and efficient implementation in three-dimensional BEM codes are introduced.

For the sake of simplicity of the expressions presented below, the following notation conventions will be used: the quantities on the left-hand side are evaluated at the point $\boldsymbol{x}$ and the quantities on the right-hand side at the point $\widehat{\boldsymbol{x}}$, the symbols $\boldsymbol{x}$ and $\widehat{\boldsymbol{x}}$ being omitted, and $C = \cos(\theta)$ and $S = \sin(\theta)$.

Then, $H_{ik}(\boldsymbol{x})$ can be expressed in terms of $H_{ik}(\widehat{\boldsymbol{x}})$ as follows:

$$\begin{aligned}
H_{11} &= H_{11}C^2 + H_{22}S^2, \\
H_{12} &= (H_{11} - H_{22})CS, \\
H_{13} &= H_{13}C, \\
H_{22} &= H_{22}C^2 - H_{11}S^2, \\
H_{23} &= H_{13}S, \\
H_{33} &= H_{33}.
\end{aligned} \tag{A.18}$$

In general,

$$H_{ik}(\boldsymbol{x}) = f(H_{ik}(\widehat{\boldsymbol{x}}), C(\theta), S(\theta)) \tag{A.19}$$

$\widehat{U}_{ik;j}(\boldsymbol{x})$ can be expressed in terms of $\widehat{U}_{ik;j}(\widehat{\boldsymbol{x}})$ as follows:

$$\begin{aligned}
\widehat{U}_{11;1} &= \{\widehat{U}_{11;1}C^2 + (2\widehat{U}_{12;2} + \widehat{U}_{22;1})S^2\}C, \\
\widehat{U}_{11;2} &= \{(\widehat{U}_{11;1} - 2\widehat{U}_{12;2})C^2 + \widehat{U}_{22;1}S^2\}S, \\
\widehat{U}_{11;3} &= \widehat{U}_{11;3}C^2 + \widehat{U}_{22;3}S^2, \\
\widehat{U}_{12;1} &= \{\widehat{U}_{12;2}S^2 + (\widehat{U}_{11;1} - \widehat{U}_{12;2} - \widehat{U}_{22;1})C^2\}S, \\
\widehat{U}_{12;2} &= \{\widehat{U}_{12;2}C^2 + (\widehat{U}_{11;1} - \widehat{U}_{12;2} - \widehat{U}_{22;1})S^2\}C, \\
\widehat{U}_{12;3} &= (\widehat{U}_{11;3} - \widehat{U}_{22;3})CS, \\
\widehat{U}_{13;1} &= \widehat{U}_{13;1}C^2 + \widehat{U}_{23;2}S^2, \\
\widehat{U}_{13;2} &= (\widehat{U}_{13;1} - \widehat{U}_{23;2})CS, \\
\widehat{U}_{13;3} &= \widehat{U}_{13;3}C, \\
\widehat{U}_{22;1} &= \{(\widehat{U}_{11;1} - 2\widehat{U}_{12;2})S^2 + \widehat{U}_{22;1}C^2\}C, \\
\widehat{U}_{22;2} &= \{\widehat{U}_{11;1}S^2 + (2\widehat{U}_{12;2} + \widehat{U}_{22;1})C^2\}S, \\
\widehat{U}_{22;3} &= \widehat{U}_{11;3}S^2 + \widehat{U}_{22;3}C^2, \\
\widehat{U}_{23;1} &= (\widehat{U}_{13;1} - \widehat{U}_{23;2})CS, \\
\widehat{U}_{23;2} &= \widehat{U}_{13;1}S^2 + \widehat{U}_{23;2}C^2, \\
\widehat{U}_{23;3} &= \widehat{U}_{13;3}S, \\
\widehat{U}_{33;1} &= \widehat{U}_{33;1}C, \\
\widehat{U}_{33;2} &= \widehat{U}_{33;1}S, \\
\widehat{U}_{33;3} &= \widehat{U}_{33;3}.
\end{aligned} \tag{A.20}$$

$\widehat{\Sigma}_{ijk}(\boldsymbol{x})$ can be expressed in terms of $\widehat{\Sigma}_{ijk}(\widehat{\boldsymbol{x}})$ as follows:

$$
\begin{aligned}
\widehat{\Sigma}_{111} &= \{\widehat{\Sigma}_{111}C^2 + (2\widehat{\Sigma}_{122} + \widehat{\Sigma}_{221})S^2\}C,\\
\widehat{\Sigma}_{112} &= \{(\widehat{\Sigma}_{111} - 2\widehat{\Sigma}_{122})C^2 + \widehat{\Sigma}_{221}S^2\}S,\\
\widehat{\Sigma}_{113} &= \widehat{\Sigma}_{113}C^2 + \widehat{\Sigma}_{223}S^2,\\
\widehat{\Sigma}_{121} &= \{\widehat{\Sigma}_{122}S^2 + (\widehat{\Sigma}_{111} - \widehat{\Sigma}_{122} - \widehat{\Sigma}_{221})C^2\}S,\\
\widehat{\Sigma}_{122} &= \{\widehat{\Sigma}_{122}C^2 + (\widehat{\Sigma}_{111} - \widehat{\Sigma}_{122} - \widehat{\Sigma}_{221})S^2\}C,\\
\widehat{\Sigma}_{123} &= (\widehat{\Sigma}_{113} - \widehat{\Sigma}_{223})CS,\\
\widehat{\Sigma}_{131} &= \widehat{\Sigma}_{131}C^2 + \widehat{\Sigma}_{232}S^2,\\
\widehat{\Sigma}_{132} &= (\widehat{\Sigma}_{131} - \widehat{\Sigma}_{232})CS,\\
\widehat{\Sigma}_{133} &= \widehat{\Sigma}_{133}C,\\
\widehat{\Sigma}_{221} &= \{(\widehat{\Sigma}_{111} - 2\widehat{\Sigma}_{122})S^2 + \widehat{\Sigma}_{221}C^2\}C,\\
\widehat{\Sigma}_{222} &= \{\widehat{\Sigma}_{111}S^2 + (2\widehat{\Sigma}_{122} + \widehat{\Sigma}_{221})C^2\}S,\\
\widehat{\Sigma}_{223} &= \widehat{\Sigma}_{113}S^2 + \widehat{\Sigma}_{223}C^2,\\
\widehat{\Sigma}_{231} &= (\widehat{\Sigma}_{131} - \widehat{\Sigma}_{232})CS,\\
\widehat{\Sigma}_{232} &= \widehat{\Sigma}_{131}S^2 + \widehat{\Sigma}_{232}C^2,\\
\widehat{\Sigma}_{233} &= \widehat{\Sigma}_{133}S,\\
\widehat{\Sigma}_{331} &= \widehat{\Sigma}_{331}C,\\
\widehat{\Sigma}_{332} &= \widehat{\Sigma}_{331}S,\\
\widehat{\Sigma}_{333} &= \widehat{\Sigma}_{333}.
\end{aligned}
\tag{A.21}
$$

A.3 Explicit expressions of $\widehat{S}_{ijk}(\widehat{\boldsymbol{x}})$

In this section the expressions corresponding to (9.43) are introduced. $S_{ijk}(\boldsymbol{x})$ can be expressed in terms of a modulation function as

$$
S_{ijk}(\mathbf{n}, \boldsymbol{x}) = \frac{\widehat{S}_{ijk}(\mathbf{n}, \boldsymbol{x})}{4\pi r^3}, \tag{A.22}
$$

$\mathbf{n}$ being explicitly indicated for the sake of clarity, and

$$
\widehat{S}_{ijk}(\mathbf{n}, \boldsymbol{x}) = \Omega_{ia}\Omega_{jb}\Omega_{kc}\widehat{S}_{abc}(\tilde{\mathbf{n}}, \widehat{\boldsymbol{x}}). \tag{A.23}
$$

where $\tilde{\mathbf{n}}$ is the unit normal vector of $\widehat{\boldsymbol{x}}$, for $\theta = 0$. It is necessary to mention that the terms of the normal vector used in the following expressions of $\widehat{S}_{ijk}(\widehat{\boldsymbol{x}})$, $\tilde{\mathbf{n}}$, are defined by the following transformation:

$$\tilde{n}_i = \Omega_{ai} n_a, \tag{A.24}$$

where $\tilde{n}_i$ can be expressed in a expanded way as:

$$\begin{aligned} \tilde{n}_1 =& Cn_1 + Sn_2, \\ \tilde{n}_2 =& Cn_2 - Sn_1, \\ \tilde{n}_3 =& n_3. \end{aligned} \tag{A.25}$$

where $C = \cos(\theta)$ and $S = \sin(\theta)$. Finally, $\widehat{S}_{ijk}(\tilde{\mathbf{n}}, \widehat{\boldsymbol{x}})$ terms are as follows:

$$\begin{aligned}
\widehat{S}_{111} =& c_{12}\left\{c_{44}\tilde{n}_3\left[-H'_{11} + H'_{22} - \tilde{H}_{13}\left(2s + \gamma c\right) - \tilde{H}_{12}cs - H_{13}\right] + c_{66}\tilde{n}_1\left[-3\tilde{H}_{12}\right.\right. \\
&+ \left.\left(2\tilde{H}_{11} - \tilde{H}_{22}\right)c - 2H_{11} + H_{22}\right]\Big\} + c_{13}\left\{c_{44}\tilde{n}_1\left[H''_{11}s^2 - H''_{13}cs - 2H'_{13}\left(c^2 - s^2\right)\right.\right. \\
&+ \left. 4H'_{11}cs + H_{11}\left(2c^2 - s^2\right) + 3H_{13}cs\right] + \tilde{n}_3\left[c_{13}\left(-H''_{11}cs - 2H'_{11}\left(c^2 - s^2\right) - H'_{11}\right.\right. \\
&+ \left.\left. H'_{22} - \tilde{H}_{12}cs + 3H_{11}cs\right) + c_{33}\left(H''_{13}s^2 + 4H'_{13}cs + H_{13}\left(2c^2 - s^2\right)\right)\right]\Big\} \\
&+ c_{11}\left\{c_{44}\tilde{n}_3\left[-H''_{11}cs + H''_{13}c^2 - 2H'_{11}\left(c^2 - s^2\right) - 4H'_{13}cs + 3H_{11}cs + H_{13}\left(2s^2 - c^2\right)\right]\right. \\
&+ \tilde{n}_1\left[c_{12}\left(-\tilde{H}_{12} + \left(\tilde{H}_{11} - \tilde{H}_{22}\right)c - H_{11} + H_{22}\right) + c_{13}\left(-H''_{13}cs - 2H'_{13}\left(c^2 - s^2\right)\right.\right. \\
&+ \left.\left. 3H_{13}cs\right) + c_{11}\left(H''_{11}c^2 - 4H'_{11}cs + H_{11}\left(2s^2 - c^2\right)\right)\right]\Big\}, \\
\widehat{S}_{112} =& c_{66}^2\tilde{n}_2\left\{\left(2\tilde{H}_{11} - \tilde{H}_{22}\right)c - 3\tilde{H}_{12} - 2H_{11} + H_{22}\right\} + c_{66}\tilde{n}_2\left\{c_{11}\left[\left(\tilde{H}_{11} - \tilde{H}_{22}\right)c\right.\right. \\
&- \left.\left.\tilde{H}_{12} - H_{11} + H_{22}\right] + c_{13}\left[-H''_{13}cs - 2H'_{13}\left(c^2 - s^2\right) + 3H_{13}cs\right] + c_{12}\left[H''_{11}c^2\right.\right. \\
&- \left.\left. 4H'_{11}cs + H_{11}\left(2s^2 - c^2\right)\right]\right\}, \\
\widehat{S}_{113} =& c_{44}\left\{c_{44}\tilde{n}_3\left[H''_{11}s^2 - H''_{13}cs - 2H'_{13}\left(c^2 - s^2\right) + 4H'_{11}cs + H_{11}\left(2c^2 - s^2\right) + 3H_{13}cs\right]\right. \\
&+ \tilde{n}_1\left[c_{12}\left(-\tilde{H}_{12}cs - H'_{11} + H'_{22}\right) + c_{11}\left(-H''_{11}cs - 2H'_{11}\left(c^2 - s^2\right) + 3H_{11}cs\right)\right. \\
&+ \left.\left. c_{13}\left(H''_{13}s^2 + 4H'_{13}cs + H_{13}\left(2c^2 - s^2\right)\right)\right] + c_{44}\tilde{n}_1\left[-H''_{11}cs + H''_{13}c^2 - 2H'_{11}\left(c^2 - s^2\right)\right. \\
&- \left. 4H'_{13}cs + 3H_{11}cs + H_{13}\left(2s^2 - c^2\right)\right] + \tilde{n}_3\left[c_{13}\left(-\tilde{H}_{12} + \left(\tilde{H}_{11} - \tilde{H}_{22}\right)c - H_{11} + H_{22}\right)\right. \\
&+ \left.\left. c_{33}\left(-H''_{13}cs - 2H'_{13}\left(c^2 - s^2\right) + 3H_{13}cs\right) + c_{13}\left(H''_{11}c^2 - 4H'_{11}cs + H_{11}\left(2s^2 - c^2\right)\right)\right]\right\}, \\
\widehat{S}_{123} =& c_{44}^2\tilde{n}_2\left\{-\tilde{H}_{12}cs - \tilde{H}_{13}\left(2s + \gamma c\right) - H'_{11} + H'_{22} - H_{13}\right\} + c_{44}\tilde{n}_2\left\{c_{11}\left[-\tilde{H}_{12} - H'_{11}\right.\right. \\
&+ \left. H'_{22}\right] + c_{12}\left[-H''_{11}cs - 2H'_{11}\left(c^2 - s^2\right) + 3H_{11}cs\right] + c_{13}\left[H''_{13}s^2 + 4H'_{13}cs\right. \\
&+ \left.\left. H_{13}\left(2c^2 - s^2\right)\right]\right\},
\end{aligned}$$

$$
\begin{aligned}
\widehat{S}_{122} &= c_{11}\left\{c_{44}\tilde{n}_3\left[-H'_{11}+H'_{22}-\tilde{H}_{13}\left(2s+\gamma c\right)-\tilde{H}_{12}cs-H_{13}\right]+c_{66}\tilde{n}_1\left[-3\tilde{H}_{12}\right.\right.\\
&+\left.\left.\left(2\tilde{H}_{11}-\tilde{H}_{22}\right)c-2H_{11}+H_{22}\right]\right\}+c_{13}\left\{c_{44}\tilde{n}_1\left[H''_{11}s^2-H''_{13}cs-2H'_{13}\left(c^2-s^2\right)\right.\right.\\
&+\left.\left.4H'_{11}cs+H_{11}\left(2c^2-s^2\right)+3H_{13}cs\right]+\tilde{n}_3\left[c_{13}\left(-H''_{11}cs-2H'_{11}\left(c^2-s^2\right)-H'_{11}\right.\right.\right.\\
&+\left.\left.\left.H'_{22}-\tilde{H}_{12}cs+3H_{11}cs\right)+c_{33}\left(H''_{13}s^2+4H'_{13}cs+H_{13}\left(2c^2-s^2\right)\right)\right]\right\}\\
&+c_{12}\left\{c_{44}\tilde{n}_3\left[-H''_{11}cs+H''_{13}c^2-2H'_{11}\left(c^2-s^2\right)-4H'_{13}cs+3H_{11}cs+H_{13}\left(2s^2-c^2\right)\right]\right.\\
&+\tilde{n}_1\left[c_{12}\left(-\tilde{H}_{12}+\left(\tilde{H}_{11}-\tilde{H}_{22}\right)c-H_{11}+H_{22}\right)+c_{13}\left(-H''_{13}cs-2H'_{13}\left(c^2-s^2\right)\right.\right.\\
&+\left.\left.\left.3H_{13}cs\right)+c_{11}\left(H''_{11}c^2-4H'_{11}cs+H_{11}\left(2s^2-c^2\right)\right)\right]\right\},\\
\widehat{S}_{133} &= c_{13}\left\{c_{44}\tilde{n}_3\left[-H'_{11}+H'_{22}-\tilde{H}_{13}\left(2s+\gamma c\right)-\tilde{H}_{12}cs-H_{13}\right]+c_{66}\tilde{n}_1\left[-3\tilde{H}_{12}\right.\right.\\
&+\left.\left.\left(2\tilde{H}_{11}-\tilde{H}_{22}\right)c-2H_{11}+H_{22}\right]\right\}+c_{33}\left\{c_{44}\tilde{n}_1\left[H''_{11}s^2-H''_{13}cs-2H'_{13}\left(c^2-s^2\right)\right.\right.\\
&+\left.\left.4H'_{11}cs+H_{11}\left(2c^2-s^2\right)+3H_{13}cs\right]+\tilde{n}_3\left[c_{13}\left(-H''_{11}cs-2H'_{11}\left(c^2-s^2\right)-H'_{11}\right.\right.\right.\\
&+\left.\left.\left.H'_{22}-\tilde{H}_{12}cs+3H_{11}cs\right)+c_{33}\left(H''_{13}s^2+4H'_{13}cs+H_{13}\left(2c^2-s^2\right)\right)\right]\right\}\\
&+c_{13}\left\{c_{44}\tilde{n}_3\left[-H''_{11}cs+H''_{13}c^2-2H'_{11}\left(c^2-s^2\right)-4H'_{13}cs+3H_{11}cs+H_{13}\left(2s^2-c^2\right)\right]\right.\\
&+\tilde{n}_1\left[c_{12}\left(-\tilde{H}_{12}+\left(\tilde{H}_{11}-\tilde{H}_{22}\right)c-H_{11}+H_{22}\right)+c_{13}\left(-H''_{13}cs-2H'_{13}\left(c^2-s^2\right)\right.\right.\\
&+\left.\left.\left.3H_{13}cs\right)+c_{11}\left(H''_{11}c^2-4H'_{11}cs+H_{11}\left(2s^2-c^2\right)\right)\right]\right\},\\
\widehat{S}_{211} &= c_{12}\tilde{n}_2\left\{c_{13}\left[-\tilde{H}_{13}c-H'_{13}\right]+c_{12}\left[-\tilde{H}_{12}+\left(\tilde{H}_{11}-\tilde{H}_{22}\right)c-H_{11}+H_{22}\right]+c_{11}\left[2\tilde{H}_{12}\right.\right.\\
&+\left.\left.\tilde{H}_{22}c-H_{22}\right]\right\}+c_{13}c_{44}\tilde{n}_2\left\{H''_{22}s^2+4H'_{22}cs-\tilde{H}_{13}c-H'_{13}+H_{22}\left(2c^2-s^2\right)\right\}\\
&+c_{11}c_{66}\tilde{n}_2\left\{H''_{22}c^2-4H'_{22}cs-\tilde{H}_{12}+\left(\tilde{H}_{11}-\tilde{H}_{22}\right)c+H_{22}\left(2s^2-c^2\right)-H_{11}+H_{22}\right\},\\
\widehat{S}_{212} &= c_{66}\left\{\tilde{n}_1\left[c_{13}\left(-\tilde{H}_{13}-H'_{13}\right)+c_{11}\left(-\tilde{H}_{12}+\left(\tilde{H}_{11}-\tilde{H_{22}}\right)c-H_{11}+H_{22}\right)\right.\right.\\
&+\left.\left.c_{12}\left(2\tilde{H}_{12}+\tilde{H}_{22}c-H_{22}\right)\right]+c_{44}\tilde{n}_3\left[-\tilde{H}_{13}\left(2s+\gamma c\right)-\tilde{H}_{12}cs-H'_{11}+H'_{22}-H_{13}\right]\right\}\\
&+c_{66}\left\{c_{44}\tilde{n}_3\left[-H''_{22}cs-2H'_{22}\left(c^2-s^2\right)-\tilde{H}_{13}\left(2s+\gamma c\right)+3H_{22}cs-H_{13}\right]\right.\\
&+\left.c_{66}\tilde{n}_1\left[H''_{22}c^2-4H'_{22}cs-\tilde{H}_{12}+\left(\tilde{H}_{11}-\tilde{H}_{22}\right)c+H_{22}\left(2s^2-c^2\right)-H_{11}+H_{22}\right]\right\},\\
\widehat{S}_{213} &= c_{44}^2\tilde{n}_2\left\{-H''_{22}cs-2H'_{22}\left(c^2-s^2\right)-\tilde{H}_{13}\left(2s+\gamma c\right)+3H_{22}cs-H_{13}\right\}\\
&+c_{44}c_{66}\tilde{n}_2\left\{-H''_{22}cs-2H'_{22}\left(c^2-s^2\right)-\tilde{H}_{12}cs-H'_{11}+H'_{22}+3H_{22}cs\right\},\\
\widehat{S}_{222} &= c_{11}\tilde{n}_2\left\{c_{13}\left[-\tilde{H}_{13}c-H'_{13}\right]+c_{12}\left[-\tilde{H}_{12}+\left(\tilde{H}_{11}-\tilde{H}_{22}\right)c-H_{11}+H_{22}\right]+c_{11}\left[2\tilde{H}_{12}\right.\right.\\
&+\left.\left.\tilde{H}_{22}c-H_{22}\right]\right\}+c_{13}c_{44}\tilde{n}_2\left\{H''_{22}s^2+4H'_{22}cs-\tilde{H}_{13}c-H'_{13}+H_{22}\left(2c^2-s^2\right)\right\}\\
&+c_{12}c_{66}\tilde{n}_2\left\{H''_{22}c^2-4H'_{22}cs-\tilde{H}_{12}+\left(\tilde{H}_{11}-\tilde{H}_{22}\right)c+H_{22}\left(2s^2-c^2\right)-H_{11}+H_{22}\right\},
\end{aligned}
$$

$$
\begin{aligned}
\widehat{S}_{223} &= c_{44}\left\{\tilde{n}_3\left[c_{33}\left(-\tilde{H}_{13}c - H'_{13}\right) + c_{13}\left(\tilde{H}_{12} + \tilde{H}_{11}c - H_{11}\right)\right] + c_{44}\tilde{n}_1\left[-\tilde{H}_{12}cs\right.\right.\\
&\quad - \left.\tilde{H}_{13}\left(2s+\gamma c\right) - H'_{11} + H'_{22} - H_{13}\right] + c_{66}\tilde{n}_1\left[-H''_{22}cs - 2H'_{22}\left(c^2 - s^2\right) - H'_{11} - H'_{22}\right.\\
&\quad - \left.\left.\tilde{H}_{12}cs + 3H_{22}cs\right] + c_{44}\tilde{n}_3\left[H''_{22}s^2 + 4H'_{22}cs - H'_{13} - \tilde{H}_{13}c + H_{22}\left(2c^2 - s^2\right)\right]\right\},\\
\widehat{S}_{233} &= c_{13}\tilde{n}_2\left\{c_{13}\left[-\tilde{H}_{13}c - H'_{13}\right] + c_{12}\left[-\tilde{H}_{12} + \left(\tilde{H}_{11} - \tilde{H}_{22}\right)c - H_{11} + H_{22}\right] + c_{11}\left[2\tilde{H}_{12}\right.\right.\\
&\quad + \left.\left.\tilde{H}_{22}c - H_{22}\right]\right\} + c_{33}c_{44}\tilde{n}_2\left\{H''_{22}s^2 + 4H'_{22}cs - \tilde{H}_{13}c - H'_{13} + H_{22}\left(2c^2 - s^2\right)\right\}\\
&\quad + c_{13}c_{66}\tilde{n}_2\left\{H''_{22}c^2 - 4H'_{22}cs - \tilde{H}_{12} + \left(\tilde{H}_{11} - \tilde{H}_{22}\right)c + H_{22}\left(2s^2 - c^2\right) - H_{11} + H_{22}\right\},\\
\widehat{S}_{311} &= c_{12}\left\{c_{66}\tilde{n}_1\left[-2\tilde{H}_{13}\left(2s+\gamma c\right) - 2H_{13}\right] + c_{44}\tilde{n}_3\left[\tilde{H}_{33}c - \tilde{H}_{13}c - H'_{13} - H_{33}\right]\right\}\\
&\quad + c_{13}\left\{c_{44}\tilde{n}_1\left[H''_{13}s^2 - H''_{33}cs + 4H'_{13}cs - 2H'_{33}\left(c^2 - s^2\right) + H_{13}\left(2c^2 - s^2\right) + 3H_{33}cs\right]\right.\\
&\quad + \tilde{n}_3\left[c_{13}\left(-H''_{13}cs - 2H'_{13}\left(c^2 - s^2\right) - H'_{13} - \tilde{H}_{13}c + 3H_{13}cs\right) + c_{33}\left(H''_{33}s^2 + 4H'_{33}cs\right.\right.\\
&\quad + \left.\left.\left.H_{33}\left(2c^2 - s^2\right)\right)\right]\right\} + c_{11}\left\{c_{44}\tilde{n}_3\left[H''_{33}c^2 - H''_{13}cs - 4H'_{33}cs - 2H'_{13}\left(c^2 - s^2\right) + 3H_{13}cs\right.\right.\\
&\quad + \left.H_{33}\left(2s^2 - c^2\right)\right] + \tilde{n}_1\left[c_{12}\left(-\tilde{H}_{13}\left(2s+\gamma c\right) - H_{13}\right) + c_{13}\left(-H''_{33}cs - 2H'_{33}\left(c^2 - s^2\right)\right.\right.\\
&\quad + \left.\left.\left.3H_{33}cs\right) + c_{11}\left(H''_{13}c^2 - 4H'_{13}cs + H_{13}\left(2s^2 - c^2\right)\right)\right]\right\},\\
\widehat{S}_{312} &= c_{66}^2\tilde{n}_2\left\{-2\tilde{H}_{13}\left(2s+\gamma c\right) - 2H_{13}\right\} - c_{66}\tilde{n}_2\left\{c_{11}\left[-\tilde{H}_{13}\left(2s+\gamma c\right) - H_{13}\right]\right.\\
&\quad + \left.c_{13}\left[-H''_{33}cs - 2H'_{33}\left(c^2 - s^2\right) + 3H_{33}cs\right] + c_{12}\left[H''_{13}c^2 - 4H'_{13}cs + H_{13}\left(2s^2 - c^2\right)\right]\right\},\\
\widehat{S}_{313} &= c_{44}\left\{c_{44}\tilde{n}_3\left[H''_{13}s^2 - H''_{33}cs + 4H'_{13}cs - 2H'_{33}\left(c^2 - s^2\right) + H_{13}\left(2c^2 - s^2\right) + 3H_{33}cs\right]\right.\\
&\quad + \tilde{n}_1\left[c_{12}\left(-H'_{13} - \tilde{H}_{13}c\right) + c_{11}\left(-H''_{13}cs - 2H'_{13}\left(c^2 - s^2\right) + 3H_{13}cs\right) + c_{13}\left(H''_{33}s^2\right.\right.\\
&\quad + \left.\left.\left.4H'_{33}cs + H_{33}\left(2c^2 - s^2\right)\right)\right]\right\} + c_{44}\left\{c_{44}\tilde{n}_1\left[H''_{33}c^2 - H''_{13}cs - 4H'_{33}cs - 2H'_{13}\left(c^2 - s^2\right)\right.\right.\\
&\quad + \left.3H_{13}cs + H_{33}\left(2s^2 - c^2\right)\right] + \tilde{n}_3\left[c_{13}\left(-\tilde{H}_{13}\left(2s+\gamma c\right) - H_{13}\right) + c_{33}\left(-H''_{33}cs\right.\right.\\
&\quad - \left.\left.\left.2H'_{33}\left(c^2 - s^2\right) + 3H_{33}cs\right) + c_{13}\left(H''_{13}c^2 - 4H'_{13}cs + H_{13}\left(2s^2 - c^2\right)\right)\right]\right\},\\
\widehat{S}_{322} &= c_{11}\left\{c_{66}\tilde{n}_1\left[-2\tilde{H}_{13}\left(2s+\gamma c\right) - 2H_{13}\right] + c_{44}\tilde{n}_3\left[\tilde{H}_{33}c - \tilde{H}_{13}c - H'_{13} - H_{33}\right]\right\}\\
&\quad + c_{13}\left\{c_{44}\tilde{n}_1\left[H''_{13}s^2 - H''_{33}cs + 4H'_{13}cs - 2H'_{33}\left(c^2 - s^2\right) + H_{13}\left(2c^2 - s^2\right) + 3H_{33}cs\right]\right.\\
&\quad + \tilde{n}_3\left[c_{13}\left(-H''_{13}cs - 2H'_{13}\left(c^2 - s^2\right) - H'_{13} - \tilde{H}_{13}c + 3H_{13}cs\right) + c_{33}\left(H''_{33}s^2 + 4H'_{33}cs\right.\right.\\
&\quad + \left.\left.\left.H_{33}\left(2c^2 - s^2\right)\right)\right]\right\} + c_{12}\left\{c_{44}\tilde{n}_3\left[H''_{33}c^2 - H''_{13}cs - 4H'_{33}cs - 2H'_{13}\left(c^2 - s^2\right) + 3H_{13}cs\right.\right.\\
&\quad + \left.H_{33}\left(2s^2 - c^2\right)\right] + \tilde{n}_1\left[c_{12}\left(-\tilde{H}_{13}\left(2s+\gamma c\right) - H_{13}\right) + c_{13}\left(-H''_{33}cs - 2H'_{33}\left(c^2 - s^2\right)\right.\right.\\
&\quad + \left.\left.\left.3H_{33}cs\right) + c_{11}\left(H''_{13}c^2 - 4H'_{13}cs + H_{13}\left(2s^2 - c^2\right)\right)\right]\right\},\\
\widehat{S}_{323} &= c_{44}^2\tilde{n}_2\left\{\tilde{H}_{33}c - \tilde{H}_{13}c - H'_{13} - H_{33}\right\} + c_{44}\tilde{n}_2\left\{c_{11}\left[-\tilde{H}_{13}c - H'_{13}\right] + c_{12}\left[-H''_{13}cs\right.\right.\\
&\quad - \left.\left.2H'_{13}\left(c^2 - s^2\right) + 3H_{13}cs\right] + c_{13}\left[H''_{33}s^2 + 4H'_{33}cs + H_{33}\left(2c^2 - s^2\right)\right]\right\},
\end{aligned}
$$

$$\begin{aligned}\widehat{S}_{333} = {} & c_{13}\left\{c_{66}\tilde{n}_1\left[-2\tilde{H}_{13}\left(2s+\gamma c\right)-2H_{13}\right]+c_{44}\tilde{n}_3\left[\tilde{H}_{33}c-\tilde{H}_{13}c-H'_{13}-H_{33}\right]\right\}\\ & +c_{33}\left\{c_{44}\tilde{n}_1\left[H''_{13}s^2-H''_{33}cs+4H'_{13}cs-2H'_{33}\left(c^2-s^2\right)+H_{13}\left(2c^2-s^2\right)+3H_{33}cs\right]\right.\\ & +\tilde{n}_3\left[c_{13}\left(-H''_{13}cs-2H'_{13}\left(c^2-s^2\right)-H'_{13}-\tilde{H}_{13}c+3H_{13}cs\right)+c_{33}\left(H''_{33}s^2+4H'_{33}cs\right.\right.\\ & +\left.\left.H_{33}\left(2c^2-s^2\right)\right)\right]\Big\}+c_{13}\left\{c_{44}\tilde{n}_3\left[H''_{33}c^2-H''_{13}cs-4H'_{33}cs-2H'_{13}\left(c^2-s^2\right)+3H_{13}cs\right.\right.\\ & +\left.H_{33}\left(2s^2-c^2\right)\right]+\tilde{n}_1\left[c_{12}\left(-\tilde{H}_{13}\left(2s+\gamma c\right)-H_{13}\right)+c_{13}\left(-H''_{33}cs-2H'_{33}\left(c^2-s^2\right)\right.\right.\\ & +\left.\left.\left.3H_{33}cs\right)+c_{11}\left(H''_{13}c^2-4H'_{13}cs+H_{13}\left(2s^2-c^2\right)\right)\right]\Big\}. \qquad \text{(A.26)}\end{aligned}$$

In general,

$$\widehat{S}_{ijk}(\tilde{\mathbf{n}},\widehat{\boldsymbol{x}}) = f(H_{ik}(\widehat{\boldsymbol{x}}),\tilde{\mathbf{n}},\widehat{\boldsymbol{x}},c(\phi),s(\phi)) \qquad \text{(A.27)}$$

A.4 Explicit expressions of $\widehat{U}_{ik;jl}(\boldsymbol{x})$, $\widehat{\Sigma}^{loop}_{ijkl}(\boldsymbol{x},\mathbf{n})$ and $\widehat{S}_{ijk}(\boldsymbol{x})$ useful for an efficient computational implementation

In this section the expressions corresponding to (9.31), (9.44) and (A.23) which are suitable for a direct and efficient implementation in three-dimensional BEM codes are introduced.

For the sake of simplicity of the expressions presented below the following notation conventions will be used: the quantities on the left-hand side are evaluated at point $\boldsymbol{x}$ (and for the normal vector $\mathbf{n}$ in the case of $\widehat{S}_{ijk}$) and the quantities on the right-hand side at point $\widehat{\boldsymbol{x}}$ (and for the normal vector $\tilde{\mathbf{n}}$ in the case of $\widehat{S}_{ijk}$), the symbols $\boldsymbol{x}$ and $\widehat{\boldsymbol{x}}$ being omitted, and $C=\cos(\theta)$ and $S=\sin(\theta)$.

The modular function $\widehat{U}_{ik;jl}(\boldsymbol{x})$ of the second derivative kernel $U_{ik,jl}(\boldsymbol{x})$, is presented in the left hand side of (A.28), can be expressed in terms of $\widehat{U}_{ik;jl}(\widehat{\boldsymbol{x}})$, right hand side in (A.28), defined in (9.45) as follows:

$$
\begin{aligned}
\widehat{U}_{11;11} =&\widehat{U}_{11;11}C^4+\widehat{U}_{11;22}C^2S^2+4\widehat{U}_{12;12}C^2S^2+\widehat{U}_{22;11}C^2S^2+\widehat{U}_{22;22}S^4\\
\widehat{U}_{11;12} =&\widehat{U}_{11;11}C^3S-\widehat{U}_{11;22}C^3S-2\widehat{U}_{12;12}C^3S+2\widehat{U}_{12;12}CS^3+\widehat{U}_{22;11}CS^3-\widehat{U}_{22;22}CS^3\\
\widehat{U}_{11;13} =&\widehat{U}_{11;13}C^3+2\widehat{U}_{12;23}CS^2+\widehat{U}_{22;13}CS^2\\
\widehat{U}_{11;22} =&\widehat{U}_{11;11}C^2S^2+\widehat{U}_{11;22}C^4-4\widehat{U}_{12;12}C^2S^2+\widehat{U}_{22;11}S^4+\widehat{U}_{22;22}C^2S^2\\
\widehat{U}_{11;23} =&\widehat{U}_{11;13}C^2S-2\widehat{U}_{12;23}C^2S+\widehat{U}_{22;13}S^3\\
\widehat{U}_{11;33} =&\widehat{U}_{11;33}C^2+\widehat{U}_{22;33}S^2\\
\widehat{U}_{12;11} =&\widehat{U}_{11;11}C^3S+\widehat{U}_{11;22}CS^3-2\widehat{U}_{12;12}C^3S+2\widehat{U}_{12;12}CS^3-\widehat{U}_{22;11}C^3S-\widehat{U}_{22;22}CS^3\\
\widehat{U}_{12;12} =&\widehat{U}_{11;11}C^2S^2-\widehat{U}_{11;22}C^2S^2+\widehat{U}_{12;12}C^4-2\widehat{U}_{12;12}C^2S^2+\widehat{U}_{12;12}S^4-\widehat{U}_{22;11}C^2S^2\\
&+\widehat{U}_{22;22}C^2S^2\\
\widehat{U}_{12;13} =&\widehat{U}_{11;13}C^2S-\widehat{U}_{12;23}C^2S+\widehat{U}_{12;23}S^3-\widehat{U}_{22;13}C^2S\\
\widehat{U}_{12;22} =&\widehat{U}_{11;11}CS^3+\widehat{U}_{11;22}C^3S+2\widehat{U}_{12;12}C^3S-2\widehat{U}_{12;12}CS^3-\widehat{U}_{22;11}CS^3-\widehat{U}_{22;22}C^3S\\
\widehat{U}_{12;23} =&\widehat{U}_{11;13}CS^2+\widehat{U}_{12;23}C^3-\widehat{U}_{12;23}CS^2-\widehat{U}_{22;13}CS^2\\
\widehat{U}_{12;33} =&\widehat{U}_{11;33}CS-\widehat{U}_{22;33}CS\\
\widehat{U}_{13;11} =&\widehat{U}_{13;11}C^3+3\widehat{U}_{13;22}CS^2\\
\widehat{U}_{13;12} =&\widehat{U}_{13;11}C^2S-2\widehat{U}_{13;22}C^2S+\widehat{U}_{13;22}S^3\\
\widehat{U}_{13;13} =&\widehat{U}_{13;13}C^2+\widehat{U}_{23;23}S^2\\
\widehat{U}_{13;22} =&\widehat{U}_{13;11}CS^2+\widehat{U}_{13;22}C^3-2\widehat{U}_{13;22}CS^2\\
\widehat{U}_{13;23} =&\widehat{U}_{13;13}CS-\widehat{U}_{23;23}CS\\
\widehat{U}_{13;33} =&\widehat{U}_{13;33}C\\
\widehat{U}_{22;11} =&\widehat{U}_{11;11}C^2S^2+\widehat{U}_{11;22}S^4-4\widehat{U}_{12;12}C^2S^2+\widehat{U}_{22;11}C^4+\widehat{U}_{22;22}C^2S^2\\
\widehat{U}_{22;12} =&\widehat{U}_{11;11}CS^3-\widehat{U}_{11;22}CS^3+2\widehat{U}_{12;12}C^3S-2\widehat{U}_{12;12}CS^3+\widehat{U}_{22;11}C^3S-\widehat{U}_{22;22}C^3S\\
\widehat{U}_{22;13} =&\widehat{U}_{11;13}CS^2-2\widehat{U}_{12;23}CS^2+\widehat{U}_{22;13}C^3\\
\widehat{U}_{22;22} =&\widehat{U}_{11;11}S^4+\widehat{U}_{11;22}C^2S^2+4\widehat{U}_{12;12}C^2S^2+\widehat{U}_{22;11}C^2S^2+\widehat{U}_{22;22}C^4\\
\widehat{U}_{22;23} =&\widehat{U}_{11;13}S^3+2\widehat{U}_{12;23}C^2S+\widehat{U}_{22;13}C^2S\\
\widehat{U}_{22;33} =&\widehat{U}_{11;33}S^2+\widehat{U}_{22;33}C^2\\
\widehat{U}_{23;11} =&\widehat{U}_{13;11}C^2S-2\widehat{U}_{13;22}C^2S+\widehat{U}_{13;22}S^3\\
\widehat{U}_{23;12} =&\widehat{U}_{13;11}CS^2+\widehat{U}_{13;22}C^3-2\widehat{U}_{13;22}CS^2\\
\widehat{U}_{23;13} =&\widehat{U}_{13;13}CS-\widehat{U}_{23;23}CS\\
\widehat{U}_{23;22} =&\widehat{U}_{13;11}S^3+3\widehat{U}_{13;22}C^2S\\
\widehat{U}_{23;23} =&\widehat{U}_{13;13}S^2+\widehat{U}_{23;23}C^2\\
\widehat{U}_{23;33} =&\widehat{U}_{13;33}S\\
\widehat{U}_{33;11} =&\widehat{U}_{33;11}C^2+\widehat{U}_{33;22}S^2\\
\widehat{U}_{33;12} =&\widehat{U}_{33;11}CS-\widehat{U}_{33;22}CS
\end{aligned}
\tag{A.28}
$$

$$
\begin{aligned}
\widehat{U}_{33;13} =& \widehat{U}_{33;13} C \\
\widehat{U}_{33;22} =& \widehat{U}_{33;11} S^2 + \widehat{U}_{33;22} C^2 \\
\widehat{U}_{33;23} =& \widehat{U}_{33;13} S \\
\widehat{U}_{33;33} =& \widehat{U}_{33;33}
\end{aligned}
$$

$$
\begin{aligned}
\widehat{U}_{ik;jl} &= \widehat{U}_{ki;jl} \\
\widehat{U}_{ik;jl} &= \widehat{U}_{ik;lj}.
\end{aligned} \tag{A.29}
$$

The modular function $\widehat{\Sigma}^{loop}_{ijkl}(\boldsymbol{x})$ of the kernel $\Sigma^{loop}_{ijkl}(\boldsymbol{x})$, can be expressed in terms of $\widehat{\Sigma}^{loop}_{ijkl}(\widehat{\boldsymbol{x}})$, defined in (9.51), as follows:

$$
\begin{aligned}
\widehat{\Sigma}_{1111} =& \widehat{\Sigma}_{1111} C^4 + 2\widehat{\Sigma}_{1122} C^2 S^2 + 4\widehat{\Sigma}_{1212} C^2 S^2 + \widehat{\Sigma}_{2222} S^4, \\
\widehat{\Sigma}_{1112} =& \widehat{\Sigma}_{1111} C^3 S - \widehat{\Sigma}_{1122} C^3 S - 2\widehat{\Sigma}_{1212} C^3 S + 2\widehat{\Sigma}_{1212} C S^3 + \widehat{\Sigma}_{1122} C S^3 - \widehat{\Sigma}_{2222} C S^3; \\
\widehat{\Sigma}_{1113} =& \widehat{\Sigma}_{1113} C^3 + 2\widehat{\Sigma}_{1223} C S^2 + \widehat{\Sigma}_{1322} C S^2, \\
\widehat{\Sigma}_{1122} =& \widehat{\Sigma}_{1111} C^2 S^2 + \widehat{\Sigma}_{1122} C^4 - 4\widehat{\Sigma}_{1212} C^2 S^2 + \widehat{\Sigma}_{1122} S^4 + \widehat{\Sigma}_{2222} C^2 S^2, \\
\widehat{\Sigma}_{1123} =& \widehat{\Sigma}_{1113} C^2 S - 2\widehat{\Sigma}_{1223} C^2 S + \widehat{\Sigma}_{1322} S^3, \\
\widehat{\Sigma}_{1133} =& \widehat{\Sigma}_{1133} C^2 + \widehat{\Sigma}_{2233} S^2, \\
\widehat{\Sigma}_{1212} =& \widehat{\Sigma}_{1111} C^2 S^2 - 2\widehat{\Sigma}_{1122} C^2 S^2 + \widehat{\Sigma}_{1212} C^4 - 2\widehat{\Sigma}_{1212} C^2 S^2 + \widehat{\Sigma}_{1212} S^4 + \widehat{\Sigma}_{2222} C^2 S^2, \\
\widehat{\Sigma}_{1213} =& \widehat{\Sigma}_{1113} C^2 S - \widehat{\Sigma}_{1223} C^2 S + \widehat{\Sigma}_{1223} S^3 - \widehat{\Sigma}_{1322} C^2 S, \\
\widehat{\Sigma}_{1222} =& \widehat{\Sigma}_{1111} C S^3 + \widehat{\Sigma}_{1122} C^3 S + 2\widehat{\Sigma}_{1212} C^3 S - 2\widehat{\Sigma}_{1212} C S^3 - \widehat{\Sigma}_{1122} C S^3 - \widehat{\Sigma}_{2222} C^3 S, \\
\widehat{\Sigma}_{1223} =& \widehat{\Sigma}_{1113} C S^2 + \widehat{\Sigma}_{1223} C^3 - \widehat{\Sigma}_{1223} C S^2 - \widehat{\Sigma}_{1322} C S^2, \\
\widehat{\Sigma}_{1233} =& \widehat{\Sigma}_{1133} C S - \widehat{\Sigma}_{2233} C S, \\
\widehat{\Sigma}_{1313} =& \widehat{\Sigma}_{1313} C^2 + \widehat{\Sigma}_{2323} S^2, \\
\widehat{\Sigma}_{1322} =& \widehat{\Sigma}_{1113} C S^2 + \widehat{\Sigma}_{1322} C^3 - 2\widehat{\Sigma}_{1223} C S^2, \\
\widehat{\Sigma}_{1323} =& \widehat{\Sigma}_{1313} C S - \widehat{\Sigma}_{2323} C S, \\
\widehat{\Sigma}_{1333} =& \widehat{\Sigma}_{1333} C, \\
\widehat{\Sigma}_{2222} =& \widehat{\Sigma}_{1111} S^4 + 2\widehat{\Sigma}_{1122} C^2 S^2 + 4\widehat{\Sigma}_{1212} C^2 S^2 + \widehat{\Sigma}_{2222} C^4, \\
\widehat{\Sigma}_{2223} =& \widehat{\Sigma}_{1113} S^3 + 2\widehat{\Sigma}_{1223} C^2 S + \widehat{\Sigma}_{1322} C^2 S, \\
\widehat{\Sigma}_{2233} =& \widehat{\Sigma}_{1133} S^2 + \widehat{\Sigma}_{2233} C^2, \\
\widehat{\Sigma}_{2323} =& \widehat{\Sigma}_{1313} S^2 + \widehat{\Sigma}_{2323} C^2, \\
\widehat{\Sigma}_{2333} =& \widehat{\Sigma}_{1333} S, \\
\widehat{\Sigma}_{3333} =& \widehat{\Sigma}_{3333}.
\end{aligned} \tag{A.30}
$$

Finally, the modular function $\widehat{S}_{ijk}(\boldsymbol{x},\mathbf{n})$ of the integral kernel $S_{ijk}(\boldsymbol{x},\mathbf{n})$, can be expressed in terms of $\widehat{S}_{ijk}(\widehat{\boldsymbol{x}},\tilde{\mathbf{n}})$ defined in (A.26), as follows:

$$
\begin{aligned}
&\widehat{S}_{111} = \{\widehat{S}_{111}C^2 + (2\widehat{S}_{122} + \widehat{S}_{221})S^2\}C,\\
&\widehat{S}_{112} = \{(\widehat{S}_{111} - 2\widehat{S}_{122})C^2 + \widehat{S}_{221}S^2\}S,\\
&\widehat{S}_{113} = \widehat{S}_{113}C^2 + \widehat{S}_{223}S^2,\\
&\widehat{S}_{121} = \{\widehat{S}_{122}S^2 + (\widehat{S}_{111} - \widehat{S}_{122} - \widehat{S}_{221})C^2\}S,\\
&\widehat{S}_{122} = \{\widehat{S}_{122}C^2 + (\widehat{S}_{111} - \widehat{S}_{122} - \widehat{S}_{221})S^2\}C,\\
&\widehat{S}_{123} = (\widehat{S}_{113} - \widehat{S}_{223})CS,\\
&\widehat{S}_{131} = \widehat{S}_{131}C^2 + \widehat{S}_{232}S^2,\\
&\widehat{S}_{132} = (\widehat{S}_{131} - \widehat{S}_{232})CS,\\
&\widehat{S}_{133} = \widehat{S}_{133}C,\\
&\widehat{S}_{221} = \{(\widehat{S}_{111} - 2\widehat{S}_{122})S^2 + \widehat{S}_{221}C^2\}C,\\
&\widehat{S}_{222} = \{\widehat{S}_{111}S^2 + (2\widehat{S}_{122} + \widehat{S}_{221})C^2\}S,\\
&\widehat{S}_{223} = \widehat{S}_{113}S^2 + \widehat{S}_{223}C^2,\\
&\widehat{S}_{231} = (\widehat{S}_{131} - \widehat{S}_{232})CS,\\
&\widehat{S}_{232} = \widehat{S}_{131}S^2 + \widehat{S}_{232}C^2,\\
&\widehat{S}_{233} = \widehat{S}_{133}S,\\
&\widehat{S}_{331} = \widehat{S}_{331}C,\\
&\widehat{S}_{332} = \widehat{S}_{331}S,\\
&\widehat{S}_{333} = \widehat{S}_{333}.
\end{aligned}
\tag{A.31}
$$

Bibliography

[1] A. Agrawal and A.M. Karlsson. On the reference length and mode mixity for a bimaterial interface. *Journal of Engineering Materials and Technology*, 129:580–587, 2007.

[2] Airbus. Carbon Fibre Reinforced Plastics. Determination of fracture toughness energy of bonded joints. Mode I. G1C. Issue 1. *AITM 1-0053*, 2006.

[3] MH. Aliabadi. A new generation of boundary element methods in fracture mechanics. *International Journal of Fracture*, 86:91–125, 1997.

[4] MH. Aliabadi. Boundary Element Formulations in Fracture Mechanics. *Applied Mechanics Reviews*, 50:83–96, 1997.

[5] MH. Aliabadi. *The Boundary Element Method, Applications in Solids and Structures*, volume 2. John Wiley & Sons: Chichester, 2002.

[6] MH. Aliabadi and AL. Saleh. Fracture mechanics analysis of cracking in plain and reinforced concrete using the boundary element method. *Engineering Fracture Mechanics*, 69:267–280, 2002.

[7] E. Anderson, Z. Bai, C. Bischof, S. Blackford, J. Demmel, J. Dongarra, J. Du Croz, A. Greenbaum, S. Hammarling, A. McKenney, and D. Sorensen. *LAPACK Users' Guide*. Society for Industrial and Applied Mathematics, Philadelphia, PA, third edition, 1999.

[8] MP. Ariza and J. Domínguez. Boundary element formulation for 3D transversely isotropic cracked bodies. *International Journal for Numerical Methods in Engineering*, 60:719–753, 2004.

[9] R. Avila, V. Mantič, and F. París. *Aplication of the boundary element method to elastic orthotropic materials in 2D: numerical aspects.*

In: Boundary Elements XIX. Computational Mechanics Publications: Southampton, Boston, 1997.

[10] J. Baláš, J. Sládek, and V. Sládek. *Stress Analysis by Boundary Element Method*. Elsevier: Amsterdam, 1989.

[11] L. Bank-Sills and D. Ashkenazi. A note on fracture criteria for interface fracture. *International Journal of Fracture*, 103:177–188, 2000.

[12] GI. Barenblatt. The formation of equilibrium cracks during brittle fracture. General ideas and hypotheses. Axially-symmetric cracks. *Journal of Applied Mathematics and Mechanics*, 23:622–636, 1959.

[13] DM. Barnett. The precise evaluation of derivatives of the anisotropic elastic Green's functions. *Physica Status Solidi (b)*, 49:741–748, 1972.

[14] A. Barroso, V. Mantič, and F. París. Computing stress singularities in transversely isotropic multimaterial corners by means of explicit expressions of the orthonormalized Stroh-eigenvectors. *Engineering Fracture Mechanics*, 76:250–268, 2009.

[15] Z. Bažant and J. Planas. *Fracture and size effect in concrete and other quasibrittle materials*. CRC PRESS: Boca Raton, 1998.

[16] Y. Benveniste and T. Miloh. Imperfect soft and stiff interfaces in two-dimensional elasticity. *Mech Mater*, 33:309–323, 2001.

[17] JM. Berthelot. Transverse cracking and delamination in cross-ply glass–fiber and carbon–fiber reinforced plastic laminates: static and fatigue loading. *Applied Mechanics Reviews*, 56:111–147, 2003.

[18] D. Bigoni, SK. Serkov, M. Valentini, and AB. Movchan. Asymptotic models of dilute composites with imperfectly bonded inclusions. *International Journal of Solids and Structures*, 35:3239–3258, 1998.

[19] L. S. Blackford, J. Choi, A. Cleary, E. D'Azevedo, J. Demmel, I. Dhillon, J. Dongarra, S. Hammarling, G. Henry, A. Petitet, K. Stanley, D. Walker, and R. C. Whaley. *ScaLAPACK Users' Guide*. Society for Industrial and Applied Mathematics, Philadelphia, PA, 1997.

[20] A. Blázquez. *Non-conforming contact between orthotropic solids. Aplication to Iosipescu test (in Spanish)*. PhD. Thesis, Universidad de Sevilla, 1996.

[21] A. Blázquez. Transversal and delamination crack onset and growth in $[0/90]_S$ laminates. *GERM Private Comunication*, 2010.

[22] A. Blázquez, V. Mantič, F. París, and J. Cañas. On the removal of rigid body motions in the solution of elastostatic problems by direct BEM. *International Journal for Numerical Methods in Engineering*, 39:4021–4038, 1996.

[23] A. Blázquez, V. Mantič, F. París, and L. N. McCartney. Stress State characterization of delamination cracks in [0/90] symmetric laminates by BEM. *International Journal of Solids and Structures*, 45:1632–1662, 2008.

[24] A. Blázquez, V. Mantič, F. París, and L. N. McCartney. BEM analysis of damage progress in 0/90 laminates. *Engineering Analysis with Boundary Elements*, 33:762–769, 2009.

[25] A. Blázquez, F. París, and V. Mantič. BEM solution of two-dimensional contact problems by weak application of contact conditions with nonconforming discretizations. *International Journal of Solids and Structures*, 35:3259–3278, 1998.

[26] G. Bolzon, R. Fedele, and G. Maier. Parameter identification of a cohesive crack model by Kalman filter. *Computer Methods in Applied Mechanics and Engineering*, 13:74–89, 2002.

[27] M. Bonnet. *Boundary Integral Equation Methods for Solids and Fluids*. Wiley: Chichster, 1995.

[28] M. Bonnet, G. Maier, and C. Polizzotto. Symmetric Galerkin boundary element method. *Applied Mechanics Reviews*, 51:669–704, 1998.

[29] CA. Brebbia, JCF. Telles, and LC. Wrobel. *Boundary Element Techniques*. Springer: Berlin, 1984.

[30] JM. Burgers. Some considerations on the field of stress connected with dislocations in a regular crystal lattice. *Proc. Koninklijke Nederlandse Akademie van Wetenschappen*, 42:293–378, 1939.

[31] FC. Buroni and A. Saez. Three-dimensional Green's function and its derivative for materials with general anisotropic magneto-electro-elastic coupling. *Proceedings of the Royal Society A*, 466:515–537, 2010.

[32] G.T. Camacho and M. Ortiz. Computational modelling of impact damage in brittle materials. *International Journal of Solid and Structures*, 33:2899–2938, 1996.

[33] G.G. Camanho, C.G. Dávila, and M.F. de Moura. Numerical simulation of mixed-mode progressive delamination in composite materials. *Journal of Composite Materials*, 37:1415–1438, 2003.

[34] A. Carpinteri. Cusp catastrophe interpretation of fracture instability. *Journal of the Mechanics and Physics of Solids*, 37:567–582, 1989.

[35] A. Carpinteri. Post-peak and post-bifurcation analysis on cohesive crack propagation. *Engineering Fracture Mechanics*, 32:265–278, 1989.

[36] A. Carpinteri and G. Colombo. Numerical analysis of catastrophic softening behaviour (snap-back instability). *Computers & Structures*, 31:607–636, 1989.

[37] A. Carpinteri, P. Cornetti, and N. Pugno. Edge debonding in FRP strengthened beams: Stress versus energy failure criteria. *Engineering Structures*, 31:2436–2447, 2009.

[38] A. Carpinteri, M. Paggi, and G. Zavarise. Snap-back instability in micro-structured composites and its connection with superplasticity. *Strength, Fracture and Complexity*, 3:61—72, 2005.

[39] A. Chandra and S. Mukherjee. *Boundary Element Methods in Manufacturing*. Oxford University Press: Oxford, 1997.

[40] N. Chandra and C. Shet. A Micromechanistic Perspective of Cohesive Zone Approach in Modeling Fracture. *Computer Modeling in Engineering and Sciences*, 5:21–34, 2004.

[41] C. Chang and M. Mear. Boundary element method for two dimensional linear elastic fracture analysis. *International Journal of Fracture*, 74:219–251, 1995.

[42] T. Chen and FZ. Lin. Numerical evaluation of derivatives of the anisotropic piezoelctric Green's functions. *Mechanics Research Communications*, 20:501–506, 1993.

[43] WT. Chen. On some problems in transversely isotropic elastic materials. *Journal of Applied Mechanics*, 33:347–355, 1966.

[44] J. Cook, J. E. Gordon, C.C. Evans, and D.M. Marsh. A Mechanism for the Control of Crack Propagation in All-Brittle Systems. *Proceedings of the Royal Society of London. Series A, Mathematical and Physical Sciences*, 282:508–520, 1964.

[45] E. Correa. *Micromechanical study of the "matrix failure" in fiber reinforced composites (in Spanish).* PhD. Thesis, Universidad de Sevilla, 2008.

[46] E. Correa, V. Mantič, and F. París. A micromechanical view of interfibre failure of composite materials under compression transverse to the fibres. *Composites Science and Technology*, 68:2010–2021, 2008.

[47] E. Correa, V. Mantič, and F. París. Numerical characterisation of the fibre-matrix interface crack growth in composites under transverse compression. *Engineering Fracture Mechanics*, 75:4085–4103, 2008.

[48] MA. Crisfield. *Non-linear Finite Element Analysis of Solids and Structures*, volume 2. Wiley: Chichester, 1997.

[49] TA. Cruse. *Boundary Element Analysis in Computational Fracture Mechanics.* Kuwler Academic Publishers: Boston, 1988.

[50] C. Dávila, C. Rose, and P. Camanho. A procedure for superposing linear cohesive laws to represent multiple damage mechanisms in the fracture of composites. *International Journal of Fracture*, 158:211–223, 2009.

[51] PH. Dederichs and G. Liebfried. Elastic Green's function for anisotropic cubic crystals. *Physical Review*, 188:1175–1183, 1969.

[52] E. Denarié, VE. Saouma, A. Iocco, and D. Varelas. Concrete fracture process zone characterization with fiber optics. *Journal of Engineering Mechanics*, 127:494–502, 2001.

[53] P. Destuynder, F. Michavila, A. Santos, and Y. Ousset. Some theoretical aspects in computational analysis of adhesive lap joints. *International Journal for Numerical Methods in Engineering*, 35:1237–1262, 1992.

[54] J. Dongarra, J. Bunch, C. Moler, and P. Stewart. Linpack, 1984.

[55] D. Dugdale. Yielding of steel sheets containing slits. *Journal of the Mechanics and Physics of Solids*, 8:100–104, 1960.

[56] M. Elices, GV. Guinea, J. Gómez, and J. Planas. The cohesive zone model: advantages, limitations and challenges. *Engineering Fracture Mechanics*, 69:137–163, 2002.

[57] HA. Elliot. Three-dimensional stress distributions in hexagonal aelotropic crystals. *Proceedings of the Cambridge Philosophical Society*, 44:522–533, 1948.

[58] F. Erdogan. *Fracture mechanics of interfaces, In: Damage and Failure of Interfaces*. Balkema Publishers: Rotterdam, 1997.

[59] A. G. Evans, M. Rühle, B. J. Dalgleish, and P. G. Charalambides. The fracture energy of bimaterial interfaces. *Metallurgical Transactions A*, 21:2419–2429, 1990.

[60] VI. Fabrikant. *Applications of Potential Theory in Mechanics. Selection of New Results*. Kluwer Academic Publishers: Dordrecht, 1989.

[61] M. Fafard and B. Massicotte. Geometrical Interpretation of the arc-length method. *Computers & Structures*, 46:603–615, 1993.

[62] G. Fairweather and A. Karageorghis. The method of fundamental solutions for elliptic boundary value problems. *Advances in Computational Mathematics*, 9:69–95, 1998.

[63] A. Frangi. *Regularization of boundary element formulations by the derivative transfer method, In: Singular Integrals in the Boundary Element Method*. Computational Mechanics Publishers, 1998.

[64] A. Frangi and G. Novati. Symmetric BE method in two-dimensional elasticity: evaluation of double integrals for curved elements. *Computational Mechanics*, 19:58–68, 1996.

[65] I. Fredholm. Sur les équations de l'équilibre d'um corps solide élastique. *Acta Mathematica*, 23:1–42, 1900.

[66] Z. Gao. A circular inclusion with imperfect interface: Eshelby's tensor and related problems. *Journal of Applied Mechanics*, 62:860–866, 1995.

[67] AC. Garg. Delamination - A damage mode in composite structures. *Engineering Fracture Mechanics*, 29:557–584, 1988.

[68] G. Geymonat, F. Krasucki, and S. Lenci. Mathematical analysis of a bonded joint with a soft thin adhesive. *Mathematics and Mechanics of Solids*, 4:201–225, 1999.

[69] M. Goland and E. Reissner. The stresses in cemented joints. *Journal of Applied Mechanics*, 11:A17–A27, 1944.

[70] GH. Golub and CF. Van Loan. *Matrix Computations*. Johns Hopkins University Press, third edition, 1996.

[71] E. Graciani. *BEM formulation and implementation for axisymmetric contact problems. Application to fiber-matrix interface in composite materials (in Spanish)*. PhD. Thesis, Universidad de Sevilla, 2006.

[72] E. Graciani, V. Mantič, F. París, and A. Blázquez. Weak formulation of axi-symmetric frictionless contact problems with boundary elements: Application to interface cracks. *Computer and Structures*, 83:836–855, 2005.

[73] E. Graciani, V. Mantič, F. París, and J. Varna. Numerical analysis of debond propagation in the single fibre fragmentation test. *Composites Science and Technology*, 69:2514–2520, 2009.

[74] LJ. Gray. *Evaluation of singular and hypersingular Galerkin boundary integrals: direct limits and symbolic computation, In: Singular Integrals in the Boundary Element Method*. Computational Mechanics Publishers, 1998.

[75] LJ. Gray and GH. Paulino. Symmetric Galerkin boundary integral fracture analysis for plane orthotropic elasticity. *Computational Mechanics*, 20:26–33, 1997.

[76] R. Han, MS. Ingber, and HL. Schreyer. Progression of failure in fiber-reinforced materials. *Computers Materials & Continua*, 4:163–176, 2006.

[77] MT. Hanson. Some observations on the potential functions for transverse isotropy in the presence of body forces. *International Journal of Solids and Structures*, 35:3793–3813, 1998.

[78] F. Hartmann, C. Katz, and B. Protopsaltis. Boundary elements and symmetry. *Archive of Applied Mechanics (Ingenieur Archiv)*, 55:440–449, 1985.

[79] Z. Hashin. Thermoelastic properties of fiber composites with imperfect interface. *Mechanics of Materials*, 8:333–348, 1990.

[80] Z. Hashin. Thin interphase/imperfect interface in elasticity with application to coated fiber composites. *Journal of the Mechanics and Physics of Solids*, 50:2509–2537, 2002.

[81] AK. Head. The Galois unsolvability of the sextic equation of anisotropic elasticity. *Journal of Elasticity*, 9:9–20, 1979.

[82] A. Hilleborg, M. Modeer, and P.E. Petersson. Analysis of a crack formation and crack growth in concrete by fracture mechanics and finite elements. *Cement and Concrete Research*, 6:773–782, 1976.

[83] SM. Hölzer. How to deal with hypersingular integrals in the symmetric BEM. *Communications in Numerical Methods in Engineering*, 9:219–232, 1993.

[84] TB. Hu, CD. Wang, and JL. Laio. Elastic solutions of displacements for a transversely isotropic full space with inclined planes of symmetry subjected to a point load. *International Journal for Numerical and Analytical Methods in Geomechanics*, 31:1401–1442, 2007.

[85] JW. Hutchinson and Z. Suo. *Mixed mode cracking in layered materials*, volume 29 of *Advances in Applied Mechanics*. Academic Press: New York, 1992.

[86] VL. Indenbom and SS. Orlov. Construction of Green's functions in terms of Green's function of lower dimension. *Journal of Applied Mathematics and Mechanics*, 32:414—-420, 1968.

[87] ISO. Fibre-reinforced plastic composites – Determination of mode I interlaminar fracture toughness, G_{IC}, for unidirectionally reinforced materials. *ISO 15024*, 2001.

[88] M.E. Jiménez. *Modeling of the interlaminar fracture toughness test in composite materials (in Spanish).* Final Project, Universidad de Sevilla, 2006.

[89] M.E. Jiménez, J. Cañas, V. Mantič, and J.E. Ortiz. Numerical and experimental study of the interlaminar fracture test of composite-composite adhesively bonded joints. (in Spanish). *Materiales Compuestos 07, Asociación Española de Materiales Compuestos, Universidad de Valladolid*, pages 499–506, 2007.

[90] M. F. Kanninen. An augmented double cantilever beam model for studying crack propagation and arrest. *International Journal of Fracture*, 9:83–92, 1973.

[91] A. Kelly and WR. Tyson. Tensile properties of fiber reinforced metals: copper/tungsten and copper/molybdenum. *Journal of the Mechanics and Physics of Solids*, 13:329–350, 1965.

[92] A. Klarbring. Derivation of a model of adhesively bonded joints by the asymptotic expansion method. *International Journal of Engineering Science*, 29:493–512, 1991.

[93] M. Kočvara, A. Mielke, and T. Roubíček. A rate-independent approach to the delamination problem. *Mathematics and Mechanics of Solids*, 11:423–427, 2006.

[94] E. Kröner. Das Fundamentalintegral der anisotropen elastischen Differentialgleichungen. *Zeitschrift für Physik*, 136:402—-410, 1953.

[95] G. Kuhn and H. Mang. *On symmetrization in boundary element elastic and elastoplastic analysis, In: Discretization methods in structural mechanics*. Springer: Berlin, 1990.

[96] JC. Lachat and JO. Watson. Effective numerical treatment of boundary integral equations: a formulation for three-dimensional elastostatics. *International Journal for Numerical Methods in Engineering*, 10:991–1005, 1976.

[97] F. Lebon and F. Zaittouni. Asymptotic modelling of interfaces taking contact conditions into account: Asymptotic expansions and numerical implementation. *International Journal of Engineering Science*, 48:111–127, 2010.

[98] VG. Lee. Explicit expression of derivatives of elastic Green's functions for general anisotropic materials. *Mechanics Research Communications*, 30:241—249, 2003.

[99] VG. Lee. Derivatives of the three-dimensional Green's functions for anisotropic materials. *International Journal of Solids and Structures*, 46:3471—3479, 2009.

[100] L. Lejček. The Green function of the theory of elasticity in an anisotropic hexagonal medium. *Czechoslovak Journal of Physics*, B19:799–803, 1969.

[101] S. G. Lekhnitskii. *Theory of Elasticity of an Anisotropic Body.* Mir Publishers: Moscow, 1981.

[102] S. Lenci. Analysis of a crack at a weak interface. *International Journal of Fracture*, 108:275–290, 2001.

[103] IM. Lifshitz and LN. Rozentsweig. Construction of the Green tensor for the fundamental equation of elasticity theory in the case of unbounded elastically anisotropic medium. *Zhurnal Eksper. i Teoreticheskoi Fiziki*, 17:783–791, 1947.

[104] M. Loloi. Boundary integral equation solution of three-dimensional elastostatic problems in transversely isotropic solids using closed-form displacement fundamental solutions. *International Journal for Numerical Methods in Engineering*, 48:823–842, 2000.

[105] J. Lothe. *Disclocations in anisotropic media. In: Elastic Strain Fields and Dislocation Mobility.* North-Holland: Amsterdam, 1992.

[106] G. Maier and A. Frangi. Symmetric boundary element method for 'discrete' crack modelling of fracture processes. *Computer Assisted Mechanics and Engineering Sciences*, 5:201–226, 1998.

[107] G. Maier, S. Miccoli, G. Novati, and S. Sirtori. *A Galerkin symmetric boundary element method in plasticity: formulation and implementation, In: Advances in Boundary Element Techniques.* Springer: Berlin, 1993.

[108] G. Maier, G. Novati, and Z. Cen. Symmetric boundary element method for quasi-brittle fracture and frictional problems. *Computational Mechanics*, 13:74–89, 1993.

[109] G. Maier and C. Polizzotto. A Galerkin approach to boundary element elastoplastic analysis. *Computer Methods in Applied Mechanics and Engineering*, 60:175–194, 1987.

[110] K. Malén. A unified six-dimensional treatment of elastic Green's functions and dislocations. *Physica Status Solidi B*, 44:661–672, 1971.

[111] V. Mantič. A new formula for the C-matrix in the Somigliana identity. *Journal of Elasticity*, 33:191–201, 1993.

[112] V. Mantič. Interface crack onset at a circular cylindrical inclusion under a remote transverse tension. Application of a coupled stress and energy criterion. *International Journal of Solids and Structures*, 46:1287–1304, 2009.

[113] V. Mantič, A. Blázquez, E. Correa, and F. París. *Analysis of interface cracks with contact in composites by 2D BEM. In: Fracture and damage of composites, Series: Advances in fracture mechanics*, volume 8. WIT Press: Southampton, Boston, 2006.

[114] V. Mantič and F. París. Explicit formulae of the integral kernels and C-matrix in the 2D Somigliana identity for orthotropic materials. *Engineering Analysis with Boundary Elements*, 15(3):283–288, 1995.

[115] V. Mantič and F. París. Symmetrical representation of stresses in the Stroh formalism and its application to a dislocation and a dislocation dipole in an anisotropic elastic medium. *Journal of Elasticity*, 47:101–120, 1997.

[116] V. Mantič and F. París. Symmetry properties of the kernels of the hypersingular integral and the corresponding regularized integral in the 2D Somigliana stress identity for isotropic materials. *Engineering Analysis with Boundary Elements*, 20:163–168, 1997.

[117] V. Mantič and F. París. Relation between SIF and ERR based measures of fracture mode mixity in interface cracks. *International Journal of Fracture*, 130:557–569, 2004.

[118] LN. McCartney and A. Blázquez. Delamination model for cross-plu laminates subject to triaxial loading and thermal stresses. *ICCM 17, Edinburgh*, 2009.

[119] S.G. Mogilevskaya and S.L. Crouch. A Galerkin boundary integral method for multiple circular elastic inclusions with homogeneously imperfect interfaces. *International Journal of Solids and Structures*, 39:4723–4746, 2002.

[120] S. Mukherjee and YX. Mukherjee. *Boundary methods: elements, contours and nodes*. CRC Press: Boca Raton, 2005.

[121] C. Müller-Karger, C. González, MH. Aliabadi, and M. Cerrolaza. Three dimensional BEM and FEM stress analysis of the human tibia under pathological conditions. *Computer Modeling in Engineering & Sciences*, 2:1–13, 2001.

[122] JA. Nairn. Numerical implementation of imperfect interfaces. *Computational Materials Science*, 40:525–536, 2007.

[123] G. Nakamura and K. Tanuma. A formula for the fundamental solution of anisotropic elasticity. *Quarterly Journal of Mechanics and Applied Mathematics*, 50:179–194, 1997.

[124] A. Needleman. A continuum model for void nucleation by inclusion debonding. *Journal of Applied Mechanics*, 54:525–532, 1987.

[125] D. Ngo, K. Park, G.H. Paulino, and Y. Huang. On the constitutive relation of materials with microstructure using a potential-based cohesive model for interface interaction. *Strength, Fracture and Complexity*, 77:1153—1174, 2010.

[126] T.K. O'Brien. *Analysis of local delaminations and their influence on composite laminate behavior. In: Delamination and debonding of materials.* ASTM STP 876, Philadelphia, 1984.

[127] JE. Ortiz and AP. Cisilino. Boundary element method for J-integral and stress intensity factor computations in three-dimensional interface cracks. *International Journal of Fracture*, 133:197–222, 2005.

[128] M. Ortiz and A. Pandolfi. Finite-Deformation irreversible cohesive elements for three dimensional crack propagation analysis. *International Journal for Numerical Methods in Engineering*, 44:1267–1283, 1999.

[129] Y. Pan and T. Chou. Point force solution for an infinitetransversely isotropic solid. *Journal of Applied Mechanics*, 98:608–612, 1976.

[130] F. París, A. Blázquez, L. N. McCartney, and V. Mantič. Characterization and evolution of matrix and interface related damage in $[0/90]_S$ laminates under tension. Part I: Numerical predictions. *Composites Science and Technology*, 70:1168–1175, 2010.

[131] F. París and J. Cañas. *Boundary Element Method, Fundamentals and Applications.* Oxford University Press: Oxford, 1997.

[132] F. París, E. Correa, and V. Mantič. Kinking of transverse interface cracks between fiber and matrix. *Journal of Applied Mechanics*, 74:703–716, 2007.

[133] F. París, E. Correa, and J. Ca nas. Micromechanical view of failure of the matrix in fibrous composite materials. *Composites Science and Technology*, 63:1041–1052, 2003.

[134] F. París, J.C. del Caño, and J. Varna. The fiber-matrix interface crack — A numerical analysis using boundary elements. *International Journal of Fracture*, 82:11—29, 1996.

[135] A-V. Phan, JAL. Napier, LJ. Gray, and T. Kaplan. Symmetric-Galerkin BEM simulation of fracture with frictional contact. *International Journal for Numerical Methods in Engineering*, 57:835–851, 2003.

[136] AV. Phan, LJ. Gray, and T. Kaplan. On the residue calculus evaluation of the 3-D anisotropic elastic Green's function. *Communications in Numerical Methods in Engineering*, 20:335–341, 2004.

[137] AV. Phan, LJ. Gray, and T. Kaplan. Residue approach for evaluating the 3D anisotropic elastic Green's function: multiple roots. *Engineering Analysis with Boundary Elements*, 29:570–576, 2005.

[138] J. Planas, M. Elices, GV. Guinea, FJ. Gómez, DA. Cendón, and I. Arbilla. Generalizations and specializations of cohesive crack models. *Engineering Fracture Mechanics*, 70:1759–1776, 2003.

[139] WH. Press, SA. Teukolsky, WT. Vetterling, and BP. Flannery. *Numerical Recipes in FORTRAN. The art of scientific computing.* Cambridge University Press: Cambridge, 2 edition, 1992.

[140] SA. Ragon, Z. Gürdal, and LT. Watson. A comparison of three algorithms for tracing nonlinear equilibrium paths of structural systems. *International Journal of Solids and Structures*, 39:689–698, 2002.

[141] E. Ramm. *Strategies for tracing the non-linear response near limit-points. In: Non-linear finite element analysis in structural mechanics. Proceeding European US Workshop.* Springer: Berlin, 1981.

[142] T. Reilly and A. Burstein. The elastic and ultimate properties of compact bone tissue. *Journal of Biomechanics*, 8:393–405, 1975.

[143] E. Riks. An incremental approach to the solution of snapping and buckling problems. *International Journal of Solids and Structures*, 15:529–551, 1979.

[144] FJ. Rizzo. An integral equation approach to boundary value problems of classical elastostatics. *Quarterly of Applied Mathematics*, 25:83–95, 1967.

[145] FJ. Rizzo and DJ. Shippy. Some observations on Kelvin's solution in classical elastostatics as a double tensor field with implications for Somigliana integral. *Journal of Elasticity*, 13:91–97, 1983.

[146] DJ. Roberts, A-V. Phan, HV. Tippur, LJ. Gray, and T. Kaplan. SGBEM modeling of fatigue crack growth in particulate composites. *Archive of Applied Mechanics*, 80:307–322, 2010.

[147] T. Roubíček, L. Scardia, and C. Zanini. Quasistatic delamination problem. *Continuum Mechanics and Thermodynamics*, 21:223–235, 2009.

[148] J. Rungamornrat. *A Computational Procedure for Analysis of Fractures in Three Dimensional Anisotropic Media.* PhD Thesis, The University of Texas, 2004.

[149] J. Rungamornrat. Weakly-singular, weak-form integral equations for cracks in three-dimensional anisotropic media. *International Journal of Solids and Structures*, 45:1283—-1301, 2008.

[150] A. Sáez, MP. Ariza, and J. Domínguez. Three-dimensional fracture analysis in tranversely isotropic solids. *Engineering Analysis with Boundary Elements*, 20:287–298, 1997.

[151] MA. Sales and LJ. Gray. Evaluation of the anisotropic Green's function and its derivatives. *Computers and Structures*, 69:247–254, 1998.

[152] A. Salvadori. *Quasi brittle fracture mechanics by cohesive crack models and symmetric galerkin boundary element method.* PhDF Thesis, Politecnico di Milano, 1999.

[153] A. Salvadori. A symmetric boundary integral formulation for cohesive interface problems. *Computational Mechanics*, 22:381–391, 2003.

[154] A. Salvadori. *Numerical simulations of cohesive interface problems via boundary integral equations.* Proceedings of IABEM 2006: Graz, 2006.

[155] NA. Schclar. *Anisotropic Analysis Using Boundary Elements.* Computational Mechanics Publications: Southampton, 1994.

[156] R. Seydel. *Practical Bifurcation And Stability Analysis - From Equilibrium to Chaos.* Springer: New York, 1994.

[157] YC. Shiah, CL. Tan, and VG. Lee. Evaluation of explicit-form fundamental solutions for displacements and stresses in 3D anisotropic elastic solids. *Computer Modeling in Engineering and Sciences*, 34:205–226, 2008.

[158] G. B. Sinclair. On the influence of cohesive stress-separation laws on elastic stress singularities. *Journal of Elasticity*, 44:203–221, 1996.

[159] S. Sirtori. General stress analysis method by means of integral equations and boundary elements. *Meccanica*, 14:210–218, 1979.

[160] S. Sirtori, G. Maier, G. Novati, and S. Miccoli. A Galerkin symmetric boundary element method in elasticity: formulation and implementation. *International Journal for Numerical Methods in Engineering*, 35:255–282, 1992.

[161] A. Sutradhar, G. Paulino, and LJ. Gray. *Symmetric Galerkin Boundary Element Method*. Springer: Berlin, 2008.

[162] CL. Tan, YC. Shiah, and CW. Lin. Stress analysis of 3D generally anisotropic elastic solids using the boundary element method. *Computer Modeling in Engineering and Sciences*, 41:195–214, 2009.

[163] K. Tanuma. Surface-impedance tensors of transversely isotropic elastic materials. *Quarterly Journal of Mechanics and Applied Mathematics*, 49:29–48, 1996.

[164] TE. Tay. Characterization and analysis of delamination fracture in composites: An overview of developments from 1990 to 2001. *Applied Mechanics Reviews*, 56:1–31, 2003.

[165] TCT. Ting. *Anisotropic Elasticity Theory and Applications.* Oxford University Press: Oxford, 1996.

[166] TCT. Ting. A modified Leknitskii formalism *à la* Stroh for anisotropic elasticity and classifications of the 6×6 matrix $\mathbf{N}$. *Proceedings of the Royal Society A: Mathematical, Physical and Engineering Sciences*, 455:69–89, 1999.

[167] TCT. Ting and VG. Lee. The three-dimensional elastostatic Green's function for general anisotropic linear elastic solids. *Quarterly Journal of Mechanics and Applied Mathematics*, 50:407–426, 1997.

[168] F. Tonon, E. Pan, and B. Amadei. Green's functions and boundary element method formulation for 3D anisotropic media. *Computers and Structures*, 79:469–482, 2001.

[169] M. Toya. A crack along the interface of a circular inclusion embedded in an infinite solid. *Journal of the Mechanics and Physics of Solids*, 22:325—-348, 1974.

[170] J. Varna, LA. Berglund, and ML. Ericson. Transverse single fiber test for interfacial debonding in composites 2: Modelling. *Composites Part A: Applied Science and Manufacturing*, 28:317—326, 1997.

[171] J. Varna, F. París, and JC. del Caño. The effect of crack-face contact and fibre/matrix debonding in transverse tensile loading. *Composites Science and Technology*, 57:523—-532, 1997.

[172] R. Vodička, V. Mantič, and F. París. Note on the removal of rigid body motions in the solution of elastostatic traction boundary value problems by SGBEM. *Engineering Analysis with Boundary Elements*, 30:790–798, 2006.

[173] CY. Wang. Elastic fields produced by a point source in solids of general anisotropy. *Journal of Engineering Mathematics*, 32:41–52, 1997.

[174] X. Wang, E. Pan, and LJ. Sudak. Uniform stresses inside an elliptical inhomogeneity with an imperfect interface in plane elasticity. *Journal of Applied Mechanics*, 75:054501.1–054501.6, 2008.

[175] P. Wen. The elastic solution of concentrated force acting in orthogonal anisotropic half-plane and constant element fundamental formulae of boundary element method. *Applied Mathematics and Mechanics*, 13:1163–1172, 1992.

[176] DJ. Wilkins, JR. Eisenmann, RA. Camin, WS. Margolis, and RA. Benson. *Characterizing Delamination Growth in Graphite-Epoxy. In: Damage in Composite Materials.* ASTM - STP/STP775-EB/STP34326S, 1982.

[177] RC. Williams, A-V. Phan, HV. Tippur, T. Kaplan, and LJ. Gray. SGBEM analysis of crack growth and particle(s) interactions due to elastic constants mismatch. *Engineering Fracture Mechanics*, 74:314—-331, 2007.

[178] JR. Willis. The elastic interaction energy of dislocation loops in anisotropic media. *Quarterly Journal of Mechanics and Applied Mathematics*, 18:419–433, 1965.

[179] R. Wilson and T. Cruse. Efficient implementation of anisotropic three dimensional boundary-integral equation stress analysis. *International Journal for Numerical Methods in Engineering*, 12:1383–1397, 1978.

[180] S. Wolfram. *Mathematica, A system for doing mathematics by computer*. Addison-Wesley:Redwood City, 1991.

[181] K. Wu. Generalization of the Stroh Formalism to 3-Dimensional Anisotropic Elasticity. *Journal of Elasticity*, 51:213–225, 1998.

[182] M. Xie and A. Levy. Defect propagation at a circular interface. *International Journal of Fracture*, 144:1–20, 2007.

[183] X-P. Xu and A. Needleman. Void nucleation by inclusion debonding in a crystal matrix. *Modelling and Simulation in Materials Science and Engineering*, 1:111–132, 1993.

[184] H. Zhang, ML. Ericson, J. Varna, and LA. Berglund. Transverse single-fiber test for interfacial debonding in composites: 1. Experimental observations. *Composites Part A: Applied Science and Manufacturing*, 28A:309—-315, 1997.

Publications

The following international and national publications have been originated during the work in the present thesis.

International Journal Papers

1. L. Távara, J.E. Ortiz, V. Mantič, F. París. Unique real-variable exrpessions of displacement and traction fundamental solutions covering all transversely isotropic elastic materials for 3D BEM. *International Journal for Numerical Methods in Engineering*, **74**:776–798, 2008.

2. L. Távara, V. Mantič, E. Graciani, J. Cañas, F. París. Analysis of a crack in a thin adhesive layer between orthotropic materials: An application to composite interlaminar fracture toughness test. *CMES - Computer Modeling in Engineering and Sciences*, **58**:247-270, 2010.

3. L. Távara, V. Mantič, A. Salvadori, L.J. Gray, F. París. SGBEM for cohesive cracks in homogeneous media. *Key Engineering Materials*, In press, 2010.

4. L. Távara, V. Mantič, E. Graciani, F. París. BEM analysis of crack onset and propagation along fiber-matrix interface under transverse tension using a linear elastic-brittle interface model. *Engineering Analysis with Boundary Elements*, In press, 2010.

5. L. Távara, V. Mantič, J.E. Ortiz, F. París. Unique real-variable expressions of the integral kernels in the stress hypersingular boundary integral equation covering all transversely isotropic elastic materials for 3D BEM. In preparation.

6. V. Mantič, L. Távara, J.E. Ortiz, F. París. Recent developments in the evaluation of the 3D fundamental solution and its derivatives for transversely isotropic materials. In preparation.

7. L. Távara, V. Mantič, A. Salvadori, L.J. Gray, F. París. Cohesive crack formulation and implementation in 2D SGBEM. In preparation.

Book Chapters

1. L. Távara, V. Mantič, J. Cañas, E. Graciani, F. París. BEM analysis of crack onset and growth in composites using the linear elastic-brittle interface model. In: E.J. Sapountzakis (Eds.), *Recent Developments in Boundary Element Methods* , WIT Press, Southampton, 2010, pp. 281–294.

Conferences papers

International

1. L. Távara, V. Mantič, E. Graciani, J. Cañas, F. París. BEM model of mode I crack propagation along a weak interface applied to the interlaminar fracture toughness test of composites. *BeTeq 2008* July 9^{th}-11^{th} 2008, Seville, Spain

2. V. Mantič, L. Távara, J.E. Ortiz, F. París. Application of the Stroh formalism for anisotropic elasticity to the evaluation of the 3D fundamental solution and its derivatives. Recent developments for transversely isotropic elastic materials. *BeTeq 2008* July 9^{th}-11^{th} 2008, Seville, Spain (Keynote Lecture)

3. L. Távara, V. Mantič, E. Graciani, J. Cañas, F. París. Analysis of a crack in a thin adhesive layer between orthotropic materials applied to composite interlaminar fracture toughness test. *Composites 2009 - 2nd ECCOMAS Thematic Conference on the Mechanical Response of Composites* April 1^{st}-3^{rd} 2009, London, UK

4. L. Távara, V. Mantič, A. Salvadori, L.J. Gray, F. París. Implementation of a symmetric boundary integral formulation for cohesive cracks in homogeneous media and at interfaces. *BeTeq 2009* July 22^{th}-24^{th} 2009, Athens, Greece

5. L. Távara, V. Mantič, E. Graciani, J. Cañas, F. París. Caracterización de inicio y crecimiento de grietas de interfaz entre fibra y matriz bajo cargas transversales usando el modelo de interfaz débil *COMAT-COMP'09 - V International Conference on Science and Technology of Composite Materials* October 7^{th}-9^{th} 2009, Donostia - San Sebastián, Spain

6. L. Távara, V. Mantič, A. Salvadori, L.J. Gray, F. París. Implementation of a symmetric boundary integral formulation for cohesive cracks in homogeneous media and at interfaces. *Integral Equations: recent numerical developments and new applications* October 29^{th}-30^{th} 2009, Parma, Italy

7. L. Távara, V. Mantič, J.E. Ortiz, F. París. Real-variable expressions of the integral kernels in the 3D somigliana displacement and stress identities for transversely isotropic materials. *Integral Equations: recent numerical developments and new applications* October 29^{th}-30^{th} 2009, Parma, Italy

8. L. Távara, V. Mantič, E. Graciani, F. París. A BEM analysis of the fibre size effect on the debond growth along the fibre-matrix interface. *BeTeq 2010* July 12^{th}-14^{th} 2010, Berlin, Germany

National

1. L. Távara, V. Mantič, E. Graciani, J. Cañas, F. París. Modelado del crecimiento de una grieta en modo I a lo largo de una interfaz débil mediante el MEC. Aplicación al ensayo de fractura interlaminar de materiales compuestos. *XXV Encuentro del GEF* March, 5^{th}-7^{th} 2008, Sigüenza (Spain).

2. L. Távara, V. Mantič, L.J. Gray, F. París, A. Salvadori. Formulation and implementation of cohesive fracture models in the symmetric galerkin boundary element method. Study of mode I crack growth. *XXVI Encuentro del GEF* March, 25^{th}-27^{th} 2009, Santander (Spain).

3. L. Távara, V. Mantič, E. Graciani, F. París. Caracterización de grietas de interfaz entre fibra y matriz bajo cargas transversales uniaxiales usando la teoría de interfaz débil. *MetNum09* June 29^{th} - July 2^{nd} 2009, Barcelona (Spain).